Adapting buildings heating and cooling power need models at the district scale

Loïc Frayssinet

▶ **To cite this version:**

Loïc Frayssinet. Adapting buildings heating and cooling power need models at the district scale. Architecture, space management. Université de Lyon, 2018. English. NNT : 2018LYSEI071 . tel-01988658v2

HAL Id: tel-01988658
https://hal.science/tel-01988658v2

Submitted on 9 Apr 2019

HAL is a multi-disciplinary open access archive for the deposit and dissemination of scientific research documents, whether they are published or not. The documents may come from teaching and research institutions in France or abroad, or from public or private research centers.

L'archive ouverte pluridisciplinaire **HAL**, est destinée au dépôt et à la diffusion de documents scientifiques de niveau recherche, publiés ou non, émanant des établissements d'enseignement et de recherche français ou étrangers, des laboratoires publics ou privés.

N°d'ordre NNT : 2018LYSEI071

THESE de DOCTORAT DE L'UNIVERSITE DE LYON
opérée au sein de
l'**Institut National des Sciences Appliquées de Lyon**

Ecole Doctorale N° 162
Mécanique, Energétique, Génie Civil, Acoustique

Spécialité/ discipline de doctorat :
Thermique Energétique

Soutenue publiquement le 26/10/2018, par :
Loïc Frayssinet

Adapter les modèles de chauffage et climatisation des bâtiments en puissance à l'échelle du quartier

---

Adapting buildings heating and cooling power need models at the district scale

---

Devant le jury composé de :

Fraisse, Gilles	Professeur	LOCIE – Université Savoie Mont Blanc	Rapporteur
Inard, Christian	Professeur	LaSIE – Université de La Rochelle	Rapporteur
Duplessis, Bruno	Maître assistant	CES – Mines ParisTech	Examinateur
Musy, Marjorie	Directrice de recherche	CEREMA / GEM – Ecole Centrale Nantes	Examinateur
Kuznik, Frédéric	Professeur	CETHIL – INSA Lyon	Directeur de thèse
Roux, Jean-Jacques	Professeur	CETHIL – INSA Lyon	Co-directeur de thèse

Cette thèse est accessible à l'adresse : http://theses.insa-lyon.fr/publication/2018LYSEI071/these.pdf
© [L. Frayssinet], [2018], INSA Lyon, tous droits réservés

Département FEDORA – INSA Lyon - Ecoles Doctorales – Quinquennal 2016-2020

SIGLE	ECOLE DOCTORALE	NOM ET COORDONNEES DU RESPONSABLE
CHIMIE	**CHIMIE DE LYON** **http://www.edchimie-lyon.fr** Sec. : Renée EL MELHEM Bât. Blaise PASCAL, 3e étage **secretariat@edchimie-lyon.fr** INSA : R. GOURDON	M. Stéphane DANIELE Institut de recherches sur la catalyse et l'environnement de Lyon IRCELYON-UMR 5256 Équipe CDFA 2 Avenue Albert EINSTEIN 69 626 Villeurbanne CEDEX **directeur@edchimie-lyon.fr**
E.E.A.	**ÉLECTRONIQUE, ÉLECTROTECHNIQUE, AUTOMATIQUE** **http://edeea.ec-lyon.fr** Sec. : M.C. HAVGOUDOUKIAN **ecole-doctorale.eea@ec-lyon.fr**	M. Gérard SCORLETTI École Centrale de Lyon 36 Avenue Guy DE COLLONGUE 69 134 Écully Tél : 04.72.18.60.97 Fax 04.78.43.37.17 **gerard.scorletti@ec-lyon.fr**
E2M2	**ÉVOLUTION, ÉCOSYSTÈME, MICROBIOLOGIE, MODÉLISATION** **http://e2m2.universite-lyon.fr** Sec. : Sylvie ROBERJOT Bât. Atrium, UCB Lyon 1 Tél : 04.72.44.83.62 INSA : H. CHARLES **secretariat.e2m2@univ-lyon1.fr**	M. Philippe NORMAND UMR 5557 Lab. d'Ecologie Microbienne Université Claude Bernard Lyon 1 Bâtiment Mendel 43, boulevard du 11 Novembre 1918 69 622 Villeurbanne CEDEX **philippe.normand@univ-lyon1.fr**
EDISS	**INTERDISCIPLINAIRE SCIENCES-SANTÉ** **http://www.ediss-lyon.fr** Sec. : Sylvie ROBERJOT Bât. Atrium, UCB Lyon 1 Tél : 04.72.44.83.62 INSA : M. LAGARDE **secretariat.ediss@univ-lyon1.fr**	Mme Emmanuelle CANET-SOULAS INSERM U1060, CarMeN lab, Univ. Lyon 1 Bâtiment IMBL 11 Avenue Jean CAPELLE INSA de Lyon 69 621 Villeurbanne Tél : 04.72.68.49.09 Fax : 04.72.68.49.16 **emmanuelle.canet@univ-lyon1.fr**
INFOMATHS	**INFORMATIQUE ET MATHÉMATIQUES** **http://edinfomaths.universite-lyon.fr** Sec. : Renée EL MELHEM Bât. Blaise PASCAL, 3e étage Tél : 04.72.43.80.46 Fax : 04.72.43.16.87 **infomaths@univ-lyon1.fr**	M. Luca ZAMBONI Bât. Braconnier 43 Boulevard du 11 novembre 1918 69 622 Villeurbanne CEDEX Tél : 04.26.23.45.52 **zamboni@maths.univ-lyon1.fr**
Matériaux	**MATÉRIAUX DE LYON** **http://ed34.universite-lyon.fr** Sec. : Marion COMBE Tél : 04.72.43.71.70 Fax : 04.72.43.87.12 Bât. Direction **ed.materiaux@insa-lyon.fr**	M. Jean-Yves BUFFIÈRE INSA de Lyon MATEIS - Bât. Saint-Exupéry 7 Avenue Jean CAPELLE 69 621 Villeurbanne CEDEX Tél : 04.72.43.71.70 Fax : 04.72.43.85.28 **jean-yves.buffiere@insa-lyon.fr**
MEGA	**MÉCANIQUE, ÉNERGÉTIQUE, GÉNIE CIVIL, ACOUSTIQUE** **http://edmega.universite-lyon.fr** Sec. : Marion COMBE Tél : 04.72.43.71.70 Fax : 04.72.43.87.12 Bât. Direction **mega@insa-lyon.fr**	M. Jocelyn BONJOUR INSA de Lyon Laboratoire CETHIL Bâtiment Sadi-Carnot 9, rue de la Physique 69 621 Villeurbanne CEDEX **jocelyn.bonjour@insa-lyon.fr**
ScSo	**ScSo*** **http://ed483.univ-lyon2.fr** Sec. : Viviane POLSINELLI Brigitte DUBOIS INSA : J.Y. TOUSSAINT Tél : 04.78.69.72.76 **viviane.polsinelli@univ-lyon2.fr**	M. Christian MONTES Université Lyon 2 86 Rue Pasteur 69 365 Lyon CEDEX 07 **christian.montes@univ-lyon2.fr**

*ScSo : Histoire, Géographie, Aménagement, Urbanisme, Archéologie, Science politique, Sociologie, Anthropologie

Cette thèse est accessible à l'adresse : http://theses.insa-lyon.fr/publication/2018LYSEI071/these.pdf
© [L. Frayssinet], [2018], INSA Lyon, tous droits réservés

Adapting building heating and cooling power need models at the district scale

Abstract

District-scale building energy models are generally simplified to cope with a lack of data and to reduce computational cost. However, the impacts of these simplifications on model accuracy are not systematically studied, particularly when considering power demand.

The present manuscript introduces a methodology to determine the suitability of any simplifications, notably those at the district scale, and considering the power demand. This methodology was applied to usual simplifications of the building envelope model thanks to a specific platform developed in the frame of this thesis. This platform enables automatically generating and simulating building energy models with different modelling levels of detail from geographical information systems. The parallelisation of the building energy simulations was notably implemented at the district scale in order to benefit from the model structure and to efficiently reduce the computational duration.

The definition of indicators related to specific simulation objectives appears to be a necessary step when focusing on power demand. The results show a higher sensitivity to simplifications of the power demand than the annual energy consumption. These effects are quantified and physically analysed. The district-scale ability to attenuate the impacts of simplifications and to integrate statistical sources of data were demonstrated. The resulting quantification of the impacts of the simplifications made it possible to guide the adaptations of models to the simulation objectives and to the technical constraints. Such contribution aims to increase the efficiency and to favour the development of city-scale energy simulations, which are particularly needed to cope with future challenges.

Cette thèse est accessible à l'adresse : http://theses.insa-lyon.fr/publication/2018LYSEI071/these.pdf
© [L. Frayssinet], [2018], INSA Lyon, tous droits réservés

Résumé

Les modèles énergétiques des bâtiments à l'échelle du quartier sont généralement simplifiés pour faire face au manque de données et pour réduire le coût de calcul. Cependant, l'impact de ces simplifications sur la validité des modèles n'est pas systématiquement analysée, en particulier lorsqu'on s'intéresse à la courbe de charge.

Pour combler ce manque, une méthodologie permettant de quantifier la validité des simplifications, notamment vis-à-vis de la courbe de charge, est proposée. Cette méthodologie est appliquée aux simplifications couramment utilisée pour les modèles thermiques d'enveloppe de bâtiments grâce à une plateforme numérique développée dans le cadre de cette thèse. Cette plateforme permet de générer et simuler automatiquement des modèles énergétiques de bâtiments, avec différents niveaux de détails, à partir de données issues de systèmes d'information géographique. La parallélisation des simulations énergétiques des bâtiments est utilisée à l'échelle du quartier, afin de tirer avantage de la structure du modèle global et de réduire les temps de calculs.

La définition d'indicateurs spécifiques selon l'objectif de simulation apparait clairement comme l'étape essentielle lorsque l'on s'intéresse à la courbe de charge. Les résultats indiquent que la puissance est plus sensible aux simplifications que la consommation annuelle d'énergie. Les différents effets induits sont quantifiés et analysés physiquement. La capacité de l'échelle du quartier à atténuer les impacts des simplifications et d'intégrer les données statistiques est démontrée. La quantification des impacts des simplifications permet de guider l'adaptation des modèles vis-à-vis des objectifs de simulation et vis-à-vis des contraintes techniques. Cette contribution a pour objectif d'améliorer la performance des simulations énergétiques à l'échelle de la ville, et de favoriser leur développement, afin de répondre aux enjeux futurs.

Cette thèse est accessible à l'adresse : http://theses.insa-lyon.fr/publication/2018LYSEI071/these.pdf
© [L. Frayssinet], [2018], INSA Lyon, tous droits réservés

Remerciements

Je remercie en premier lieu mes directeurs de thèses de m'avoir donné l'opportunité de travailler et d'approfondir ce sujet passionnant et prometteur qu'est la thermique du bâtiment et pour la liberté et l'autonomie qu'ils ont su m'accorder.

Je remercie vivement les membres du jury pour leur relecture et leurs retours enrichissants.

Je tiens aussi à remercier mes encadrants d'EDF : Maya Milliez, pour la première partie de ma thèse, et Jean-Luc Hubert, qui m'ont ouvert de nombreuses portes au sein des différents groupes d'EDF et plus largement de l'écosystème professionnel de l'énergétique du bâtiment et ainsi permis d'élargir mon domaine d'action.

Toujours au sein d'EDF, j'ai réellement apprécié les rencontres et les échanges avec l'ex-équipe EnerBat, en particulier avec Mathias Bouquerel, Mathieu Schumann, Hassan Bouia et Benoit Charrier. Je mets volontairement Denis Covalet à part, pour le remercier particulièrement pour son aide méthodique et efficace dans l'encadrement du stage de Mustapha Ouhimd, malgré les nombreux rebondissements techniques. Merci aussi à Mustapha pour la pérennisation de mes développements.

Je change de centre de R&D pour remercier très chaleureusement Jean-Philippe Tavella pour sa disponibilité, sa patience et sa compréhension lors de nos nombreux allers-retours (formateurs !) pour l'utilisation de DACCOSIM.

Je reste en région parisienne pour remercier Thomas Berthou pour les échanges enrichissants et fructueux que nous avons pu avoir notamment grâce au cas d'étude auquel il m'a permis d'accéder.

Revenons au CETHIL avec une attention particulière pour le service administratif du labo, sans qui rien ne serait possible ! Merci en particulier à Sophie Grenier, Elisa Serin, Florence Canale et Nazaré Marques. Même si je n'ai pas eu à travailler avec eux, je remercie l'équipe de l'atelier pour leur bonne humeur et leur sympathie contagieuse.

Je remercie l'ensemble des membres du laboratoire, et plus spécifiquement l'ex-groupe bâtiment, Abdelkrim Trabelsi, Christian Obrecht, Damien David, Kevyn Johannes et Etienne Vergnault, pour nos échanges et leurs conseils, et plus particulièrement les deux derniers, pour la découverte des sentiers de VTT dans les monts d'or. Je n'oublie évidemment pas Lucie Merlier, que je tiens à remercier tout particulièrement pour l'aide, le soutien –plus que bienvenus- qu'elle a pu m'apporter lors de cette thèse, ainsi que pour son dynamisme, sa persévérance et même son exigence ! Je lui souhaite une très bonne continuation pour la suite de sa carrière, qui sera, j'en suis sûr, prometteuse.

Je tiens à remercier les convives du CNRS, notamment Serge Buathier, Cédric Galizzi, Loïc Guilmard et Anthony Buthod pour ces moments conviviaux de détente, auxquels j'inclue bien volontiers Manuel Kuhni pour sa grande sympathie.

J'ai évidemment une pensée particulière pour mes collègues doctorants pour les bons moments passés ensemble et les franches rigolades. Dans le désordre le plus total, merci à Abdou, Martin, Eloïse, Remi, Kévin, Francesco, Claudia, Loïc, Damien ($\times$2), Khriscia, Nicolas, Christophe, Julie, Sébastien, Chi Kien, Ghady, Hazem, Ali, Etienne, Aurélia, Sandra, Adrien, Bao, Samuel et Luyi. Je mets évidemment à part mes ex-co-bureaux, les docteurs Quenret Moutin et Thissac Laybaut, qui ont œuvré dur pour égailler au quotidien ma thèse. Merci les amis !

Cette thèse est accessible à l'adresse : http://theses.insa-lyon.fr/publication/2018LYSEI071/these.pdf
© [L. Frayssinet], [2018], INSA Lyon, tous droits réservés

Enfin, je ne pourrai conclure sans penser à mes amis de plus longue date et à toute ma famille et belle-famille, toujours à mes côtés et attentionnée, avec une pensée particulière pour ma femme et notre bébé, ainsi qu'à mes grands-parents, mon frère et mes parents.

Cette thèse est accessible à l'adresse : http://theses.insa-lyon.fr/publication/2018LYSEI071/these.pdf
© [L. Frayssinet], [2018], INSA Lyon, tous droits réservés

Contents

Cette thèse est accessible à l'adresse : http://theses.insa-lyon.fr/publication/2018LYSEI071/these.pdf
© [L. Frayssinet], [2018], INSA Lyon, tous droits réservés

Cette thèse est accessible à l'adresse : http://theses.insa-lyon.fr/publication/2018LYSEI071/these.pdf
© [L. Frayssinet], [2018], INSA Lyon, tous droits réservés

Cette thèse est accessible à l'adresse : http://theses.insa-lyon.fr/publication/2018LYSEI071/these.pdf
© [L. Frayssinet], [2018], INSA Lyon, tous droits réservés

Cette thèse est accessible à l'adresse : http://theses.insa-lyon.fr/publication/2018LYSEI071/these.pdf
© [L. Frayssinet], [2018], INSA Lyon, tous droits réservés

List of Abbreviations

BEM	**B**uilding **E**nergy **M**odel
BIM	**B**uilding **I**nformation **M**odel
CES	**C**ity **E**nergy **S**imulation
CHTC	**C**onvective **H**eat **T**ransfer **C**oefficient
DEM	**D**istrict **E**nergy **M**odel
FMI	**F**unctional **M**ockup **I**nterface
FMU	**F**unctional **M**ockup **U**nit
GHG	**G**reen**H**ouse **G**ases
GIS	**G**eographic **I**nformation **S**ystem
LoD	**L**evel **o**f **D**etail
LW	**L**ong-**W**ave
RC	**R**esistance **C**apacitance
UBES	**U**rban **B**uilding **E**nergy **S**imulation
VOI	**V**ariable **O**f **I**nterest

Subscripts

abs	absorbed
cd	conductive
ctr	controlled
cv	convective
dfh	diffuse horizontal
drn	direct normal
eq	equivalent
ext	external/outside
g	global
gnd	ground
hg	heat gain
in	indoor/internal/inside
$infil$	infiltration
op	operative
out	outdoor
rad	(LW) radiation/radiant
S	surface
sol	solar
tr	transmitted
$vent$	ventilation
win	window

Cette thèse est accessible à l'adresse : http://theses.insa-lyon.fr/publication/2018LYSEI071/these.pdf
© [L. Frayssinet], [2018], INSA Lyon, tous droits réservés

Cette thèse est accessible à l'adresse : http://theses.insa-lyon.fr/publication/2018LYSEI071/these.pdf
© [L. Frayssinet], [2018], INSA Lyon, tous droits réservés

List of Symbols

a	thermal diffusivity	$\mathrm{m^2\,s^{-1}}$
b	reduction coefficient	-
c	specific heat capacity	$\mathrm{J\,kg^{-1}\,K^{-1}}$
E	Energy	J
e	thickness	m
F	view factor	-
f	frequency	Hz
h	heat transfer coefficient	$\mathrm{W\,m^{-2}\,K^{-1}}$
J	radiosity	W
K	air permeability	$\mathrm{m^3\,s^{-1}\,Pa^{-2/3}}$
T	temperature	K or °C
t	time	s
P	(energy system) power	W
p	pressure	Pa
Q	air flow rate	$\mathrm{m^3\,s^{-1}}$
S	area	$\mathrm{m^2}$
U	U-value	$\mathrm{W\,m^{-2}\,K^{-1}}$
V	volume	$\mathrm{m^3}$
v	(wind) velocity	$\mathrm{m\,s^{-1}}$
x	distance	m
α	absorption coefficient	-
ε	emissivity	-
η	(heat exchanger) efficiency	-
θ	transmission coefficient	-
κ	diversity factor	-
λ	thermal conductivity	$\mathrm{W\,m^{-1}\,K^{-1}}$
ρ	density	$\mathrm{kg\,m^{-3}}$
ϱ	reflection coefficient	-
σ	Stefan-Boltzmann constant	$\mathrm{W\,m^{-2}\,K^{-4}}$
τ	characteristic time	s
Φ	(heat) power	W
ϕ	(heat) flux	$\mathrm{W\,m^{-2}}$

Cette thèse est accessible à l'adresse : http://theses.insa-lyon.fr/publication/2018LYSEI071/these.pdf
© [L. Frayssinet], [2018], INSA Lyon, tous droits réservés

Cette thèse est accessible à l'adresse : http://theses.insa-lyon.fr/publication/2018LYSEI071/these.pdf
© [L. Frayssinet], [2018], INSA Lyon, tous droits réservés

Chapter 1

Introduction

Contents

1.1 Urban buildings and district energy models

1.1.1 Context

The energy behaviour of buildings plays many key roles in the major challenges of the future. These roles are emphasized by the considerable global increase in urbanisation.

Importance of cities According to the UN (2014), approximately 3.9 billion people lived in cities in 2014 (66 % of the total population), more than 5 times greater than that in 1950 (30 %). The urban population is expected to increase by 66 % until 2050. As a consequence, the number of cities and their size will increase. This urban sprawl has many harmful consequences, such as the worrying loss of biodiversity (IPBES, 2016) and the exacerbation of natural disasters, notably via the increase of the exposure (GFDRR, 2016), as such flooding and heat waves. These consequences impact the environment and public health. Heat waves are particularly related to urban physics and building energy behaviour, because of the urban heat island effect (Oke, 1982).

Energy issues Issues directly related to energy are particularly crucial with respect to global warming mitigation specification. Indeed, in 2015, more than 80 % of the world primary source of energy relies on combustion of fossil fuels (IEA, 2017), contributing to 65 % of the greenhouse gases (GHG) emissions (IPCC, 2014).

To cope with global warming, the international community had committed to the Paris agreements to *'[hold] the increase in the global average temperature to well below 2 °C above pre-industrial levels'* (UN, 2015). Concretely, this commitment implies not emitting more than about 1.000 $Gt_{eq.CO_2}$ of greenhouse gases during the following

Cette thèse est accessible à l'adresse : http://theses.insa-lyon.fr/publication/2018LYSEI071/these.pdf
© [L. Frayssinet], [2018], INSA Lyon, tous droits réservés

years (IPCC, 2014). Such constraint notably implies to drastically change the whole global energy paradigm, and more generally our behaviour, because of their dependency on fossil fuels. To highlight the importance of the necessary changes and their urgency, today, the annual GHG emissions rate, continuously increasing over the time, is approximately 50 $\mathrm{Gt}_{\mathrm{eq.CO_2}}/\mathrm{year}$. Hence, at constant emissions, the budget will be entirely consumed within only 20 years. This situation is even more urgent given that the increase of the GHG emissions is historically linked to the population growth (IPCC, 2014). Mitigation of global warming is hence clearly a daunting task, and even more worrying that global warming exacerbates previous issues. However, it can be seen as a motivating opportunity to built and reinvent a sustainable and responsible world.

The key role of the building sector The building sector is concerned by both urbanisation and energy issues. It has been particularly identified as a priority target for mitigation strategies as it belongs to the major contributor to GHG emissions, with 19 % of the worldwide energy GHG emissions[1], and even more in developed countries (in Europe for instance), whereas this emissions may be strongly and efficiently reduced (IPCC, 2014).

The main source of reduction, which is particularly economically interesting and currently available, may be reached thanks to building insulation. The use of efficient energy systems, and the optimisation of their design, in concert with optimal building design also belong to *final energy reduction* mitigation measures.

Reductions of GHG emissions may also be achieved thanks to *switch* the energy used in buildings *to low-carbon energy carriers* coming from renewable sources of energy. District scale implementation offers advantages for the integration of these sources. Indeed, energy production may be shared via networks. Furthermore, sharing generally makes it possible to reduce the size of the global system, potentially including energy storage, compared to individual distributed systems and to optimize operation. Moreover, it is suitable to integrate intermittent renewable energy with *smart grids*. Smart grids aim to manage energy consumption and production from one building to other.

Need for tools In order to support these changes, tools are expected by city decisions makers and urban and building planners to guide their choices and their practices consistent with previous issues. As these issues are related to urban buildings and district-level energy behaviour, their modelling is crucial.

1.1.2 State of the art

The increasing need for urban buildings and district energy models is highlighted by Keirstead, Jennings, and Sivakumar (2012). They identified 219 research papers concerning urban energy models within the past 30 years. Heating and cooling energy demand models for urban buildings were reviewed by the author (Frayssinet et al., 2018b). Main outlines of this article, available in Appendix D, are briefly summarized below. Heating and cooling were addressed as the issues previously identified are mainly related to these energy uses.

[1] It includes direct, produced within the building, and indirect, produced out of the building, emissions, related to electricity and heat used in buildings. Emissions associated to the material embodied energy (cement and steel productions for example) are also target of reduction, but are accounted in the industry sector.

Cette thèse est accessible à l'adresse : http://theses.insa-lyon.fr/publication/2018LYSEI071/these.pdf
© [L. Frayssinet], [2018], INSA Lyon, tous droits réservés

Among the different existing approaches, only the *micro-simulation* category, belonging to *engineering bottom-up* approaches, is retained. *Engineering* models are based on physical phenomena. As a consequence, only this approach is able to test different scenarios, with changes in the envelope (refurbishment) or of the energy system, for example. Moreover, possible technological breakthroughs may be modelled. In contrast with *statistical* or data-driven models, which are based on historical data. Furthermore, district *micro-simulations* explicitly model all buildings in the district. This approach make it possible to spatially analyse the results.

In this approach, 3 main simulation objective categories were identified (Fig. 1.1):

(A) Studying the interactions of buildings with the urban environment;

(B) Estimating the energy consumption of buildings;

(C) Simulating the power demand.

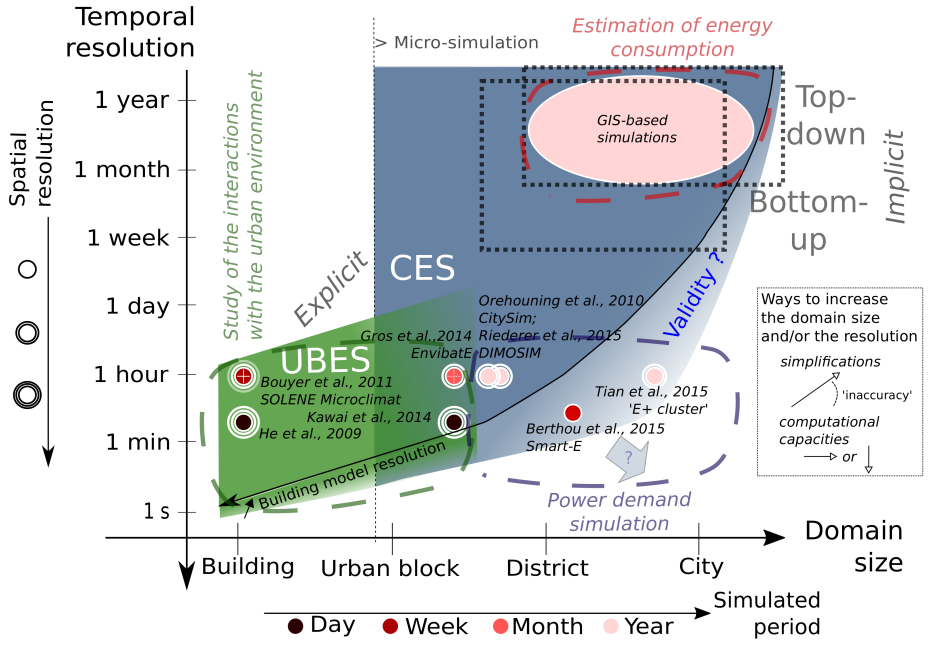

FIGURE 1.1: Comparison of the domains of availability of the different categories of energy simulation of urban buildings (From (Frayssinet et al., 2018b))

These simulation objectives effectively aim to answer building issues introduced hereafter. For instance, for some representative tools, belong these identified in (Frayssinet et al., 2018b), their objectives are:

(A) *'[to quantify] the influences of outdoor configurations and surface materials on indoor and outdoor environments'* (He, Hoyano, and Asawa, 2009) or *'to evaluate the microscale urban planning elements impact on the energy behaviour of target buildings'* (Bouyer, Inard, and Musy, 2011)–related to the consequences of the urban development on the indoor and outdoor conditions for energy, comfort and public health considerations.

Cette thèse est accessible à l'adresse : http://theses.insa-lyon.fr/publication/2018LYSEI071/these.pdf
© [L. Frayssinet], [2018], INSA Lyon, tous droits réservés

(B) *'to predict the heating energy demand of urban districts and analyze strategies for improving building standard'* (Strzalka et al., 2011) or *'to obtain a city-wide energy mapping of the (residential) built environment'* (Agugiaro, 2015)–related to the identification of building energy saving potential.

(C) *'to help short-term grid balance'* with respect to *'demand response strategies implemented on residential buildings in a smart grid context'* (Berthou et al., 2015) or to consider *'local energy system for heating, cooling and domestic hot water preparation, thermal networks as well as local and/or central energy production and storage'* of buildings (Riederer et al., 2015)–related to the integration of renewable sources of energy.

1.1.3 Issues

However, micro-simulations face the 2 main following technical issues:

- First, as all buildings of the district are explicitly modelled, numerous simulations have to be run, leading to a high computational cost, which is potentially prohibitive.
- Second, large amounts of data are needed to feed the models, but the data availability is often limited (numerous unknowns) or incoherent (i.e., statistical data for deterministic models).

These issues particularly concern the C-category as these models have a high spatial and temporal resolution (detailed models), a large spatial domain and often a long simulation period.

To cope with these limitations, the solution is generally to simplify the model, in order to reduce the computational cost and the needed data (as for the A-category). This strategy is evidenced by the numerous simplifications, specifically developed for district energy models, proposed in the literature. As identified in (Frayssinet et al., 2018b), these simplifications mainly concern radiation modelling, urban climate modelling and envelope modelling. The development of statistical models (Swan and Ugursal, 2009) is an alternative but is not compatible with micro-simulations.

1.2 Field of study

1.2.1 Main issues

As seen before, current city energy models, regardless of approach, necessarily rely on different kinds of simplifications. However, *are the simplifications suitable?* This question is particularly crucial for the C-category, as the need of simplifications is high, due to identified technical issues, simultaneously with the expected level of detail (Fig. 1.1). The main objective of this work is to *study the simplifications suitability*.

The main simplifications of building and district models are first identified in Chapter 2, thanks to a detailed review of the modelling process. Then, the methodology developed to analyse the *suitability* of these simplifications is introduced in Chapter 3. The tool chain developed to test the suitability of the main simplifications is detailed in Chapter 4, and is then applied to case studies in Chapter 5, first at

Cette thèse est accessible à l'adresse : http://theses.insa-lyon.fr/publication/2018LYSEI071/these.pdf
© [L. Frayssinet], [2018], INSA Lyon, tous droits réservés

the building scale and then at the district scale. The final chapter discusses the main results and open perspectives[2].

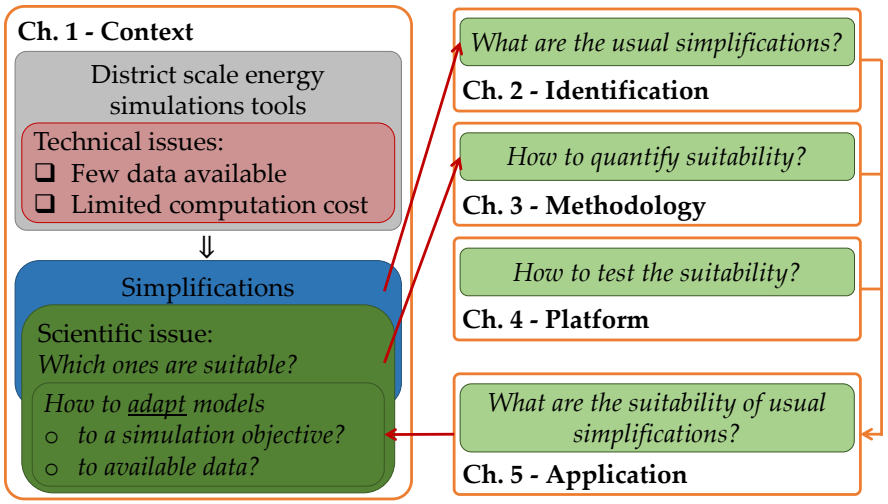

FIGURE 1.2: Contents sketch

These steps aim to answer the following scientific issue: *how to build a district energy model given technical issues*? This issue is further analysed during the methodology definition, notably in Sec. 3.1.2. Answering such issue may guide the development of district energy micro-simulations, for the C-category in particular, which is critical with respect to technical issues.

1.2.2 Scope of the study

As building thermal behaviour is the most expensive part of energy simulations and hence the main target of simplification (see Chap. 2), only **envelope modelling** and directly related phenomena are addressed in the present work (Fig. 1.3). As a result, only the building energy consumption related to the envelope is considered, which corresponds to **heating and cooling** (and excludes others energy uses such as domestic hot water, lighting and others electric appliances). More precisely, this consumption corresponds to **energy needs**, as no energy system is modelled (see Chap. 2). In reality, the needs differ from consumption due to system energy behaviour (regulation, inertia, yield, etc.).

As a consequence, as the models used focus only on envelope modelling, the simulation results probably deviate from reality as occupant and energy system interactions are not accounted for. However, in the frame of this work, the objective is first to better model the envelopes to then integrate them in a comprehensive model.

1.2.3 Glossary

The district scale is addressed rather than the city scale. There is no common definition of the district scale. In the present manuscript, the district scale is considered starting when a *certain representativeness* appears (see Sec. 3.2.4). The city scale is then simply a assembly of districts.

[2]The chapters are quite independent. Readers can directly go to the chapter that concerns their interest (methodology, modelling, platform, results). Prerequisites are clearly identified and referenced to the corresponding section.

Cette thèse est accessible à l'adresse : http://theses.insa-lyon.fr/publication/2018LYSEI071/these.pdf
© [L. Frayssinet], [2018], INSA Lyon, tous droits réservés

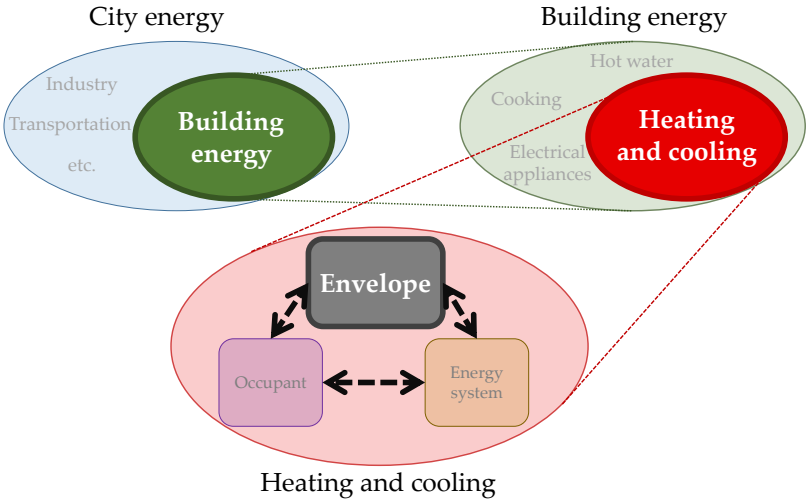

FIGURE 1.3: Scope of the study

The term *power* corresponds to the instant energy variation. In order to simplify the writing, the term *power* is voluntary improperly used to indicate mean power when it is estimated during the shortest time-steps (usually an hour), whereas it not corresponds to the real definition of the word which is the instant energy variation.

Cette thèse est accessible à l'adresse : http://theses.insa-lyon.fr/publication/2018LYSEI071/these.pdf
© [L. Frayssinet], [2018], INSA Lyon, tous droits réservés

Chapter 2

Building to district energy model

Contents

In order to identify the common simplifications used in building and district energy models, this chapter introduces the modelling principles and details retained in the developed modelling platform (Chap. 4). In the following, the different variants of these modelling assumption are identified and associated with a specific label written in blue in square brackets: [label]. These assumptions are summarized in Appendix B to ease later references.

2.1 Building energy model

The basic principle of a building energy model[1] (BEM) relies on the separation of the building into different type of elements, essentially, air volumes and walls (Fig. 2.1). These elements are then associated with specific equations that describe their energy behaviour, including the related energy transfers with other adjacent elements. The whole BEM simply consists of the assembly of the sets of equations, as described in this chapter.

[1] Based on engineering model, also called *white-box* model.

Cette thèse est accessible à l'adresse : http://theses.insa-lyon.fr/publication/2018LYSEI071/these.pdf
© [L. Frayssinet], [2018], INSA Lyon, tous droits réservés

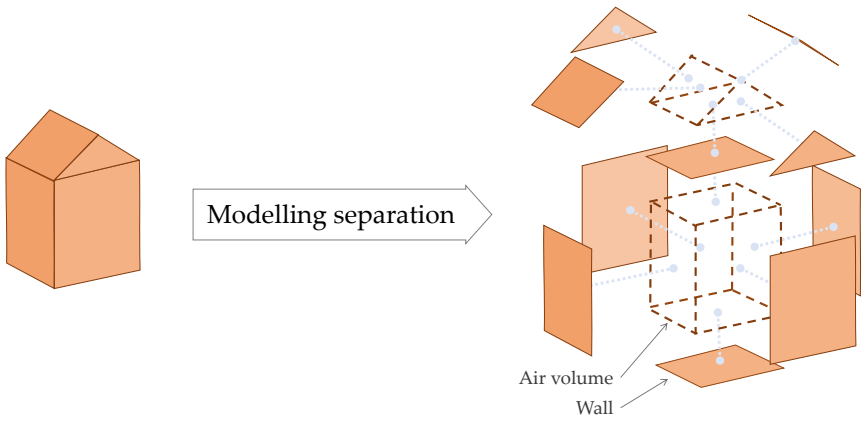

FIGURE 2.1: Example of building energy model separation

Zoning The separation of the building depends of the desired level of detail, the simulation objective and the data availability, but it is advised to differentiate air volumes, called *thermal zones*, having different thermal behaviour. The thermal behaviour of a zone notably depends on the setpoint temperature and its internal heat gains (including solar heat gains that depend on the zone orientation of window positions). The coarsest BEM may consider a unique volume for the whole building and these are called *monozone* models in contrast with *multizone* models. Because of a general lack of detailed data at the city scale, the default BEM is monozone [Zoning-0]. The following arbitrary zoning configurations are also considered (Fig. 2.2):

- Floor zoning: each level is associated to a thermal zone [Zoning-lvl];
- Orientation zoning: each wall orientation is associated to an adjacent thermal zone [Zoning-ori];
- Combined zoning: a combination of the two previous zoning [Zoning-cmb].

In the first case, the zone interface walls are the floors; if unknown, the number of stories is deduced based on the usual ceiling height. In the second case, the orientation zoning is defined according to the ASHRAE 90.1 appendix G as used by Dogan, Reinhart, and Michalatos (2014), and the interface walls are fictional partitions.

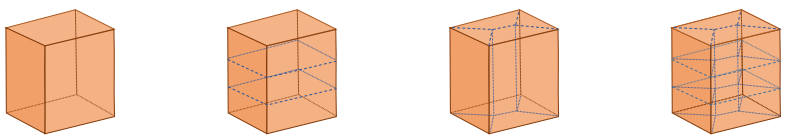

(A) Zoning-0 (B) Zoning-lvl (C) Zoning-ori (D) Zoning-cmb

FIGURE 2.2: Zoning variants

Facade The walls, defined during the building separation, are partitions or interior floors, possibly fictional, when they separate thermal zones, and are roofs, exterior

Cette thèse est accessible à l'adresse : http://theses.insa-lyon.fr/publication/2018LYSEI071/these.pdf
© [L. Frayssinet], [2018], INSA Lyon, tous droits réservés

floors or part of the facade when they separate a zone from the exterior. In this last case, a facade may contain 2 different elements, namely, opaque and transparent walls (i.e., walls and windows). Consequently, in the modelling process, the facade element is split into 2 parts, walls and windows, depending on their respective dimensions (Fig. 2.3). In the following, the term *wall* refers to the global category (wall and windows), but the modelling specificities of windows are specifically detailed later (Sec. 2.1.2).

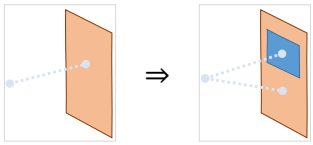

FIGURE 2.3: Separation of a facade containing walls and windows

Note concerning the description of heat transfers.

In order to make this formal part more accessible, in the figures and in the text, we choose to consider the heating period to describe the common direction of the heat transfers as it is well experienced by many people, where energy consumption related to building air conditioning is dominant, notably in Europe. During this period, buildings lose heat: it goes from inside (hot) to outside (cold). In some configurations, the heat flow can be in the reverse side. This case occurs when wall interior temperature becomes higher than the air temperature. For example, if an inside face of a wall is overheated by transmitted solar flux or for internal walls, when the air temperature decreases as these walls have higher thermal inertia. However, this fact does not change the equations introduced hereafter, and the flow simply becomes negative. Therefore, for the sake of simplicity, and in order to avoid redundancies, the behaviour in these particular periods and in summer are not detailed.

2.1.1 Air volume energy balance

Let us start with a thermal zone of the building decomposition. It is assumed that the properties of the air volume (V_{air} [m^3]) are spatially homogeneous, in particular the temperature ($T_{air.in}$ [K]) . This assumption is relevant if the volume is well mixed, which is the case in a usual room, notably because of the activities of inner occupants[2]. Note that only sensible heat transfers are modelled, and moisture and related latent heat transfers are neglected, hence, following energy balances only concerns the sensible part. This assumption is often used in BEM but may causes non-negligible biases, in particular in humid climate, for cooling, and for hygroscopic materials (Mendes et al., 2003).

In winter, it is clear that heating is necessary to keep the indoor temperature within comfort range as the temperature otherwise tends to decrease because of heat loss.

Internal convective heat transfer In most existing buildings (which are not energetically efficient), the majority of the heat loss is due to envelope losses. The heat of the air volume is released towards the surrounding walls through convection. The

[2]However, this assumption may be inappropriate in cases with high ceiling heights because of temperature stratification. In these cases, which are not considered here, detailed models using zonal approaches or computational fluid dynamics methods are needed.

Cette thèse est accessible à l'adresse : http://theses.insa-lyon.fr/publication/2018LYSEI071/these.pdf
© [L. Frayssinet], [2018], INSA Lyon, tous droits réservés

resulting heat flow between the air volume and any surrounding wall i ($\Phi_{cv.in}^{(i)}$ [W]) are modelled using Newton's law:

$$\Phi_{cv.in}^{(i)} = h_{cv.in} \cdot S^{(i)} \cdot (T_{air.in} - T_{S.in}^{(i)}) \tag{2.1}$$

where $h_{cv.in}$ [$\mathrm{W\,m^{-2}\,K^{-1}}$] is the internal convective heat transfer coefficient (CHTC) and $S^{(i)}$ [$\mathrm{m^2}$] and $T_{S.in}^{(i)}$ [K] represent the inside area and the inside wall surface temperature of the wall i, respectively .

Air renewal Heat loss also comes from air renewal caused by controlled ventilation and infiltration. The resulting heat flux induced by ventilation (Φ_{vent} [W]) is:

$$\Phi_{vent} = \rho_{air} \cdot Q_{air} \cdot c_{air} \cdot (T_{air.in} - T_{inlet}) \tag{2.2}$$

where Q_{air} [$\mathrm{m^3\,s^{-1}}$] is the air flow rate generated by the venting system; ρ_{air} [$\mathrm{kg\,m^{-3}}$] and c_{air} [$\mathrm{J\,kg^{-1}\,K^{-1}}$] represent the air density and specific heat capacity, respectively; and T_{inlet} [K] represents the inlet air temperature. In our model, air flows between thermal zones are not considered. As a consequence, the inlet temperature is equal to the outdoor air temperature ($T_{air,out}$ [K]) in the case of infiltrations and simple mechanical ventilation[3]. In case of a cross-flow ventilation the inlet air temperature is warmed up by the exhaust air, leading to the following relations: $T_{air.out} < T_{inlet} < T_{air.in}$. Knowing the efficiency of the heat exchanger system ($\eta = \frac{T_{inlet} - T_{air.out}}{T_{air.in} - T_{air.out}}$), it is possible to write the following:

$$\Phi_{vent} = (1 - \eta) \cdot \rho_{air} \cdot Q_{air} \cdot c_{air} \cdot (T_{air.in} - T_{air.out}) \tag{2.3}$$

In most BEMs, infiltration is not modelled [Infil-0] or coarsely considered with an arbitrary constant flow rate, whereas infiltration strongly depends on external wind conditions. Their flow rate can be estimated using a mass balance of the indoor volume [Infil-1]. For a thermal zone surrounded by N walls, numbered from 1 to N, we get:

$$\sum_{i=1}^{N} Q_{infil}^{(i)} = \sum_{i=1}^{N} K^{(i)} \cdot \Delta p^{(i)2/3} = 0 \tag{2.4}$$

where $Q_{infil}^{(i)}$ [$\mathrm{m^3\,s^{-1}}$] is the infiltration flow rate through the wall i, $K^{(i)}$ [$\mathrm{m^3\,s^{-1}\,Pa^{-2/3}}$] is its permeability, and $\Delta p^{(i)}$ [Pa] is the pressure difference between its outside and inside faces. In order to compute the air pressures, it is necessary to consider aeraulic variables and specific related models, which can strongly increase the computational cost. Possible methods are indicated in Sec. 5.1.4 as this section concerns environmental variables modelling.

Similarly than previously (Eg. 2.2), the corresponding heat losses are (Φ_{infil} [W]):

$$\Phi_{infil} = \rho_{air} \cdot Q_{infil} \cdot c_{air} \cdot (T_{air.in} - T_{air.out}) = \rho_{air} \cdot c_{air} \cdot (T_{air.in} - T_{air.out}) \cdot \frac{1}{2} \sum_{i=1}^{N} |Q_{infil}^{(i)}| \tag{2.5}$$

The $\frac{1}{2}$ factor indicates that half of the infiltration enters the air volume while the other part leaves because of dry air mass conservation.

[3] Complementary, it is assumed that thermal zones are not lower than a housing to avoid case were the exhausted air flow of a room comes from surroundings.

Cette thèse est accessible à l'adresse : http://theses.insa-lyon.fr/publication/2018LYSEI071/these.pdf
© [L. Frayssinet], [2018], INSA Lyon, tous droits réservés

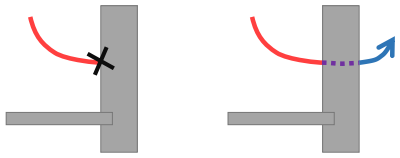

(A) Infil-0 (B) Infil-1

FIGURE 2.4: Infiltration model variants

Heat gains In contrast to heat losses, the air volume is heated by the convective part of the energy system (P [W]) and internal heat gains (Φ_{hg} [W]). These heat gains notably come from human metabolism and various indoor uses and are often linked with occupant behaviour (cooking, electrical appliances, etc.). The temporal dynamics of these heat flows are usually modelled using standard schedules or a specific occupant model in more advanced approaches (detailed in Sec. 4.2.1). As envelope behaviour is focused on in this work, and to prevent internal heat gains 'perturbations', these heat gains were coarsely accounted for with a constant mean value (excepted in the specific analysis in Sec. 5.2.4).

Energy balance Finally, the air volume energy balance of a thermal zone surrounded by N walls is as follows:

$$P + \Phi_{hg} - \Phi_{vent} - \Phi_{infil} - \sum_{i}^{N} \Phi_{cv.in}^{(i)} = \rho_{air} \cdot V_{air} \cdot c_{air} \cdot \frac{\partial T_{air.in}}{\partial t} \tag{2.6}$$

Note that all flows and temperatures are implicitly time dependant and characteristics constant, except if otherwise specified. The right part of the equation corresponds to the variation of the stored thermal energy within the zone air volume, which buffers the variation of the indoor air temperature (inertia). As its characteristic time is generally much lower than the time-step, this element is often neglected.

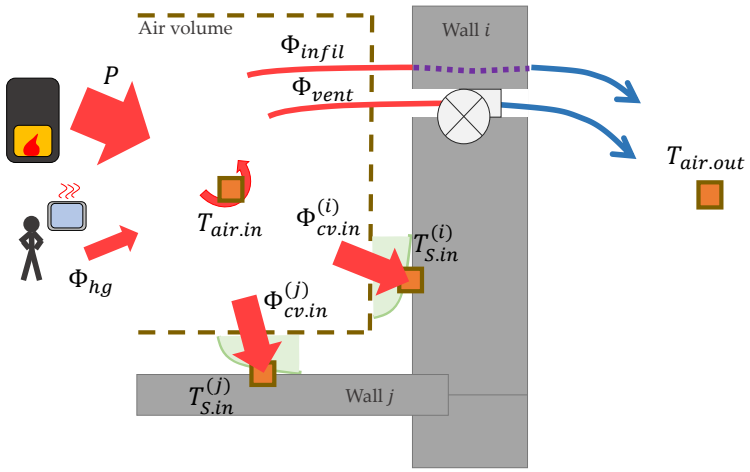

FIGURE 2.5: Air volume energy balance

Two solution strategies are available for the previous equation:

Cette thèse est accessible à l'adresse : http://theses.insa-lyon.fr/publication/2018LYSEI071/these.pdf
© [L. Frayssinet], [2018], INSA Lyon, tous droits réservés

(1) Either $T_{air.in}$ is fixed, and consequently, P is unknown – conditioned mode.

(2) Either P is known, and consequently, $T_{air.in}$ is unknown – free floating mode.

During heating periods, the objective of the heating system is to keep the controlled temperature ($T_{ctr.in}$) to a specific setpoint ($T_{ctr.in} = T_{setpoint}$), which consists of the first possibility. Hence, P corresponds to the power that completes the internal heat gains in order to counter balance the losses and consequently keeps $T_{ctr.in}$ at the setpoint. This case refers to the *ideal* energy needs of the building. In reality, the energy system is regulated, and the regulation is not perfect: rather, the indoor air temperature moves around the setpoint. Furthermore, the controlled temperature is generally assumed to be $T_{air.in}$ [Control-0], but in real energy systems, this controlled temperature is much more closer to the operative temperature ($T_{op.in}$ [K]) [Control-1], which is approximated by the mean of the air and the averaged inside surface temperatures (defined more precisely in the following). Moreover, comfort considerations are more related to the operative temperature than the air temperature.

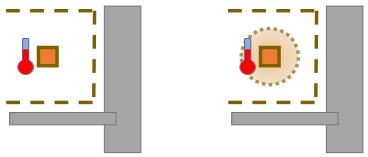

(A) Control-0 (B) Control-1

FIGURE 2.6: Controlled temperature variants

With the first solving strategy, as regulation is not modelled when considering ideal needs, only the heating needs related to the thermal behaviour of the envelope are considered via P. However, the second strategy notably occurs during floating temperature periods, when the indoor air temperature is lower than the setpoint, and consequently P is null.

In order to prevent changes in the solving strategy during simulation depending on the indoor air temperature value, in practice, P is always known and $T_{air.in}$ unknown. Indeed, a (proportional-integral) estimator, knowing the past temperature variations, estimates the ideal needs so that the resulting indoor temperature equals the setpoint during heating periods. The indoor air temperature is deduced by solving Eq. 2.6 with the power estimated by the estimator. If well parametrised the regulator leads to negligible residuals, i.e., the regulator accurately estimates the heating needs. During floating temperature periods, the power is simply set to zero.

A useful representation of the equations is to use the following general matrix form:

$$\mathbf{C} \cdot \dot{\mathrm{T}} = \mathbf{A} \cdot \mathrm{T} + \mathbf{B} \cdot \mathrm{U} \tag{2.7}$$

where T is the unknown vector, U is the solicitation vector, $\mathbf{C}$ is the capacitance matrix, $\mathbf{A}$ is the conductance matrix and $\mathbf{B}$ is the command matrix.

For the considered air volume energy balance (Eq. 2.6), and similarly for any thermal zones:

Cette thèse est accessible à l'adresse : http://theses.insa-lyon.fr/publication/2018LYSEI071/these.pdf
© [L. Frayssinet], [2018], INSA Lyon, tous droits réservés

$$\begin{cases} \mathrm{T} = \begin{pmatrix} T_{air.in} \\ T_{S.in}^{(1)} \\ \vdots \\ T_{S.in}^{(N)} \end{pmatrix}, \mathrm{U} = \begin{pmatrix} T_{air.out} \\ \Phi_{hg} \\ P \end{pmatrix} \\ \mathbf{C} = \begin{pmatrix} \rho_{air} \cdot V_{air} \cdot c_{air} & 0 & \cdots & 0 \end{pmatrix} \\ \mathbf{A} = \begin{pmatrix} \sum_i^N h_{cv.in} \cdot S^{(i)} + \rho_{air} \cdot ((1-\eta) \cdot Q_{air} + Q_{infil}) \cdot c_{air} & -h_{cv.in} \cdot S^{(1)} \\ & \cdots \quad -h_{cv.in} \cdot S^{(N)} \end{pmatrix} \\ \mathbf{B} = \begin{pmatrix} -\rho_{air} \cdot ((1-\eta) \cdot Q_{air} + Q_{infil}) \cdot c_{air} & 1 & 1 \end{pmatrix} \end{cases}$$

The variables of the solicitation vector are respectively known from the weather file, the occupant behaviour model and the power estimator. This set of equations contains N+1 unknowns (T) and only one equation, which is clearly not enough to solve it. The energy balances of the walls represent the next step in completing the mathematical problem, notably regarding the inside surface temperatures.

2.1.2 Wall energy balance

Additional equations are needed to determine the wall inside surface temperatures and hence the convective heat losses through them. Let us consider the wall i that encloses, among others, the previous considered air volume.

Inside wall surface

The inside surface temperature $T_{S.in}^{(i)}$ results from the balance of the received and lost heat fluxes.

Internal convective heat transfer As seen previously, the inside surface of the wall i receives the internal convective heat transfer $\Phi_{cv.in}^{(i)}$ from the air volume (Eq. 2.1).

Absorbed solar flow The inside surface can received and absorbed a part of the solar heat flow transmitted by windows into the thermal zone[4] ($\Phi_{tr.sol}^{(i)}$ [W]) either directly or after reflections on the other internal surfaces. As floors usually receive the greatest part of the transmitted solar heat flow, it is commonly assumed that the whole flow is absorbed by the floors [trSol-0]. Otherwise, part of this flow could be allocated to all internal surfaces according to specific ratios. Most advanced techniques use sun patch tracking methods. For the sake of simplicity, and in order to test the previous assumption, a modelling variant using allocation proportional to respective wall areas is also used [trSol-1].

Internal long-wave radiation Wall inside surfaces can receive long-wave (LW) radiation from the radiative part of the indoor heat gains (not accounted for except in the parameter sensitivity analysis in Sec. 5.1.3) or from other surrounding surfaces. Indeed, a surface j, assumed as a grey body, diffusely emits a flow $\Phi_{LW}^{(j)}$ [W] equal to:

$$\Phi_{LW}^{(j)} = \sigma \cdot \varepsilon_{in}^{(j)} \cdot S^{(j)} \cdot T_{S.in}^{(j)4} \tag{2.8}$$

[4] The dependence of the glass transmission coefficient with the solar angle is accounted for.

Cette thèse est accessible à l'adresse : http://theses.insa-lyon.fr/publication/2018LYSEI071/these.pdf
© [L. Frayssinet], [2018], INSA Lyon, tous droits réservés

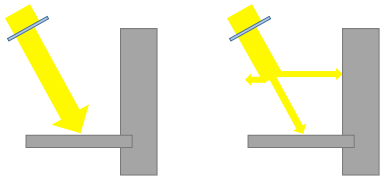

(A) trSol-0 (B) trSol-1

FIGURE 2.7: Transmitted solar flux allocation variants

where σ is the Stefan-Boltzmann constant ($\simeq 5.67\,\mathrm{W\,m^{-2}\,K^{-4}}$) and $\varepsilon_{in}^{(j)}$ is the emissivity of inside face of the surface j. Only a fraction $F_{j,i}$, called the view factor, is directly received by the surface i. As the surfaces are assumed to be grey bodies, they reflect a part of the LW radiation they receive. Hence, an additional part is received due to multiple reflections. Nonetheless, the amount of energy emitted depends on the surface temperature, itself depending on the amount of energy received. In order to solve this intertwining multiple reflections problem, the *radiosity* formulation is used. The radiosity $J^{(j)}$ [W] is defined as the total flow that comes from the surface j (the sum of the emitted and reflected flows):

$$J^{(j)} = \sigma \cdot \varepsilon_{in}^{(j)} \cdot S^{(j)} \cdot T_{S.in}^{(j)4} + \varrho_{LW}^{(j)} \cdot I_{LW}^{(j)} \tag{2.9}$$

where $\varrho_{LW}^{(j)}$ is the LW reflection coefficient and $I_{LW}^{(j)}$ [W] is the (unknown) total LW flow received by the surface j (including all reflections).

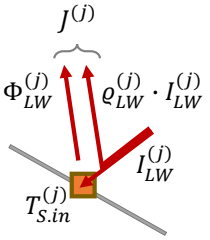

FIGURE 2.8: Radiosity

Therefore, the net radiation exchanged by the surface i surrounded by N surfaces ($\Phi_{rad.in}^{(i)}$ [W]) is as follows:

$$\Phi_{rad.in}^{(i)} = \sum_{j=1}^{N} S^{(j)} \cdot F_{j,i} \cdot J^{(j)} - S^{(i)} \cdot J^{(i)} \tag{2.10}$$

This multi-reflection problem can be solved using matrix solving or ray-tracing methods, both of which require a detailed knowledge of the geometry of the internal walls inside thermal zones. As this information is generally unknown during the first building design stages or at the city scale, we use the following assumptions:

- First, it is assumed that the surface LW properties are the same for each surface (ε_{in}, ϱ_{LW}).
- Second, there is no reflection ($\varrho_{LW} = 0$), and hence, as the building materials are opaque to LW radiation, the received flow is entirely absorbed. This last

Cette thèse est accessible à l'adresse : http://theses.insa-lyon.fr/publication/2018LYSEI071/these.pdf
© [L. Frayssinet], [2018], INSA Lyon, tous droits réservés

assumption is justified by the fact that building material properties are close to black body ($\varepsilon \simeq 1$). However, even if this last assumption implies $\varepsilon = 1$ according to the Kirchhoff's law, we choose to keep a ε value close but not equal to 1 but an absorption coefficient equal to 1.

With these assumptions, and according to the view factor reciprocity relationship ($S^{(j)} \cdot F_{j,i} = S^{(i)} \cdot F_{i,j}$) and complementarity relationship ($\sum_i^N F_{i,j} = 1$), the previous equation can be rewritten as follows:

$$\Phi^{(i)}_{rad.in} = S^{(i)} \cdot \varepsilon_{in} \cdot \sigma \cdot \sum_j^N F_{i,j} \cdot (T^{(j)4}_{S.in} - T^{(i)4}_{S.in}) = S^{(i)} \cdot \sum_j^N F_{i,j} \cdot h^{i,j}_{rad.in} \cdot (T^{(j)}_{S.in} - T^{(i)}_{S.in}) \quad (2.11)$$

where $h^{i,j}_{rad.in} = \varepsilon_{in} \cdot \sigma \cdot (T^{(j)2}_{S.in} + T^{(i)2}_{S.in}) \cdot (T^{(j)}_{S.in} + T^{(i)}_{S.in})$ [$\mathrm{W\,m^{-2}\,K^{-1}}$] is the internal radiative heat transfer coefficient, which is assumed to be constant[5] ($h_{rad.in}$).

Last, because of a lack of knowledge, the view factors are approximated[6] by $F_{i,j} = \frac{S^{(j)}}{\sum_k^N S^k}$. The resulting equation is as follows:

$$\Phi^{(i)}_{rad.in} = h_{rad.in} \cdot S^{(i)} \cdot (T_{rad.in} - T^{(i)}_{S.in}) \quad (2.12)$$

where $T_{rad.in} = \frac{\sum_k^N S^{(k)} \cdot T^{(k)}_{S.in}}{\sum_k^N S^k}$ is the zone radiant temperature (the average inside surface temperatures).

This formulation is deliberately similar to the equation of the internal convective heat transfer (Eq. 2.1). It is typical to approximate $T_{rad.in}$ with $T_{air.in}$ [intLW-0]. Then it is possible to merge Eq. 2.1 and Eq. 2.12:

$$\Phi^{(i)}_{rad.in} + \Phi^{(i)}_{cv.in} = h_{g.in} \cdot S^{(i)} \cdot (T_{air.in} - T^{(i)}_{S.in}) \quad (2.13)$$

where $h_{g.in}$ is the global transfer coefficient and is equal to $h_{cv.in} + h_{rad.in}$.

This approximation is quite coarse as surface temperatures are noticeably different from the air temperature. To account for surface temperatures, Eq. 2.13 can be rewritten [intLW-1] as follows:

$$\Phi^{(i)}_{rad.in} + \Phi^{(i)}_{cv.in} = h_{g.in} \cdot S^{(i)} \cdot (T_{op.in} - T^{(i)}_{S.in}) \quad (2.14)$$

where $T_{op.in}$ [K] is the operative temperature and is equal to $\frac{T_{air.in} + T_{rad.in}}{2}$. This formulation implicitly assumed $h_{cv.in} = h_{rad.in} = \frac{h_{g.in}}{2}$. In this formulation, in contrast to the previous one, the surface temperatures are coupled via $T_{op.in}$.

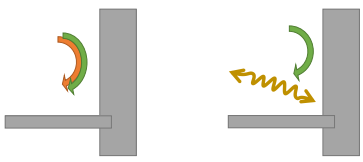

(A) intLW-0 (B) intLW-1

FIGURE 2.9: Internal LW radiation modelling variants

[5] For the usual range of building inside surface temperature, $h_{rad.in} \in [4.5, 6.5]$ $\mathrm{W\,m^{-2}\,K^{-1}}$.
[6] With this assumption, $F_{i,i} = 0$ is lost for convex surfaces.

Cette thèse est accessible à l'adresse : http://theses.insa-lyon.fr/publication/2018LYSEI071/these.pdf
© [L. Frayssinet], [2018], INSA Lyon, tous droits réservés

Conduction The heat losses are diffused by conduction through the wall. According to Fourier's law, assuming a unidimensional flow[7], the heat flow diffused by conduction through the wall i at its inside interface ($\Phi^{(i)}_{cd.in}$ [W]) is:

$$\Phi^{(i)}_{cd.in} = -\lambda^{(i,1)} \cdot S^{(i)} \cdot \frac{\partial T^{(i)}(x)}{\partial x} \mid_{x=0} \tag{2.15}$$

where $\lambda^{(i,1)}$ [W m^{-1} K^{-1}] is the conductivity of the wall at the interface, $T^{(i)}(x)$ [K] is the temperature through the wall, and x is the spatial dimension perpendicular to the wall such that the position of the inside surface is $x = 0$ and x increases when going toward the outside (see Fig. 2.11). Hence, $T^{(i)}(x = 0) = T^{(i)}_{S.in}$.

Multi-dimensional conduction that occurs at materials junctions, called *thermal bridges*, cannot be accounted for because of the unidimensional assumption. Usually, static thermal bridge coefficients are used to prevent this drawback. However, in our model, for the sake of generality and because of a lack of detailed knowledge, we choose to slightly overestimate the wall material thermal conductivity (in accordance with the TABULA methodology (Rochard et al., 2015), making it possible to roughly account for the supplementary heat losses due to thermal bridges with dynamic behaviour (linked to the overall material).

Energy balance Finally, the balance at the inside wall surface is as follows:

$$\Phi^{(i)}_{tr.sol} + \Phi^{(i)}_{cv.in} + \Phi^{(i)}_{rad.in} = \Phi^{(i)}_{cd.in} \tag{2.16}$$

At the inner interface, the heat losses through the wall ($\Phi^{(i)}_{cd.in}$) are equal to the heat flux given by the air volume ($\Phi^{(i)}_{cv.in}$) and the surrounding surfaces ($\Phi^{(i)}_{rad.in}$) plus the gains due to the transmitted solar flux ($\Phi^{(i)}_{tr.sol}$). This last flow indirectly acts as heat gains for the air volume as it reduces (or inverts) the convective heat transfer by warming up the inside surface temperature but depends on the dynamics of the conductive heat transfer. Precisely, this phenomenon is studied in the next subsection.

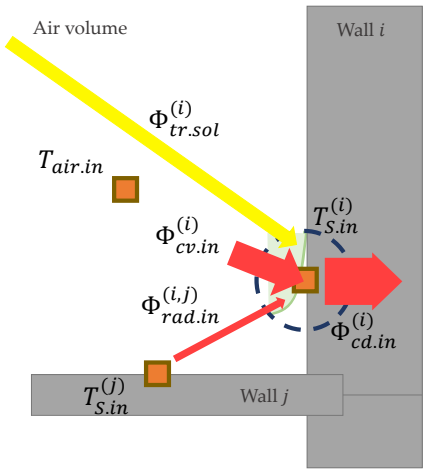

FIGURE 2.10: Wall i inside surface energy balance

[7] As the wall thickness is significantly lower than the other spatial dimensions

Cette thèse est accessible à l'adresse : http://theses.insa-lyon.fr/publication/2018LYSEI071/these.pdf
© [L. Frayssinet], [2018], INSA Lyon, tous droits réservés

In modelling terms, this step adds N equations (one per wall) to the the global set of equations but generates N new unknowns: the $\Phi_{cd.in}^{(i)}$. Before writing it in the previous general matrix form (Eq. 2.7), it is preferable to differently formulate these new unknowns. This is also the aim of the next subsection. As a consequence, the general matrix formulation can only be found in the following paragraph (with Eq. 2.20).

Within the material

Let us still focus on the wall i. In the following, for the sake of clarity, as no confusion is possible, the subscript (i) is not written but is implicit.

Conduction The unidimensional conduction through a homogeneous layer m of the wall i (see Fig. 2.11) is described by the following heat equation:

$$\frac{\partial T}{\partial t} - \frac{\lambda^{(m)}}{\rho^{(m)} \cdot c^{(m)}} \cdot \frac{\partial^2 T}{\partial x^2} = 0 \tag{2.17}$$

where $\lambda^{(m)}$ [$\mathrm{W\,m^{-1}\,K^{-1}}$], $\rho^{(m)}$ [$\mathrm{kg\,m^{-3}}$] and $c^{(m)}$ [$\mathrm{J\,kg^{-1}\,K^{-1}}$] are the thermal conductivity, the density and the specific heat capacity of the layer m, respectively (and are assumed constant in the temperature range considered and over time). For the whole wall fabric made of M layers, this equation is associated with each layer. Similarly, continuity relationships in terms of temperatures (T) and fluxes ($-\lambda \cdot \frac{\partial T}{\partial x}$) are imposed on the layer interfaces to link all heat equations.

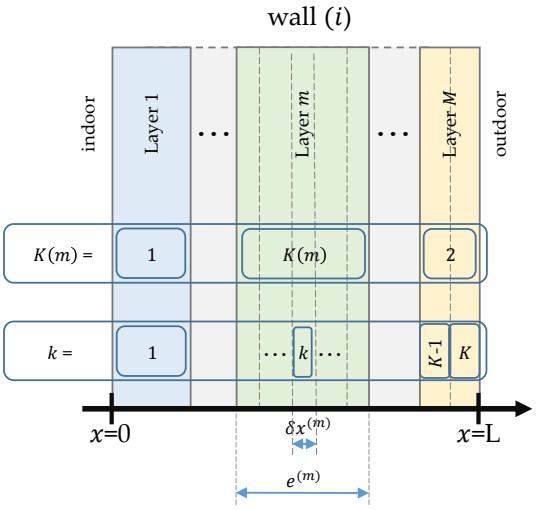

FIGURE 2.11: Wall notations

Solving these equations usually relies on numerical methods based on spatial discretisation of the domain (Fig. 2.11). We choose to discretised each layer m in a finite number $K^{(m)}$ of equidistant mesh elements. For analysis purposes, and for physical considerations, this number is defined as a function of the layer thermal penetration depth length and hence as a function of the inherent thermal properties

Cette thèse est accessible à l'adresse : http://theses.insa-lyon.fr/publication/2018LYSEI071/these.pdf
© [L. Frayssinet], [2018], INSA Lyon, tous droits réservés

of the material[8] as follows:

$$K^{(m)} = \max\left(\left\{1, \left\lfloor \frac{e^{(m)}}{\sqrt{a^{(m)} \cdot \tau}} \right\rfloor\right\}\right) = \frac{e^{(m)}}{\delta x^{(m)}} \tag{2.18}$$

where $\lfloor \cdot \rfloor$ is the floor function, $e^{(m)}$ [m] is the layer thickness, $a^{(m)} = \frac{\lambda^{(m)}}{\rho^{(m)} \cdot c^{(m)}}$ [$\mathrm{m^2\,s^{-1}}$] is the material diffusivity, and $\delta x^{(m)}$[m] is the mesh element thickness. With this definition, the meshing resolution is controlled by the parameter τ [s].

If wall i is a window, as the characteristic time of its material is very low ($\frac{e^{(m)2}}{a^{(m)}} < 30$ s) compared to usual time steps and τ values used (see Sec. 5.1.1), the whole window is modelled with 1 layer discretised in only 1 element ($K^{(m)} = 1$) without thermal mass ($c^{(m)} = 0$).

We choose the finite volume formulation to model the conduction: each discrete element k is assumed to have a homogeneous mean temperature $T^{(k)}$, which corresponds to the temperature at the centre of the element. With this method, the discrete form of the Eq. 2.17 but for the whole multi-layered wall becomes:

$$\begin{cases} \forall k \in \left[1, \sum_m^M K^{(m)} = K\right], & \\ \rho^{(k)} \cdot c^{(k)} \cdot \delta x^{(k)} \cdot \dot{T}^{(k)} & = \left(\frac{T^{(k-1)} - T^{(k)}}{\frac{\delta x^{(k-1)}}{2 \cdot \lambda^{(k-1)}} + \frac{\delta x^{(k)}}{2 \cdot \lambda^{(k)}}} + \frac{T^{(k+1)} - T^{(k)}}{\frac{\delta x^{(k+1)}}{2 \cdot \lambda^{(k+1)}} + \frac{\delta x^{(k)}}{2 \cdot \lambda^{(k)}}} \right) \\ \rho^{(1)} \cdot c^{(1)} \cdot \delta x^{(1)} \cdot \dot{T}^{(1)} & = \left(\frac{T^{(0)} - T^{(1)}}{\frac{\delta x^{(1)}}{2 \cdot \lambda^{(1)}}} + \frac{T^{(2)} - T^{(1)}}{\frac{\delta x^{(2)}}{2 \cdot \lambda^{(2)}} + \frac{\delta x^{(1)}}{2 \cdot \lambda^{(1)}}} \right) \\ \rho^{(K)} \cdot c^{(K)} \cdot \delta x^{(K)} \cdot \dot{T}^{(K)} & = \left(\frac{T^{(K-1)} - T^{(K)}}{\frac{\delta x^{(K-1)}}{2 \cdot \lambda^{(K-1)}} + \frac{\delta x^{(K)}}{2 \cdot \lambda^{(K)}}} + \frac{T^{(K+1)} - T^{(K)}}{\frac{\delta x^{(K)}}{2 \cdot \lambda^{(K)}}} \right) \end{cases} \tag{2.19}$$

with the boundary temperatures $T^{(0)}$ and $T^{(K+1)}$ for the inside and outside wall surface temperatures ($T_{S.in}$ and $T_{S.ext}$), respectively.

The continuity relationships are intrinsically included in this discrete formulation. With this formulation, each equation can be seen as the energy balance of an element k using resistance-capacitance analogy, as illustrated in Fig. 2.12. It can easily be rewritten with the general matrix formulation (Eq. 2.7) with the following:

[8] In practice, the number of elements is chosen arbitrarily or according to rule of thumb but rarely depending on the material thermal properties.

Cette thèse est accessible à l'adresse : http://theses.insa-lyon.fr/publication/2018LYSEI071/these.pdf
© [L. Frayssinet], [2018], INSA Lyon, tous droits réservés

$$
\begin{cases}
\mathrm{T} = \begin{pmatrix} T_{S.in} \\ T^{(1)} \\ \vdots \\ T^{(k)} \\ \vdots \\ T^{(K)} \\ T_{S.out} \end{pmatrix}, \mathrm{U} = \begin{pmatrix} 0 \end{pmatrix} \\
\mathbf{C} = \begin{pmatrix} 0 & C^{(1)} & & & & & \\ & \ddots & & & & & \\ & & C^{(k)} & & & & \\ & & & \ddots & & & \\ & & & & C^{(K)} & 0 & \end{pmatrix} \\
\mathbf{A} = \begin{pmatrix} K^{(1,0)} & -\bar{K}^{(1)} & K^{(1,2)} & & & & \\ & \ddots & \ddots & \ddots & & & \\ & & K^{(k,k-1)} & -\bar{K}^{(k)} & K^{(k,k+1)} & & \\ & & & \ddots & \ddots & \ddots & \\ & & & & K^{(K,K-1)} & -\bar{K}^{(K)} & K^{(K,K+1)} \end{pmatrix} \\
\mathbf{B} = \begin{pmatrix} 0 & \cdots & 0 \end{pmatrix}^{\top}
\end{cases}
$$

with:

$$
\begin{cases}
C^{(k)} = \rho^{(k)} \cdot c^{(k)} \cdot \delta x^{(k)} \\
K^{(k,l)} = \begin{cases} \frac{2 \cdot \lambda^{(k)}}{\delta x^{(k)}} \\ \left(\frac{\delta x^{(l)}}{2 \cdot \lambda^{(l)}} + \frac{\delta x^{(k)}}{2 \cdot \lambda^{(k)}} \right)^{-1} \end{cases} & \text{if } l = 0 \text{ or } l = K+1; \\ & \text{else.} \\
\bar{K}^{(k)} = K^{(k,k-1)} + K^{(k,k+1)}
\end{cases}
$$

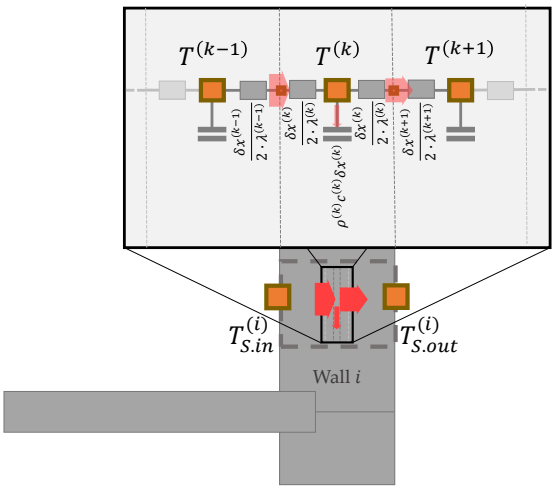

FIGURE 2.12: Wall discrete element energy balance

Finally, the energy balance of the wall i adds K equations, depending on the level of discretisation. This step has to be repeated for every wall of the BEM separation. It clearly appears that the conduction into the envelope generates the highest

Cette thèse est accessible à l'adresse : http://theses.insa-lyon.fr/publication/2018LYSEI071/these.pdf
© [L. Frayssinet], [2018], INSA Lyon, tous droits réservés

part of the BEM equations. As a consequence, conduction is the main target of the adaptations, notably towards the level of discretisation (Frayssinet et al., 2018b), via τ in our case [Cond-τ].

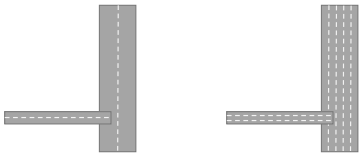

(A) Cond-τ_1 (B) Cond-$\tau_2 < \tau_1$

FIGURE 2.13: Conduction discretisation variants

Flashback to inside surface balance Thanks to the discretisation defined above, the previous energy balance of the inside surface (Eq. 2.16) can now be expanded. Indeed:

$$\Phi_{cd,in} = -\lambda^{(1)} \cdot S \cdot \frac{\partial T}{\partial x} \mid_{x=0} = -2 \cdot \lambda^{(1)} \cdot S \cdot \frac{T^{(1)} - T_{S.in}}{\delta x^{(1)}} \tag{2.20}$$

In the general matrix form (Eq. 2.7), the terms of the inside surface energy balance are as follows:

$$\begin{cases} \mathrm{T} = \begin{pmatrix} T_{S.in} \\ T^{(1)} \\ T_{air.in} \\ T_{rad.in} \end{pmatrix}, \mathrm{U} = \begin{pmatrix} \Phi_{tr.sol} \end{pmatrix} \\ \mathbf{C} = \begin{pmatrix} 0 & 0 & 0 & 0 \end{pmatrix} \\ \mathbf{A} = \begin{pmatrix} -\left(h_{cv.in} + h_{rad.in} + \frac{2 \cdot \lambda^{(1)}}{\delta x^{(1)}}\right) & \frac{2 \cdot \lambda^{(1)}}{\delta x^{(1)}} & h_{cv.in} & h_{rad.in} \end{pmatrix} \\ \mathbf{B} = \begin{pmatrix} \frac{1}{S^{(i)}} \end{pmatrix} \end{cases}$$

As $\mathbf{C} = (0\ 0\ 0\ 0)$, this equation is algebraic. Note that depending on the assumption [intLW], $T_{rad.in}$ may be a combination of all the inside surface temperatures and consequently leading to couplings between them.

Assessment This step makes it possible to add equations in order to complete the whole problem. $T_{S.in}$ is now expressed as a function of new unknowns: the wall temperatures $T^{(k)}$. However, an equation is associated to each $T^{(k)}$. Nonetheless, a equation is missing for $T_{S.out}$. The next part aims to introduce this equation.

In case of internal walls, this surface temperature is adjacent to the same or another thermal zone and is therefore included in its energy balance. Otherwise, the wall outside face is facing outdoor, and this case is studied in the following part.

Concerning the internal walls within a thermal zone (partitions or floors, depending on the zoning), they are often not modelled [Inertia-1]. The default variant used in our BEM accounts for them [Inertia-0].

Outside wall surface

At the outside surface of the walls, the envelope losses are dissipated to outdoors by convection and radiation. Losses can also be reduced or reversed by absorbed solar flows.

Cette thèse est accessible à l'adresse : http://theses.insa-lyon.fr/publication/2018LYSEI071/these.pdf
© [L. Frayssinet], [2018], INSA Lyon, tous droits réservés

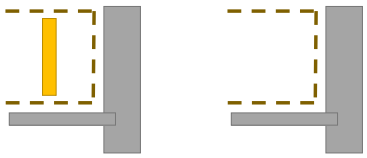

(A) Inertia-0 (B) Inertia-1

FIGURE 2.14: Internal inertia modelling variants

External convective heat transfer The external convection is expressed similar to the internal convective heat transfer (Eq. 2.1), as follows:

$$\Phi_{cv.ext}^{(i)} = h_{cv.ext} \cdot S^{(i)} \cdot (T_{S.ext}^{(i)} - T_{air.out}) \tag{2.21}$$

where $h_{cv.ext}$ [$\mathrm{W\,m^{-2}\,K^{-1}}$] is the external CHTC, $S^{(i)}$ [$\mathrm{m^2}$] is the outside wall area (usually assumed equal to the inside one, hence not differentiated) and $T_{air.out}$ [K] is the outdoor air temperature.

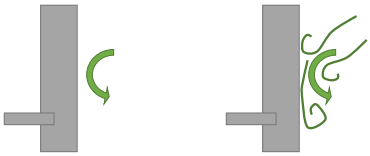

(A) extConv-0 (B) extConv-1

FIGURE 2.15: External CHTC modelling variants

The external CHTC could be assumed to be constant [extConv-0], indoor, or wind dependant [extConv-1]. Indeed, the range of variation of the external wind-speed is larger than that indoors and significantly affects the CHTC. In this last case, the wind dependancy relation defined in the French thermal regulation (RT 2012) is used, $h_{cv.ext} = 4 + 4 \cdot v$, where v [$\mathrm{m\,s^{-1}}$] is, in our model, the wall normal projected wind velocity.

External long-wave radiation As well as for the internal LW radiations exchanges, following the same first assumptions (Eq. 2.11), we can write the following:

$$\Phi_{rad.ext}^{(i)} = S^{(i)} \cdot \varepsilon_{ext}^{(i)} \cdot \sigma \cdot \sum_{j=1}^{N} F_{i,j} \cdot (T_{S.ext}^{(i)4} - T_{S.ext}^{(j)4}) = S^{(i)} \cdot \sum_{j=1}^{N} F_{i,j} \cdot h_{rad.ext}^{(i,j)} \cdot (T_{S.ext}^{(j)} - T_{S.ext}^{(i)}) \tag{2.22}$$

where $\varepsilon_{ext}^{(i)}$ is the emissivity of the outside wall surface.

The default assumption, which is valid for buildings isolated in open areas, assumes that the external environment is made of 2 elements, namely, the soil and the sky. Hence, we get the following:

$$\Phi_{rad.ext}^{(i)} = S^{(i)} \cdot svf \cdot h_{rad.ext}^{(i,sky)} \cdot (T_{S.ext}^{(i)} - T_{sky}) + S^{(i)} \cdot (1 - svf) \cdot h_{rad.ext}^{(i,soil)} \cdot (T_{S.ext}^{(i)} - T_{soil}) \tag{2.23}$$

where svf is the sky-view factor ($F_{i,sky}$), T_{sky} [K] is the sky vault temperature and T_{soil} [K] is the soil surface temperature. The sky vault temperature is either directly

Cette thèse est accessible à l'adresse : http://theses.insa-lyon.fr/publication/2018LYSEI071/these.pdf
© [L. Frayssinet], [2018], INSA Lyon, tous droits réservés

available in the weather data or is estimated according to other weather data. The soil temperature is usually unknown as specific soil thermal models are needed but almost never implemented. The soil temperature is generally approximated by the outdoor air temperature $T_{air.out}$.

Two modelling variants are considered. Either the external heat transfer radiative coefficient $h_{rad.ext}$ is linearised as in Eq. 2.11 [extLW-0] or kept detailed [extLW-1].

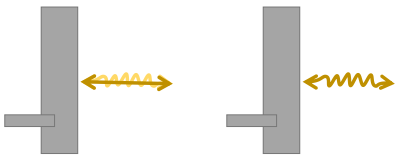

(A) extLW-0 (B) extLW-1

FIGURE 2.16: External radiative LW heat transfer coefficient modelling variants

Absorbed solar flow The external wall receives on its outside face direct solar flux from the sun, diffuse solar flux from the atmosphere, and diffuse reflection from the surrounding environment. The weather file generally gives direct normal ($\phi_{drn.sol}$ [$\mathrm{W\,m^{-2}}$]) and diffuse horizontal solar fluxes ($\phi_{dfh.sol}$ [$\mathrm{W\,m^{-2}}$]). The solar flow absorbed by the wall i is:

$$\Phi^{(i)}_{abs.sol} = \alpha^{(i)} \cdot S^{(i)} \cdot \left(\phi_{drn.sol} \cdot \langle \vec{n}^{(i)}, \vec{\gamma} \rangle_+ + svf \cdot \phi_{dfh.sol} + (1 - svf) \cdot \varrho_{sol.gnd} \cdot \phi_{sol \to gnd} \right) \tag{2.24}$$

where $\alpha^{(i)}$ is the solar absorption coefficient of the wall i, $\langle \vec{n}^{(i)}, \vec{\gamma} \rangle_+$ is the positive value of the scalar product between the wall normal and the solar angle, $\varrho_{sol.gnd}$ is the solar reflection coefficient of the environment, and $\phi_{sol \to gnd}$ is the flux coming from the sky received by the ground. Details of the calculation of the reflected part, the last term, are given in Appendix A.1.

The same formulation is used for the solar flow transmitted by windows ($\Phi_{tr.win.sol}$ [W]) but replacing $\alpha^{(i)}$ with $\theta^{(i)}$, the solar transmission coefficient (the model used considers a transmission coefficient that depends on the solar incident angle). According to previous definitions, for a given zone: $\sum_{i=1}^{N} \Phi^{(i)}_{tr.win.sol} = \sum_{i=1}^{N} \Phi^{(i)}_{tr.sol}$.

Energy balance Finally, the balance at the outside wall surface is as follows:

$$\Phi^{(i)}_{cd.ext} + \Phi^{(i)}_{abs.sol} = \Phi^{(i)}_{cv.ext} + \Phi^{(i)}_{rad.ext} \tag{2.25}$$

Cette thèse est accessible à l'adresse : http://theses.insa-lyon.fr/publication/2018LYSEI071/these.pdf
© [L. Frayssinet], [2018], INSA Lyon, tous droits réservés

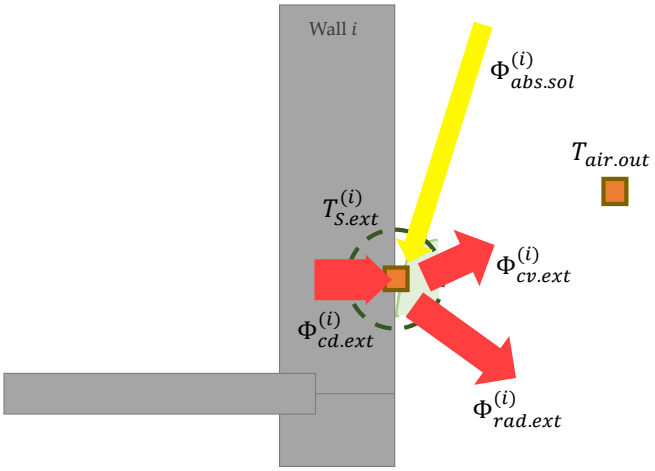

FIGURE 2.17: Wall i outside surface energy balance

Using the general matrix formulation[9] (Eq. 2.7), we get again an algebraic set of equations, as follows:

$$\begin{cases} \mathrm{T} = \begin{pmatrix} T_{S.ext} \\ T^{(N)} \end{pmatrix}, \mathrm{U} = \begin{pmatrix} T_{air.out} \\ T_{sky} \\ \Phi_{abs.sol} \end{pmatrix} \\ \mathbf{C} = \begin{pmatrix} 0 & 0 \end{pmatrix} \\ \mathbf{A} = \begin{pmatrix} -(h_{cv.ext} + h_{rad.ext} + \frac{2 \cdot \lambda^{(K)}}{\delta x^{(K)}}) & -\frac{2 \cdot \lambda^{(K)}}{\delta x^{(K)}} \end{pmatrix} \\ \mathbf{B} = \begin{pmatrix} h_{cv.ext} + (1 - svf) \cdot h_{rad.ext} & svf \cdot h_{rad.ext} & \frac{1}{S^{(i)}} \end{pmatrix} \end{cases}$$

Floor specificity If the wall i is a floor exposed to the soil or a buffer space (such as a car park or a crawl space), clearly no solar flow is absorbed. Furthermore, it is assumed that the net radiation exchange is null and that the outside temperature for the convective heat transfer is equal to $b \cdot T_{air.out} + (1 - b) \cdot T_{air.in}$, with b being a reduction coefficient as defined in the French thermal regulation.

2.1.3 Overall building energy balance

Following the heat looses, and thanks to the 4 successive energy balances (air volume, inside wall face, within the wall, and outside wall face; Fig. 2.19) for each element of the building separation, it is possible to link the indoor air temperatures and consequently the building needs, to the outdoor weather variables. According to previous energy balances, the appearance of an overall building energy model in its general matrix form is given in Fig. 2.20, 2.21 and 2.22 (non-zero terms are coloured as a function of the energy balance they coming from). The envelope clearly appears as a filter between outdoor and indoor conditions (Fig. 2.19).

Once can note that the matrix problem is nearly diagonal, but any equation is independent. Terms related to the unidimensional conduction only concerns direct neighbour temperatures. In contrast, terms not directly adjacent to the diagonal generally indicate coupling between non-adjacent temperatures. In general, the more the diagonal the matrix problem, the more easy it is to solve. In practice, for solving

[9] With [extLW-0] and $T_{gnd} = T_{air.out}$.

Cette thèse est accessible à l'adresse : http://theses.insa-lyon.fr/publication/2018LYSEI071/these.pdf
© [L. Frayssinet], [2018], INSA Lyon, tous droits réservés

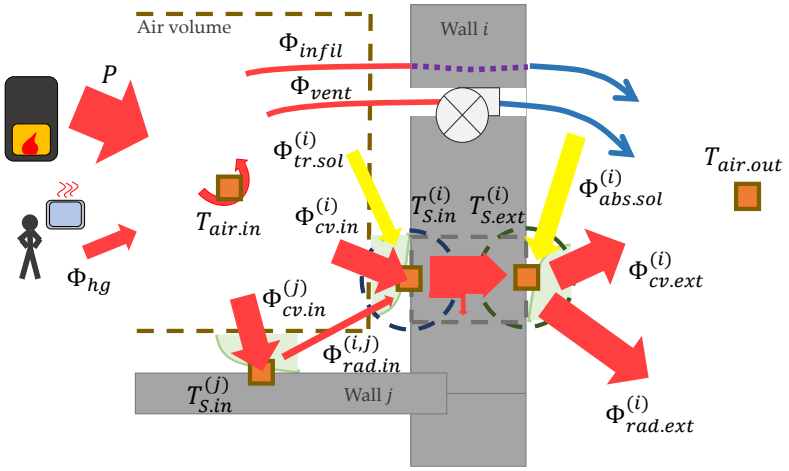

FIGURE 2.18: Whole building energy balance

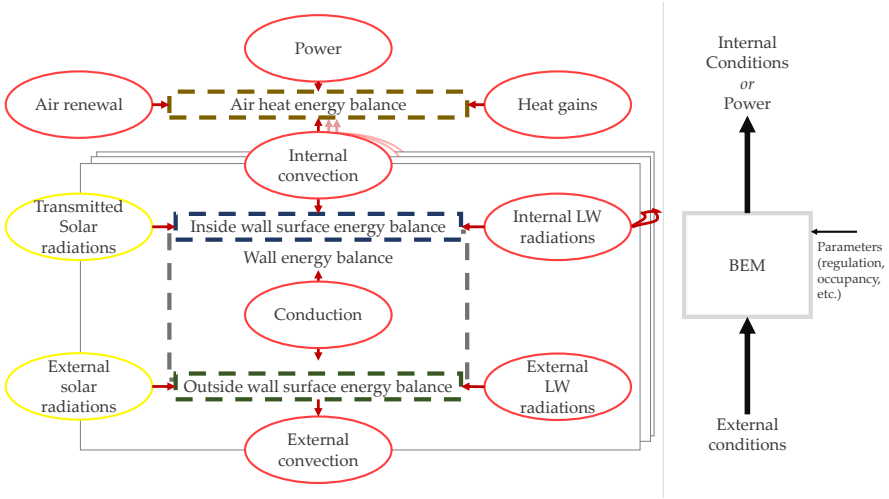

FIGURE 2.19: Building energy model overview

such a matrix problem, the algebraic equations are split from the others in a separated system to make the remaining system invertible. The tools used in our work to create and simulate BEM are introduced in Chapter 4.

2.1.4 Reducing the matrix problem size

As seen previously, and as notably illustrated in Fig. 2.21, the majority of the equations in the overall BEM comes from the conductive heat transfer problem, and this number is even greater if the level of discretisation is high (Eq. 2.19). As they are partial derivative equations, they contribute the most to the numerical cost of the simulations because of the solving process. In order to limit the computational cost, a common method consists of reducing the discretisation, notably by the resistance-capacitance (RC) method. This method consists of discretising the wall into few nodes (generally 1 to 3), which are associated with resistances and capacitances and parametrized, as in Fig. 2.12. The number of nodes may be reduced even more

Cette thèse est accessible à l'adresse : http://theses.insa-lyon.fr/publication/2018LYSEI071/these.pdf
© [L. Frayssinet], [2018], INSA Lyon, tous droits réservés

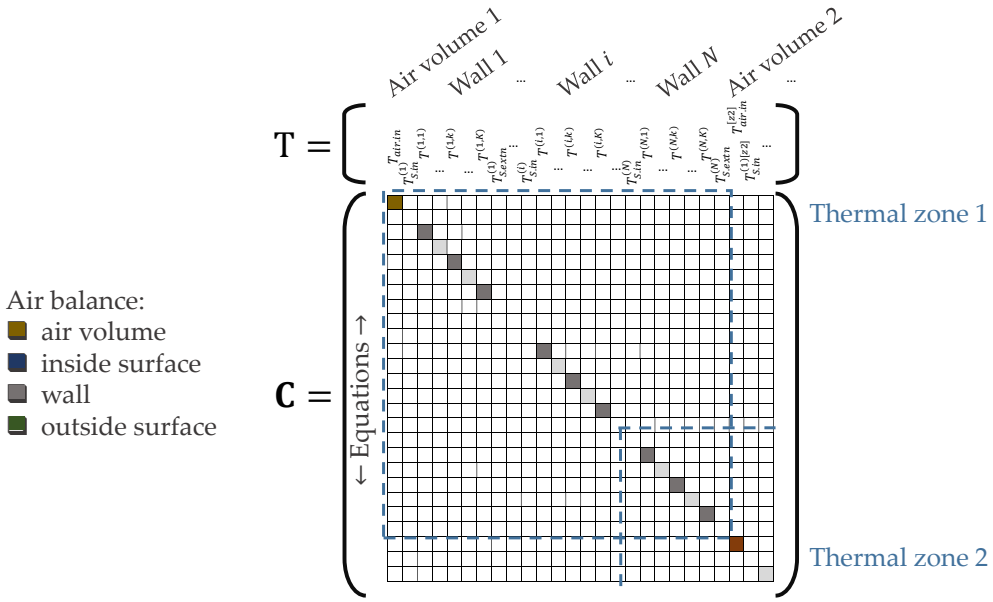

FIGURE 2.20: BEM capacitance matrix

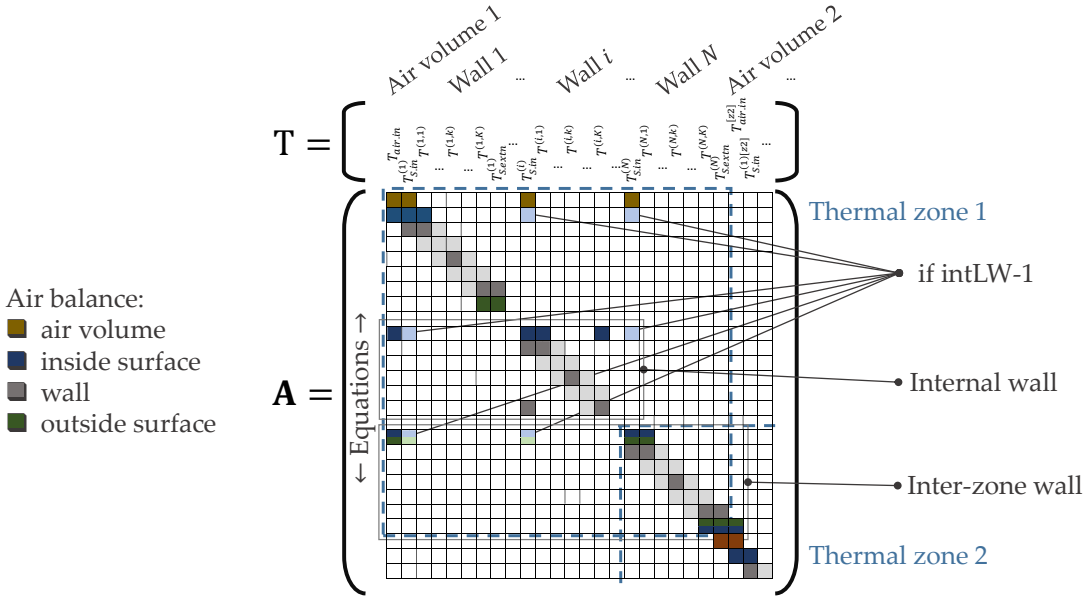

FIGURE 2.21: BEM conductance matrix

by simplifying the geometry of a mono-zone building to only one equivalent external wall. Such a modelling approach is not detailed further (see specific models developed by Bouyer, Inard, and Musy (2011), Lauster et al. (2014) and Fonseca and Schlueter (2015) for instance), except the reduction of the geometric complexity.

Cette thèse est accessible à l'adresse : http://theses.insa-lyon.fr/publication/2018LYSEI071/these.pdf
© [L. Frayssinet], [2018], INSA Lyon, tous droits réservés

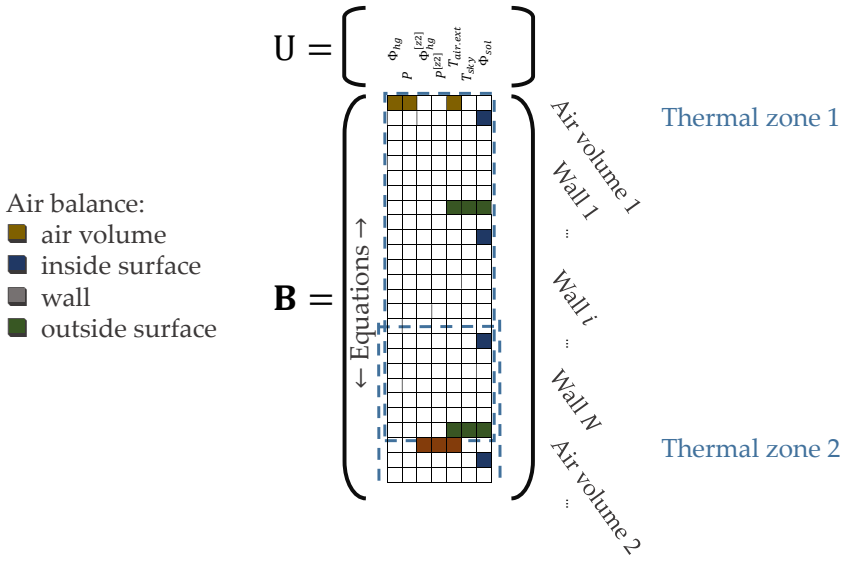

FIGURE 2.22: BEM command matrix

However, the impact of RC models is partially analysed in Sec. 5.1.1. The parametrisation of the resistances and the capacitances is analytically non-trivial (Roux, 1984; Fraisse et al., 2002) and is often parametrised thanks to identification methods (see works of Berthou et al. (2014), Raillon and Ghiaus (2017) and Thebault (2017) for instance).

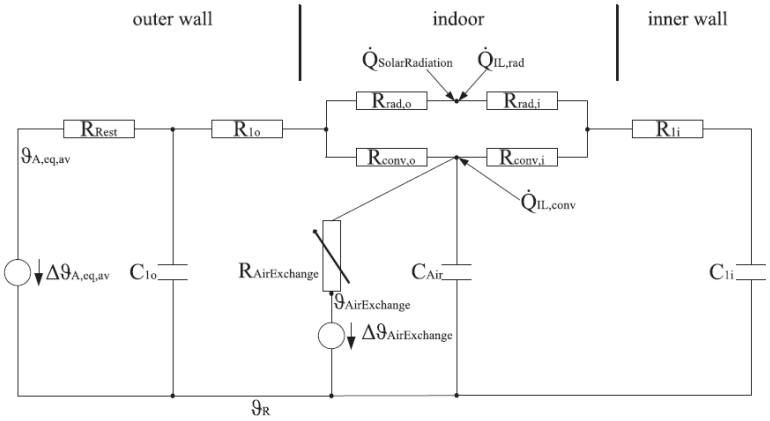

FIGURE 2.23: Example of RC model for a building zone
(From (Lauster et al., 2014))

Equivalent wall

Without using an RC analogy, Kim et al. (2014), developed a method to model only one *equivalent* wall per building model. It is assumed that the whole envelope is

Cette thèse est accessible à l'adresse : http://theses.insa-lyon.fr/publication/2018LYSEI071/these.pdf
© [L. Frayssinet], [2018], INSA Lyon, tous droits réservés

made of the same material. Hence, the area of this equivalent wall is the sum of the area of the different building walls (Fig. 2.24a). Furthermore, as solar fluxes are orientation dependant, it is necessary to aggregate the individual transmitted and absorbed solar flux in order to determine the equivalent incoming solar flux of the equivalent wall (Fig. 2.24b).

This method makes it possible to reduce the matrix size thanks to the use of only 1 wall energy balance rather than as much as the number of walls (N) defined in the geometry.

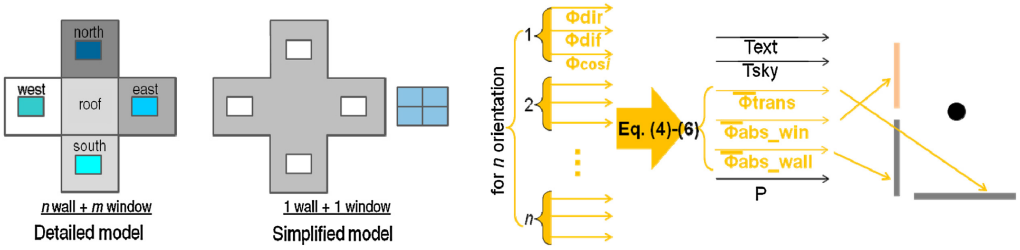

(A) Equivalent envelope principle (B) Equivalent solar fluxes associated

FIGURE 2.24: Equivalent envelope method
(From (Kim et al., 2014))

This method is considered in our study with some improvements [EqEnv-1] in order to consider buildings with various wall materials (notably with respect to the roof and the floor) and different surface properties:

- The initial thermo-physical parameters of the equivalent wall (referred to as eq) are those of the wall type having the greatest area (same materials and same number of layers).
- The conductivity of each layer of the equivalent wall is corrected as follows in order to get the same overall U-value (U [$\mathrm{W\,m^{-2}\,K^{-1}}$]):

$$\lambda_{eq} \rightarrow \lambda_{eq} \cdot \frac{\sum_i^N S^{(i)} \cdot U^{(i)}}{S_{eq} \cdot U_{eq}} \tag{2.26}$$

  with $U^{(i)} = \left(\sum_k^{K^{(i)}} \frac{\delta x^{(k)}}{\lambda^{(k)}} \right)^{-1}$.

- The capacitance of each layer of the equivalent wall is corrected as follows to get the same overall thermal mass:

$$c_{eq} \rightarrow c_{eq} \cdot \frac{\sum_i^N S^{(i)} \cdot C^{(i)}}{S_{eq} \cdot C_{eq}} \tag{2.27}$$

  with $C^{(i)} = \sum_k^{K^{(i)}} \delta x^{(k)} \cdot \rho^{(k)} \cdot c^{(k)}$.

- The equivalent sky view factor and emissivity are computed as follows:

$$\varepsilon_{ext.eq} = \sum_i^N \frac{S^{(i)} \cdot \varepsilon_{ext}^{(i)}}{S_{eq}} \tag{2.28}$$

$$svf_{eq} = \sum_i^N \frac{S^{(i)} \cdot \varepsilon_{ext}^{(i)} \cdot svf^{(i)}}{S_{eq} \cdot \varepsilon_{eq}} \tag{2.29}$$

Cette thèse est accessible à l'adresse : http://theses.insa-lyon.fr/publication/2018LYSEI071/these.pdf
© [L. Frayssinet], [2018], INSA Lyon, tous droits réservés

The justification for these last formulations is given in Appendix A.2.

The default model, without an equivalent envelope, corresponds to the modelling variant [EqEnv-0].

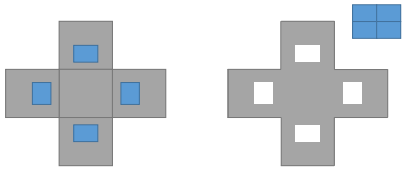

(A) EqEnv-0 (B) EqEnv-1

FIGURE 2.25: Equivalent envelope modelling

Mathematical reduction

Apart from modelling reduction methods, mathematical reduction methods based on the state-space formulation (Eq. 2.7) exist. This formulation may be rewritten as follows:

$$\dot{\mathrm{T}} = \mathbf{A}' \cdot \mathrm{T} + \mathbf{B}' \cdot \mathrm{U} \tag{2.30}$$

with $\mathbf{A}' = \mathbf{C}^{-1} \cdot \mathbf{A}$ and $\mathbf{B}' = \mathbf{C}^{-1} \cdot \mathbf{B}$. This matrix problem can be diagonalised via the change of the basis matrix $\mathbf{P}$, as follows:

$$\dot{\mathrm{X}} = \mathbf{D} \cdot \mathrm{X} + \mathbf{B}'' \cdot \mathrm{U} \tag{2.31}$$

with $\mathrm{T} = \mathbf{P} \cdot \mathrm{X}$, $\mathbf{D} = \mathbf{P}^{-1} \cdot \mathbf{A}' \cdot \mathbf{P}$, $\mathbf{B}'' = \mathbf{P}^{-1} \cdot \mathbf{B}'$ and such that $\mathbf{D}$ is diagonal. The diagonal terms (λ_d) of $\mathbf{D}$ are called eigenvalues. $\mathbf{P}$ is chosen so that these eigenvalues are sorted from the lowest to highest values. $\mathbf{P}$ contains the so-called eigenvectors. With this formulation, T is expressed as a linear combination of independent eigenvectors, which are also called *modes*.

As the mathematical reduction methods need constant and time-invariant matrix coefficients, only the state-space matrix describing the wall energy balance (Eq. 2.1.2) is considered (which is precisely the major source of equations). Necessarily, the term $\mathbf{B}' \cdot \mathrm{U}$ has to be rewritten so that the non-constant and time-invariant terms are all included in U.

The reduction of the problem relies on the decomposition of the modes into the 2 following categories: non-dominant ($\mathrm{X_s}$) and dominant modes ($\mathrm{X_l}$). Eq. 2.31 becomes:

$$\begin{pmatrix} \dot{\mathrm{X}}_\mathrm{s} \\ \dot{\mathrm{X}}_\mathrm{l} \end{pmatrix} = \begin{pmatrix} \mathbf{D_s} & \\ & \mathbf{D_l} \end{pmatrix} \cdot \begin{pmatrix} \mathrm{X_s} \\ \mathrm{X_l} \end{pmatrix} + \begin{pmatrix} \mathbf{B''_s} \\ \mathbf{B''_l} \end{pmatrix} \cdot \mathrm{U}$$

It is then considered that between the observational time step, $\dot{\mathrm{X}}_\mathrm{s} = 0$ as these modes are non dominant. Consequently:

$$\begin{cases} 0 = \mathbf{D_s} \cdot \mathrm{X_s} + \mathbf{B''_s} \cdot \mathrm{U} \\ \dot{\mathrm{X}}_\mathrm{l} = \mathbf{D_l} \cdot \mathrm{X_l} + \mathbf{B''_l} \cdot \mathrm{U} \end{cases} \tag{2.32}$$

Therefore, the reduction makes it possible to reduce the number of partial derivative equations (for which solving is costly) to algebraic ones (for which solving is immediate).

Cette thèse est accessible à l'adresse : http://theses.insa-lyon.fr/publication/2018LYSEI071/these.pdf
© [L. Frayssinet], [2018], INSA Lyon, tous droits réservés

Depending on the method, the dominant modes are selected with respect to their respective eigenvalues (Marshall method), to their influence on the output (Litz method), to their 'energy' (linear aggregation method) or to the notion of 'commandability' and 'controllability' (Moore method, notably used by Kim et al. (2014)) but using diagonalisation in a specific *balanced* basis. Reduction method comparison may be found in (Palomo, Bonnefous, and Déqué, 1997). For a given output error tolerance, the last methods generally make it possible to further reduce the number of dominant modes. Hence, in contrast to the equivalent envelope adaptation of the RC analogy, the mathematical reduction methods makes it possible to reduce the number of the most solving-expensive equations while making the modelling detailed without simplifying the geometry or the conductive problem description.

In our work, we use the usual diagonalisation, as a physical meaning is associated. Indeed, the opposite and inverse value of the eigenvalue is homogeneous to a time (called characteristic time, and written $\tau_d = -\frac{1}{\lambda_d}$). The modes with the shortest characteristic time quickly reach their stationary state and hence are categorised as non-dominant (their dynamics are negligible). The criterion of separation between short (non-dominant) and long (dominant) modes is generally defined to $\frac{\delta t}{4}$, where δt is the observational time-step (Marshall method, see more explanations in Appendix A.3).

In order to determine the effect of the mathematical reduction, the number of reduced modes is modifiable: if π modes are reduced, the reduced modes correspond to the π modes with the shortest characteristic times [Red-π].

$$\dot{X} = \begin{pmatrix} 0 \\ \vdots \\ 0 \\ \dot{X}_{\pi+1} \\ \vdots \\ \dot{X}_{\nu} \end{pmatrix}$$

(A) Red-π

FIGURE 2.26: Envelope reduction

2.2 District energy model

A district is made of numerous buildings, and therefore, in micro-simulation, a district energy model (DEM) is simply an assembly of BEM (Fig. 2.27). However, interactions between buildings exist but are not accounted for in the BEM. Indeed, by default, the buildings are assumed to be isolated in a open area. Within a district, interactions come from the following:

- solar shadings and reflections caused by surrounding buildings;
- inter-buildings LW radiative exchanges;
- coupling between adjoining buildings.

Another source of building interactions is via local microclimates. Indeed, buildings modify the local microclimate due to their thermal behaviour and their morphology (globally, increases in temperature, decreases in wind velocity, etc.), and

Cette thèse est accessible à l'adresse : http://theses.insa-lyon.fr/publication/2018LYSEI071/these.pdf
© [L. Frayssinet], [2018], INSA Lyon, tous droits réservés

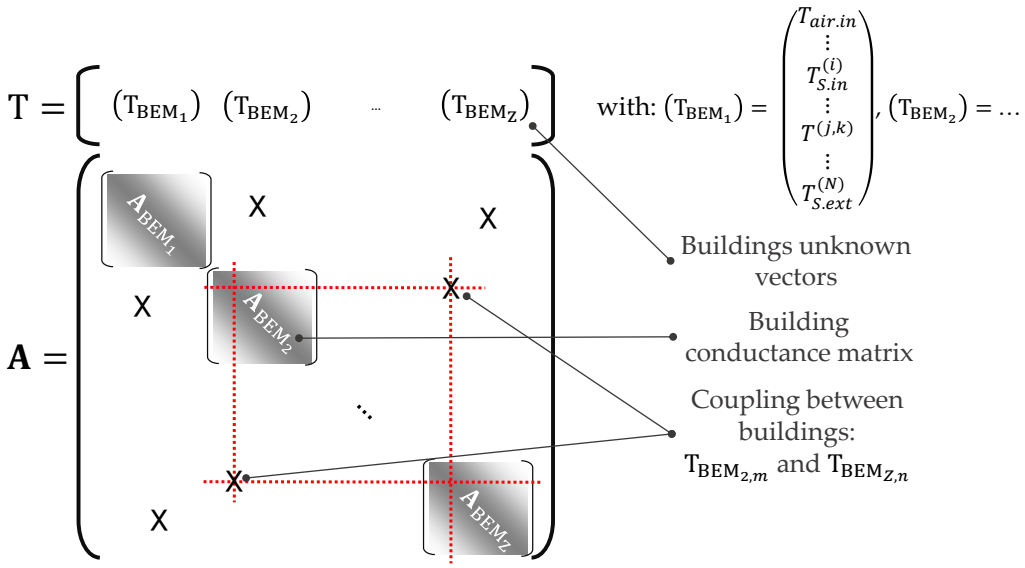

FIGURE 2.27: DEM conductance matrix

reciprocally, the microclimate modifies the building thermal behaviour. This microclimate impact is studied in a specific part (Sec. 5.1.4) and is not modelled in our approach because of the generally prohibitive computational cost associated.

At the district scale, the modelling variants consist of both considering and not considering these couplings.

Note about the reduction. At the district scale, the following different strategies may be considered:

(I) reducing the global model at the district scale;

(II) reducing the model at the building scale, and assembling the reduced models at the district scale.

As the numerical cost of the reduction of a matrix problem increase with a power higher than 1 with the matrix size, it is probably less costly to individually reduce the building models (strategy II) and even more if parallelising the processes. However, the level of reduction may be higher with the district model as the whole problem is considered. This issue, notably studied by Kim et al. (2015), is not analysed further.

2.2.1 Solar shadings and reflections

In urban areas, the solar flux reaching a building depends on the surrounding buildings because of shade (decrease) and reflections (increase). These effects depend on the urban environment of each building, and consequently, the received flux has to be computed specifically for each building facade and cannot be directly deduced from the weather data, unlike in Eq. 2.24 [Solar-0]. The size of the solicitation vector U is consequently increased (a term for each facade element).

Cette thèse est accessible à l'adresse : http://theses.insa-lyon.fr/publication/2018LYSEI071/these.pdf
© [L. Frayssinet], [2018], INSA Lyon, tous droits réservés

When considering solar shadings and reflections, the incoming solar flow of each wall is modified [Solar-1]:

$$\begin{cases} \Phi^{(i)}_{abs.sol} \rightarrow r^{(i)}_{abs} \cdot \Phi^{(i)}_{abs.sol} \\ \Phi^{(i)}_{tr.win.sol} \rightarrow r^{(i)}_{tr.win} \cdot \Phi^{(i)}_{tr.win.sol} \end{cases}$$

where the rs are the computed coefficients accounting for the modifications induced by the urban environment. If the diffuse solar flux is assumed to be isotropic, the corresponding coefficient is constant and corresponds to the sky view factor. Otherwise, the effect is dependent of the solar angle and hence has to be estimated at each time-step.

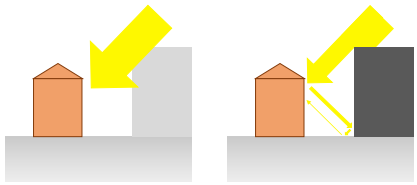

(A) Solar-0 (B) Solar-1

FIGURE 2.28: Shadings and reflections modelling variants

This building interaction is not a coupling as it is independent of the thermal behaviours of buildings; rather, it only depends on the district geometry. The computation of the resulting flow is consequently a pre-process. In our case, it is computed thanks to a ray-tracing method (tool used detailed in Sec. 4.2.2).

Note that these coefficients are averaged over the whole facade without specific distinctions between walls and windows. This modelling choice is due to the lack of information about the window positions in our input data. Their areas are only deduced from the window-to-wall ratio. Furthermore, the number of facades is defined according to the different orientations and zonings. In order to be coherent with the zone separation, no more detailed spatial resolution are considered to account more accurately the spatial variations of the incoming solar flux.

2.2.2 Inter-building long-wave radiative exchanges

At the building scale, without thermal information about the surroundings, the soil and the urban surface temperature are approximated by the air temperature [LWRad-0]. However, at the district scale, all the surface temperatures of all buildings are known (but not for the soil in our case, which is still approximated). As a consequence, the complete formulation of the Eq. 2.22 may be used [LWRad-1]. In the DEM, the view factors are also computed with a ray-tracing method (detailed in Sec. 4.2.2).

With this last modelling variant, each facade i seeing a facade j generates a coupling between the respective surface temperatures $T^{(i)}_{S.ext}$ and $T^{(j)}_{S.ext}$ and hence possibly between different BEMs (see Fig. 2.27).

Nonetheless, as for the solar flux, wall ($wall$) and window (win) surfaces are not differentiated from whole facades in the view factor computation. Hence, a facade equivalent radiant surface temperature ($T_{S.ext.rad-eq}$ [K]) is defined as follows:

$$(S_{win}+S_{wall})\cdot T^4_{S.ext.rad-eq} = S_{win}\cdot\varepsilon_{ext.win}\cdot T^4_{S.ext.win}+S_{wall}\cdot\varepsilon_{ext.wall}\cdot T^4_{S.ext.wall} \quad (2.33)$$

Cette thèse est accessible à l'adresse : http://theses.insa-lyon.fr/publication/2018LYSEI071/these.pdf
© [L. Frayssinet], [2018], INSA Lyon, tous droits réservés

where $wall$ and win refer to wall and windows characteristics, respectively.

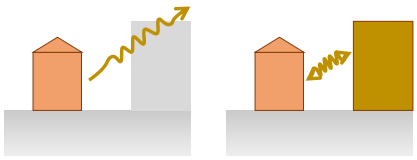

(A) LWRad-0 (B) LWRad-1

FIGURE 2.29: Inter-building LW radiative exchanges modelling variants

2.2.3 Coupling between adjoining building

In case of adjoining buildings, there is a direct coupling at the party wall interface [Adjoin-1]. Let us consider a party wall between building A and B, respectively numbered i_A and j_B. One half of this party wall is modelled in the respective BEMs, and the 2 continuity relationships are imposed at the interface, as follows:

$$\begin{cases} \Phi_{cd.ext}^{(i_A)} + \Phi_{cd.ext}^{(j_B)} = 0 \\ T_{S.ext}^{(i_A)} = T_{S.ext}^{(j_B)} \end{cases} \iff T_{S.ext}^{(i_A)} = T_{S.ext}^{(j_B)} = \frac{T^{(i_A,K_{i_A})} + T^{(j_B,K_{j_B})}}{2}$$

As previously indicated, this modelling variant creates couplings in the DEM between adjoining BEMs.

The modelling of adjoining walls is often problematic as the building division of a district bloc is generally unknown or is very uncertain (see building division improvements of Pedrinis (2017) for example). As a consequence, in addition to the assumption that this coupling is negligible, the coupling can be not considered [Adjoin-0]. Concretely, the half party walls are assumed adiabatic at their outer face.

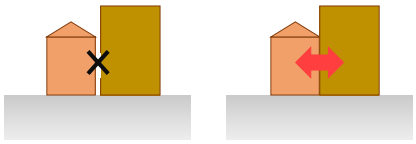

(A) Adjoin-0 (B) Adjoin-1

FIGURE 2.30: Adjoining wall modelling variants

2.3 Chapter conclusions

The main principles of building and district energy models were introduced in this chapter, focusing on the envelope modelling. It was notably highlighted that the conductive heat problem constitutes the heaviest part of the model to solve. Furthermore, it was evidenced that BEMs are not originally suitable for the district scale and require specific supplementary models. In order to relate the different modelling variants to data availability and computational implications, Table 2.1 specifies the

Cette thèse est accessible à l'adresse : http://theses.insa-lyon.fr/publication/2018LYSEI071/these.pdf
© [L. Frayssinet], [2018], INSA Lyon, tous droits réservés

	Building internal layout	Permeability	Exterior wind pattern	Leakage position	System regulation	Window position	Window characteristics	Fabric composition	Material characteristics	Building shape	District geometry	Modelling surrounding buildings	Affect computational cost
[Zoning]	×												×
[Infil]	×	×	×	×						×	×		×
[Control]	×				×								(×)
[trSol]	×					×	×			×			
[intLW]	×												(×)
[Cond]								×	×				×
[Inertia]	×							×	×				(×)
[extConv]			×								×		
[extLW]													×
[EqEnv]										×			×
[Red]													×
[Solar]										×	×		
[LWrad]										×	×	×	×
[Adjoin]										×	×	×	×

TABLE 2.1: Main information related to the modelling variants

main related information and their impact on the computational cost. Detailed models obviously requiring more detailed information.

Different modelling variants were retained in order to analyse the impact of the related assumptions on the model relevance. The next chapter aims to propose a methodology in order to quantify these impacts and hence the suitability of the simplifications.

Cette thèse est accessible à l'adresse : http://theses.insa-lyon.fr/publication/2018LYSEI071/these.pdf
© [L. Frayssinet], [2018], INSA Lyon, tous droits réservés

Cette thèse est accessible à l'adresse : http://theses.insa-lyon.fr/publication/2018LYSEI071/these.pdf
© [L. Frayssinet], [2018], INSA Lyon, tous droits réservés

Chapter 3

Quantifying simplification suitability

Contents

3.1 Usual approaches

3.1.1 Short review

Different building and district energy model variants were identified in the previous chapter (summarised in Appendix B). Most of these model variants were established because of a lack of information or to reduce the simulation computational cost. However, how can the suitability of these models be evaluated?

For instance, among the district energy model adaptations identified in (Frayssinet et al., 2018b), for the 3 different model categories, to 'validate' their adaptations Robinson and Stone (2005) compared the results of the simplified radiosity algorithm they developed with a reference software RADIANCE; Kämpf and Robinson (2007) compared their simplified thermal model with a reference model ESP-r;

Cette thèse est accessible à l'adresse : http://theses.insa-lyon.fr/publication/2018LYSEI071/these.pdf
© [L. Frayssinet], [2018], INSA Lyon, tous droits réservés

and Flor and Dominguez (2004) compared the air temperature they computed with a zonal model with experimental results.

3.1.2 Contribution

As seen previously, the *suitability* of an adaptation is commonly deduced by determining its effects on the model output. These effects are quantified by comparing the output of the simplified model with a reference (Coakley, Raftery, and Keane, 2014). The simplification is said to be suitable if the deviation between the simplified model output and the reference is not *too high*, i.e., is lower than a threshold tolerance (Fig. 3.1). If the reference is the measurement results, this process is called *model validation*. In our cases, the reference comes from the results of a reference model.

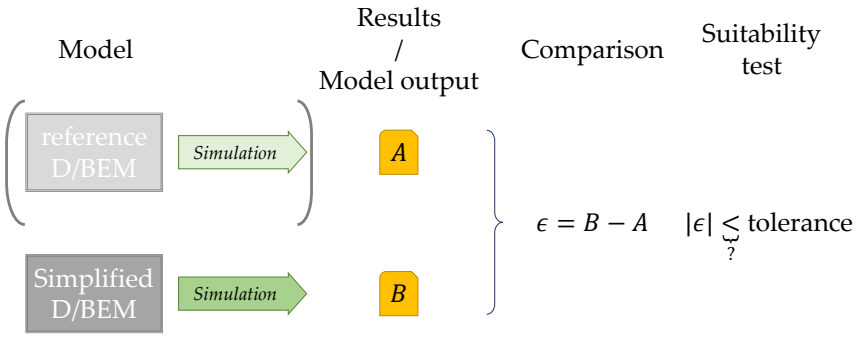

FIGURE 3.1: Common simplification suitability test process

The identified simplifications are usually based on previous-generation building simulations that focused on the annual energy consumption of energy-inefficient buildings (Clarke, 2007). However, the suitability of these usual simplifications are already questionable for recent high-efficiency buildings (e.g., (Bontemps et al., 2013; Bontemps, Mora, and Schumann, 2016)). They also are questionable when observing the output at short time steps and not only in terms of total annual energy, (C-category identified in Chapter 1).

Both limitations are present in district-scale energy simulations as districts may contain any type of building and are often used for power load analysis. Furthermore, they generally imply increasing model complexity, which tends to increase the computational cost and the amount of input data, but decreases in the input data are usually necessary because of the large studied spatial domain.

The objective of this chapter is to develop a methodology capable of studying:

- the suitability of usual simplifications, notably at short time steps;
- and the suitability of the usual simplifications at the district scale.

Indeed, at this scale, the aggregation of numerous buildings is expected to make the simplifications more suitable as the usual use of statistical and coarser models

Cette thèse est accessible à l'adresse : http://theses.insa-lyon.fr/publication/2018LYSEI071/these.pdf
© [L. Frayssinet], [2018], INSA Lyon, tous droits réservés

at this scale seems to justified this approach. This effect was notably evidenced by Talebi, Haghighat, and Mirzaei (2017) by comparing district scale and building scale model errors. The related issues are as follows:

- *Does the district scale has an attenuation effect on the suitability of simplifications?* Indeed, it could be expected that the diversity of buildings in a district may de-synchronize the individual effects of simplifications and hence, reduce the global effect at the district scale, compared to the sum of the individual effect.
- *Can an energy* macro *model at the district scale be deduced from the micro-simulation of its buildings?* In a similar way that the behavior of a concrete beam can be model at the macro-scale, without modelling the behaviour of its different elements (sand grains, aggregate, etc.) at the micro-scale.

Both issues are particularly addressed in Sec. 3.2.4, and illustrated in Sec. 5.2.

To the best knowledge of the author, no common methodology has been developed for such objectives, which consequently represents a central contribution of our work.

The final objective of the methodology developed is to quantify the effect of the usual simplifications in order to:

- select the suitable simplifications and the associated input data, for a given simulation objective and associated variable of interest (VOI) to decrease the computational cost and the needed data;
- and reciprocally to determine the reachable simulation objective, given the necessary simplifications imposed by the available data and limited computational capabilities.

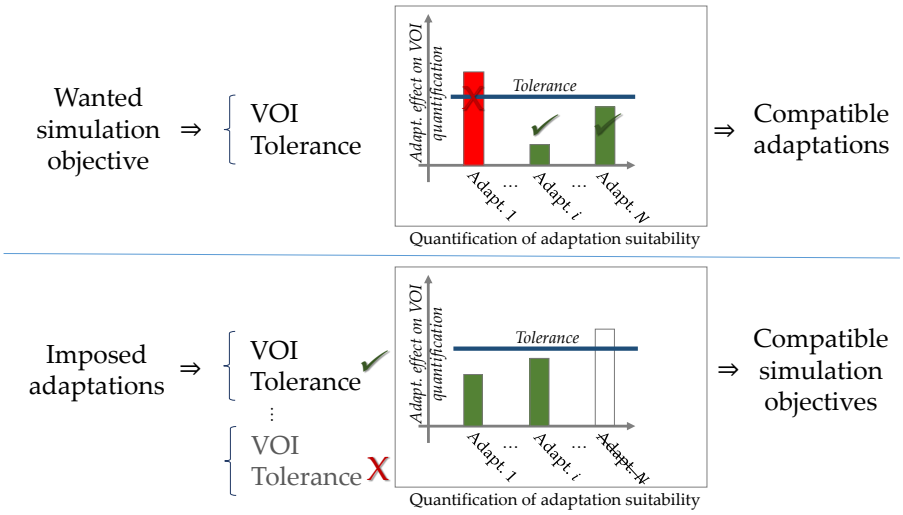

FIGURE 3.2: Objective of quantifying the adaptation effect

In the following, the word *simplification* is replaced with *adaptation*, to indicate that models simplifications are made to adapt the model to a specific objective, such as to match available data or to reduce the computational cost.

Cette thèse est accessible à l'adresse : http://theses.insa-lyon.fr/publication/2018LYSEI071/these.pdf
© [L. Frayssinet], [2018], INSA Lyon, tous droits réservés

3.2 Methodology

The objective of this section is to define a methodology to quantify the effect of an adaptation of the model to conclude about its suitability.

The proposed methodology is the most general possible, but in the presentation, some elements are specifically defined to apply the methodology in some specific cases but in a general approach. However, these elements can be modified to suit specific simulation objectives.

3.2.1 Global principle

The adaptation effect is quantified by comparing adapted model simulation results with the reference results in terms of VOI. An adaptation is considered suitable if the deviation between both VOIs is lower than a given tolerance (Fig. 3.4). The definition of the VOI and the tolerance depend of the simulation objective, i.e., the focal aspect and the desired accuracy.

In the most generic considered cases, the simulation result is $P(t)$ [W], to consider short time evolutions during the considered period T_P [s] ($t \in T_P$). Due to the numerical temporal resolution and for coherence with the inputs, $P(t)$ is regularly sampled with a time step δt. P is the resulting time series: $P = \{p_1, \cdots, p_i, \cdots, p_N\} = \{P(t = \delta t), \cdots, P(t = i \cdot \delta t), \cdots, P(t = N \cdot \delta t)\}$. The total energy need during the period is $E = \int_{T_P} P(t) \cdot dt$ [J], which could be estimated[1] with the time series P as follows: $E \approx \delta t \cdot \sum_1^N p_i = \tilde{E}$.

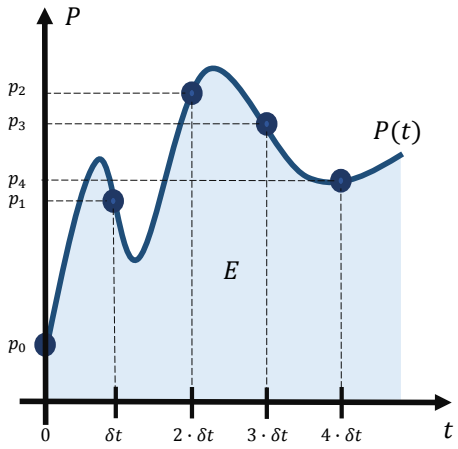

FIGURE 3.3: Power curve

As the quantification of the adaptation effects is commonly based on scalar results (usually the total energy needs), a problem arises when considering the power curve (Fig. 3.4). In this case, indicators are needed to extract scalars that quantify relevant characteristics of the time series (VOI). Some graphical representations are sometimes used (as in (Robinson and Stone, 2005) and (Kim et al., 2014) for instance). However, an infinite number of characteristics could be defined as illustrated in the following. The choice depends on the simulation objective.

To the knowledge of the author, no specific indicators have been specifically defined when studying the adaptation suitability with respect to the power curve in

[1] Riemann's integral.

Cette thèse est accessible à l'adresse : http://theses.insa-lyon.fr/publication/2018LYSEI071/these.pdf
© [L. Frayssinet], [2018], INSA Lyon, tous droits réservés

building and district energy models. As a consequence, a set of 5 indicators is proposed to cover a large spectrum of simulation objectives. Several indicators may be chosen, notably if considering the computational time. But, in this case, multi-criteria analysis are needed to conclude about adaptation suitability. Such analysis are not considered further in the present work.

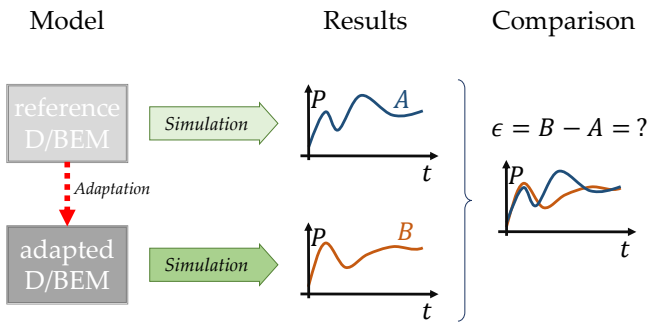

FIGURE 3.4: Comparing power curves issue

3.2.2 Indicators

Let the superscripts (0) and (a) refer to the reference and the adapted model, respectively.

The first four indicators are based on the time series differences (Fig. 3.5a), which are defined as follows:

$$D = \{p_i^{(a)} - p_i^{(0)}, i \in [1, N]\} = \{d_i, i \in [1, N]\} \tag{3.1}$$

- **The mean**:

$$\mathrm{m}(D) = \sum_{i=1}^{N} \frac{d_i}{N} \tag{3.2}$$

  This indicator gives the mean differences between the two power curves. Using this indicator to quantify the adaptation effect is equivalent to considering the effect on the total energy need. Indeed, $\tilde{E} = N \cdot \delta t \cdot m(P)$, and hence, $N \cdot \delta t \cdot m(D) = \tilde{E}^{(a)} - \tilde{E}^{(0)}$. The sign of this indicator indicates whether the adaptation causes a mean under or over-estimation.

- **The rectified mean**:

$$\mathrm{rm}(D) = \mathrm{sign}\Big(\mathrm{m}(D)\Big) \cdot \sum_{i=1}^{N} \frac{|d_i|}{N} \tag{3.3}$$

  where $\mathrm{sign}(.)$ is the function that returns the sign of the variable.

  This indicator is similar to the previous indicator but with the absolute value. Deviations are considered rather than differences. Consequently, there is

Cette thèse est accessible à l'adresse : http://theses.insa-lyon.fr/publication/2018LYSEI071/these.pdf
© [L. Frayssinet], [2018], INSA Lyon, tous droits réservés

no compensation between positive and negative differences, and $|\mathrm{rm(D)}| \geq |\mathrm{m}(D)|$. If $\mathrm{rm}(D) = \mathrm{m}(D)$, then all the differences have the same sign, which is to say that the adaptation causes strict under or over-estimation.

- **The standard deviation**:

$$\sigma(D) = \sqrt{\sum_{i=1}^{N} \frac{\Big(d_i - \mathrm{m}(D)\Big)^2}{N}} \tag{3.4}$$

The standard deviation gives an indication of the scattering of the time series differences. A low standard deviation indicates that the differences are nearly constant over the time-steps (but not that the mean deviation is close to zero).

- **The absolute maximum**:

$$\mathrm{M}(D) = \max_{i \in [1,N]} \Big(|d_i|\Big) \tag{3.5}$$

This indicator, also called the infinite norm, returns the maximal deviation between the two time series. This is the most restrictive indicator as it assures that for all time-step, the deviation is under this value. This indicator may be used when the accuracy of the power curve is needed at all times.

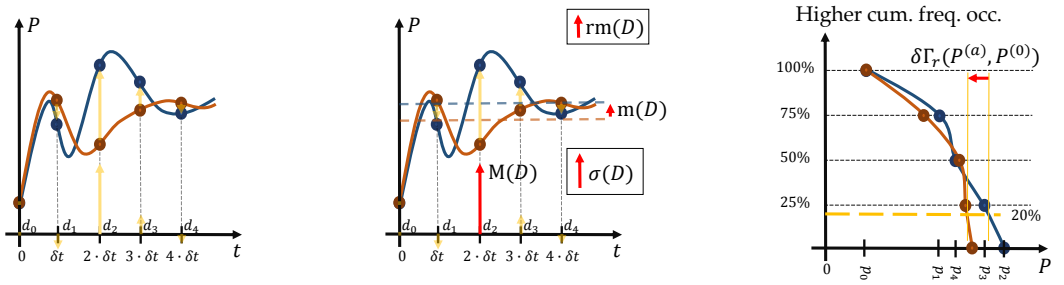

(A) Time series differences

(B) Related indicators

(C) Cum. freq. of higher occ. curve

FIGURE 3.5: Comparing two time series

Cumulative frequency of higher occurrences The last indicator is based on the cumulative frequency of the higher power occurrences curve. This curve (see Fig. 3.5c) associates each power level of the time series with the percentage of occurrences in the time series that are higher, as follows:

$$p_i \mapsto 100 \cdot \frac{\mathrm{card}\Big(\{p_j | p_j \geq p_i \text{ and } p_j > 0\}\Big)}{\mathrm{card}\Big(\{p_j | p_j > 0\}\Big)} \tag{3.6}$$

where $\mathrm{card}(.)$ is the function that returns the set cardinality. Non-zero powers are not accounted for to only account for the energy system working period (excluding floating temperature periods).

The inverse function, written as $\Gamma_P(.)$ in the following, is more commonly used. $\Gamma_P(r)$ returns the power level for which r % of the elements of P are higher. These kind of considerations are particularly used for energy system design.

Cette thèse est accessible à l'adresse : http://theses.insa-lyon.fr/publication/2018LYSEI071/these.pdf
© [L. Frayssinet], [2018], INSA Lyon, tous droits réservés

- **Difference in design level**:

$$\delta\Gamma_r(P^{(a)}, P^{(0)}) = |\Gamma_{P^{(a)}}(r) - \Gamma_{P^{(0)}}(r)| \tag{3.7}$$

  This last indicator quantifies the deformation of the cumulative frequency of higher occurrence curve of the power at a given relative design frequency (20 % used by default).

Figures 3.5b and 3.5c clearly highlight that quantifying the adaptation effect depends on the chosen indicator. However, each indicator focuses on a particular aspect of the power curve (VOI), and their choice depends on the modelling objective. Each indicator is not systematically linked to a specific simulation objective but is complementary to other to give a global idea of the effect of adaptation the power curve. Specific combinations or modifications of these indicators could be defined to suit a specific simulation objective.

Weight In particular, when simulations are used to study energy networks, generally, power peaks are of interest as they are essential parameters for the design of district energy supply and storage systems. To account for these kinds of specificities, the time series differences D could be weighted to highlight some parts of the power curve. Then, the indicators integrate these weights.

To illustrate the previous point, the following arbitrary weight is considered in the present work:

$$d_i \to d_i \cdot \frac{p_i^{(0)}}{\Gamma_{P^{(0)}}(20)} \tag{3.8}$$

Hence, the difference increases if the reference power level at the same time belongs to the 20 % highest values and otherwise decreases proportionally to the power level (Fig. 3.6). Any other specific weight could be defined to suit the simulation objective.

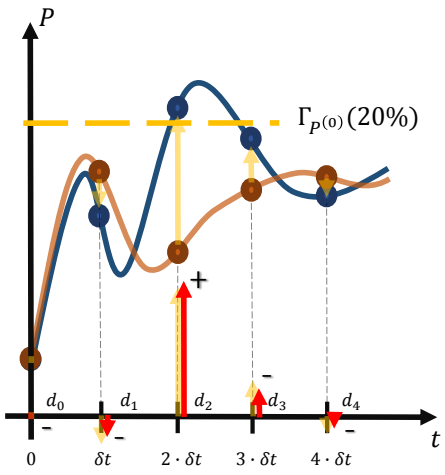

FIGURE 3.6: Time series differences weighting

Relative indicators The indicators defined previously return scalar values in watt. Relative indicators are needed to compare heating and cooling and also to compare

Cette thèse est accessible à l'adresse : http://theses.insa-lyon.fr/publication/2018LYSEI071/these.pdf
© [L. Frayssinet], [2018], INSA Lyon, tous droits réservés

different buildings (with different materials, different shapes, etc.). As for indicators, an infinite number of references can be defined with respect to the power curve. The reference chosen is the mean non-zero power (to exclude the floating temperature periods) of the reference model. This choice gives an order of magnitude of the deviation: a relative indicator higher than 100 % indicates deviations, relative to the indicator chosen, higher than the mean power, and that are hence probably intolerable. The representativeness of this relative reference is notably confirmed in Sec. 5.2.

Period definition In the more general case, the annual period is considered to test all possible typical combinations of thermal loads occurring during a whole year. However, for some simulation objectives, this period can be limited, for example to critical heating or cooling periods.

Otherwise, cooling and heating powers are separated to analyse them individually. Indeed, building behaviour is fundamentally different in both cases, and simulations often focus only on one of them.

The definition of the transition between heating and cooling periods is not clear. A necessary condition to apply times series difference-based indicators is that the periods for the adaptation and the reference results are the same. In the case of zero matching, the shortest period could be extended with zero values. Defining the end of a period at its last occurrence can lead to a misquantification of the adaptation effect. Indeed, adaptation may cause over or under estimations, leading to power needs during the floating temperature periods of the reference, notably at times close to the transition to this kind of periods.

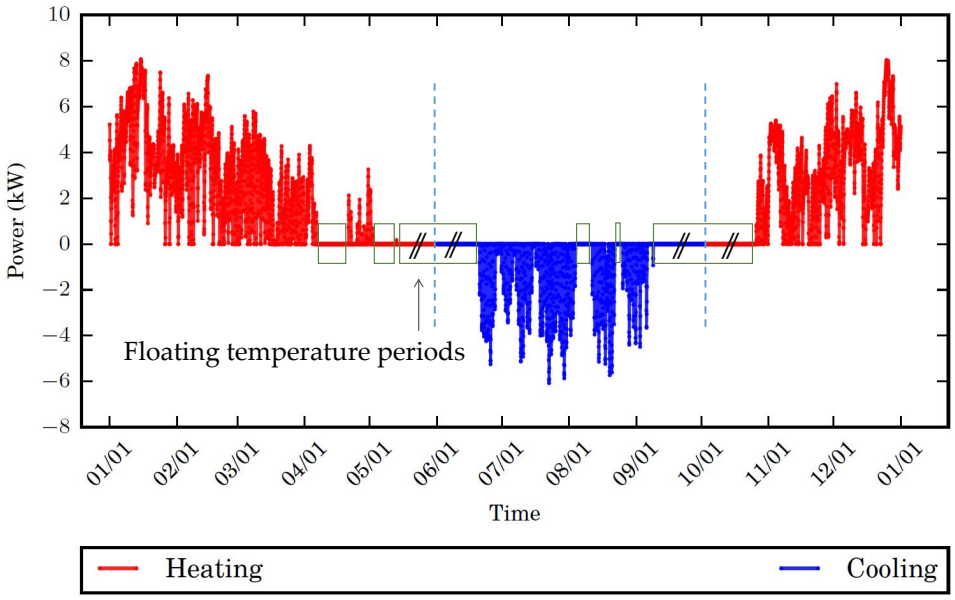

FIGURE 3.7: Heating and cooling periods

To avoid these misestimations, we chose to cut-up the period at the midpoint between the last occurrence of heating and the first occurrence of cooling and vice versa (Fig. 3.7). For practical reasons, the cut up is moved to the closest end of day. Periods were only computed for the reference results and applied to the adapted model results. This choice does not guarantee that heating (and reciprocally cooling) of the adapted results only occurs during the respective period of the reference. In

Cette thèse est accessible à l'adresse : http://theses.insa-lyon.fr/publication/2018LYSEI071/these.pdf
© [L. Frayssinet], [2018], INSA Lyon, tous droits réservés

these cases, deviations are still considered but in the other period. These border effects are considered negligible. Nonetheless, more elaborate cuts could be defined, based on the value of the floating temperature for example, but are not considered further.

Note that, at district scale, heating and cooling can occur simultaneously. Indeed, notably during mid-season, some buildings may need heating (if shaded for example) while others need cooling (if sun exposed). In these cases cooling and heating periods are considered independently (they are not consecutive), and the larger periods belong all buildings is retained for all the buildings of the district.

Considering phase differences In case of time phase differences between the 2 time series, important deviations can be measured whereas the 2 time series are just not in phase. These deviations are why specific measures were developed to 're-synchronise' time series before measuring deviation, such as the *Dynamic Time Wrapping* method (notably used by Grandjean (2013)). The shortcoming of this method is that a mean difference is measured. Therefore, a term-by-term comparison (time series differences) is not kept, and time phase differences are not penalised except if defining an equivalence between time and power. These 2 drawbacks could be corrected by adapting the method. However, the minimal time phase difference is equal to the time step considered and, in general, is already considered too important over the time phase tolerance. Thus, such methods were not used in this work but could be used as additional indicators for other specific simulation objectives. The proposed corrections and details about this method are presented in Appendix A.4.

Sampling influence It is expected that the adaptation effect changes with the sampling period of the result. The sampling period also depends of the simulation objective (yearly, daily, and other effects). To study this influence, the sampling period is artificially modified thanks to the Haar wavelet decomposition method (Fig. 3.8), starting from the shorter time-step to mid-year period (sampling periods considered: 45 mn, 1.5 h, 3 h, 6 h, 12 h, 1 day, 2 days, 4 days, 8 days, 16 days, 32 days, 64 days, 128 days and 256 days).

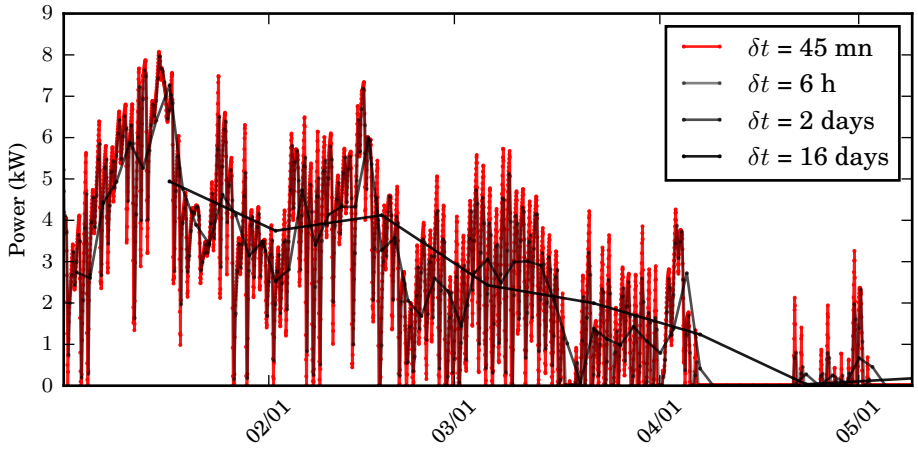

FIGURE 3.8: Haar wavelet decomposition of the heating curve for different sampling periods (δt)

Details of the method are given in Appendix A.5. With this decomposition, it is possible to study the transition of the adaptation effects from local effects (at the

Cette thèse est accessible à l'adresse : http://theses.insa-lyon.fr/publication/2018LYSEI071/these.pdf
© [L. Frayssinet], [2018], INSA Lyon, tous droits réservés

minimal time step) to the mean effect. These transitions are evidenced using the representation shows in Fig. 3.9. In this figure, the indicators are normalized with respect to their values at the shortest time step to have a global view of all indicators[2]. The norms values are directly indicated in the figure. Hence, in the graph, the y-axis indicates the remaining percentage whith the increase in the sampling period.

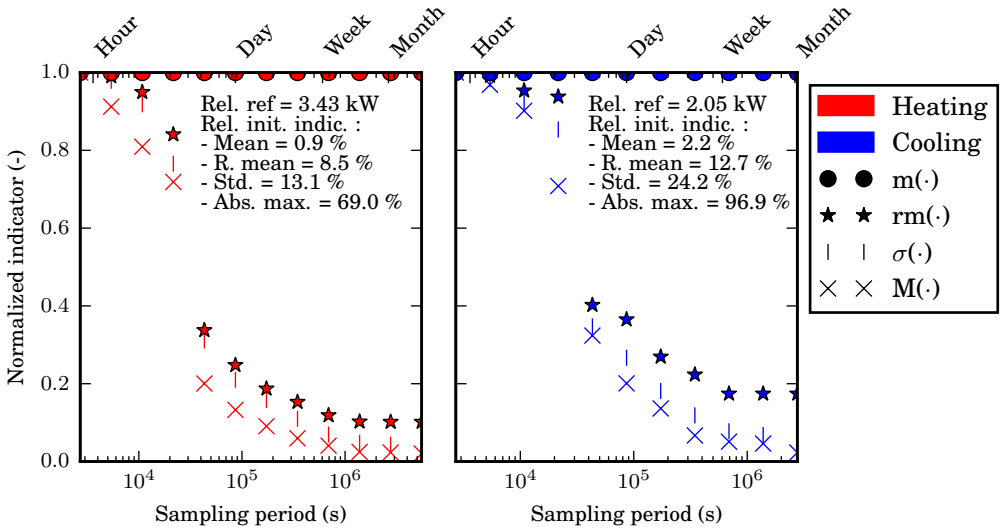

FIGURE 3.9: Sampling influence on the indicators

This method may be extended using more elaborate frequency decomposition methods. However, as these methods depend on the simulation objective, they are not detailed further. The objective is to introduce complementary information to help define a specific indicator, particularly for different time steps, and to a lesser extent, to understand the physical implications.

3.2.3 Complementary analysis representations

To analyse the adaptation effects beyond the information given by the retained indicators and to give additional information for other potential simulation objectives, a set of complementary representations, introduced hereafter, is associated with each adaptation effect. To avoid to affect the readability of the present manuscript in the results chapter (Chap. 5), these figures are mainly given in Appendix C.

Remember that the objective is to compare the power curve of the adapted model with the reference (Fig. 3.10). Note the absolute values of the powers are considered in the following to compute time series differences (Eq. 3.1), and hence, cooling is represented and always considered with absolute (positive) values.

The first representation used to analyse the adaptation effects (Fig. 3.11) gives the temporal evolution of the time series relative differences (absolute scales are given in twin axes) and the values of the 3 first indicators defined above.

[2] As the minimal time step is different from the original time step (45 mn vs. 1 h) and the time series is shorter (to apply the method), the norms of the indicators may be different from original estimations but are very close.

Cette thèse est accessible à l'adresse : http://theses.insa-lyon.fr/publication/2018LYSEI071/these.pdf
© [L. Frayssinet], [2018], INSA Lyon, tous droits réservés

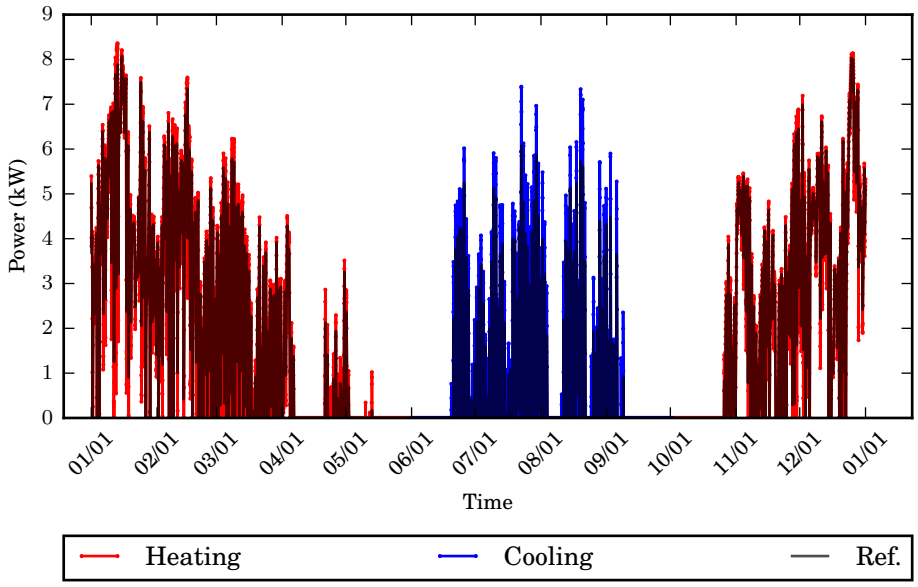

FIGURE 3.10: Comparison of adapted and reference model results

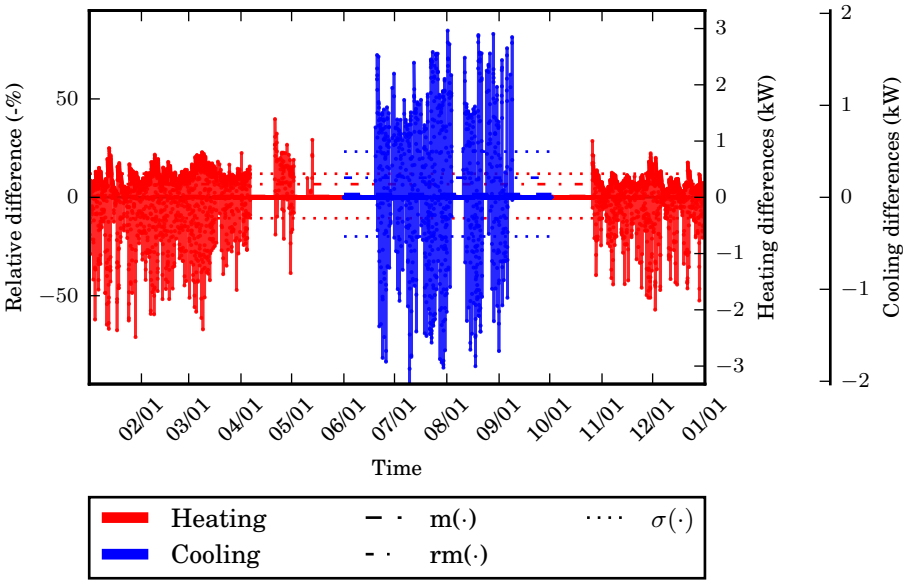

FIGURE 3.11: Relative differences in temporal evolution

The second representation (Fig. 3.12) is based on the cumulative frequency of higher power occurrence curves. The associated indicator, the difference in design level (by default, $\delta\Gamma_{20}$), is illustrated in the same figure.

Cette thèse est accessible à l'adresse : http://theses.insa-lyon.fr/publication/2018LYSEI071/these.pdf
© [L. Frayssinet], [2018], INSA Lyon, tous droits réservés

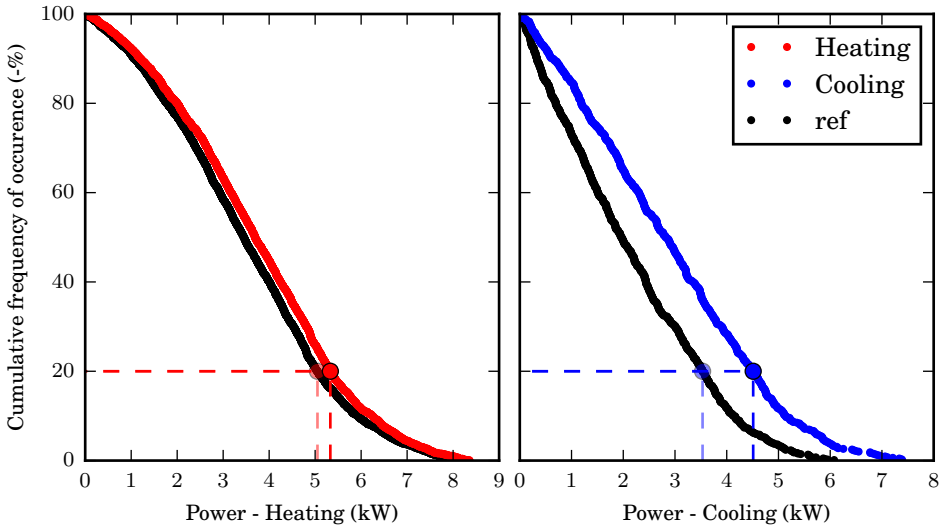

FIGURE 3.12: Cumulative frequency of higher occurrence curves

According to the defined methodology, adaptations are quantified based on the indicators defined previously. These adaptations are visually plotted as shown in Fig. 3.13. To have a more complete overview of the statistical distribution, *boxplots* are also used (Fig. 3.14). In the *boxplot* representation, the red line corresponds to the median value; the rectangular box contains values belonging to the second and the third quartiles (50 % of the central values); the 2 peripheral dot lines (whiskers) length is equal to 1.5 times the interquartile width except if the maximal values are lower; and extreme values out of these whiskers are individually identified by a cross.

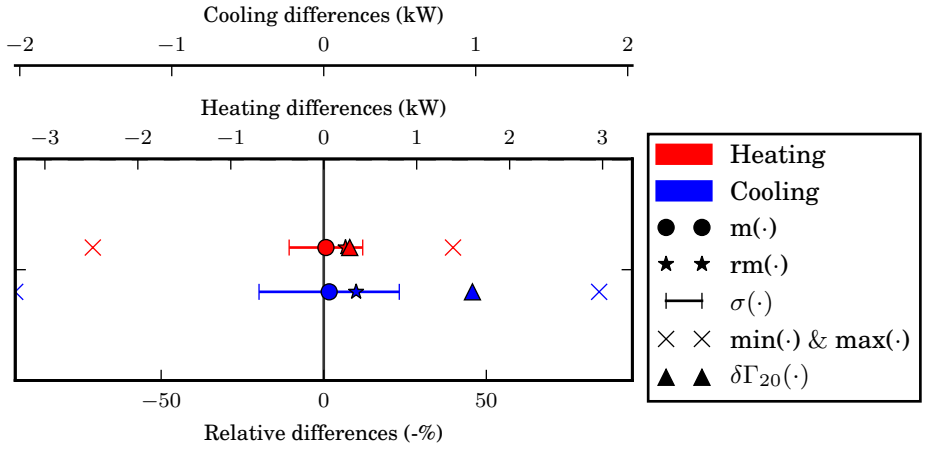

FIGURE 3.13: Indicators representation

Cette thèse est accessible à l'adresse : http://theses.insa-lyon.fr/publication/2018LYSEI071/these.pdf
© [L. Frayssinet], [2018], INSA Lyon, tous droits réservés

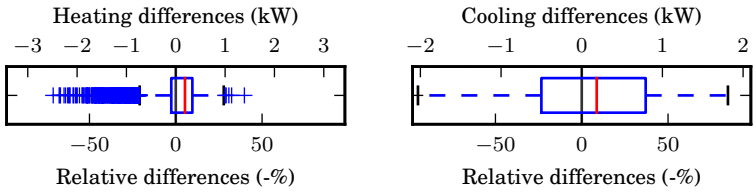

FIGURE 3.14: Boxplots of the differences

When physically analysing the time series differences, it is useful to use the *heatmap* representation of the differences (daily decomposition of the time series, Fig. 3.15) and the *daily boxplot* representation of the differences (daily statistical distribution, Fig. 3.16). These representations help understand the daily effect pattern of adaptations.

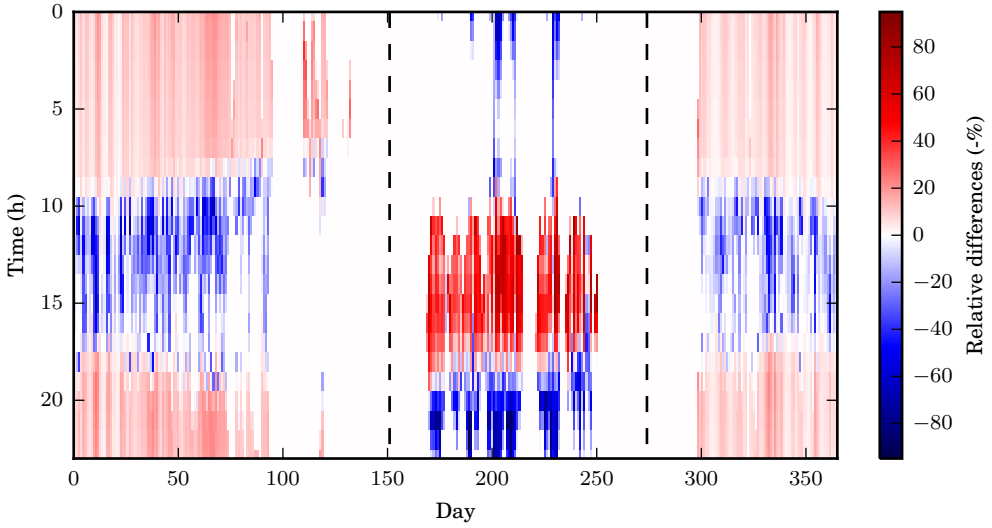

FIGURE 3.15: Heatmap representation of the differences

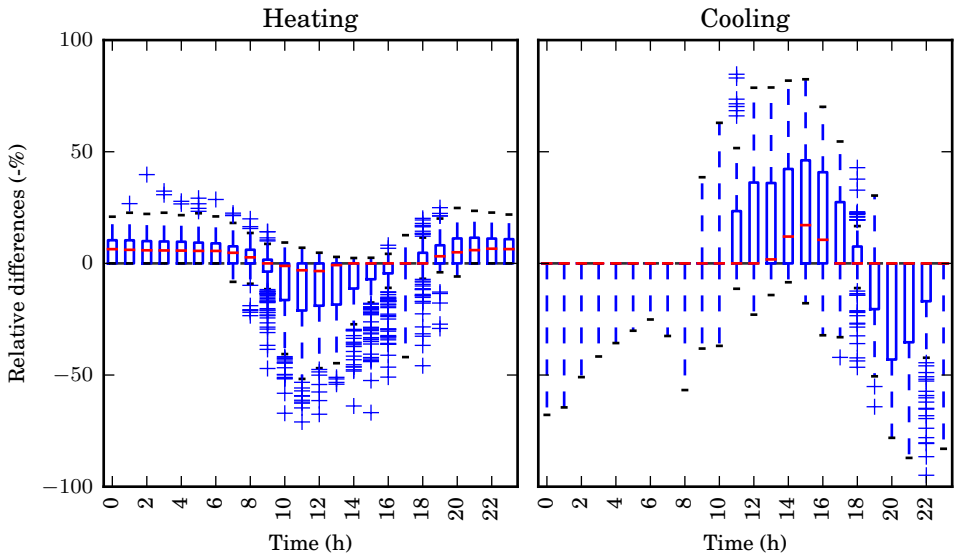

FIGURE 3.16: Daily boxplot representation of the differences

Cette thèse est accessible à l'adresse : http://theses.insa-lyon.fr/publication/2018LYSEI071/these.pdf
© [L. Frayssinet], [2018], INSA Lyon, tous droits réservés

Moreover, another representation based on the plotting of the adapted model results as a function of the reference results is used (Fig. 3.17). Each point corresponds to a discrete time $i \cdot \delta t$. Its coordinates are $(P^{(0)}(t = i \cdot \delta t), P^{(a)}(t = i \cdot \delta t)) = (p_i^{(0)}, p_i^{(a)})$. The adapted model differs from the reference if the points move away of the diagonal. If the points are above, in absolute values, the adapted model under-estimates, and if they are below, it over-estimates. This representation indicates whether the adapted results follow the same pattern as the reference (follows the diagonal) or a proportional pattern (lower or higher linear function) and if the differences occur for specific power levels.

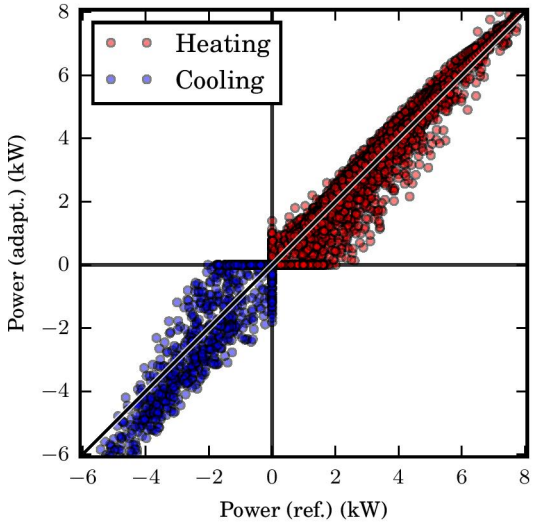

FIGURE 3.17: Adapted model results versus reference results

Last, the correlations between weather input variables (identified in the solicitation vector U, Eq. 2.7) and time series differences are studied to determine whether some dependencies exist (Fig. 3.18). The existence of strong dependencies may simplify the effect prediction, but also indicates physical-related phenomena. The weather input variables identified before are completed with the total horizontal solar flux ($\phi_{toth.Sol}$), the wind direction (dir(v)), the reference power (P) and its temporal variation (dP/dt). The correlation between two variables (X and Y) is quantified with the Pearson correlation coefficient:

$$p_{X,Y} = \frac{\mathrm{cov}(X, Y)}{\sigma(X) \cdot \sigma(Y)} \tag{3.9}$$

where cov is the covariance.

The closer to 1 the absolute value of this coefficient is, the more correlated the time series is, and a negative coefficient indicates the opposite variations.

Cette thèse est accessible à l'adresse : http://theses.insa-lyon.fr/publication/2018LYSEI071/these.pdf
© [L. Frayssinet], [2018], INSA Lyon, tous droits réservés

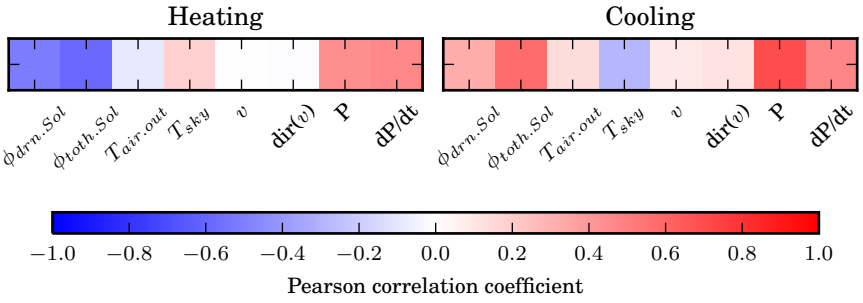

FIGURE 3.18: Time series differences in correlation with weather inputs and model output

3.2.4 District-scale specificities

Diversity

As indicated above, the district scale is of particular interest. This interest relies on the phenomenon in which at the district scale, due to the aggregation of individual energy consumers, mutualisation makes it possible to reduce the overall energy production system size. Indeed, due to the diversity of consumer behaviour, the individual peaks of demand, which control the sizing, are not exactly simultaneous, and consequently, the global peak is lower than the sum of the individual ones and the variations are relatively less abrupt (Fig. 3.19a). This smoothing effect is related to the district *diversity*, and in our case it is expected to smooth adaptation effects.

The probable source of diversity that may affect building energy behaviour at the district scale is the variety of building shapes, construction materials, and occupant behaviours. The variety of shape both affects the building spatial characteristics and its weather-induced thermal loads (notably solar and radiant temperature in our model).

The complementary part of the coincidence factor (notably used by Grandjean (2013)) is used to quantify the diversity effect at the district scale as follows:

$$\kappa^{(a)} = 1 - \frac{\mathrm{ind}\left(\sum_{b=1}^{N_b} P_b^{(a)}, \sum_{b=1}^{N_b} P_b^{(0)}\right)}{\sum_{b=1}^{N_b} \mathrm{ind}\left(P_b^{(a)}, P_b^{(0)}\right)} \tag{3.10}$$

where N_b is the total number of buildings in the considered district, P_b is the power of the building b and $\mathrm{ind}(\cdot)$ is any of the indicators defined above. The sums in the numerator of the fraction correspond to the total power of the district for the adapted and reference models, respectively. This indicator quantifies the percentage of reduction of the adaptation effect (measured by the indicator $\mathrm{ind}(\cdot)$) caused by the district scale compared to the sum of individual effects (Fig. 3.19b).

The analysis of correlations (Fig. 3.18) may discriminate between adaptations with potential low smoothing effect in cases where time series differences are highly correlated to input variables that do not vary from one building to another.

Cette thèse est accessible à l'adresse : http://theses.insa-lyon.fr/publication/2018LYSEI071/these.pdf
© [L. Frayssinet], [2018], INSA Lyon, tous droits réservés

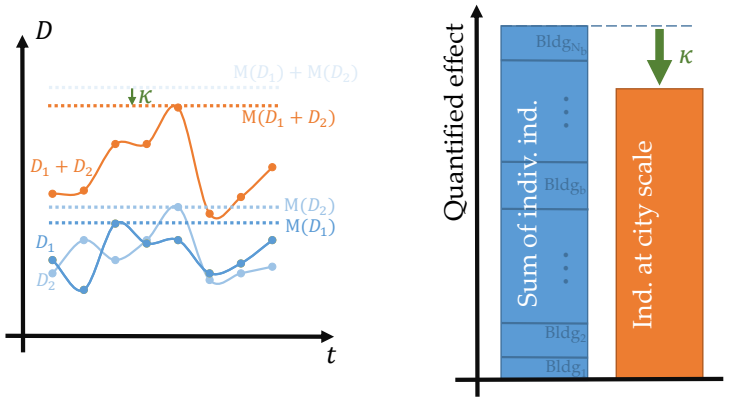

(A) Smoothing effect (B) Diversity quantification

Indicator representativeness

The spatial scale of the district may also influence the relative value of the indicators measuring the adaptations suitability. Are these indicators are representative of the district?

We assumed that the answer is yes if the relative value of the indicators is robust (nearly unaffected) to the removal of some buildings of the district, whatever they are (Fig. 3.20). The objective is to determine whether the indicator estimation converge whatever the combination of buildings and if the scattering of the results is low. If both cases are true, it can be concluded that the indicator is representative of the district scale.

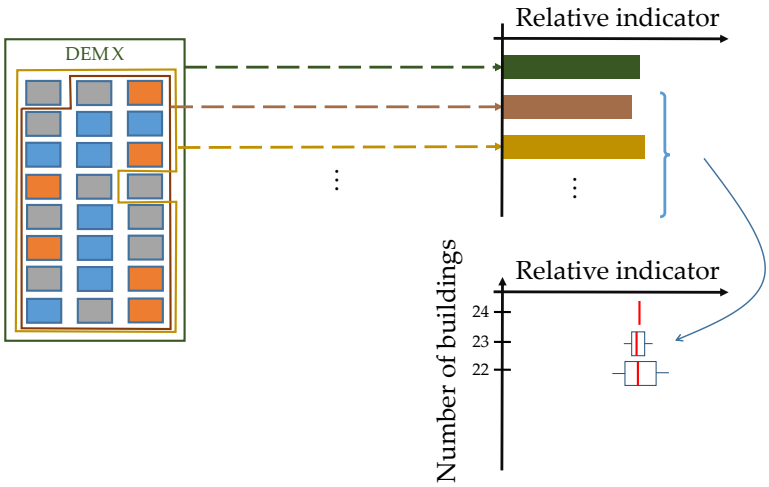

FIGURE 3.20: Analysis of indicator convergence

Statistical invariance

At the city scale, some information is only known statistically, such as the occupant behaviour and the building typology. This information is inferred in order to apply specific properties to each BEM. Even though this process, whatever the random draw, does not affect the statistical distribution of the information, it affects individual BEM results and consequently the DEM result. However, how much these results are affected?

Cette thèse est accessible à l'adresse : http://theses.insa-lyon.fr/publication/2018LYSEI071/these.pdf
© [L. Frayssinet], [2018], INSA Lyon, tous droits réservés

To analyse the impact of statistical information on the DEM, the following methodology is proposed: numerous random draws are performed (Fig. 3.22), and district-scale results are compared. If this impact is low (low scattering between results), the DEM is called statistically invariant to the studied source of data. Nonetheless, the spatial scale may influence the statistical invariance. As illustrated in Fig. 3.22 it is expected that the increase in the district size decreases the scattering of the results due to a higher sample size, according to the central limit theorem. Its applicability in our case is discussed here-after.

A meaning of the central limit theorem is that the more the measures for a noised variable, the better the estimation given by the mean of these measurements. Basically, for n individual measures, the standard deviation of the mean is:

$$\sigma_m = \frac{\sigma}{n^{\frac{1}{2}}} \tag{3.11}$$

with σ the measurement standard deviation.

In other word, the higher the sample of measurement used to compute the mean, the less uncertain is the mean (Fig. 3.21).

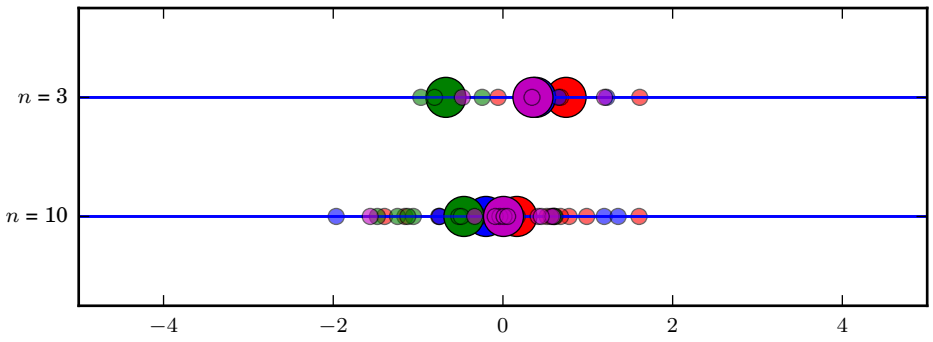

FIGURE 3.21: Illustration of the central limit theorem
The biggest dots are the mean of the little dots of the same color: 4 different estimations with two size of sample (n). The scattering of the mean is lower with the largest sample. A centred normal distribution is used.

The analogy with the district scale is the following:

- the measure uncertainty $\leftrightarrow$ the stochastic perturbation due to occupant behaviour or parameter uncertainty;
- the measure $\leftrightarrow$ the relative effect due to a perturbation for a building;
- the mean $\leftrightarrow$ the mean relative effect due to a perturbation at district scale (made of n buildings).

If this trend is observable in our case at district scale, that means that the impact of the uncertainty due to stochastic unknowns (occupant behavior or material properties) may became negligible at a sufficiently high district scale (with a sufficiently important number of aggregated buildings).

However, 2 aspects differ from the theorem framework:

- first, the random variable (the measurement) is a time-series, hence the it is not possible to quantify a unique standard deviation as done with scalar value;

Cette thèse est accessible à l'adresse : http://theses.insa-lyon.fr/publication/2018LYSEI071/these.pdf
© [L. Frayssinet], [2018], INSA Lyon, tous droits réservés

- second, the different random variable has to be independent and identically distributed, that is difficult to evaluate with time-series.

Despite the first identified divergence, to quantify the scattering of the time-series differences, with respect to the reference, we computed the relative indicators ($\mathrm{ind}(\cdot)$, Sec. 3.2.2) for each k estimation:

$$I = \left\{\mathrm{ind}(P^{(k)}, P^{(0)}), k \in [1, K]\right\} \tag{3.12}$$

Then we compute the standard deviation of the different estimates of the indicator: $\sigma(I)$.

Even if the theorem is not strictly applicable, if the computed standard deviations follow a decrease in power $\frac{1}{2}$ with the district scale (number of building) as in Eq. 3.11, conclusions are similar.

FIGURE 3.22: Statistical invariance analysis

This specificity is essential at the district scale to have confidence in the simulation results despite the statistical uncertainties.

3.3 Link with sensitivity analysis

A specific global methodology, sensitivity analysis, proposes powerful methods to determine the influence of model characteristics on model results. Tian (2013) reviewed such methods used for building energy modelling. However, as evidenced hereafter, in their original formulations, these methods are not suitable for use in our central case. Nevertheless, the methodology proposed in the previous section is an adaptation of one of these methods. Nonetheless, in one specific case study (Sec. 5.1.4), sensitivity analysis methods are used in their original formulation and with some modifications.

Linking the proposed methodology with sensitivity analysis makes it possible to insert this method in a formal framework in addition to proposing possible extensions.

Cette thèse est accessible à l'adresse : http://theses.insa-lyon.fr/publication/2018LYSEI071/these.pdf
© [L. Frayssinet], [2018], INSA Lyon, tous droits réservés

3.3.1 Principle

Sensitivity analysis (Saltelli et al., 2008; Popelin and Dutfoy, 2014; Chastaing, 2013) is based on uncertainty analysis. Indeed, modelling processes contain many sources of uncertainty, such as

- model uncertainty, due to the translation of phenomena into sets of equations;
- numerical uncertainty, due to equation solving methods;
- parametric uncertainty, due to variability or a lack of knowledge.

The main objectives of uncertainty analysis are

- to understand the influence or rank the importance of uncertainties;
- to validate a model;
- to compare relative system performance;
- to demonstrate system's compliance.

The aim of sensitivity analysis is associated with the 2 first items.

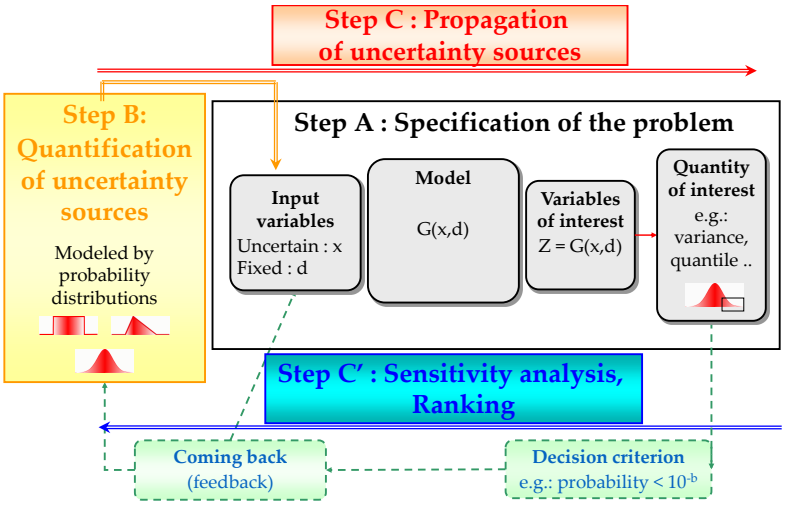

FIGURE 3.23: Global methodology of uncertainty management. (From (Popelin and Dutfoy, 2014))

A global sensitivity analysis process is divided into 4 steps (Fig. 3.23). In our case, this step corresponds to

A. Problem specification: definition of the used model, its inputs, its uncertain characteristics, and the variable of interest (the focal part of the simulation results);

B. Uncertainty quantification: quantification of the distribution of probability of the considered uncertain inputs;

C. Uncertainty propagation: the input uncertainties are propagated through the model for various sets of the uncertain characteristics. These sets depend on the sensitivity analysis method used (see next subsection);

Cette thèse est accessible à l'adresse : http://theses.insa-lyon.fr/publication/2018LYSEI071/these.pdf
© [L. Frayssinet], [2018], INSA Lyon, tous droits réservés

C'. Sensitivity analysis: sensitivity indexes, depending of the method, are computed from the simulation results of the uncertainty propagation.

These steps are defined in the following in each case study when applying the adaptation effect quantification methodology (Chap. 5).

Application In our framework, the objective of the sensitivity analysis is to understand the influence of uncertainties to accredit models (select suitable ones). The uncertainties considered are epistemic as they are due to a lack of information and are consequently theoretically reducible thanks to better knowledge (as opposed to stochastic uncertainties, which come from intrinsic variability and are irreducible).

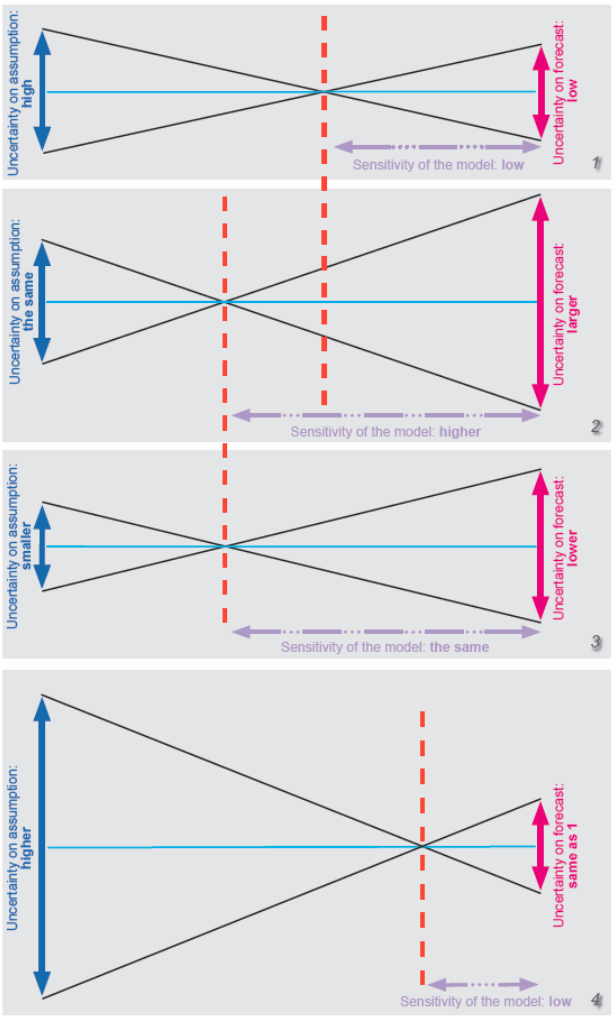

FIGURE 3.24: Link between sensitivity and input and output uncertainties
(From (Chouquet, 2007), cited in (Bontemps, 2015))

The main divergence of the usual sensitivity analysis with respect to the methodology proposed is that they are designed for parametric uncertainties, whereas in our case, model uncertainties are focused on. Notably, the quantification of sources of uncertainty by probability distributions, which are suited to parametric uncertainties, is not suitable for model uncertainties but is the central part of uncertainty management methodology. Furthermore, the influence of the source of uncertainty

Cette thèse est accessible à l'adresse : http://theses.insa-lyon.fr/publication/2018LYSEI071/these.pdf
© [L. Frayssinet], [2018], INSA Lyon, tous droits réservés

is quantified via the notion of sensitivity, which consider relative effects (Fig. 3.24 –*forecast* corresponds to the model resulting variable of interest), but it is inappropriate to define a relative reference in case of model uncertainty. That feature is the reason why we choose to talk about *adaptation effects* and not the *sensitivity of models to adaptation*. These two points are illustrated in the next section.

3.3.2 Main methods

Let Y be the variable of interest in the model, which depends on the parameters x_1, ... , x_N.

Local sensitivity analysis

With this method, the sensitivity of the model s_n to a parameter x_n corresponds to the partial derivative, which is approximated as follows:

$$s_n^{(0)} = \frac{\partial Y}{\partial x_n}\left(x_1 = x_1^{(0)}, \cdots, x_N = x_N^{(0)}\right) \tag{3.13}$$

$$\approx \frac{Y\left(x_1^{(0)}, \cdots, x_n^{(0)} + \Delta_n, \cdots, x_N^{(0)}\right) - Y\left(x_1^{(0)}, \cdots, x_n^{(0)}, \cdots, x_N^{(0)}\right)}{\Delta_n} \tag{3.14}$$

This sensitivity is said to be local because it is evaluated for the set of parameters $x_1^{(0)}$, ... , $x_N^{(0)}$. An evaluation in $x_1^{(1)}$, ... , $x_N^{(1)} \neq x_1^{(0)}$, ... , $x_N^{(0)}$ is different if the model is not linear. Similarly, the choice of the parameter step Δ_n impacts this evaluation. Solutions are proposed in the following method to compensate these drawbacks.

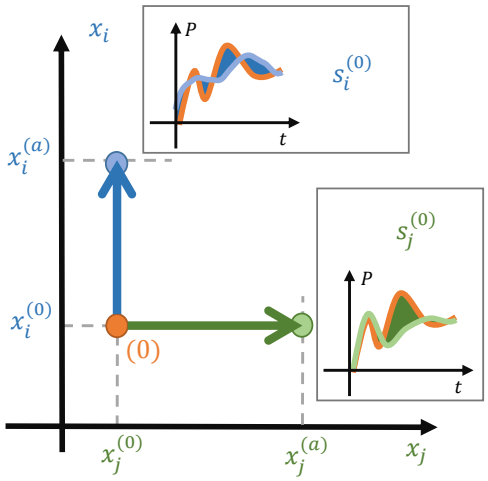

FIGURE 3.25: Design of the experiment in the parameter space for local sensitivity analysis and an illustration of the effects on the power curve

In our cases, model uncertainties are considered rather than parameter uncertainties. However, the different variations of modelling may be considered as parameters ($x_n \equiv \text{model}_n$) but with discrete values ($\text{model}_n^{(0)}$ = reference model, and $\text{model}_n^{(a)}$ = adapted model). For example the transmitted solar flux can be modelled according to $x_{tr.Sol}^{(0)}$ = [trSol-0] or $x_{tr.Sol}^{(a)}$ = [trSol-1]. Hence, if $x_n^{(0)} \equiv \text{model}_n^{(0)}$, then $x_n^{(0)} + \Delta_n \equiv \text{model}_n^{(a)}$. Δ_n corresponds to the transition from the reference model to

Cette thèse est accessible à l'adresse : http://theses.insa-lyon.fr/publication/2018LYSEI071/these.pdf
© [L. Frayssinet], [2018], INSA Lyon, tous droits réservés

the adapted one. However, Δ_n cannot be quantified as a scalar value, so how can the model transition be quantified? Furthermore, given that our objective is to quantify adaptation effect and not to evaluate sensitivity (Fig. 3.24), the denominator of Eq. 3.14 is ignored. Using the previous notation, we come back to Eq. 3.1:

$$Y(x_1^{(0)}, \cdots, x_n^{(0)} + \Delta_n, \cdots, x_N^{(0)}) - Y(x_1^{(0)}, \cdots, x_n^{(0)}, \cdots, x_N^{(0)}) \equiv P^{(a)} - P^{(0)} = D \quad (3.15)$$

As the result is a time series, indicators (Sec. 3.2.2) have to be applied.

Time series sensitivity index may be computed, with the complete formulation (Eq. 3.14) and compatible cases. However, the cause and the effect are not always synchronous, mainly due to inertia, leading to misrepresentations of the results. It may be possible to resynchronise input causes with output effects. However, such a method is not convincing, whereas applying the indicators is more suitable.

Morris method

To compensate for the drawbacks linked to the potential non-linearity of the models studied, the Morris method consists of repeating the evaluation of Eq. 3.14 M times for each parameter on different sets of parameters, as follows:

$$\begin{aligned} s_n^{(0)} &= \frac{\partial Y}{\partial x_n}(x_1^{(0)}, \cdots, x_N^{(0)}) \\ s_n^{(1)} &= \frac{\partial Y}{\partial x_n}(x_1^{(1)}, \cdots, x_N^{(1)}) \\ &\vdots \\ s_n^{(M)} &= \frac{\partial Y}{\partial x_n}(x_1^{(M)}, \cdots, x_N^{(M)}) \end{aligned}$$

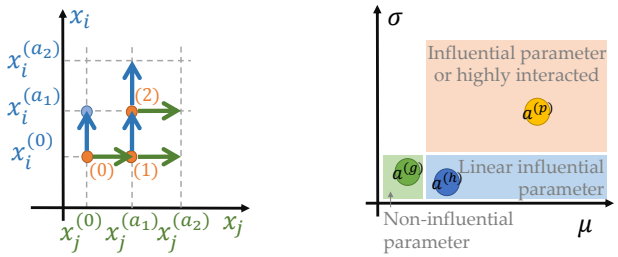

(A) Example of design of experiment

(B) Analysis of the parameter influence

FIGURE 3.26: Morris method

The parameter space is regularly sampled in a M^N grid so that $x_n^{(m)} + \Delta_n = x_n^{(m+1)}$. The definition of this set of parameters depends on the design of experiments chosen (example in Fig. 3.26a). Based on the defined design of experiments, two

Cette thèse est accessible à l'adresse : http://theses.insa-lyon.fr/publication/2018LYSEI071/these.pdf
© [L. Frayssinet], [2018], INSA Lyon, tous droits réservés

indicators are used to quantify the parameter sensitivity, as follows:

$$\mu_n = \sum_{m=1}^{M} \frac{s_n^{(m)}}{M} \tag{3.16}$$

$$\sigma_n = \sqrt{\sum_{m=1}^{M} \frac{(s_n^{(m)} - \mu_n)^2}{M-1}} \tag{3.17}$$

where μ_n is the mean sensitivity of the model to the parameter x_n and σ_n indicates the scattering of the x_n-related sensitivities. It is common to qualitatively compare the influence of the parameters and categorize them using a $\mu - \sigma$ plot (Fig. 3.26b), as follows:

- if $\mu_n \simeq 0$ and $\sigma_n \simeq 0$, then parameter x_n is non-influential;
- if $\sigma_n \simeq 0$, then the parameter x_n has a linear influence;
- else, the parameter is influential or has important interaction effects.

This method accounts for non-linearity but cannot distinguish influential parameters from highly interacted parameters.

The Morris method can be applied in our main case studies with the same precaution detailed previously (considering effects rather than sensitivity).

Sobol index

The Sobol method, as with the Morris method, is based on design of experiments to consider a global sensitivity analysis. The first-order sensitivity index is computed as follow based on the variance decomposition:

$$s_n = \frac{\mathrm{V}(\mathrm{E}(Y|x_n))}{\mathrm{V}(Y)} \tag{3.18}$$

where $\mathrm{V}(.)$ is the variance and $\mathrm{E}(.)$ is the expected value. $Y|x_n$ distinguishes all outputs into M categories depending on the value of x_n: $Y|x_n = \{Y|(x_n = x_n^{(1)}), \cdots, Y|(x_n = x_n^{(M)})\}$. In the previous equation (Eq. 3.18), the numerator corresponds to the variance of the expected values of each of these elements.

The Sobol index s_n measures the part of the total variance due to the parameter x_n. The higher the Sobol index is, the more influential the parameter is. According to the variance decomposition, $s_n \leq 1$.

The first order index does not consider any interaction effect. Interaction effects may be estimated using higher-order indexes, the sum of which is called the total sensitivity index.

The advantage of this formulation, in our specific case study, is that the output Y can be time dependent (does not require indicators), leading to time-dependent Sobol indexes (Fig. 3.27, which was notably used by Bontemps (2015)), for which an indicator could be useful for aggregating information. Furthermore, this formulation does not use Δ_n linked to x_n and consequently does not require quantifying the transition related to model adaptation.

Cette thèse est accessible à l'adresse : http://theses.insa-lyon.fr/publication/2018LYSEI071/these.pdf
© [L. Frayssinet], [2018], INSA Lyon, tous droits réservés

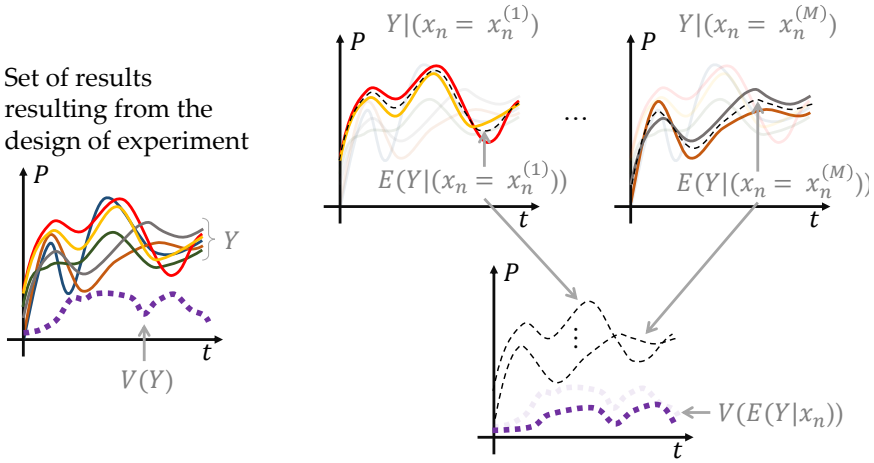

FIGURE 3.27: Sobol sensitivity index construction with a time dependant variable of interest

3.3.3 Application for time-dependent inputs or outputs

The particularity of the case study analysed in Section 5.1.4 is that the modelling uncertainty can be considered as parametric uncertainty but with functional parameters. Indeed, in this section, building environmental variable modelling effects are considered, and the modification of the model can be associated with the modification of the corresponding environmental variable, which is a time-dependant input of the BEM and can be considered as a model functional parameter.

Uncertainty analysis based on functional parameters was conducted by Nanty (2006) for example, but more specifically for building environmental variables by Goffart, Rabouille, and Mendes (2016). However, a functional statistical framework is considered as not sufficiently developped by Iooss (2011). However, such an analysis needs a large series of inputs in different conditions to quantify functional parameter uncertainty distributions (i.e., different yearly weather data in (Goffart, Rabouille, and Mendes, 2016) to analyse the impact of weather variability). However, only 3 different configurations per variable are available in our case. Furthermore, these environmental variables are very sensitive to the urban scene. Consequently, a representative uncertainty distribution may be very difficult to determine, particularly if considering inter-correlation which may be strongly affected by the urban configuration. An analysis is proposed in Sec. 5.1.4 accounting for these limitations.

Concerning the time-dependency of the output, rather than using indicators as proposed in this contribution, Campbell, McKay, and Williams (2006) proposed to expand the functional output in a appropriate functional coordinate system. The principle is similar as it consists on focusing on specific feature or pattern of the curve, but its applicability still limited in our specific main study because of the model uncertainty consideration. Furthermore, the definition of the coordinate system is clearly identified as the '*main art*', as for the indicator definition.

Cette thèse est accessible à l'adresse : http://theses.insa-lyon.fr/publication/2018LYSEI071/these.pdf
© [L. Frayssinet], [2018], INSA Lyon, tous droits réservés

3.4 Chapter conclusions

The present chapter introduces the methodology defined to quantify simplifications suitable for different simulations objectives, or technical constraints. This quantification aims to help adaptations selection. It is particularly able to consider power load curves.

This methodology was identified as similar to general sensitivity analysis methods. The main differences and limitations of the applicability of usual sensitivity analysis methods in our specific case were evidenced. Nonetheless, the most advanced sensitivity analysis methods, which notably account for non linearity (Morris and Sobol methods), were not used in the main study, except in Sec. 5.1.4. Indeed, our objective is to estimate the adaptation effect. Hence, the supplementary details given by the interacted effects (second and following orders) are not crucial. Furthermore, the local adaptation effects are quantified around a common BEM, which is commonly used. The sensitivity around other combinations of adaptations, even if more detailed and supposedly closer to reality, changes in common use and common modelling, which is the key focus of this work. Moreover, some modelling combinations may be incompatible. Last, as only 2 or 3 modelling levels are defined, the statistical functions used are based on very little sampling, leading to questionable representativeness of the statistical results. In addition, the parameter (modelling) space has to be regularly sampled, but, as the quantification of deviation between models is not possible, the regularity and the related impact are also questionable.

The key part of this methodology is the definition of a relevant indicator that corresponds to the simulation objective. Such a definition, when considering power load curves, is almost never specifically defined in the literature, and is consequently a necessary target. To compensate for this lack in the literature, some general indicators have been proposed to give an overview of the adaptation effects in Chapter 5. Furthermore a complementary set of various representations aims to give the opportunity for readers to estimate the adaptation effects with respect to their specific indicator.

Cette thèse est accessible à l'adresse : http://theses.insa-lyon.fr/publication/2018LYSEI071/these.pdf
© [L. Frayssinet], [2018], INSA Lyon, tous droits réservés

Cette thèse est accessible à l'adresse : http://theses.insa-lyon.fr/publication/2018LYSEI071/these.pdf
© [L. Frayssinet], [2018], INSA Lyon, tous droits réservés

Chapter 4

Modelling and simulation platform

Contents

4.1 Objective

In order to apply the methodology presented previously, a specific tool chain was developed. As a reminder, the objective of the methodology is to quantify the impact of model adaptations, in particular on power at the district scale. The methodology relies on the comparisons of the results of simulations of various types of building energy models (different adaptations).

The first step in the tool chain consists of generating building energy models. As a district energy model is composed of a substantial number of buildings models, an **automatic building energy model generator** is needed for practicality. Moreover, numerous adaptations are considered, and hence, the building model generator has to be **modular**.

The second step consists of simulating these models. Because of the high computational cost, resulting in potentially high levels of model details, and because of the high number of models (due to the number of buildings in the district and the number of experiments), it is beneficial to **distribute the simulations** to reduce the simulation duration.

The last step consists of an **analysis of results** with the methods previously introduced (Chap. 3).

The tools and the data used in these 3 steps (Fig. 4.1) and their orchestration are detailed hereafter. Alternative methods found in the literature are also introduced to identify possible improvements and/or merging for the present tool chain. The tool chain developed this work, which automatically manages the different steps, is

Cette thèse est accessible à l'adresse : http://theses.insa-lyon.fr/publication/2018LYSEI071/these.pdf
© [L. Frayssinet], [2018], INSA Lyon, tous droits réservés

written in Python[1] and is called MoDEM, which stands for *Modular District Energy Modeller*. A sketch of the created tool chain principle is given in Fig. 4.3.

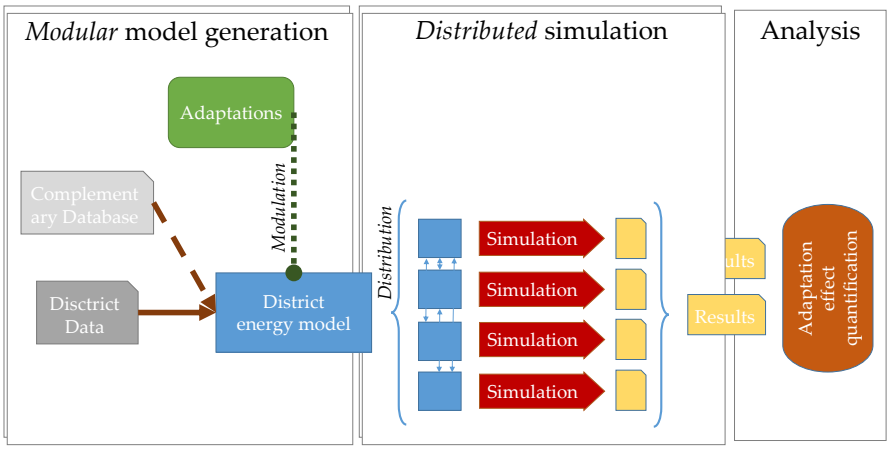

FIGURE 4.1: Sketch of the tool chain objective

4.2 Tool chain

4.2.1 Data source

In order to generate a district energy model, district information is obviously needed. The management of the district scale data is currently growing quickly, in particular using Geographic Information System (GIS). GIS relies on geometrical data, that represent a specific territory (a district in our case), complete with various structured semantic information, such as type description, use, construction period, and other descriptors. A number of cities around the world, are developing GISs. For example, the 'Grand Lyon' metropolis provides open access to such databases[2]. However, the quality of these data often does not suit energy model specifications because of unclosed geometry, the presence of multiple facets in collinear surfaces, or a lack of or incorrect building splitting (see works of Pedrinis (2017) for instance).

An important effort of standardization and interoperability is currently being carried out using the CityGML open format[3], which has become a reference format for district information systems (this format is already used for various applications, including solar atlases, thermal diagnostics, over-flow information, and lighting studies for instance).

In parallel, at the building scale, Building Information Models (BIMs) are becoming established, and are even mandatory in some countries (Fig. 4.2). As with GIS, these numerical models aim to structure building data from architects to workers and from the design to operation stages. The main formats used are gbXML and IFC[4].

[1] *Python homepage - https://www.python.org/*
[2] Available at https://data.grandlyon.com/.
[3] *CityGML homepage - https://www.citygml.org/*
[4] *gbXML homepage - http://www.gbxml.org/*; *IFC Overview summary - http://www.buildingsmart-tech.org/specifications/ifc-overview/ifc-overview-summary*

Cette thèse est accessible à l'adresse : http://theses.insa-lyon.fr/publication/2018LYSEI071/these.pdf
© [L. Frayssinet], [2018], INSA Lyon, tous droits réservés

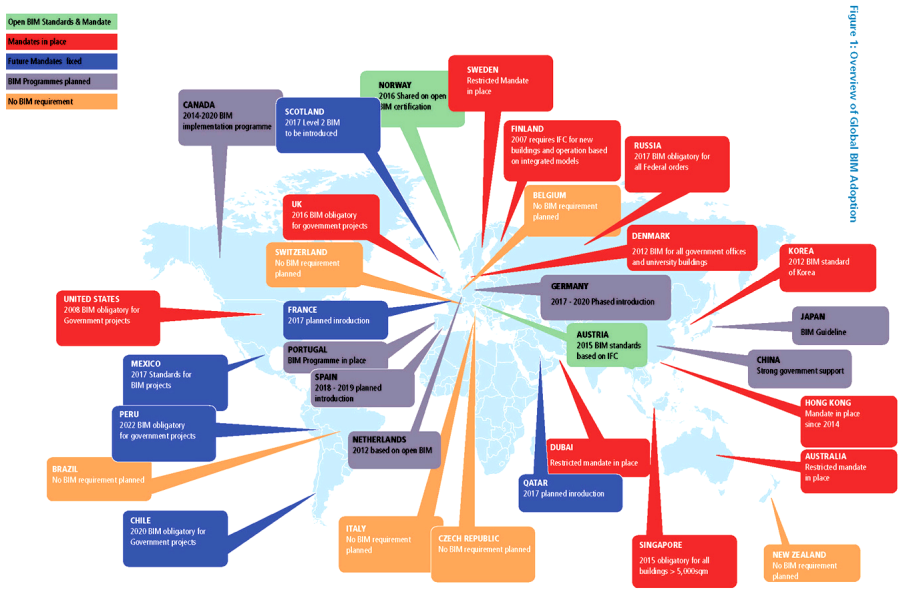

FIGURE 4.2: Overview of Global BIM Adoption
(From (McAuley, Hore, and West, 2017))

The junction between BIM and GIS is in progress (as works of Hijazi (2011)). Nonetheless, as BIMs are especially available for new buildings, there is a great lack of information for existing buildings, which is generally crucial for district models.

At the moment, in most cases, there is a discrepancy between the needs of district models and the data supplied. A key point to improving district models is to create a convergence between city energy modellers, city geographers and even geomatic specialists. This manuscript modestly hopes to contribute to such a convergence through the identification of necessary data for different simulation objectives, thanks to the quantification of the suitability of adaptations (Fig. 3.2).

Geometrical data

Because of a lack of information about the construction materials of the buildings considered in the available test cases, only geometrical data from the district GIS are used. Concretely, these geometrical data comprise the details of the buildings zones (volume) and the enclosure surfaces (area, orientation and adjacent zones).

As a starting point, SketchUp[5] models were used, because of its friendly use and wide adoption, notably in architecture schools (`*.skp` format). Ultimately, the CityGML and IFC formats will be used, with semantic information linked to information about the construction materials of the buildings.

The geometrical data are rewritten in a temporary specific XML file by the MERUBBI tool (`*.bsp`), a pretreatment platform developed in the frame of the MERUBBI research project[6] (Lauzet et al., 2016; Ribault et al., 2017). The XML format is particularly suited to model generation thanks to parsing.

[5] *SketchUp homepage - `https://www.sketchup.com/`*

[6] *Projet MERUBBI - Méthodes d'Exploitation des Ressources Utiles du Bâtiment Bioclimatique dans son Ilot - `http://anr-merubbi.fr/` [French]*

Cette thèse est accessible à l'adresse : http://theses.insa-lyon.fr/publication/2018LYSEI071/these.pdf
© [L. Frayssinet], [2018], INSA Lyon, tous droits réservés

Thermo-physical data

As information on the construction materials of the buildings are not directly available in the GIS used they were deduced from the French residential building typology (Rochard et al., 2015) defined in the European TABULA project[7]. The aim of this project was to classify European national building stocks and to estimate their consumption and the potential energy savings. Each typology is divided into 4 building categories (single-family house, terraced house, multi-family house and apartment block) and 10 construction periods. From these categories, a set of example buildings is proposed notably with a description of the building materials and the system used. Construction periods are known in the studied cases (they could be relatively easily deduced thanks to knowledge about the urbanization period or as a function of the architecture morphology), and building type is deduced with respect to the morphology.

The typology gives U-value for façade elements and construction materials. Related thermo-physical properties (thermal conductivity, density, and specific thermal capacity) are deduced from a database principally originated from the modelling library detailed hereafter. The material thickness is not always available in the typology, and hence, adjustments are necessary to match the specified U-value (either the thickness or the conductivity is adjusted). Therefore, this step makes it possible to enrich the geometrical building data description with thermo-physical parameters. Some other buildings necessary data are not available in the typology (e.g. emissivity, albedo, etc.). They were deduced from default values, notably based on the dataset of the model library used.

In this study, only residential buildings are considered because of the typology used and because their use is much more known and less diverse than those in the tertiary sector. Moreover, this process is highly uncertain, but remember that the objective is not to model reality but rather to feed a district model with coherent and representative values, overcoming a lack of data to test envelope modelling at the district scale. Nonetheless, the uncertainty of data inference will be studied in the next chapter (Sec. 5.2.4).

A similar data enrichment process, TEASER (Remmen et al., 2018), was initially developed for the AixLib Modelica library (Fuchs et al., 2015) and adapted to the OpenIDEAS Modelica library (Baetens et al., 2015) by Ina, Glenn, and Dirk (2017). This approach is notably also able to use information from TABULA typologies.

In addition, concerning GIS, for further extensions of the tool chain, a specific application domain extension) was created in CityGML to store district energy model-related data (Nouvel et al., 2015).

Occupant information

At the district scale, when considering the power curve, it is necessary to consider the notion of diversity. Diversity is the fact that the overall power peak at the district scale is lower than the sum of the individual maximal peaks of each consumer. This phenomenon is due to the non-concomitance of the individual power peaks. This notion is fundamental as it reduces the system size requirement at aggregate scale. This non-concomitance is mainly due to the diversity of consumer behaviours: consumers do not perform the same tasks at the same time. Consideration of this effect is necessary to reproduce realistic power curves. Furthermore, this effect may

[7] http://episcope.eu/building-typology/

Cette thèse est accessible à l'adresse : http://theses.insa-lyon.fr/publication/2018LYSEI071/these.pdf
© [L. Frayssinet], [2018], INSA Lyon, tous droits réservés

influence the adaptation effects (as already discussed in Sec. 3.2.4 and is tested in Sec. 5.2.2).

The diversity of building occupants is mostly examined for electrical demand mainly due to electrical devices (Grandjean, 2013). Concerning heating and cooling needs, the diversity linked to the occupants concerns the variations in the internal heat gain (depending on the occupancy, the devices used, and other factors) and the diversity of energy system settings (temperature setpoint). In most cases, diversity is not considered, and consequently, the internal heat gains and the setpoint temperature are defined according to identical reference schedule. In specific cases, the diversity is modelled using temporally dynamic scenarios of internal heat gains and of setpoint temperature.

These dynamic scenarios are acquired from the SMACH tool, an EDF R&D agent based model (Huraux, Sabouret, and Haradji, 2015; Reynaud et al., 2017). This tool is able to generate activity scenarios for each person in a family with a time-step of 1 minute considering interactions in particular due to housing conditions (comfort). This tool is based on monitoring real conditions of a set of different family types. A statistical population can be generated from city statistical data (type of housing, socio-professional category, etc.) to generate representative city housing scenarios[8].

For our needs, a set of 1,000 monthly scenarios aggregated at the housing level were generated based on statistics on Lyon, France. These scenarios contain the hourly evolution of the number of occupants and of the temperature setpoint and descriptions of the housing and the household. The scenarios last only one month to limit the computing cost and because they are quasi-periodic (for longer simulations, they are repeated). As only the shape of the building is known and not its constituting housing, an aggregate scenario at the building level is generated by randomly assembling the housing scenarios until the total housing floor area nearly corresponds to the estimated floor area of the building[9]. The number of occupants is summed, and the setpoint temperature is weighted by the floor area and averaged.

In the BEM, the internal heat gains are modulated by the occupancy ratio (the number of occupants divided by the total number of occupants), and the set-point temperature is directly imposed (only the heating setpoint temperature is available in the scenarios, and cooling ones are defined by symmetry with respect to 23.5 °C).

This method is obviously rough for estimating the schedule of dynamic internal gains, in particular for the internal heat gains due to electrical devices that are only related to occupancy and for the occupant behaviour, which is non-coupled with current thermal comfort. However, this level of modelling is sufficient for our requirements.

Other agent-based models were notably developped by Robinson, Wilke, and Haldi (2011) and Pflugradt and Muntwyler (2017). In contrast, other tools generating occupant scenarios identified in other DEM platforms (identified in (Frayssinet et al., 2018b)) are based on stochastic modelling. For example, CitySim (Robinson et al., 2009) use works of Page et al. (2008); Page (2007); DIMOSIM (Riederer et al., 2015) use model developped by Gay and Schetelat (2014); SMART-E (Berthou et al., 2015) use similar approach than those developped by Vorger, Schalbart, and Peuportier (2014); Vorger (2014); and the Modelica library OpenIDEAS (Baetens et al., 2015) use the StROBe module (Baetens and Saelens, 2016). No further details

[8] SMACH is also able to generate the electric load curve due to housing electrical appliances from these activity scenarios.

[9] A first level of diversity is hence considered: from housing to building.

Cette thèse est accessible à l'adresse : http://theses.insa-lyon.fr/publication/2018LYSEI071/these.pdf
© [L. Frayssinet], [2018], INSA Lyon, tous droits réservés

were given in the present manuscript as the SMACH tool is suitable to our objectives. To go further, information about occupant behaviour models may be found in (Yan et al., 2015).

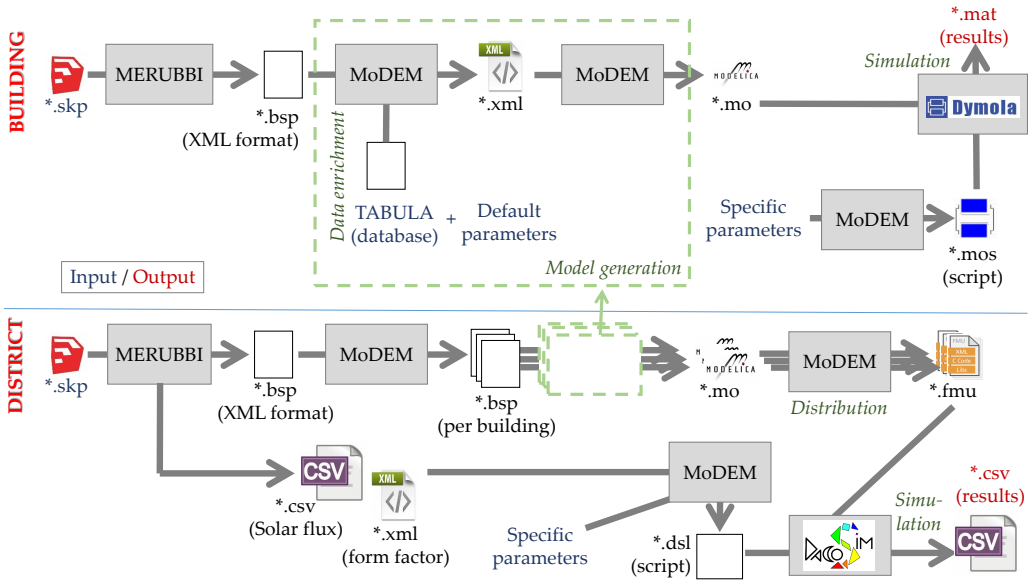

FIGURE 4.3: Detail of the created tool chain

4.2.2 Energy Model

Thanks to the data source described above, all data needed to create the district energy model are available.

Building Energy Model

The BEMs are created using the BuildSysPro Modelica library. Modelica[10] is an object-oriented, equation-based and acausal programming language that was developed to support all engineering domains and hence is particularly suitable to our scope.

More specifically, the BuildSysPro[11] library were used. This tool is an 0D/1D building energy library developed by EDF R&D and adapted to French building stocks (Plessis, Kaemmerlen, and Lindsay, 2014; Schumann et al., 2016). This tool has notably been used for experimental validations of high-efficiency buildings (Bontemps et al., 2013; Bontemps, 2015) and to study the interactions between buildings and their energy systems (Blervaque et al., 2012; Blervaque, 2014).

The generation of BEMs relies on the assembly of building element sub-models (walls, windows, air zones, and others) for each geometrical element of the extracted XML file (Fig. 4.4). The sub-models are parametrized in accordance with the data source and the default or specific parameters. The resulting file is a Modelica model (`*.mo`). The model structure and parametrisation depend on the adaptations considered. This modularity of the model implies different sub-models and different

[10] *Modelica Association - https://www.modelica.org/*

[11] An open version is available here: https://github.com/edf-enerbat/buildyspro.

Cette thèse est accessible à l'adresse : http://theses.insa-lyon.fr/publication/2018LYSEI071/these.pdf
© [L. Frayssinet], [2018], INSA Lyon, tous droits réservés

connections between them, which have to be compatible regardless of the adaptation combination (Sec. 2.1). This automatic process is managed by specific Python code developed during this thesis.

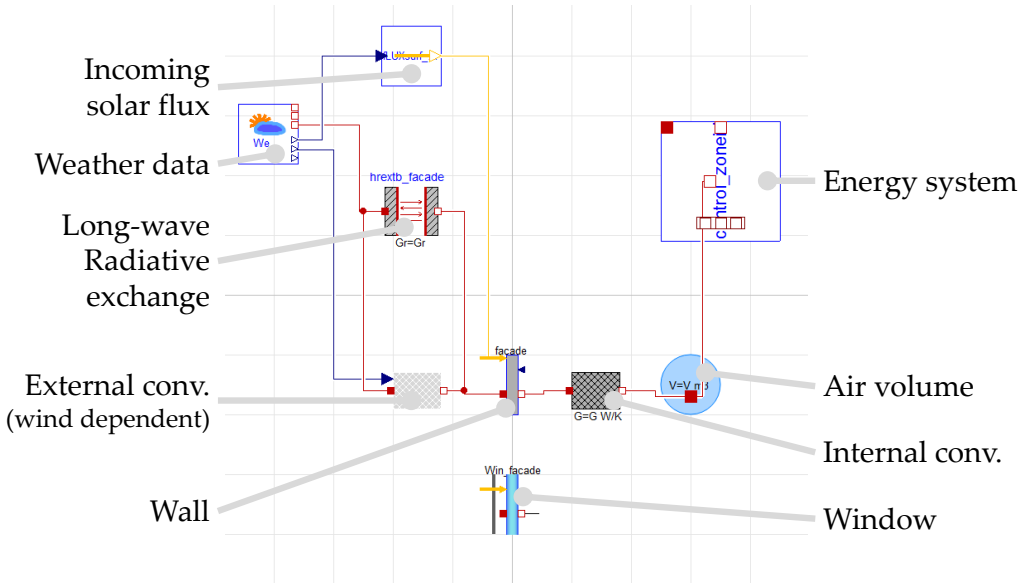

FIGURE 4.4: Glimpse of the BEM using BuildSysPro with Dymola

The modelling and the simulation, at the building scale, are managed with the Dymola environment[12], via a Modelica script (`*.mos`), using notably the `BuildingsPy` Python package[13] and specifically developed functions. Dymola manages the solving of the set of equations defined in the Modelica model, and proposes various solvers for the simulation. The 'Dassl' time-step adaptation solver was used in our simulations as it shown to be the most robust during specific preliminary tests. Because of hourly weather data, the observational time-step was set to 1 h. Annual simulations last about 1 to 2 minutes for the reference models (define later) on a 2.5 GHz and 8 GB RAM computer. The BEM were numerically initialized starting the simulation 1 month earlier.

For information, other Modelica libraries developed for building energy modelling were notably introduced and compared by Tittelein et al. (2016), and some of them are involved in the Annex 60 (Wetter and Treeck, 2017), an Internal Energy Agency (IEA) project aiming to merge development and validation efforts on building energy modelling and that led to the Annex60 Modelica library. The BuildSysPro library was notably involved in this project.

District Energy Model

As the BEM is an assembly of the sub-models, the DEM is an assembly of BEMs. However, this DEM is not written in the Modelica language as the resulting model

[12] *Dymola homepage - https://www.3ds.com/products-services/catia/products/dymola/*

[13] Developed by the LBNL laboratory to ease the processing of Modelica models and simulation results (*BuildingsPy documentation - http://simulationresearch.lbl.gov/modelica/buildingspy/*).

Cette thèse est accessible à l'adresse : http://theses.insa-lyon.fr/publication/2018LYSEI071/these.pdf
© [L. Frayssinet], [2018], INSA Lyon, tous droits réservés

may be too computationally intensive to simulate as it is, and it is much more beneficial to distribute the BEM simulations, notably because they consist of numerous problems of similar weight (BEM) that are relatively weakly linked (Sec. 2.2).

To be distributed, the BEM are converted with Dymola into Functional Mockup Units (FMUs, `*.fmu`)[14], that include both a model and a numerical solver, according to the Functional Mockup Interface (FMI), an open-source and community driven standard developed for coupled simulation and model exchange[15].

The distributed co-simulations of the FMU are managed via a specific script (`*.dng`) by DACCOSIM[16] (Distributed Architecture for Controlled CO-SIMulation), an FMI compatible master algorithm generator developed the RISEGrid institute which is jointly launched by EDF and CentraleSupélec (Galtier et al., 2015). A specific Python application called DacRun makes it possible to distribute the simulation to clusters.

In compliance with Chapter 2, the same adaptations than at the building scale can be considered by modifying the BEMs of the DEM, and 3 specific adaptations are available at district scale (Sec. 2.2). The modelling of these 3 district-scale adaptations necessitate the following specific information and elements:

- Solar shadings and reflections.

  The shading and inter-reflection effects are accounted for using the ray-tracing method available in the MERUBBI tool (an error tolerance of 10^{-2}, and 2 reflections are considered for the computation, after a local sensitivity analysis). The BEM solar inputs are accordingly modified for each facade [Solar-1].

- Inter-building LW radiative exchanges.

  Form factors are computed with the ray-racing method in the MERUBBI tool, for a density of 1,000 points per square meter. The 'viewed' equivalent surface temperatures are coupled only for [LWRad-1].

- Coupling between adjoining buildings.

  For [Adjoin-1], the interface temperatures between adjoining buildings are coupled.

Both of the previous modelling adaptations, when detailed, imply a coupling between FMUs and are managed with DACCOSIM with a constant time-step of 900 s. Therefore, the radiant temperature 'received' by a facade corresponds to the surrounding surface temperature 900 s before. No noticeable deviations were observed when using time step-adaptive coupling or lower time steps[17]. Run simulations lasted about 30 mn for a district made of 23 buildings for the reference model, on the same computer described here-above having 8 cores. The distribution of the simulation on these cores divided the computational time by about 3, but further more detailed analysis about the simulation performance will be carried out with the new version of DACCOSIM.

[14] The Binary Model Export licence is necessary to run the FMUs without a Dymola licence regardless of the original platform (needed when distributing on clusters do not having licence)

[15] *Functional Mock-up Interface* - `http://fmi-standard.org/`

[16] Available at `https://sourcesup.renater.fr/daccosim`

[17] DACCOSIM coupling does not rely on iteration until convergence but potentially relies on time step adaptation (if the estimated error is higher than the tolerance, the time step is reduced, and the last estimation is re-estimated).

Cette thèse est accessible à l'adresse : http://theses.insa-lyon.fr/publication/2018LYSEI071/these.pdf
© [L. Frayssinet], [2018], INSA Lyon, tous droits réservés

4.2.3 Results analysis

The simulation results were analysed according to the methodology previously defined (Chap. 3) with usual Python functions. However, some C++ specific libraries, as GAML[18] and TimeSeries used in a collaborative project link to this tool chain, seems to be more suitable. Indeed, they respectively are design to load and manage dynamically large files (time-series), and efficiently compute arithmetical operations on such large files. These libraries are developed by professors and students of CentralSupelec.

Note that some observed effects may be due to numerical errors due to the solving process. Hence, uncertainty quantified may contain numerical uncertainty. However, the numerical errors are assumed negligible over model uncertainty effects as the solver and the model were well-established. It is confirmed by the physical analysis carried on in the following chapter.

4.3 Chapter conclusions

The developed platform aims to take advantage of existing tools and software to efficiently and automatically create modular district energy models. This tool chain enables the simulation of the power demand of a district considering the main interaction and coupling between buildings. Moreover, the distribution of the simulation make it possible to reduce the computational time, favouring the use of detailed model at district scale and limiting the need of simplifications because of up-scaling, by contrast with the common use of simplified models at district scale.

The generated district models were not validated but were based on the already tried and tested BuildSysPro library. Furthermore, the models were compared to another district energy model, SMART-E (Frayssinet et al., 2018a). This comparison evidenced modelling bias due to the different modelling approach but reinforced the physical modelling approach. The comparison consequently highlighted the need for information about the suitability of modelling choices, particularity at short time steps, which is what this contribution aims to do.

Further developments are expected for this tool chain, notably to improve the computational time and efficiency of the different processes, to complete it, to merge parallel existing developments and to ease interoperability. Notably, the framework of Annex 60 (Wetter and Treeck, 2017), which will continue within the IBPSA Project 1[19], is very close to the objectives of this platform. Indeed, the different tasks of this project were as follows:

- Activity 1.1: Modelica
- Activity 1.2: Co-simulation and Model Exchange Using the FMI Standard
- Activity 1.3: BPS Code Generation from Building Information Models
- Activity 1.4: Workflow Automation Tools

Furthermore, the definition of a DESTEST, a common district case study, as introduced in the Annex 60, is particularly welcomed to enhance and support DEM development.

[18] Available at https://github.com/HerveFrezza-Buet/gaml

[19] *IBPSA project 1 homepage - https://ibpsa.github.io/project1/*

Cette thèse est accessible à l'adresse : http://theses.insa-lyon.fr/publication/2018LYSEI071/these.pdf
© [L. Frayssinet], [2018], INSA Lyon, tous droits réservés

Cette thèse est accessible à l'adresse : http://theses.insa-lyon.fr/publication/2018LYSEI071/these.pdf
© [L. Frayssinet], [2018], INSA Lyon, tous droits réservés

Chapter 5

Effect of adaptations

Contents

Thanks to the platform described previously, the methodology introduced in Chapter 3 is applied for two building types, for all the adaptations introduced in Chapter 2, at the building scale and then at the district scale. A wide range of representations are used to analyse the adaptation effects, but only the more interesting representations are given in the following chapter. All others are included in the Appendix C to make it possible for the reader to check specific features depending on their simulation objectives. The global methodology of uncertainty management (Fig. 3.23) is used to support the analysis. The different steps are identified by paragraph titles.

5.1 Building scale

A - Problem specification A generic 10 m cubic building, oriented towards the cardinal directions is considered. A generic building is retained, rather than a real one, to give comprehensible and representative results that are more easily generalisable. The main characteristics of this building (Table 5.1) are based on the French TABULA typology (Rochard et al., 2015) for the 'multi-family house built before 1915' category. This period of construction is chosen because, in France, the majority of the buildings of this type were built during it. To highlight the influence of the envelope performance on the adaptation effects, a second parametrisation is considered

Cette thèse est accessible à l'adresse : http://theses.insa-lyon.fr/publication/2018LYSEI071/these.pdf
© [L. Frayssinet], [2018], INSA Lyon, tous droits réservés

		Init	*Perf*
Wall	Materials	Stone, Coating	Wooden frame, wood fibre
	U-value [$W\,m^{-2}\,K^{-1}$]	1.70	0.18
Roof	Materials	Tiles, wood, mineral wool, plaster	Concrete, polyurethane
	U-value [$W\,m^{-2}\,K^{-1}$]	1.35	0.15
Window	U-value [$W\,m^{-2}\,K^{-1}$]	2.60	1.40
Ventilation	Type	Natural	Mechanical, double flow (efficiency: 0.80)
	Air change rate [vol^{-1}]	0.50	0.40
Infiltration	Air tightness [$m^3\,h^{-1}\,m^{-2}$]	2.0	1.0

TABLE 5.1: Main parameters of building case studies

based on the last construction period (after 2012) corresponding to the last French regulation and consequently to a high energy performance building. Hereafter, *Init* refers to the older state, whereas *Perf* refers to the last one. For this last state, no specific passive techniques are modelled to reduce cooling needs (shading, natural ventilation, and others), and hence, the effects on cooling needs are only analysed with respect to the envelope basic behaviour. The setpoint temperatures are, by default, set to 19 °C and 28 °C for heating and cooling, respectively, according to the French regulation[1].

In the more general prospect, the variable of interest is the year-round power need curve in order to account for all dynamics of a representative year (Fig. 5.1). Heating and cooling were separately analysed. The Meteonorm weather data for the city of Lyon are used. The indicators previously defined (Sec. 3.2.2) are applied to extract specific features of adaptations effects on the power curve, with respect to different variables of interest.

5.1.1 Modelling conductive heat transfer

Discretisation resolution

B - Uncertainty quantification The first source of uncertainty accounted for is the spatial discretisation of the conduction problem [Cond-τ]. Indeed, the discretisation is often hardly simplified, notably at district scale, as the more detailed it is, the more equations describing the model are needed (Eq. 2.19).

[1]There is no consideration as to whether the setpoints are representative of reality as the aim is to focus on the envelope model. However, more realistic setpoints are accounted for when using occupant behaviour models in Sec. 5.2.4.

Cette thèse est accessible à l'adresse : http://theses.insa-lyon.fr/publication/2018LYSEI071/these.pdf
© [L. Frayssinet], [2018], INSA Lyon, tous droits réservés

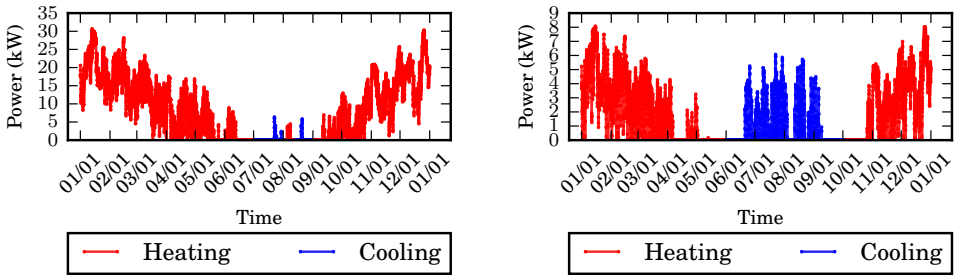

(A) *Init* (B) *Perf*

FIGURE 5.1: Power curve of the reference model

Init		Stone	Coating
τ = 59 s	Nodes	64	4
	Nodes/cm	1.6	2.0
τ = 900 s	Nodes	16	1
	Nodes/cm	0.4	0.5
τ = 15 days	Nodes	1	1
	Nodes/cm	0.025	0.5
Perf		Frame	Wood fibre
τ = 59 s	Nodes	77	4
	Nodes/cm	3.85	1
τ = 900 s	Nodes	19	1
	Nodes/cm	0.95	0.25
τ = 15 days	Nodes	1	1
	Nodes/cm	0.05	0.25

TABLE 5.2: Number of mesh in wall layers for the 2 extreme and intermediate discretisation resolutions

C - Uncertainty propagation According to the methodology developed in Chapter 3, model uncertainty is considered using different discretisation resolutions as defined through the parameter τ (Eq. 2.18): from 59 s to 15 days. Between these 2 limits, a modelling variant is defined as soon as the increase in τ implies an increment of the number of mesh points of any layer of the building envelope model[2]. For the methodology defined (Chap. 3), the reference is defined to be the model with the minimal characteristic time (supposed to be the most accurate) and with all other adaptations identified in 2.1 to their default formulation, i.e.,: [*label*-0].

C′ - Results analysis To give a synthetic overview of all indicators (Sec. 3.2.2), all indicators are plotted in the same graph with normalized values (Fig. 5.2 and 5.3). The norm is the respective indicator for the most simplified model (τ = 15 days), the relative value of which (to the mean non-zero power) is written in the graph.

As expected, because of the lower mesh resolution, the differences between the simplified models and the reference model increase with τ. Nonetheless, the standard deviations, the rectified mean differences, the differences of design level and particularly the mean differences are negligible, notably compared to the maximal

[2]The definition of τ, via the floor function, causes a discrete behaviour.

Cette thèse est accessible à l'adresse : http://theses.insa-lyon.fr/publication/2018LYSEI071/these.pdf
© [L. Frayssinet], [2018], INSA Lyon, tous droits réservés

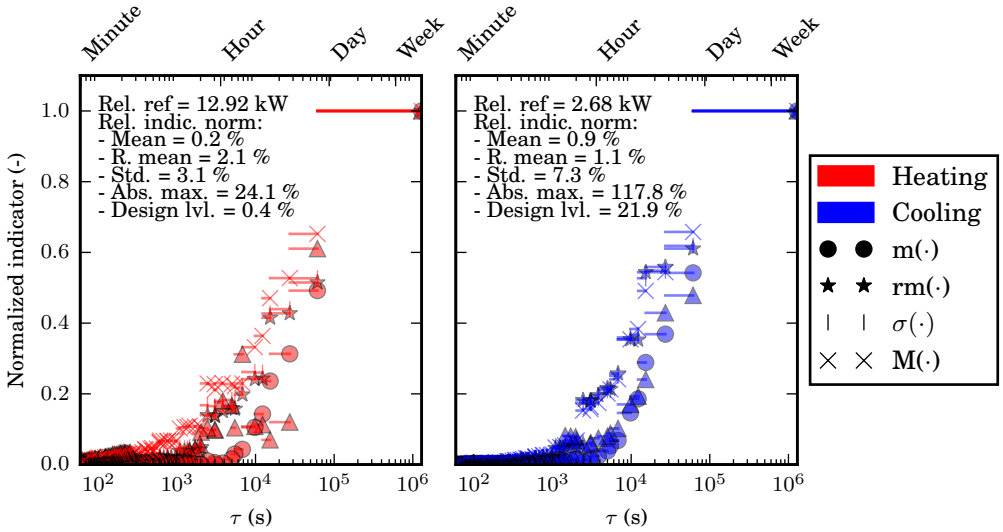

FIGURE 5.2: Conduction discretisation resolution effects: *Init*

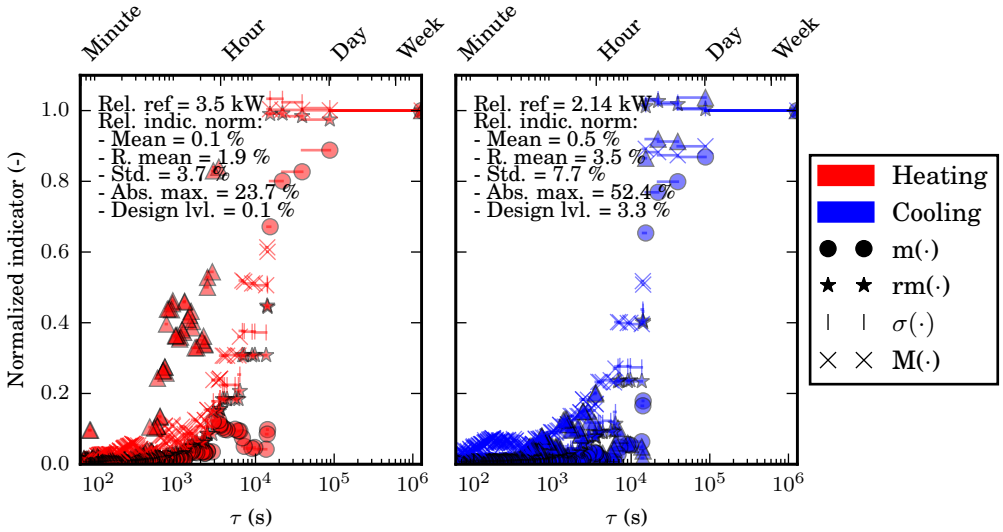

FIGURE 5.3: Conduction discretisation resolution effects: *Perf*

deviations. This last one increases up to 24 % for heating and for the *Init* and the *Perf*, to 52 and 118 %, respectively, for cooling. For the *Init*, the cooling needs are very low, and as a consequence, the relative difference can be important as soon as the cooling period increases due to adaptations.

These observations confirm that high differences rarely occur but are locally important. The maximal differences are correlated with the derivative of the power needs, notably for the lowest resolution (Fig. C.4). Indeed, in these cases, the meshes are thicker, and therefore, more thermal mass is affected during temperature variations, leading to delays in the thermal response, in particular for the quickest variations, as induced by solar flow. This phenomenon may also explain why cooling, which is more intermittent and very sensitive to solar flow, is more impacted than heating. By extrapolation, these time delays may be observed during setpoint change, such as for flexibility studies.

Cette thèse est accessible à l'adresse : http://theses.insa-lyon.fr/publication/2018LYSEI071/these.pdf
© [L. Frayssinet], [2018], INSA Lyon, tous droits réservés

The increase is not regular: rather, a first gap is observed for τ that is approximately equal to 2000 s, which is approximately half of the weather data time step (δt). This gap may be explained by the fact that for higher resolution, the mesh element thickness is higher than the thermal penetration depth length of the material[3], for the highest meteorological loads frequencies (the maximal observable frequency is $\frac{1}{2\cdot\delta t}$ according to the sampling theorem). In other words, the highest thermal load frequencies are not diffused through the mesh element because of its excessive thickness (Fig. 5.4a); they are entirely attenuated. Hence, after this gap, the higher the mesh thickness is (the higher τ is), the more the highest frequencies are eliminated (Fig. 5.4b).

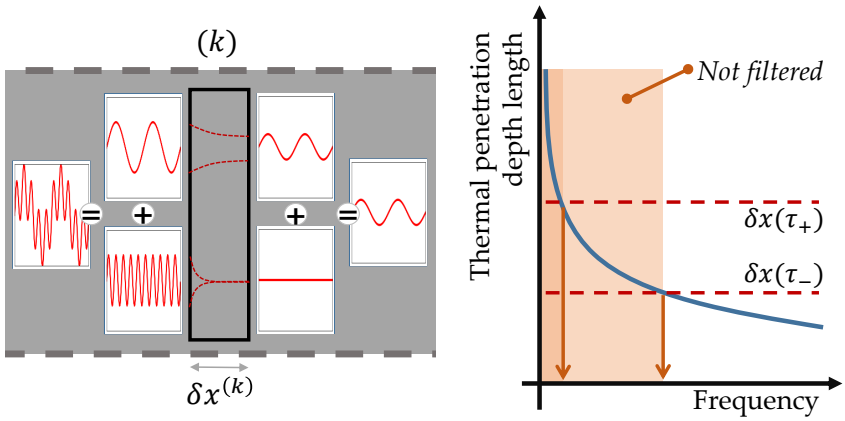

(A) Illustration on the mesh k (B) Effect of the discretisation

FIGURE 5.4: Filtering effect

Furthermore, the fact that the discretisation does not impact the annual energy needs (the mean differences are nearly null) justifies the use of coarse meshing in the district energy platform, notably with the wide use of the RC analogy model (Frayssinet et al., 2018b). Indeed, only the transient term of the heat equation is modified, but the steady-state term is unchanged. However, it is important to keep in mind that this choice affects the dynamics, in particular the fastest dynamics[4].

Reduction

B - Uncertainty quantification Solving the conductive heat transfer problem may be eased thanks to mathematical reduction methods (Sec. 2.1.4, [Red-π]). The resulting uncertainty due to these methods is analysed.

C - Uncertainty propagation The model uncertainty is considered using different levels of reduction (π), including from the model that is not reduced (π = 0) to the model that is entirely reduced (π = 92 for *Init* and 126 for *Perf*). The maximal level of reduction corresponds to the number of thermal modes in the model.

The reference model is the same as the previous model except that τ is set to 900 s [Cond-900] to reduce the computational cost[5] while not noticeably modifying

[3] Which is equal to $\sqrt{\frac{a}{\pi\cdot f}}$ for a f-harmonic thermal load in semi-infinite homogeneous material

[4] Note that thickness RC elements are often optimized with respect to this constraint, i.e., the peripheral layers are thinner than in the core.

[5] Reduced by about 6 and 20 times for the *Init* and *Perf*, respectively

Cette thèse est accessible à l'adresse : http://theses.insa-lyon.fr/publication/2018LYSEI071/these.pdf
© [L. Frayssinet], [2018], INSA Lyon, tous droits réservés

the results, according to the previous analysis. This reference model is not reduced and hence corresponds to [Red-0].

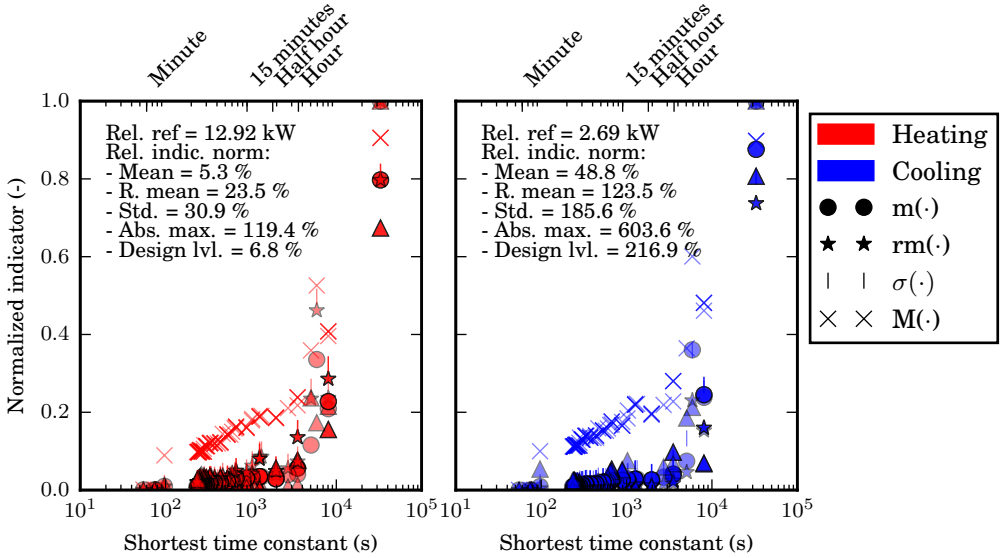

FIGURE 5.5: Reduction effects: *Init*

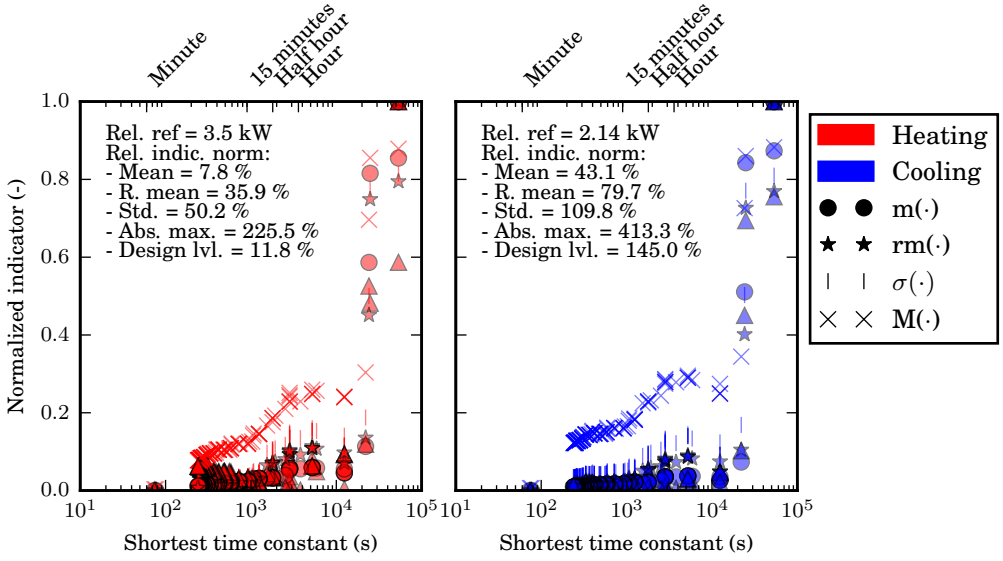

FIGURE 5.6: Reduction effects: *Perf*

C′ - Results analysis As presented previously, similar synthetic overviews of all indicators with normalized values are shown in Fig. 5.2 and 5.3. The x-axis corresponds to the shortest time constants of the reduced models, the dynamic of time constants of the complete model ($\pi = 0$) shorter than this abscissa being neglected (Sec. 2.1.4). The time constants range from a second to approximately 15 h.

As expected, the differences increase with the shortest time constant, i.e., with the level of reduction, particularly the maximal ones. Cooling shows a higher sensitivity to reduction than heating, highlighting again the importance of the envelope dynamics for the power needs. Note that the differences increase abruptly for the

Cette thèse est accessible à l'adresse : http://theses.insa-lyon.fr/publication/2018LYSEI071/these.pdf
© [L. Frayssinet], [2018], INSA Lyon, tous droits réservés

last levels of reduction, i.e., for shortest time constants, approximately 1 h for the *Init* and approximately 3 h for the *Perf*. Up to this level, the mean, rectified mean differences and standard deviation remain lower than 10 % of their highest values, i.e., the values are negligible, in particular for heating. The maximal deviations remain lower than 20 to 30 % of their highest values, which is not negligible notably because of the very high values of the norms. In addition, the maximal deviation suddenly reaches approximately 10 % until the shortest time constant of approximately 100 s.

The Moore method recommends keeping the modes with a time constants which are higher than $\frac{\delta t}{4}$. A notable increase in the differences is effectively observed near this value (900 s in our case).

Therefore, the reduction mainly locally affects the power curve but strongly while not noticeably impacting the main trend except for the extreme levels of reduction. This behaviour is coherent with the progressive loss of the shortest dynamics.

Last, note that very efficient mathematical reduction methods exist (see Sec. 2.1.4) and can, a priori, make it possible to further reduce the models for the same tolerance but are not analysed further here.

5.1.2 Building model assumptions

B - Uncertainty quantification The other sources of modelling uncertainty accounted for are the other building scale adaptations identified in Sec. 2.1. The reference model is the same as that presented previously (with τ set to 900 s [Cond-900] and is not reduced [Red-0]).

C - Uncertainty propagation The effect of each adaptation is quantified by individually changing the modelling variant: [*label*-0] to [*label*-1]. Hence, the effects are quantified locally around the reference model (Sec. 3.2).

C′ - Result analysis Fig. 5.7 gives an overview of the effect of the adaptations as introduced in Sec. 3.2.2. Table 5.3 summarizes indicator values. A first global conclusion, similar to that presented previously, is that the adaptations are globally suitable with respect to the annual needs as the mean differences are low (below 1 % in most cases and up to 20 % in the extreme worst case), but locally important deviations exist (the maximal deviations are over 20 % in most cases and reach 348 % in the extreme worst case). The difference in design level indicator has a similar behaviour to the mean but is notably amplified for cooling needs, notably so for the *Init*, for the same reasons detailed before (intermittent and low relative references).

Second, the relative effects are quite similar regardless of envelope performance. This observation confirms the choice of the relative reference (Sec. 3.2.2). In absolute values, except concerning the design level, the cooling differences have the same order of magnitude for *Init* and *Perf*, whereas the heating differences for *Perf* are approximately 4 times lower than those for *Init* (see the twin axes of Fig. 5.7). This difference is mainly explained by the fact that the heating needs of *Perf* are 4 times lower than those of *Init*. Consequently, in the case of absolute tolerances for the choice of suitable adaptations, highly energy-efficient buildings can be more adapted than inefficient ones.

The adaptations effects are analysed individually hereafter, notably to determine the physically related phenomena, understand implications of adaptations and evidence modelling biases. The comments are often based on the observations of the series of plots, defined in Sec. 3.2.3 available in Appendix C. This appendix is detachable in order to support the following explanations.

Cette thèse est accessible à l'adresse : http://theses.insa-lyon.fr/publication/2018LYSEI071/these.pdf
© [L. Frayssinet], [2018], INSA Lyon, tous droits réservés

Init

label	m(·)		rm(·)		$\sigma(\cdot)$		M(·)		$\delta\Gamma_{20}(\cdot)$	
Cond-59	0	-0	0	-0	0	0	2	3	-0	-0
Cond-1296000	0	1	2	1	3	7	23	114	0	22
Red-90	-0	0	-0	0	0	0	0	0	0	-0
Red-10	1	4	6	6	8	25	43	220	2	40
Zoning-lvl	1	3	1	4	3	16	24	126	-4	-61
Zoning-ori	0	0	0	1	1	4	15	49	-2	-38
Zoning-cmb	1	4	1	5	3	17	27	134	-5	-78
Infil-1	5	-1	5	-1	7	4	56	62	9	17
Control-1	3	0	4	1	4	4	47	38	8	25
trSol-1	-0	1	-3	2	5	10	19	103	1	29
intLW-1	-13	-1	-14	-2	14	9	51	90	-29	-71
Inertia-1	4	-3	4	-4	5	19	41	177	-1	-20
extConv-1	-9	20	-9	20	8	57	73	348	-7	68
extLW-1	-1	-0	-1	-0	1	1	4	11	-1	-8
EqEnv-1	-1	-3	-6	-3	9	20	38	226	-2	-110

Perf

label	m(·)		rm(·)		$\sigma(\cdot)$		M(·)		$\delta\Gamma_{20}(\cdot)$	
Cond-59	0	-0	0	-0	0	0	3	4	-0	-0
Cond-1296000	0	0	2	3	4	8	23	52	0	3
Red-90	0	1	0	1	1	4	21	56	-1	-2
Red-10	0	1	3	4	6	10	54	103	-1	-7
Zoning-lvl	0	1	1	1	2	5	40	84	-2	-3
Zoning-ori	0	2	0	5	4	9	35	54	-4	-29
Zoning-cmb	1	3	2	5	5	10	41	88	-6	-32
Infil-1	12	-6	12	-6	16	16	114	143	17	-5
Control-1	1	0	2	2	4	5	38	39	5	15
trSol-1	1	2	7	10	11	22	71	95	8	46
intLW-1	-3	-2	-8	-8	11	16	49	73	-16	-44
Inertia-1	2	3	2	4	7	14	82	164	-2	-1
extConv-1	-6	16	-6	16	8	29	81	215	-3	34
extLW-1	-1	0	-1	0	1	1	21	11	-1	0
EqEnv-1	12	-10	13	-12	15	26	80	176	7	-58

TABLE 5.3: Model assumptions effects at the building scale (Heating; Cooling)

Cette thèse est accessible à l'adresse : http://theses.insa-lyon.fr/publication/2018LYSEI071/these.pdf
© [L. Frayssinet], [2018], INSA Lyon, tous droits réservés

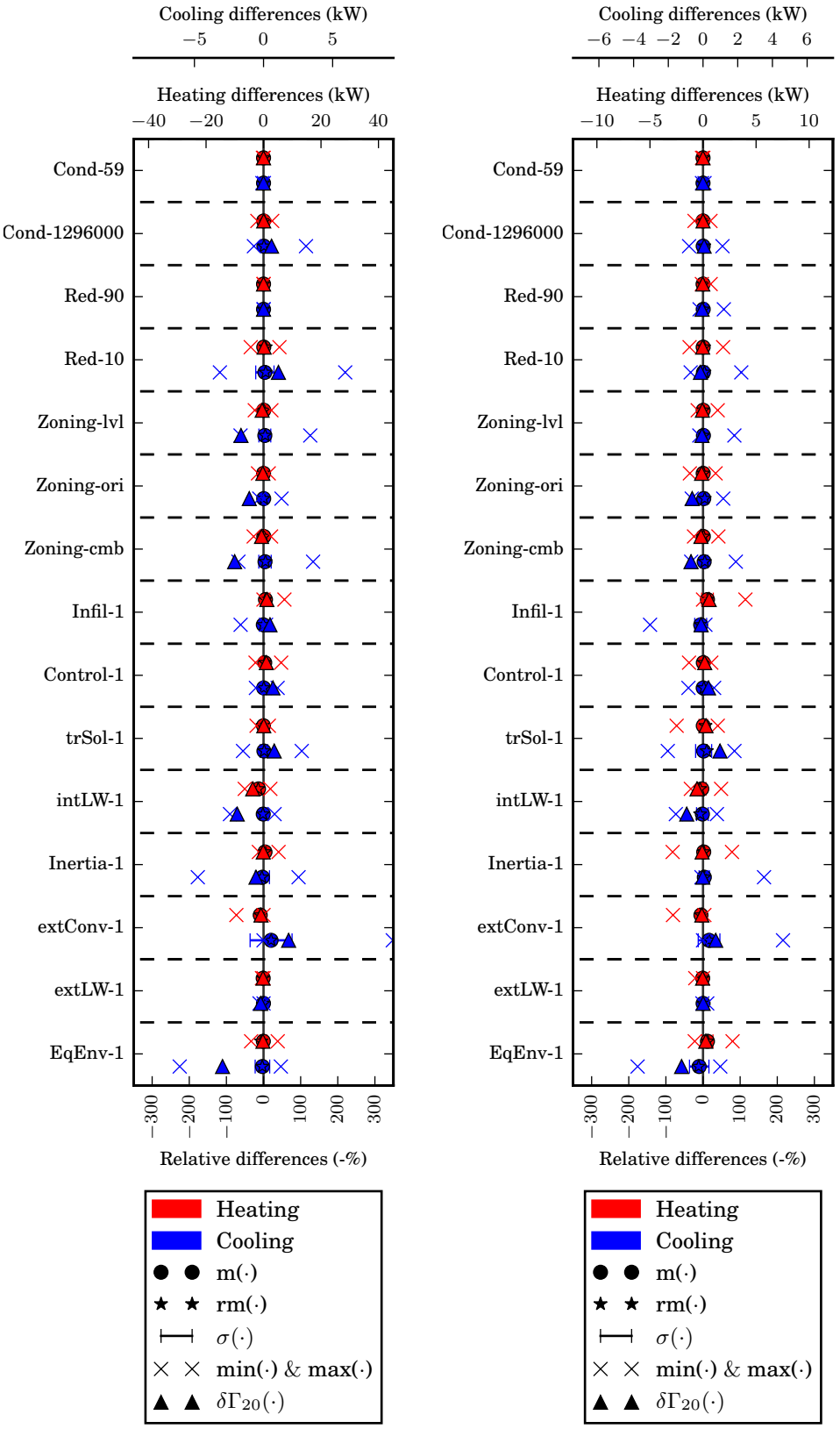

(A) *Init* (B) *Perf*

FIGURE 5.7: Overview of the building-scale adaptations effects

Cette thèse est accessible à l'adresse : http://theses.insa-lyon.fr/publication/2018LYSEI071/these.pdf
© [L. Frayssinet], [2018], INSA Lyon, tous droits réservés

Infiltration [Infil]

Because of air renewal, infiltration systematically increases heating needs. The effect is clearly correlated to wind speed. In contrast, cooling needs decrease as the ventilation prevents over-heating due to solar heat gains. Because of the wind dependency of infiltration, no specific pattern is evidenced, and the differences are scattered through time.

Perf is more sensitive to infiltration than *Init*, whereas airtightness is higher. Indeed, the part of the losses due to air renewal is higher in high efficient buildings.

In addition, the solving time is approximately 8 times higher because of the specific formulation in using power law (Eq. 2.5) and the addition of Modelica *fluid ports* that account for the thermo-physical properties of humid air.

Controlled temperature [Control]

Controlling the operative temperature rather than the air temperature causes an over estimation of heating and cooling needs. In winter, this over estimation is due to the fact that operative temperature is generally lower than air temperature, because of the cooler temperature of the walls, notably out of sunny periods. Oppositely, in summer during sunny periods, operative temperature is higher than air temperature, leading to over cooling. Solar radiations (absence or presence) tend to create opposite effects. Indeed, solar heat gains, complementary with the midday air temperature warming, increase wall surfaces temperatures and consequently operative temperature.

Transmitted solar flux allocation [trSol]

Distributing the transmitted solar flux to all the internal surfaces rather than only to the floors causes under heating during the sunny periods and over heating otherwise. This is because solar heat is more efficiently exploited directly thanks to the higher surface of exchange during sunny periods and hence less stored out of these periods. Logically, the opposite pattern is observed for cooling. The correlation with the solar flux is obviously high.

The daily pattern also explained the decrease in the maximal heating error, up to 70 % and 90 % for *Init* and *Perf*, respectively, for daily sampling compared to hourly sampling. This adaptation does not affect the amount of energy received but only its dynamics and hence does not affect the annual need. However, the difference in design level is noticeably increased except for *Init* because for these cases, the transmitted solar power is of the same order of magnitude as the mean power.

Internal long-wave radiation [intLW]

The heat losses are lower when considering the internal radiative heat transfer as the operative temperature is lower than the internal air temperature and closer to the external air temperature. The operative temperature is lower than the internal air temperature due to the contribution of the wall internal surface temperatures. This statement concerns the heating, and the opposite is observed for cooling.

The deviation between internal air and operative temperatures occurs throughout the year (expected during floating temperature periods, when it is nearly null), leading to mean deviation, affecting the annual needs and the level of design. This adaptation almost acts as an under-estimation of the global building U-values. The

Cette thèse est accessible à l'adresse : http://theses.insa-lyon.fr/publication/2018LYSEI071/these.pdf
© [L. Frayssinet], [2018], INSA Lyon, tous droits réservés

deviations are lower and higher for heating and cooling, respectively, during midday as surface temperatures are closer to the internal air temperature because of the midday warming and solar gain. The differences are correlated to power as higher differences between indoor and outdoor air temperature, and consequently between internal air and surface temperatures, imply higher needs.

As for [Control], this simulation is 2 times costly because of internal surface temperature coupling (see Fig. 2.22).

Internal inertia [Inertia]

The deletion of the internal inertia reduces the floating temperature periods (sometimes causing boundary effects: heating needs during the defined cooling period and vice versa) as the buffer effect due to inertia is consequently reduced. Hence, the deviations principally concern lower power levels (around these periods). The differences mainly occur after the sunny days, when the over-heated internal surfaces release their heat. Ignoring the internal inertia leads to over heating and under cooling during these periods because of the absence of heat released by internal inertia. The opposite differences also occur during sunny periods as the air is heated faster without inertia. This phenomenon is dominant only for *Perf* in summer as the floors are insulated.

This daily pattern explains why the maximal deviation is reduced by 70 % with daily sampling.

External convective heat transfer [extConv]

The wind-dependant law retained for the convective heat transfer coefficient leads to a mean value lower than the constant value retained in the reference model. The heating is consequently constantly underestimated, as the losses are lower and the cooling is overestimated as the thermal gains are less dissipated. The floating temperature periods are increased during heating periods and decreased during cooling periods. The standard deviation is particularly high because of the wind speed dependency. No specific daily patterns are observed as the wind speed variation is independent of the hour.

External long-wave radiative heat transfer [extLW]

The 'un-linearisation' of the external radiative heat transfer coefficient causes a small under-estimation. The linearisation, with the constant value retained, slightly overestimates the coefficient on average. However, the 'un-linearisation' increases the computational time by a factor of approximately 3.

Equivalent envelope model [EqEnv]

This adaptation keeps the global trend but causes a noticeable scattering of the differences. Cooling is particularly affected. These effects may be explained by the fact that quasi-static properties are maintained by the equivalence process, unlike the dynamic behaviour, in particular because of the aggregation (the loss of facade particularities). However, this adaptation reduces the computational cost by a factor of approximately 2.

Cette thèse est accessible à l'adresse : http://theses.insa-lyon.fr/publication/2018LYSEI071/these.pdf
© [L. Frayssinet], [2018], INSA Lyon, tous droits réservés

Zoning [Zoning]

The different zonings mainly cause over heating and over cooling near the lower power levels (about lower than 5 kW), which is why the cooling and *Perf* are more impacted. These effects increase the occurrences of lower power, but neither impacts the annual needs nor the level of design as they concerns higher power except for *Init* and cooling.

In the case of orientation zoning, it was found by the author (Frayssinet et al., 2016) that these over consumptions are because of the partitions, only the sun-exposed zones are impacted by the solar heat gains instead all the building volume being affected. In winter, close to the floating temperature periods, the sun-exposed zones are no more heated by the solar heat gains, whereas residual heating needs are necessary for the other zones that do not benefit from these heat gains. Similarly, in summer, the solar heat gains over warm the sun-exposed zones, leading to cooling needs only in these zones. Similar disparities are observed with floor-zoning due to the floor boundary condition of the lower floor and the roof for the top boundary condition. In brief, zoning removes the mono-zone pooling effect.

However, modelling numerous zones implies a higher computational cost, up to 4 to 24 times greater than the reference, depending on the number of zones.

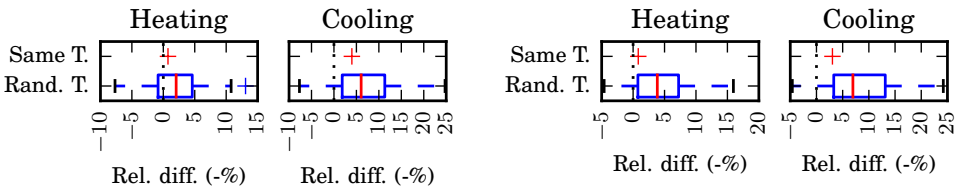

(A) *Init* (B) *Perf*

FIGURE 5.8: Diversity of setpoint effects on the mean difference

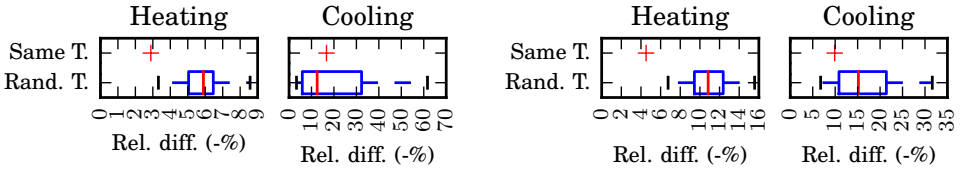

(A) *Init* (B) *Perf*

FIGURE 5.9: Diversity of setpoint effects on the standard deviation

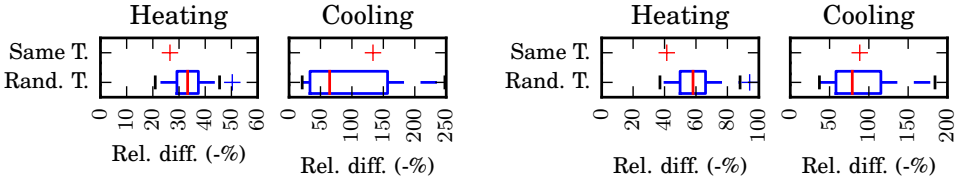

(A) *Init* (B) *Perf*

FIGURE 5.10: Diversity of setpoint effects on the absolute deviation

Cette thèse est accessible à l'adresse : http://theses.insa-lyon.fr/publication/2018LYSEI071/these.pdf
© [L. Frayssinet], [2018], INSA Lyon, tous droits réservés

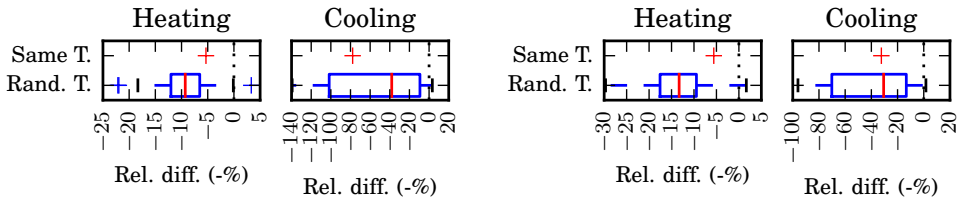

(A) *Init* (B) *Perf*

FIGURE 5.11: Diversity of setpoint effects on the difference in design level

Diversity of setpoints. Zoning aims to merge volumes with similar thermal behaviours. Disparities can be caused by the position of the volumes in the buildings, leading to different thermal loads, as shown above. Furthermore, a building is generally made of numerous housing units with specific thermal regulation, leading to major sources of disparities not accounted for here. In order to test the impact of such disparities, a specific set of experiment was defined. The reference models with the [Zoning-cmb] variant were run 100 times. For each simulation, a random distribution of the zone set-point temperatures is generated following a normal distribution of mean 19 °C and with a standard deviation of 2 °C.

The previous indicators are computed for each case. Their distribution[6] is shown in Fig. 5.8-5.11. *Same T.* refers to previous case [Zoning-cmb], where the zones temperatures are identical, whereas *Rand. T.* refers to the set of experiments defined above. Both are compared to the mono-zone reference model [Zoning-0].

The results shows that on average, the diversity of setpoints increases the impact of the zoning adaptations on the heating needs. Only the mean difference is estimated with *Same T.* in the 50 % median values. Hence, the estimation of the other indicators with *Same T.* is less representative of the mean effect of the diversity. They are generally under estimated. The effect on the cooling is mitigated, but the estimation with *Same T.* is nearly always in the 50 % median values. The ratio between the median estimation of *Rand. T.* and the estimation of *Same T.* ranges between 1.4 and 4.7 with a mean value of 2.2. In conclusion, the impact of the zoning is approximately 2 times higher in reality than that estimated with the default methodology due to the diversity of regulations within a whole building.

Focus on sampling effect

When increasing the sampling period (see Appendix C), the effects measured by the indicators are reduced except for the mean, by mathematical definition. This analysis aims to identify the transition from local maximal differences (at hourly time step) to annual mean differences.

In general, the decrease is globally faster for the first sampling periods until the daily sampling period, where the maximal deviation is generally decreased by 50 up to 90 %. This observation is probably characteristic of transient phenomena linked to the solar heat gains. Indeed, regardless of the adaptations, the daily amount of energy received is nearly unchanged, and, as seen previously, the adaptations mainly affect only the daily solar heat gains release dynamics. This is obviously false for the adaptation [Infil] and [extConv], for which the related effects are not linked to the solar flux. In addition, the decrease with the sampling period is consequently lower compared to the other adaptations.

[6] The mean and the standard deviation converge approximately 80 variants

Cette thèse est accessible à l'adresse : http://theses.insa-lyon.fr/publication/2018LYSEI071/these.pdf
© [L. Frayssinet], [2018], INSA Lyon, tous droits réservés

Parameter	Range		Related phenomenon
λ (W m^{-1} K^{-1})	-30 %	+30 %	Static heat-transfer
b_{-floor} (-)	0.1	0.9	
U_{-win} (W m^{-2} K^{-1})	0.7	3.0	
$h_{cv.in}$ (W m^{-2} K^{-1})	-30 %	+30 %	
ρc (J m^{-3} K^{-1})	-30 %	+30 %	Inertia
α (-)	0.2	0.9	Solar related
θ_{-win} (-)	0.3	0.9	
$\varepsilon_{ext-wall/win}$ (-)	0.7	1.0	LW exchange
$\varepsilon_{ext-roof}$ (-)	0.2	1.0	
$AirChgRt$ (vol^{-1})	0.2	1.0	Air renewal
$RadPart$ (-)	[0.0; 0.3; 0.6; 0.9]		Energy system
$tilt_{-roof}$ (°)	[0; 20; 40; 60]		Building shape

TABLE 5.4: Set of experiments for the parameter sensitivity analysis

Hence, as the increase in the sampling period filters the shortest dynamics, the solar-related adaptation effects are first attenuated.

5.1.3 Parameter

Apart from the modelling adaptations, the parameters can also create uncertainties. Their determination at the district scale is often based on estimations, notably for existing buildings, and hence are strongly uncertain. This uncertainty is why it is important to identify the most influential parameters to reduce the uncertainty in the results.

B - Uncertainty quantification In contrast to previous analyses, the present work is a parameter uncertainty analysis. Hence, the usual methods introduced in Sec. 3.3.2 may be used. However, because of a lack of knowledge about the parameters uncertainty distributions, the uncertainty analysis relies on a basic method that considers an extreme range of variation (see the next step).

The parameters retained are listed in Table 5.4. The related phenomena are also indicated. These parameters characterise the different thermal heat-transfers. '$RadPart$' corresponds to the part of the heating system that is emitted by radiation rather than convection. '$tilt_{-roof}$' refers to the tilt of the roof. Indeed, in many district energy models, the building shape is modelled by extrusion of the building footprint, and consequently, the tilt is equal to 0. The modification of the tilt modifies the exposed surface of the roof and the its incoming solar flux.

C - Uncertainty propagation The method retained is a local sensitivity analysis method around the reference model defined in the previous section (Sec. 5.1.2). As previously, the different indicators are used to extract specific information of the time-series differences. The sensitivity is computed according to Eq. 3.14. Relative indicators are still used. More detailed methods were not used as our objective is to have a first estimation of the local sensitivity around the parametrisation deduced from the typology. The parameter step Δ_n is defined according to extreme possible values or arbitrary to $\pm$ 30 % of the reference value (see Table 5.4).

Cette thèse est accessible à l'adresse : http://theses.insa-lyon.fr/publication/2018LYSEI071/these.pdf
© [L. Frayssinet], [2018], INSA Lyon, tous droits réservés

In order to highlight non linearities, the sensitivity is estimated in both directions ($+\Delta_n$ (associated label: + +) and $-\Delta_n$ (- -)), and also for intermediate parameter step ((+), (-); Fig. 5.12). The intermediate range is defined as 30 % of the extreme range to study the sensitivity more locally. If the different estimates are equal, this result evidences the linearity of the parameter effect for the indicator used. Otherwise, their scattering indicates the level of non-linearity. The 2 last parameters ('$RadPart$' and '$tilt_{-}roof$') are evaluated differently by evaluating them against the values presented in Table 5.4 (progressive increase of the default value). The sensitivity estimated is a slope as illustrated in Fig. 5.12.

Although numerous estimates were computed with this method, the Morris method (Sec. 3.3.2) cannot be used, because the reference model is always the same ($x_n^{(0)}$).

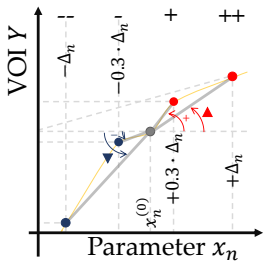

FIGURE 5.12: Parameter uncertainty propagation

To have coherent units for all sensitivity indexes, the values are normalized by the reference value, as follows:

$$\Delta_n \rightarrow \frac{\Delta_n}{x_n^{(0)}} \tag{5.1}$$

For '$RadPart$' and '$tilt_{-}roof$', the reference values are arbitrarily set to 1 and 90°, respectively.

C' - Results analysis The sensitivity is analysed in absolute values for the following indicators: the mean difference (Fig. 5.13), maximal deviation (Fig. 5.14) and the difference in design level (Fig. 5.15). Only these indicators are shown in the following to focus on the extreme characteristics of the power curve. The sensitivities of the parameters are separately analysed with respect to the different envelope element types (the use of the subscripts $wall$, $intwall$ (internal wall), win (window), $floor$, $intfloor$ (internal floor)). Specific markers are associated with the different estimates, as illustrated in Fig. 5.12 (from lower to higher values: (- -) $\triangledown$, (-) $-$, (+) $+$, (++) $\triangle$, and (+++) $\star$ in specific cases).

The most influential parameters for heating are the static losses-related parameters, notably '$U_{-}win$', '$\lambda_{-}wall$' and '$AirChRt$'. '$\theta_{-}win$' also plays an important role only for *Perf*, evidencing the key role of solar gains.

Concerning cooling, the most influential parameters are mainly the solar-related ones, including '$\theta_{-}win$', and 'α' only for *Init* due to the lower insulation of these buildings. To a lesser extent, '$U_{-}win$' is the most influential static heat-transfer related parameter as the most thermally conductive building element.

Only at short time steps (Fig. 5.14) do the solar-related and inertia-related parameters become influential as well. Within the global inertia, the internal inertia is particularly dominant. The differences in design level has similar behaviours to the mean differences, except for the *Init* cooling, which is very variable.

Cette thèse est accessible à l'adresse : http://theses.insa-lyon.fr/publication/2018LYSEI071/these.pdf
© [L. Frayssinet], [2018], INSA Lyon, tous droits réservés

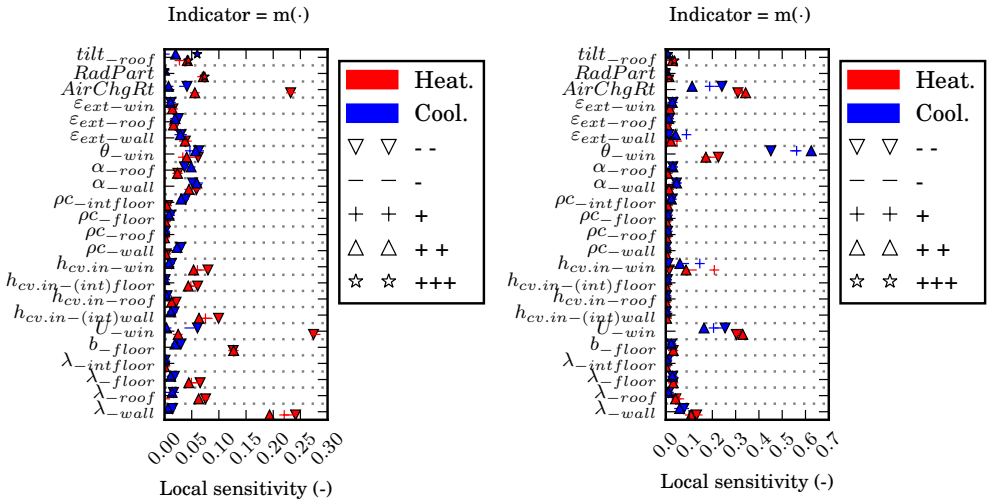

(A) *Init* (B) *Perf*

FIGURE 5.13: Parameter sensitivity analysis
indicator: mean difference

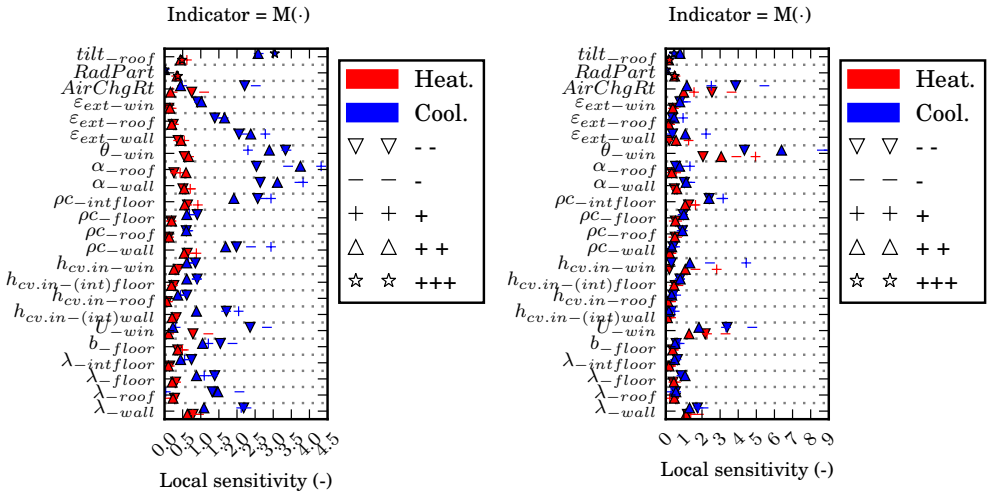

(A) *Init* (B) *Perf*

FIGURE 5.14: Parameter sensitivity analysis
indicator: maximal deviation

Note that the effects on cooling and heating are similar for *Perf*. Concerning *Init*, heating is, in relative values, more sensitive than cooling with respect to the mean difference indicator, but inversely so with respect to the maximal deviation. Hence, cooling is the most sensitive in terms of local variations. Regardless of building type, the parameter sensibilities have nearly the same order of magnitude except for 'θ_{-win}'.

Not only does the value of the parameter identified as influential but also the related characteristics and phenomena require focus. For example, some window characteristics are influential, and hence their size, their position and the incoming solar flux are also a target of concern (in particular because they are commonly roughly deduced from the window-to-wall ratio).

Cette thèse est accessible à l'adresse : http://theses.insa-lyon.fr/publication/2018LYSEI071/these.pdf
© [L. Frayssinet], [2018], INSA Lyon, tous droits réservés

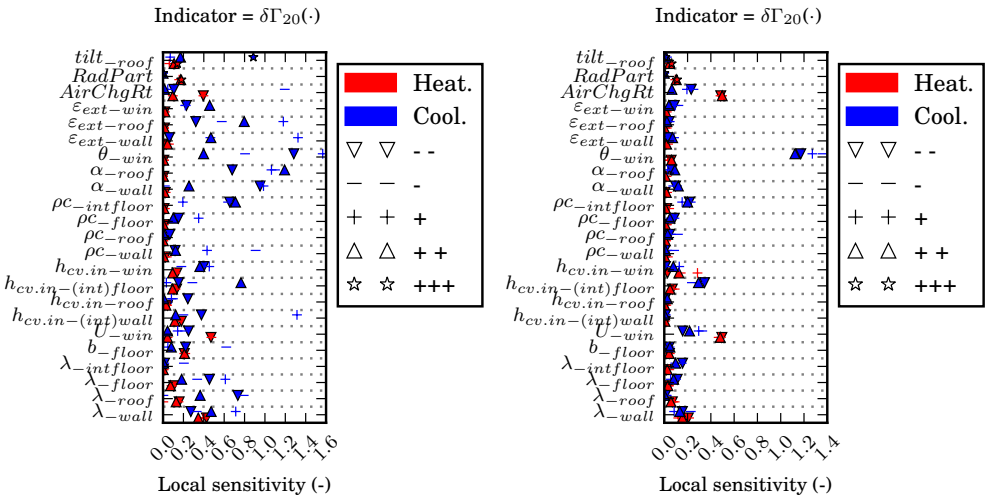

(A) *Init* (B) *Perf*

FIGURE 5.15: Parameter sensitivity analysis
indicator: difference in design level

Last, in most cases, the non-linearity measured is not predominant. The different estimates of the sensitivity index are not very scattered.

5.1.4 External conditions

This section is based on 2 articles co-written by the author (referred to as part I and part II), being submitted at the time this manuscript was written, and available in Appendix D. This section aims to extend the methodology developed in these papers. A short abstract is given in the following. For more information concerning the context and the references, please refer to these articles.

The usual BEMs fail to properly consider external conditions, notably in urban cases. Indeed, the urban environment alters the external conditions around the buildings, masks the sun, reflects solar rays, and modifies the wind pattern and the local air temperatures. The alteration depends on the urban morphology and hence is case specific. Without specific information, by default, the modelled building is considered isolated in a hypothetical open area. However, this simplification causes noticeable deviations on the building energy behaviour. Hence, the modelling of the external conditions is also a main target of adaptation. Consequently, the aim of this part is to quantify these adaptation effects, and the sensitivity of the model with respect to these external conditions.

A - Problem specification The building models considered are the same as those considered previously except that *Perf* is the renovated state of *Init* rather than a new building with the last thermal specifications. The energy performances are very similar in terms of insulation, but the air tightness is 5 times higher. Compared to the previous reference model, in order to account more accurately for external conditions, some modelling variants are retained in their detailed form: [Infil-1], [extConv-1] and [extLW-1].

Cette thèse est accessible à l'adresse : http://theses.insa-lyon.fr/publication/2018LYSEI071/these.pdf
© [L. Frayssinet], [2018], INSA Lyon, tous droits réservés

The weather considered was the same, but because of the prohibitive computational costs of the microclimate model used, the simulations were run only for two representative days in summer and in winter.

B - Uncertainty quantification The 7 external conditions accounted for are the direct (*dirSol*), atmospheric and reflected diffuse (*difSol*) short wave radiative fluxes, local air (*Tair*) and environmental radiant temperatures (*rad*), convective heat transfer coefficient (*conv*) and relative pressure next to building faces (*infil*). The local air temperature is considered separately for the inlet air renewal (*Tvent*).

These conditions were estimated using 3 model variants (part I):

(0) *Default approach*: directly with the BEM;

(1) *Microclimatic approach - Isolated configuration*: with a specific microclimate model (SOLENE-microclimate (Malys, Musy, and Inard, 2015; Musy, Malys, and others, 2014)) for an isolated building in an open area;

(2) *Microclimatic approach - Array configuration*: with the same microclimate model but for building in a theoretical urban environment (4×4 array of identical buildings).

The comparison of the different sets of external conditions indicates the effects of the modelling variant, hence the input uncertainty.

C - Uncertainty propagation In the second part of the papers (part II), the input uncertainty is propagated locally (conditions per conditions) around the *default approach* (0) and the *isolated configuration* (1) to evidence the effects of the modelling approach and the urban environment, respectively.

However, the results are specific to the particular urban configuration considered. In order to generalize the results, it is necessary to determine the sensitivity and not only the effect. Hence, the effects in a specific urban configuration may be determined by multiplying the input uncertainty by the sensitivity (Fig. 3.24).

Taking advantage of the generated sets of external conditions (3 possible states per condition), the input uncertainty was propagated but with all possible combinations of them for the transitions (0→1) and (1→2). The two transitions were analysed separately because there is a priori no coherence between a change in model and a change in urban environment. Moreover, considering both transitions together may necessitate ensuring that the 'conditions space' is regularly sampled, while the 2 transitions are a priori not comparable. Such a set of experiments is illustrated in Fig. 5.16 in 3 conditions dimensions (x_i, x_j, x_k). It corresponds to the red and green dots, whereas the experiment in part II corresponds to only the red ones. The number of combinations in this different set of experiments is $2 \times 7 = 14$ and $2 \times 2^7 = 2 \times 128$, respectively.

C' - Result analysis First, the Morris method is used to analyse the results. As indicated previously, to estimate the effects, the indicators are still used. Moreover, for the denominator of the local sensitivity (Δ_n in Eq. 3.14), as the conditions are times series, it is also necessary to use indicators. By default, we choose to use the mean difference. Last, in order to have homogeneous results units, the denominator is normalized by the range of variation of the reference condition[7]. In brief, the local

[7]Otherwise, it could be possible to estimate the flow related to all conditions in order to have a common unit.

Cette thèse est accessible à l'adresse : http://theses.insa-lyon.fr/publication/2018LYSEI071/these.pdf
© [L. Frayssinet], [2018], INSA Lyon, tous droits réservés

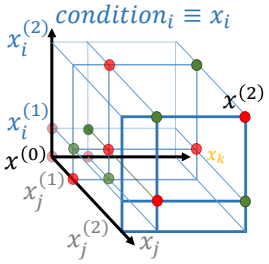

FIGURE 5.16: Set of experiments

sensitivity indexes were computed as follows:

$$s_n^{ind} = \frac{\text{ind}(Y(x_1^{(a)}, \cdots, x_n^{(b)}, \cdots, x_N^{(a)}, t) - Y(x_1^{(a)}, \cdots, x_n^{(a)}, \cdots, x_N^{(a)}, t)}{\frac{\text{m}(x_n^{(b)}(t) - x_n^{(a)}(t))}{\max(x_n^{(a)}(t)) - \min(x_n^{(a)}(t))}} \tag{5.2}$$

with (a,b) = (0,1) or (1,2), depending on the transition considered, and ind$(\cdot)$ the chosen indicator.

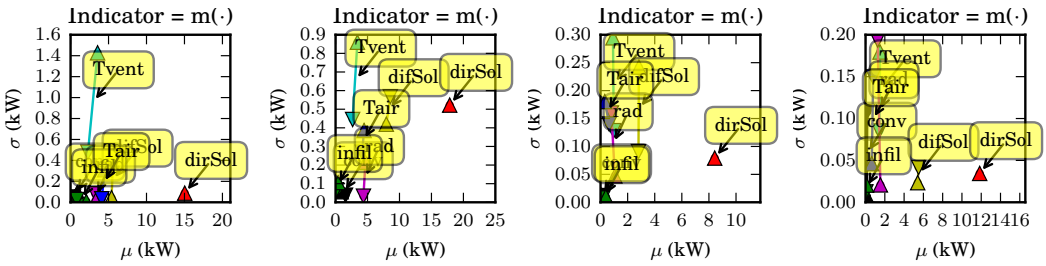

(A) *Init* - Winter (B) *Init* - Summer (C) *Perf* - Winter (D) *Perf* - Summer

FIGURE 5.17: External condition sensitivity analysis
indicator: mean difference

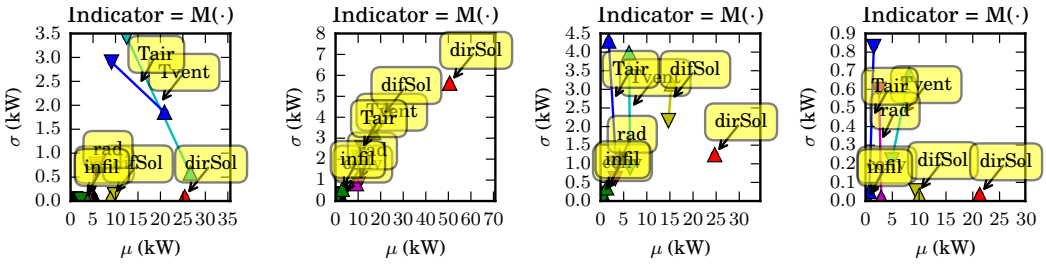

(A) *Init* - Winter (B) *Init* - Summer (C) *Perf* - Winter (D) *Perf* - Summer

FIGURE 5.18: External condition sensitivity analysis
indicator: maximal deviation

In the following figures, based on Morris method result analysis (Fig. 3.26b), '$\bigtriangledown$' and '$\bigtriangleup$' correspond to the transition (0→1) and (1→2)[8], respectively. The results (Fig. 5.17 and 5.18) show that the mean sensitivity (μ) is nearly the same regardless of the transition. Thus, the sensitivity of the building is not impacted by the approach but rather seems to be an intrinsic characteristic confirming the suitability if the proposed method. Furthermore, the variation effects (σ) are low. Hence,

[8]Only the transition (1→2) make it possible to quantify the effect of '*dirSol*'

Cette thèse est accessible à l'adresse : http://theses.insa-lyon.fr/publication/2018LYSEI071/these.pdf
© [L. Frayssinet], [2018], INSA Lyon, tous droits réservés

the sensitivity of the conditions may be analysed individually. Nonetheless, *dirSol* clearly appears as the dominant condition followed by *difSol*. The other conditions are non-influential, especially for the mean difference. An exception occurs for *Init* in winter with the maximal deviation: *Tvent* and *Tair* appear more influential. *Init* is obviously more sensitive to *Tvent* and *Tair* in winter than *Perf*. However, the results indicate that this building is more sensitive locally to the power curve than to the total daily energy. This result is probably due to the temporally local increase in the air temperature induced by the micro-climatic approaches (see part I) that notably directly affect the building needs via air renewal. *Trad* was shown to be very impacted by the model variants (part I), and this was shown to have a important impact on the building energy behaviour (part II), but present results shows that the building sensitivity to this condition is low. Hence, the important impact on the output is only due to the important range of the input. This point underlines the advantage of using sensitivity analysis methods.

Second, this case study is particularly suitable to use the time-dependant Sobol indices (see Fig. 3.27). Indeed, the size of the set of experiments is quite substantial, and the the conditions may be seen as time-dependant parameters. It is not necessary to consider the value of the inputs. Both previous characteristics make it possible to avoid the use of indicators.

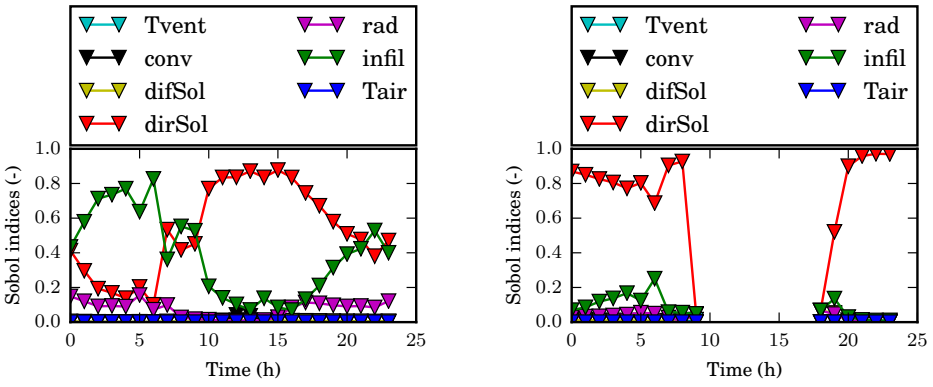

(A) *Init* - Winter (B) *Perf* - Winter

FIGURE 5.19: Time dependant Sobol indexes - Winter

Results[9] (Fig. 5.19 and 5.20) clearly show the predominance of *dirSol* in all cases[10]. This predominance does not only occur during daytime but also during nighttime, highlighting the role of inertia. The sensibility of other conditions mainly occurs around midday as they are amplified by the solar radiations. The local impact of *infil* for *Init* in winter is evidenced highlighted. Last, *rad* shows a higher influence than previously, notably in summer, in contrast to *difSol*. However, the range of variation of the conditions impacts the results as a higher range may induce a higher variance. This result probably explains the discrepancies with respect to the previous methods. In addition, this drawback limits the generalization of the results to other configurations.

[9]Only the transition (1→2) is analysed as the other does not completely account for all conditions.
[10]The period where all indexes are equal to zero corresponds to floating temperature periods.

Cette thèse est accessible à l'adresse : http://theses.insa-lyon.fr/publication/2018LYSEI071/these.pdf
© [L. Frayssinet], [2018], INSA Lyon, tous droits réservés

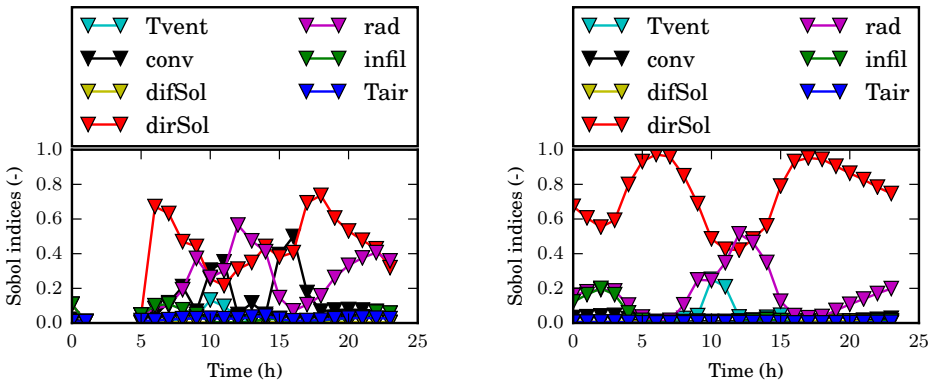

(A) *Init* - Summer (B) *Perf* - Summer

FIGURE 5.20: Time dependant Sobol indexes - Summer

5.2 District scale

A - Problem specification In order to test the influence of the district scale on the adaptation effects, the methodology is applied to a whole district. The district used comes from a collaboration with the CES MINES ParisTech laboratory, that notably led to the comparison (Frayssinet et al., 2018a) of the developed tool chain (Chap. 4) with Smart-E (Berthou et al. (2015)). This district (Fig. 5.21) is located in Paris, France. It comprises apartment blocks built during the 30's. The district contains approximately a total of 900 housings units. The thermo-physical parameters (Table 5.5) are still deduced from the TABULA typology (Rochard et al., 2015). The geometry is based on the IGN (French geographical institute) GIS database (BD TOPO). The METEONORM Paris Montsouris weather file is used. Due to the climate and the building typology, only heating needs are focused on (Fig. 5.22).

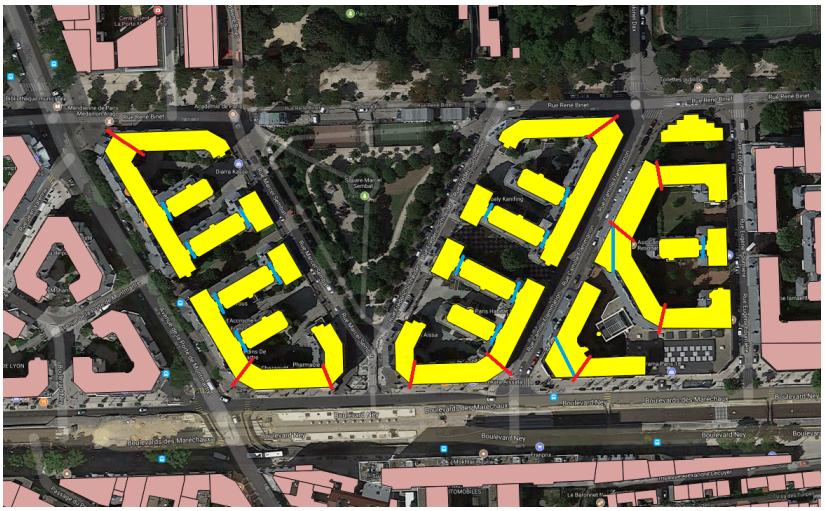

FIGURE 5.21: Aerial view of the modelled district (in yellow)

This district is homogeneous in terms of typology but contains a variety of shapes. Hence, this case study excludes the effect of typology diversity, allowing for a focus on geometry diversity effects.

Cette thèse est accessible à l'adresse : http://theses.insa-lyon.fr/publication/2018LYSEI071/these.pdf
© [L. Frayssinet], [2018], INSA Lyon, tous droits réservés

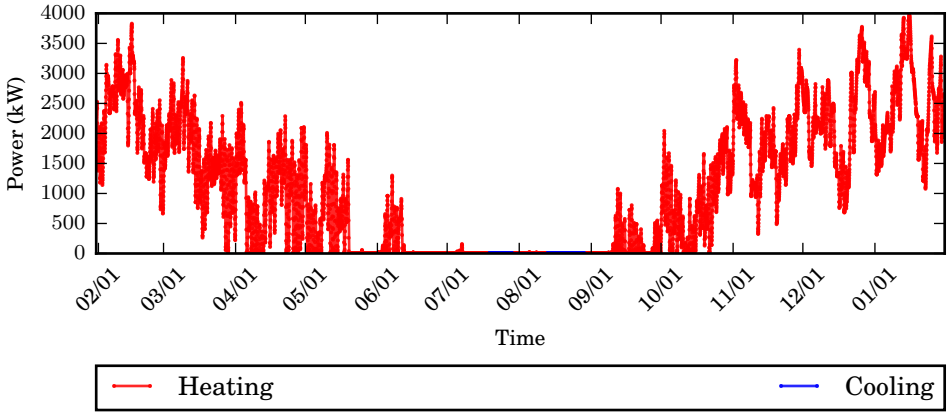

FIGURE 5.22: Simulated power curve of the reference district model

Wall	Materials	Stone, coating
	U-value [$W\,m^{-2}\,K^{-1}$]	1.70
Roof	Materials	Coating, concrete
	U-value [$W\,m^{-2}\,K^{-1}$]	3.20
Window	U-value [$W\,m^{-2}\,K^{-1}$]	2.80
Ventilation	Type	Natural
	Air change rate [vol^{-1}]	0.50

TABLE 5.5: Main parameters of the buildings in the district case study

5.2.1 District model assumptions

B - Uncertainty quantification Similar to Sec. 5.1.2, specific district-scale adaptation effects are analysed (Sec. 2.2) in addition to the same modelling adaptations effects than at the building scale except for [Infil] and [Red]. Indeed, the first implies simulating the wind flow in this specific urban case with dedicated tools, which is generally computationally expensive and is not integrated in the chain tool (Chap. 4). In addition, the second is not implemented at the district scale as the current reduction process is not sufficiently robust or computationally efficient for the moment.

The buildings were assumed to be monozone [Zoning-0]. Without information about the building arrangements, 23 buildings (with 2 adjoining walls) were defined, based on the available footprint (blue lines in Fig. 5.21). The effects of the zoning are more roughly estimated than at the building scale. Only one more detailed zoning was considered (labelled 'Zoning' in the following). The biggest buildings are divided with respect to the main orientations. This zoning generates 33 buildings with 12 adjoining walls (blue and red lines in Fig. 5.21). Nonetheless, any floor zoning is accounted for.

C - Uncertainty propagation The reference modelling variant is still the same as that in Sec. 5.1.2, i.e., [Cond-900] and all others modelling to their default variant

Cette thèse est accessible à l'adresse : http://theses.insa-lyon.fr/publication/2018LYSEI071/these.pdf
© [L. Frayssinet], [2018], INSA Lyon, tous droits réservés

label	m(·)	rm(·)	$\sigma(\cdot)$	κ_σ	M(·)	κ_M	$\delta\Gamma_{20}(\cdot)$
Cond-59	-0	-0	0	43	1	81	-0
Cond-1296000	0	3	5	2	24	7	0
Zoning	1	1	1		8		-0
Control-1	4	5	6	2	26	27	9
trSol-1	0	1	1	6	5	38	0
intLW-1	-13	-14	16	1	64	2	-30
Inertia-1	3	3	6	19	72	7	-1
extConv-1	-10	-10	10	3	74	5	-9
extLW-1	-1	-1	1	6	7	29	-2
EqEnv-1	7	7	7	3	40	11	5
Solar-0	-4	-4	5	5	37	16	-0
LWRad-0	1	1	0	18	5	39	1
Adjoin-0	0	0	0	77	0	86	-0
Adjoin-0 (z)	0	0	0		1		-1

TABLE 5.6: Model assumption relative effects at the district scale on heating and diversity effects (κ)

[*label*-0]. At the district scale, the buildings interactions are modelled with their detailed variants formulation, i.e., [Solar-1], [LWRad-1] and [Adjoining-1].

C′ - Results analysis It is particularly remarkable that the relative effects are more similar at the district scale (Fig. 5.23a and Table 5.6) than at the building scale (Fig. 5.7 and Table 5.3), whereas the weather files are not the same but comparable. Furthermore, as shown in Sec. C.4 in Appendix C, the relative indicators are nearly identical regardless of the buildings in the district. This observation seems to indicate a certain invariance of the adaptation effects with respect to the building shape. Moreover, the observation confirms the choice of the reference for the computation of the relative values (Sec. 3.2.2). Hence, the results are probably representative for any building. However, complementary analyses, for different districts, are needed to support this assertion.

The effects of the building-scale assumptions are not re-analysed at the district scale as they were already addressed in Sec. 5.1.2. Hence, only the district-scale-specific adaptations are studied hereafter. As indicated previously, complementary representations are given in Appendix C, Sec. C.3.

Solar mask and reflections [Solar]

The solar masks causes a noticeable increase in annual needs of 4 %, and can cause maximal local deviations up to 37 % due to the global decrease of the incoming solar flux. Nonetheless, there is no significant effect on the difference in design level as the effects of the solar flux are mainly noticeable for lower power.

Radiative heat transfer coupling [LWRad]

The approximation of the building outside surface temperatures by the air temperature leads to a slight over estimation of the heating need with a maximal deviation of 5 %. This over-estimation is explained by higher radiative heat losses as the air temperature is generally lower than the building surface temperatures.

Cette thèse est accessible à l'adresse : http://theses.insa-lyon.fr/publication/2018LYSEI071/these.pdf
© [L. Frayssinet], [2018], INSA Lyon, tous droits réservés

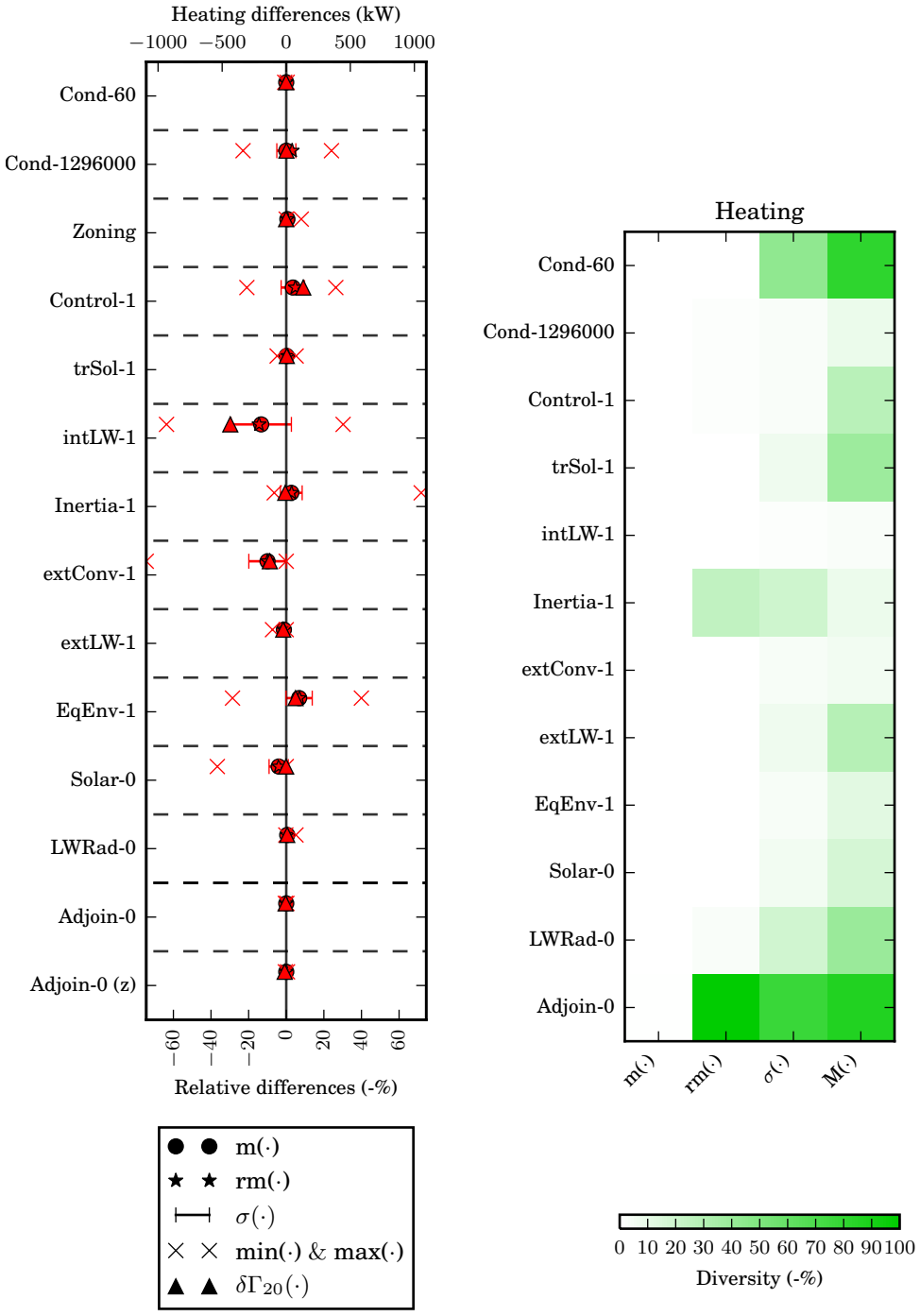

(A) Adaptation effects (B) Diversity effect

FIGURE 5.23: Overview of the district-scale adaptations effects

Adjoining buildings [Adjoin]

The coupling of the adjoining buildings has nearly no effect. However, the wall area of the adjoining building is very low compared to the total envelope surface of the

Cette thèse est accessible à l'adresse : http://theses.insa-lyon.fr/publication/2018LYSEI071/these.pdf
© [L. Frayssinet], [2018], INSA Lyon, tous droits réservés

district in the case study. Hence, the effect may probably not be properly quantified in this configuration. The label 'Adjoin-0 (z)' corresponds to the influence of [Adjoin-0] for the district model with more zones ('Zoning'). As the area of the adjoining wall is more important, the effects are also slightly increased but still negligible.

Nonetheless, concluding about this adaptation necessitates further completion of the set of experiments with case studies containing more zones and having different setpoints. Indeed, the thermal behaviours of the adjoining walls are more important under these conditions.

5.2.2 Diversity effect

The diversity factor (Eq. 3.10) is indicated in Table 5.6 and plot in Fig. 5.23b. These effects are not computed for the 'Zoning' model as the number of buildings is not the same. Only the diversity effects related to the standard deviation and maximal deviation indicators are indicated in Table 5.6 as the diversity effects of the mean difference are mathematically null, these of the rectified mean difference are quasi-null (Fig. 5.23b), and those of difference in design level make no sense[11].

Note that the diversity effect is higher when the effects are very low (notably for [Cond-60] and [Adjoin-0]). This effect is not phenomenological but is rather due to the fact that the effect tends towards zero.

Concerning the maximal deviation, the diversity is generally lower than 10 % for the most impacting adaptations. [trSol-1], [Solar-0] and [LWRad-0] have particularly high diversity effects (resp. 38, 16 and 39 %), probably because they are the most shape-related adaptations.

The diversity quantified for the standard deviation is generally approximately 2 times lower than for the maximal deviation except for the [Inertia-1], where it is almost 3 times higher. Hence, the maximal deviations caused by *IntInertia* are nearly synchronous, but globally not the others.

The diversity is computed on a sample of only 23 elements (buildings), but it seems to be enough to a have a representative value (see after). Furthermore, the diversity effect may probably be higher in other configurations, notably those considering different building typologies and occupant behaviour. However, the individual effects of the shape on the envelope model were distinctly identified.

The measurable diversity of the defined case study is only linked to the diversity of building shape. Furthermore, it is computed on a sample of only 23 elements (buildings), but it seems to be sufficient, as shown hereafter.

5.2.3 Indicator representativeness

The representativeness of the indicators may be questionable as they are computed for a district made of only 23 buildings. To analyse this aspect, the methodology defined in Sec. 3.2.4 is applied. The indicators are computed for the same district but with a varying number of buildings. 30 random sets of buildings are made for each number of buildings considered. The results show that the indicators give similar estimations regardless of the number of buildings and the combinations thereof. Furthermore, they converge to approximately 15 buildings, as illustrated for the adaptation with respect to the maximal deviation (Fig. 5.24). The results are very similar for the other adaptations and the other indicators, including the diversity

[11] The district scale difference of design level is not related to differences in the design level of each individual buildings.

Cette thèse est accessible à l'adresse : http://theses.insa-lyon.fr/publication/2018LYSEI071/these.pdf
© [L. Frayssinet], [2018], INSA Lyon, tous droits réservés

effect, and hence are not included in the manuscript. This results are coherent with the similarity between the building- and district-scale results.

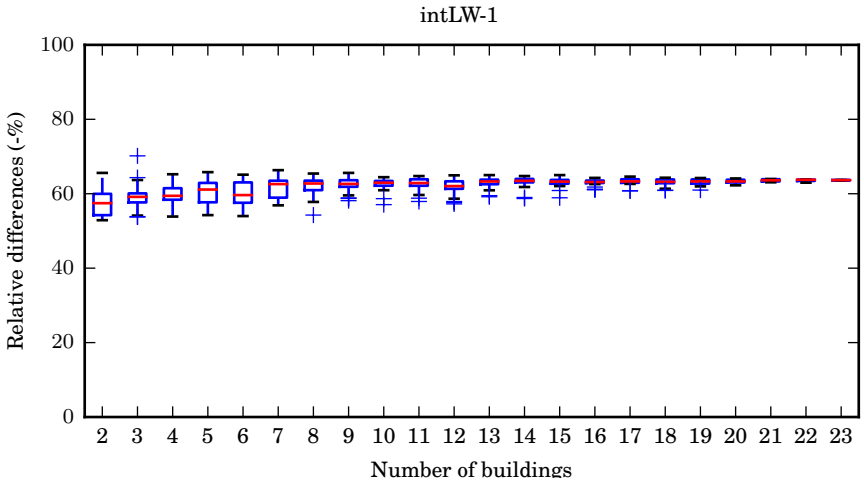

FIGURE 5.24: Convergence of the indicators

5.2.4 Statistical invariance

At the district scale, some data are inferred from statistical information. The most evident statistical information is the occupant behaviour. However, the building parameters are also inferred as the characteristics are uncertain around the typology, and the typology repartition may be only statistically known. 3 different sets of experiments were tested to analyse the influences of different sources of statistical knowledge due to occupant behaviour, parametrisation and typology. Their impacts at the district scale were still quantified by comparing the different statistical inference with a reference (one of them) and using the indicators previously defined to extract specific information. The distribution of the indicators for each comparison is analysed to estimate the scattering between the power curves (Fig. 5.25) with respect to the power curve feature focused.

Occupant behaviour 30 different district-scale occupant behaviour scenarios based on the population statistics of Lyon were generated and simulated (Sec. 4.2.1). The diversity of occupant behaviours causes low global effects, even locally (approximately 10 % for the maximal differences) except in 3 extreme cases where the maximal differences reach approximately 75 %. Furthermore, regardless of the draw, the impact is quite similar (a low scattering and range of statistical distribution).

Building parameters The same parameters accounted for in the parameter sensitivity analysis (Sec. 5.1.3) were considered uncertain. A normal distribution is associated with each parameter. This normal distribution is centred around the parameter nominal value (from the typology) with a standard deviation equal to 30 % of the nominal value. 30 different draws were simulated. The considered parameter uncertainty has a low effect on the power curve. These uncertainties are lower than 10 %, even for the maximal deviation. However, a better uncertainty quantification of the parameter is necessary to support this observation.

Cette thèse est accessible à l'adresse : http://theses.insa-lyon.fr/publication/2018LYSEI071/these.pdf
© [L. Frayssinet], [2018], INSA Lyon, tous droits réservés

Typology It was assumed that 50, 30 and 20 % of the households belong to the different typologies, namely, apartment blocks built between 1915 and 1948, apartment blocks built between 1975 and 1981 and multi-family houses built after 2012, respectively (Rochard et al., 2015). 30 different districts corresponding to this statistic were simulated. This statistical uncertainty causes the highest differences and the highest scattering of results. The median results do not exceed 20 % for the maximal deviation, but approximately 25 % of cases cause maximal deviations higher than 40 % and mean differences higher than 10 %.

Orientations In this case, the objective is to determine if the real orientation of the walls is very important. Hence, the orientation is not linked to statistical inference but rather to model uncertainty. But similar analysis may be used. The wall orientations notably impact the incoming solar fluxes. For this analysis, the district was progressively rotated 30° per 30°, leading to 12 district configurations. The orientation has nearly no influence on the results at the district scale, whereas deviations are very important at the building scale (up to 400 % for the maximal deviation). This result seems to indicate that a mean estimation of the solar heat gains is enough at the district scale rather than a detailed knowledge depending on the wall orientations. This point was notably a question raised during the model inter-comparison (Frayssinet et al., 2018a).

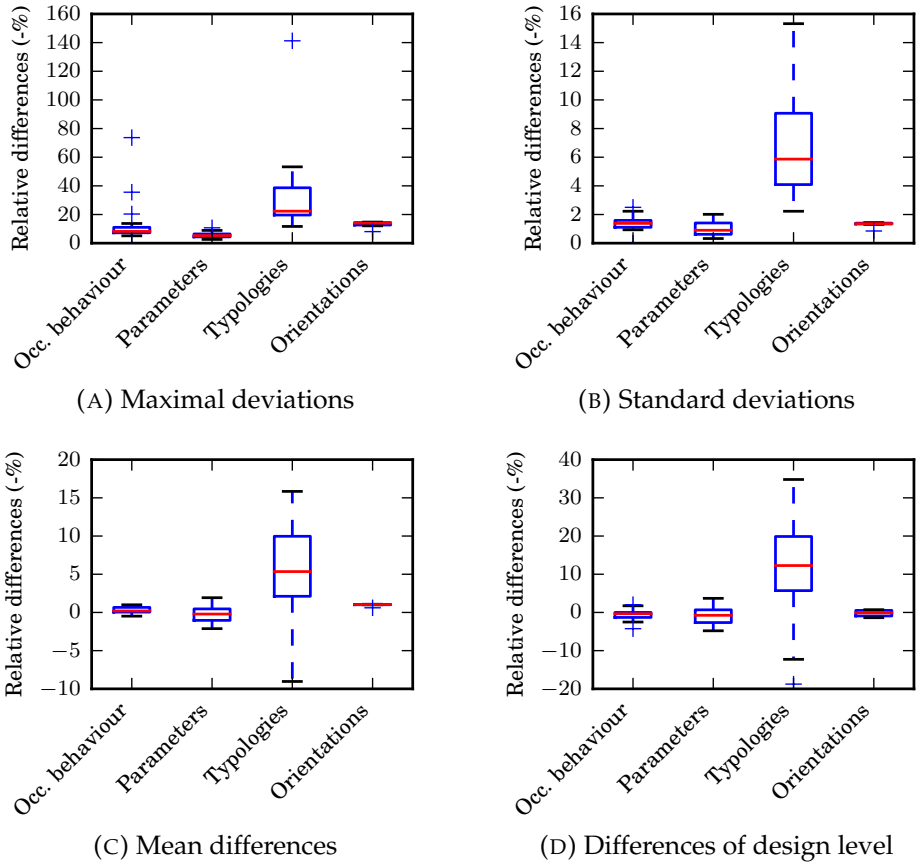

(A) Maximal deviations

(B) Standard deviations

(C) Mean differences

(D) Differences of design level

FIGURE 5.25: Scattering of the indicators

Then, the scattering of the indicator is analysed as a function of the number of buildings considered in order to evidence the influence of the spatial scale. For each spatial scale (number of building) a maximal set of 30 combinations of buildings

Cette thèse est accessible à l'adresse : http://theses.insa-lyon.fr/publication/2018LYSEI071/these.pdf
© [L. Frayssinet], [2018], INSA Lyon, tous droits réservés

was tested. The standard deviation of the indicators is quantified for each case, and their statistical distribution is plotted. Only the results for the maximal deviation are shown in Fig. 5.26 as all indicators in each case show similar behaviour: the scattering of the indicators shows a decrease in power from -0.4 to -0.7, except in the 'Orientations' case, where the decrease is higher, in power -1.4. For the other cases, this observation is very close to the central limit theorem statement (Sec. 5.2.4). Hence, the increase of the district scale makes it possible to decrease the uncertainty resulting from statistical knowledge.

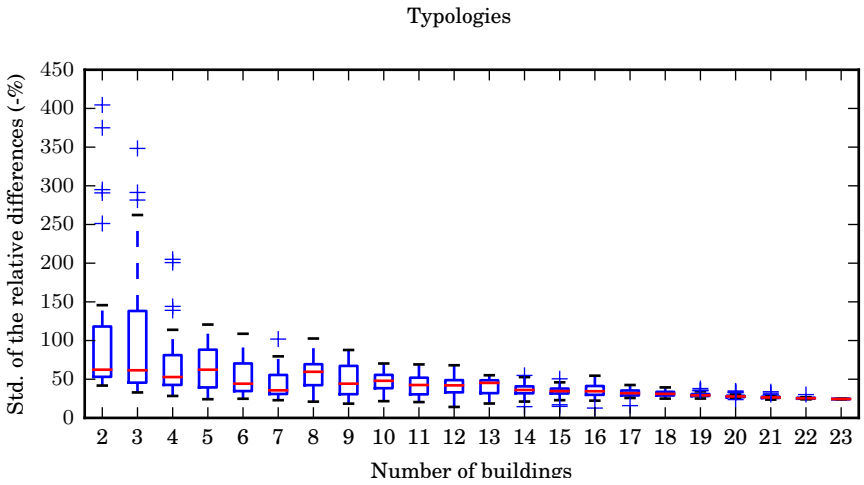

FIGURE 5.26: Effect of the district scale on statistical invariance; indicator: maximal deviation

5.3 Conclusion about the suitability of the adaptations

The previous results were general to be useful and give insights into the adaptation suitability for a various range of cases. The aim of this part is to illustrate the capability of the methodology to *select the suitable adaptations for given simulation objectives* and *to determine the reachable simulation objective given imposed adaptations*, as introduced in Sec. 3.1.2. Both capabilities are detailed here-after. They imply first the quantification of the adaptation effects (previous part of this chapter).

5.3.1 Adapting to simulation objective

The adaptation process is summarised in Fig. 5.27. Note that the coupled and interacted simplifications effects are not accounted for in the introduced process, but it may be improved thanks to further developments of global sensitivity analysis (Sec. 3.3).

An application of this process is given for the 3 following different simulation objectives:

(1) estimating the district annual performance;

(2) designing a district energy system;

(3) predicting the power curve at all times.

Cette thèse est accessible à l'adresse : http://theses.insa-lyon.fr/publication/2018LYSEI071/these.pdf
© [L. Frayssinet], [2018], INSA Lyon, tous droits réservés

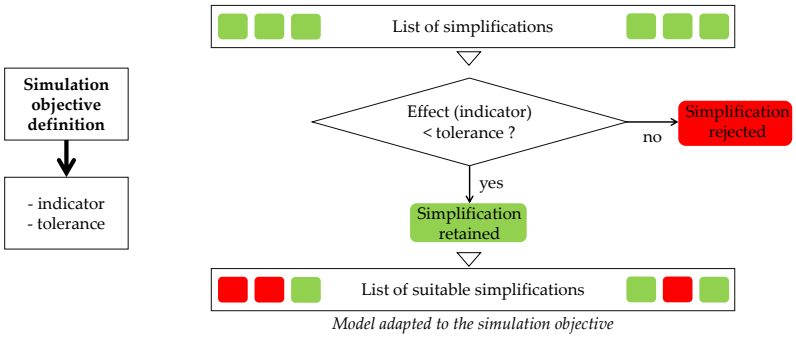

FIGURE 5.27: Adapting to simulation objective

The indicators associated with these objectives are the mean differences (m(·)), the level of design ($\delta\Gamma_{20}(\cdot)$) and the absolute deviation (M(·)), respectively. A error tolerance tl of 10 % of the mean power is chosen.

Fig. 5.28a shows the suitable adaptations for different indicators for 2 different tolerances. The colour corresponds to the relative difference in the tolerance r_{tl}, which is defined as follows:

$$r_{tl} = \frac{ind - tl}{tl} \tag{5.3}$$

where ind is the indicator value and tl is the tolerance value. The indicator equal to the tolerance corresponds to $r_{tl} = 0$ (orange); 1 time higher, to $r_{tl} = 1$ (red); and 1 time lower, to $r_{tl} = -1$ (i.e. $ind = 0$; green). The colour scale is limited to $\pm$ 100 % of the tolerance.

For the simulation objectives defined previously (Fig. 5.28a), notably according to Table 2.1, the conclusions are as follows:

(1) The only non-suitable adaptation is [intLW]. Hence, the model necessitates an estimation of the radiant temperature, for a better estimation of the internal long-wave radiation. Such a model requires information about the interior of the building (i.e., the maximal level of detail in CityGML format (LoD 4)), or at least on estimation of the internal surfaces area. The suitability of [extConv] is limit. A better estimation of the external CHTC is preferable. In a district, such an estimation may require specific micro-climate models, or, at least, correlations.

(2) The conclusions are similar to those for (1) except that [Control] is not suitable. Information about the energy system regulation is needed.

(3) The previous non-suitable adaptations are logically not suitable as the maximal deviation is more restrictive. Furthermore, a rough discretisation of the conductive problem is not suitable [Cond-1296000], and hence, roughest RC-analogy models are probably not suitable, even more if an equivalent envelope is considered [EqEnv]. Detail composition of the envelope is hence expected. The internal inertia has to be accounted for [Inertia], implying a knowledge of the internal walls of buildings. Last, the solar shade [Solar-0] as to be accounted for.

Cette thèse est accessible à l'adresse : http://theses.insa-lyon.fr/publication/2018LYSEI071/these.pdf
© [L. Frayssinet], [2018], INSA Lyon, tous droits réservés

	Acceptable range around nominal value (%)		
Parameter	Mean diff.	Diff. of design lvl.	Max. dev.
λ_{-wall}	45.5	25.5	12.7
λ_{-roof}	190.5	90.9	52.6
λ_{-floor}	181.8	117.6	36.4
$\lambda_{-intfloor}$	∞	∞	81.6
b_{-floor}	76.9	47.1	23.0
U_{-win}	66.7	39.2	17.9
$h_{cv.in-(int)wall}$	125.0	67.8	38.5
$h_{cv.,in-roof}$	666.7	285.7	133.3.0
$h_{cv.in-(int)floor}$	200.0	88.9	44.9
$h_{cv.in-win}$	153.8	87.0	31.3
ρc_{-wall}	∞	444.4	14.5
ρc_{-roof}	∞	∞	85.1
ρc_{-floor}	∞	∞	54.1
$\rho c_{-intfloor}$	∞	800.0	14.7
α_{-wall}	190.5	571.4	16.1
α_{-roof}	500.0	∞	25.5
θ_{-win}	222.2	∞	15.9
ε_{-wall}	250.0	250.0	22.9
ε_{-roof}	500.0	∞	43.0
ε_{-win}	666.7	571.4	66.7
$AirChgRt$	69.0	40.0	18.0
$RadPart$	142.9	58.8	29.1
$tilt_{-roof}$	212.7	96.8	19.5

TABLE 5.7: Parameter range for a tolerance of 10 %

Cette thèse est accessible à l'adresse : http://theses.insa-lyon.fr/publication/2018LYSEI071/these.pdf
© [L. Frayssinet], [2018], INSA Lyon, tous droits réservés

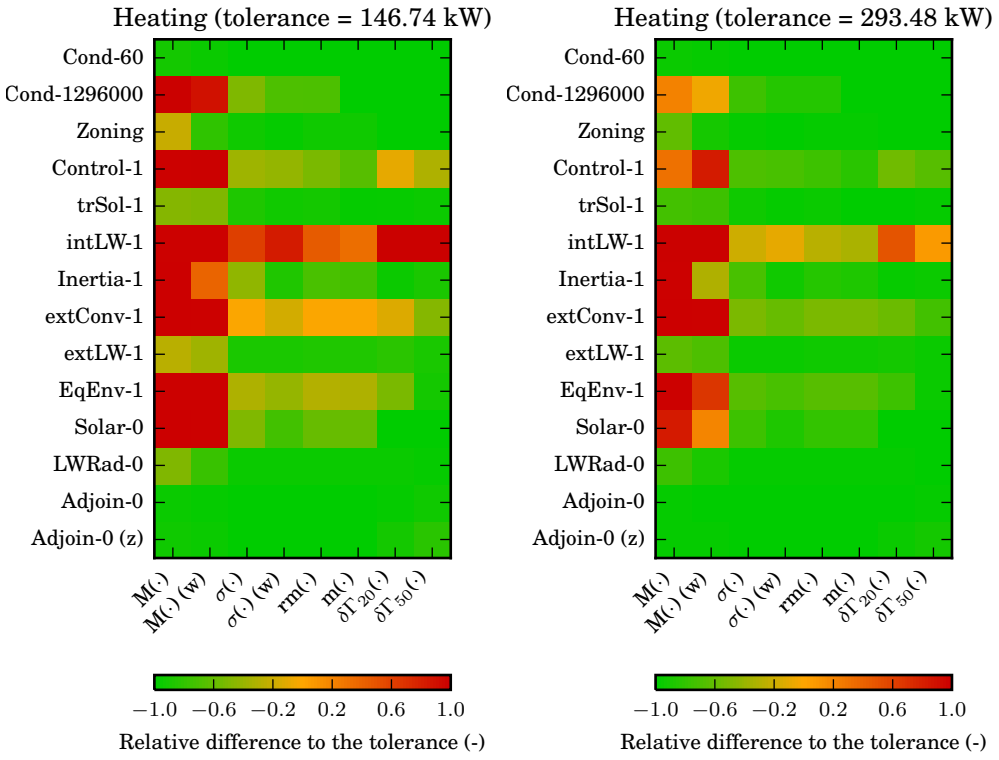

(A) Tolerance = 10 % (B) Tolerance = 20 %

FIGURE 5.28: Overview of the adaptations effects

Note that increasing the tolerance makes it possible to reduce the constraints (Fig. 5.28b). The use of the weighted indicators defined in Eq. 3.8 (referred to 'w') also reduces some constraints, notably for [Inertia], but increases in case of [Control], with respect to the maximal deviation.

According to Sec. 5.1.3, static parameters have to be estimated with accuracy in priority for (1) and (2) in addition to dynamic inertia related parameters for (3). Table 5.7 estimates the acceptable relative range of the parameters rg according to previous analysis[12] (Sec. 5.1.3). This range is estimated with the mean sensitivity index previously computed $\bar{s_n}$ and the relative tolerance tl as:

$$rg = \frac{tl}{\bar{s_n}} \tag{5.4}$$

According to Sec. 5.2.4, the district scale is enough large to infer all statistical knowledge except for (3) for typology. Moreover, detailed information on the orientation of walls is not necessary.

The results also show that because of lower heating needs, high-energy performance buildings may be more adapted than inefficient buildings if assessing at the district scale with absolute (not relative) effects (Sec. 5.1).

[12] According to the building scale results of *Init* as this typology is very similar to this of the district. Note that district effects (Sec. 3.2.4) are consequently not quantified.

Cette thèse est accessible à l'adresse : http://theses.insa-lyon.fr/publication/2018LYSEI071/these.pdf
© [L. Frayssinet], [2018], INSA Lyon, tous droits réservés

5.3.2 Determining reachable simulation objectives

As an illustration of the reverse application enabled by the adaptation quantification, let us assumed having a GIS without information about the internal layout of the buildings (LoD 1 to 3 in cityGML). According to Table 2.1, the zoning [Zoning], the infiltration [Infil], the system regulation [Control], the distribution of the transmitted solar flow [trSol], the internal LW radiation [intLW] and the internal inertia [Inertia] cannot be detailed. As a consequence, the simulation objectives (1) is achievable but with a tolerance of 13 %, (2) with a tolerance of 30 % and (3) is reachable only for a tolerance higher than 72 % (Table 5.6).

Hence, this process make it possible to determine which simulation objectives may be reached given a specific constraint. The global process is summarised in Fig. 5.29.

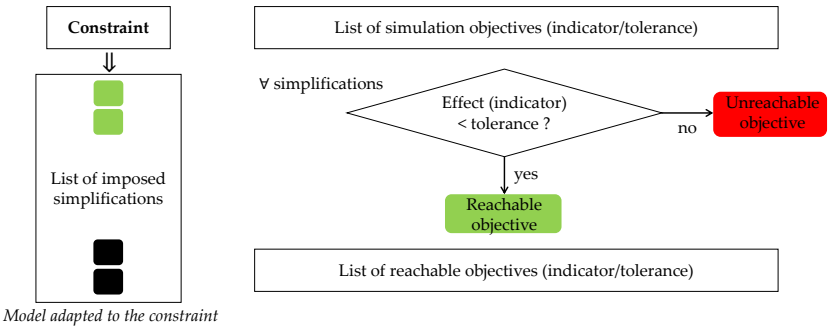

FIGURE 5.29: Reachable simulation objectives

Cette thèse est accessible à l'adresse : http://theses.insa-lyon.fr/publication/2018LYSEI071/these.pdf
© [L. Frayssinet], [2018], INSA Lyon, tous droits réservés

Chapter 6

Conclusions and outlooks

Chapter 1 highlighted the key role of building energy simulation in addressing many future issues. The district scale is shown to be particularly important for optimizing and designing integrated solutions, in a more and more urban world. However, the development of such simulation tools is limited by the computational cost and data availability constraints, in particular when focusing on power curves. Many simplifications have been proposed in the literature to address these limitations, but few studies have been carried out to analyse their effects on the simulation results, in particular apart from annual energy consumption.

The main sources of simplifications of district energy models related to heating and cooling modelling were identified in Chapter 2. The thermal conduction problem was evidenced to be the costly part of the simulation and hence the main target of simplification. Furthermore, the default building energy models are not able to properly integrate district-scale effects. The modelling choices retained in DEM are often implicit or not clearly stated. In order to ease model inter-comparisons, the definition of a modelling framework should be proposed, in particular, in the frame of the projected DESTEST benchmark (Wetter and Treeck, 2017).

In order to quantify the suitability of a simplification, a specific methodology were proposed in Chapter 3. It make it possible to define how to adapt a district energy model and to identify data needed to improve modelling confidence. The main contribution of the present work was to integrate any simulation objective in the methodology, in particular those related to the power curve. These specifications require clearly defining the simulation objectives and related indicators, which is currently infrequently discussed in the literature when focusing on power curves. The proposed methodology was linked to sensitivity analysis methods. However, the consideration of model uncertainty and time-dependent variables implies specific developments to extend the usual methods or to define specific ones. Such improvements may notably make it possible to consider and discriminate non-linear and interaction effects.

A simulation platform introduced in Chapter 4 were developed in order to automatically model and simulate a district energy model and test the suitability of the identified simplifications with the proposed methodology. As a consequence, the modelling process is modular. The platform tool chain integrates promising tools and modelling standards that are currently known to have important developments (Modelica, FMU), notably for building energy simulation at the district scale, carried out by the building energy simulation community (Wetter and Treeck, 2017). The integration of the such tools will ease the interoperability of the platform. Taking advantage of the model structure, the building energy simulations are distributed in order to reduce the computational duration and ease large scale simulation and parametric analysis. In its current state, the platform mainly focus on envelope modelling, and hence, future improvements are needed to better account for system

Cette thèse est accessible à l'adresse : http://theses.insa-lyon.fr/publication/2018LYSEI071/these.pdf
© [L. Frayssinet], [2018], INSA Lyon, tous droits réservés

regulation and occupant behaviour, which are roughly modelled, and to integrate micro-climate models. Facing DEM challenges not only relies on adaptations, but also on the use of efficient large scale numerical resources and on data collection. Furthermore, simulation platform improvements imply cooperation with other scientific fields, including, computer sciences to improve and speed-up numerical processes and geomatics for GIS management and data sciences to define indicators and analyse results.

The platform was used to apply the methodology for the identified simplifications in Chapter 5 and to make it possible to draw conclusions about the district-scale model adaptations. The results show that the usual adaptations are generally suitable with respect to annual energy estimations but that locally important effects, which are generally counter-balanced over a day, may occur on the power curve. This observation reinforces the necessity of defining specific indicators when analysing power curves. Power curves are particularly sensitive to transient phenomena, which are mainly related to solar fluxes in our model. As a consequence, cooling is more affected than heating. Note that transient phenomena may also occur because of occupant behaviour and energy system regulation. Hence, detailed information is needed to simulate these phenomena. Concerning the district scale, inter-building couplings seem to be negligible, reinforcing the advantage of distributing the building energy simulations. However, the impact of the urban environment on the incoming solar flux, which is a pre-process, is fundamental to account for. The smoothing effect of the district scale on the adaptation effects was highlighted but was shown to be quite low. However, the ability of the district scale to use statistical data was particularly evidenced, underscoring the limits of the micro-simulation approach and its transition to a statistical approach. Nonetheless, this transition implies a loss of the possibility to spatially analyse the results. The results are clearly linked to the present case study. However, the relative effects were identified as being quite representative of any building form and typology and are hence probably generalisable to other case studies. Last, this tool was not validated against real measurements. Difficulties in accessing power load curves and detailed information for an entire district in addition to the focus only on the envelope model explain this limitation. Nonetheless, the objective was to test existing modelling choices, not to directly reproduce reality. In addition, data availability is currently a fast growing domain, and the present contribution aims to help modellers identify their data requirements.

Roy (1985) wrote that a model cannot be 'good' or 'bad' but only 'adapted' to a given issue, or not. The definition of the issue, or the simulation objective, is hence the fundamental step of model adaptation. According to Roy, defining the simulation objective relies on answering the following paraphrased questions:

- Which decision is the model expected to guide? For whom and how?
- What are the possible variants to test? How can the problem be formulated?
- How are preferences defined?
- How are global preferences defined?

Therefore, as the building energy sector faces numerous challenges, numerous tools are needed to answer them. As a consequence, the simulation objectives have to be clearly clarified, and models should be specifically adapted for each one, which is notably what the present work expected to evidence and guide.

Cette thèse est accessible à l'adresse : http://theses.insa-lyon.fr/publication/2018LYSEI071/these.pdf
© [L. Frayssinet], [2018], INSA Lyon, tous droits réservés

Bibliography

Agugiaro, Giorgio (2015). "Energy planning tools and CityGML-based 3D virtual city models: experiences from Trento (Italy)". In: *Appl Geomat, 2015*.

Baetens, R. et al. (2015). "OPENIDEAS – An Open Framework for Integrated District Energy Simulations". In: *14th International Conference of IBPSA*. Hyderabad, India.

Baetens, Ruben and Dirk Saelens (2016). "Modelling uncertainty in district energy simulations by stochastic residential occupant behaviour". In: *Journal of Building Performance Simulation* 9(4), pp. 431–447.

Berthou, Thomas et al. (2014). "Development and validation of a gray box model to predict thermal behavior of occupied office buildings". In: *Energy and Buildings* 74, pp. 91–100.

Berthou, Thomas et al. (2015). "Smart-E: A Tool for Energy Demand Simulation and Optimization at the City Scale". In: *14th International Conference of IBPSA*. Hyderabad, India.

Blervaque, Hubert (2014). "Règles de modélisation des systèmes énergétiques dans les bâtiments basse consommation [French]". PhD thesis. Ecole Nationale Supérieure des Mines de Paris.

Blervaque, Hubert et al. (2012). "Comparative Analysis of Air-to-air Heat Pump Models for Building Energy Simulation". In: *IBPSA-USA Journal* 5(1), pp. 136–143.

Bontemps, Stéphanie (2015). "Validation expérimentale de modèles: application aux bâtiments basse consommation [French]". PhD thesis. Université de Bordeaux.

Bontemps, Stéphanie, Laurent Mora, and Mathieu Schumann (2016). "Validation expérimentale appliquée à la modélisation d'une cellule test de type basse consommation [French]". In: *Conférence IBPSA France*. Marne-la-Vallée.

Bontemps, Stéphanie et al. (2013). "Reliability of dynamic simulation models for building energy in the context of low-energy buildings". In:

Bouyer, Julien, Christian Inard, and Marjorie Musy (2011). "Microclimatic coupling as a solution to improve building energy simulation in an urban context". In: *Energy and Buildings* 43(7), pp. 1549–1559.

BuildingsPy documentation - `http://simulationresearch.lbl.gov/modelica/buildingspy/`.

Campbell, Katherine, Michael D. McKay, and Brian J. Williams (2006). "Sensitivity analysis when model outputs are functions". In: *Reliability Engineering & System Safety* 91, pp. 1468–1472.

Chastaing, Gaëlle (2013). "Indices de Sobol généralisés pour variables dépendantes [French]". PhD thesis. Université de Grenoble.

Chouquet, Julie (2007). "Development of a Method for Building Life Cycle Analysis at an Early Design Phase: Implementation in a Tool; Sensitivity and Uncertainty of Such a Method in Comparison to Detailed LCA Software". PhD thesis.

CityGML homepage - `https://www.citygml.org/`.

Clarke, Joseph (2007). *Energy simulation in building design*. Routledge.

Cette thèse est accessible à l'adresse : http://theses.insa-lyon.fr/publication/2018LYSEI071/these.pdf
© [L. Frayssinet], [2018], INSA Lyon, tous droits réservés

Coakley, Daniel, Paul Raftery, and Marcus Keane (2014). "A review of methods to match building energy simulation models to measured data". In: *Renewable and Sustainable Energy Reviews* 37, pp. 123–141.

Dassault Systèmes. *Dymola homepage - https://www.3ds.com/products-services/catia/products/dymola/*.

Dogan, Timur, Christoph Reinhart, and Panagiotis Michalatos (2014). "Automated multi-zone building energy model generation for schematic design and urban massing studies". In: *IBPSA eSim conference, Ottawa, Canada*.

Flor, Francisco Sanchez de la and Servando Alvarez Dominguez (2004). "Modelling microclimate in urban environments and assessing its influence on the performance of surrounding buildings". In: *Energy and Buildings* 36(5), pp. 403–413.

Fonseca, Jimeno A. and Arno Schlueter (2015). "Integrated model for characterization of spatiotemporal building energy consumption patterns in neighborhoods and city districts". In: *Applied Energy* 142, pp. 247–265.

Fraisse, Gilles et al. (2002). "Development of a simplified and accurate building model based on electrical analogy". In: *Energy and Buildings* 34, pp. 1017–1031.

Frayssinet, Loïc et al. (2016). "Modélisation à l'échelle de la ville de la demande énergétique de chauffage et de refroidissement des bâtiments - Etat de l'art et perspectives [French]". In: *Conférence IBPSA France*.

Frayssinet, Loïc et al. (2018a). "Incertitude de simulation à l'échelle du quartier : comparaison de deux modèles et analyse de sensibilité [French]". In: *Conférence IBPSA France*.

Frayssinet, Loïc et al. (2018b). "Modeling the heating and cooling energy demand of urban buildings at city scale". In: *Renewable and Sustainable Energy Reviews* 81, pp. 2318–2327.

Fuchs, Marcus et al. (2015). "Structuring the building performance Modelica library AixLib for open collaborative development". In: *14th International Conference of IBPSA*. Hyderabad, India.

Functional Mock-up Interface - http://fmi-standard.org/.

Galtier, Virginie et al. (2015). "FMI-based distributed multi-simulation with DACCOSIM". In: *Proceedings of the Symposium on Theory of Modeling & Simulation: DEVS Integrative M&S Symposium*. Society for Computer Simulation International, pp. 39–46.

Gay, C. and P. Schetelat (2014). "Low carbon district–Energy and behaviour modelling". In: *Data Models*.

gbXML homepage - http://www.gbxml.org/.

GFDRR, ed. (2016). *The making of a riskier future: How our decisions are shaping future disaster risk*. Global Facility for Disaster Reduction and Recovery.

Goffart, Jeanne, Mickael Rabouille, and Nathan Mendes (2016). "Impact des incertitudes de mesure des variables météorologiques sur le processus de comparaison mesure/simulation en simulation thermique dynamique [French]". In: *Conférence IBPSA France*. Marne-la-Vallée.

Grandjean, Arnaud (2013). "Introduction de non linéarités et de non stationnarités dans les modèles de représentation de la demande électrique résidentielle [French]". PhD thesis. Paris, ENMP.

He, Jiang, Akira Hoyano, and Takashi Asawa (2009). "A numerical simulation tool for predicting the impact of outdoor thermal environment on building energy performance". In: *Applied Energy* 86(9), pp. 1596–1605.

Hijazi, Ihab (2011). "Integrated management of indoor and outdoor utilities by utilizing BIM and 3DGIS". PhD thesis.

Cette thèse est accessible à l'adresse : http://theses.insa-lyon.fr/publication/2018LYSEI071/these.pdf
© [L. Frayssinet], [2018], INSA Lyon, tous droits réservés

Huraux, Thomas, Nicolas Sabouret, and Yvon Haradji (2015). "Study of Human Activity Related to Residential Energy Consumption Using Multi-level Simulations." In: *ICAART (1)*, pp. 133–140.

IBPSA project 1 homepage - https://ibpsa.github.io/project1/.

IEA, ed. (2017). *Key World Energy Statistics*.

IFC Overview summary - http://www.buildingsmart-tech.org/specifications/ifc-overview/ifc-overview-summary.

Ina, De Jaeger, Reynders Glenn, and Saelens Dirk (2017). "Impact of spatial accuracy on district energy simulations". In: *Energy Procedia* 132, pp. 561–566.

Iooss, Bertrand (2011). "Revue sur l'analyse de sensibilité globale de modèles numériques [French]". In: *Journal de la Société Française de Statistiques*, pp. 1–24.

IPBES, ed. (2016). *The assessment report of the Intergovernmental Science-Policy Platform on Biodiversity and Ecosystem Services on pollinators, pollination and food production*. Secretariat of the Intergovernmental Science-Policy Platform on Biodiversity and Ecosystem Servic: Bonn, Germany.

IPCC, ed. (2014). *Climate change 2014: mitigation of climate change: Working Group III contribution to the Fifth Assessment Report of the Intergovernmental Panel on Climate Change*. Cambridge University Press: New York, NY.

Keirstead, James, Mark Jennings, and Aruna Sivakumar (2012). "A review of urban energy system models: Approaches, challenges and opportunities". In: *Renewable and Sustainable Energy Reviews* 16(6), pp. 3847–3866.

Kim, Eui-Jong et al. (2014). "Urban energy simulation: Simplification and reduction of building envelope models". In: *Energy and Buildings* 84, pp. 193–202.

Kim, Eui-Jong et al. (2015). "Is it possible to Use a Single Reduced Model for a Number of Buildings in Urban Energy Simulation?" In: *14th International Conference of IBPSA*. Hyderabad, India.

Kämpf, Jérôme Henri and Darren Robinson (2007). "A simplified thermal model to support analysis of urban resource flows". In: *Energy and Buildings* 39(4), pp. 445–453.

Lauster, M. et al. (2014). "Low order thermal network models for dynamic simulations of buildings on city district scale". In: *Building and Environment* 73, pp. 223–231.

Lauzet, Nicolas et al. (2016). "What is the required level of details to represent the impact of the built environment on energy demand?" In: *International Conference on Sustainable Synergies from Buildings to the Urban Scale*.

Malys, Laurent, Marjorie Musy, and Christian Inard (2015). "Microclimate and building energy consumption: study of different coupling methods". In: *Advances in Building Energy Research*, pp. 1–24.

Marshall, S.A. (1966). "An approximate method for reducing the order of a linear system". In: *Control* 10, pp. 642–643.

McAuley, Barry, Alan Hore, and Roger West (2017). *BICP Global BIM Study - Lessons for Ireland's BIM Programme*. Tech. rep. Dublin Institute of Technology.

Mendes, N et al. (2003). "Moisture effects on conduction loads". In: *Energy and Buildings* 35(7), pp. 631–644.

Modelica Association - https://www.modelica.org/.

Musy, Marjorie, Laurent Malys, and others (2014). "The use of SOLENE-microclimat to assess adaptation strategies at the district scale". In: *IC2UHI*.

Nanty, Simon (2006). "Quantification des incertitudes et analyse de sensibilité pour codes de calcul à entrées fonctionnelles et dépendantes [French]". PhD thesis. Ecole Centrale de Lyon.

Cette thèse est accessible à l'adresse : http://theses.insa-lyon.fr/publication/2018LYSEI071/these.pdf
© [L. Frayssinet], [2018], INSA Lyon, tous droits réservés

Nouvel, Romain et al. (2015). "Development of the Citygml Application Domain Extension Energy for Urban Energy Simulation". In: *14th International Conference of IBPSA*. Hyderabad, India.

Oke, Tim R. (1982). "The energetic basis of the urban heat island". In: *Quarterly Journal of the Royal Meteorological Society* 108(455), pp. 1–24.

Page, J. et al. (2008). "A generalised stochastic model for the simulation of occupant presence". In: *Energy and Buildings* 40(2), pp. 83–98.

Page, Jessen (2007). "Simulating occupant presence and behaviour in buildings". PhD thesis. Ecole polytechnique fédérale de Lausanne.

Palomo, E., Y. Bonnefous, and F. Déqué (1997). "Guidance for the selection of a reduction technique for thermal models". In: *IBPSA*.

Pedrinis, Frédéric (2017). "Représentations et dynamique de la ville virtuelle [French]". PhD thesis. Université Lyon 2 Lumière.

Pflugradt, Noah and Urs Muntwyler (2017). "Synthesizing residential load profiles using behavior simulation". In: *Energy Procedia* 122, pp. 655–660.

Plessis, Gilles, Aurelie Kaemmerlen, and Amy Lindsay (2014). "BuildSysPro: a Modelica library for modelling buildings and energy systems". In: pp. 1161–1169.

Popelin, Anne-Laure and Anne Dutfoy (2014). "Open TURNS, an Open Source Uncertainty Engineering Software". In: *SNA + MC 2013 - Joint International Conference on Supercomputing in Nuclear Applications + Monte Carlo*.

Projet MERUBBI - Méthodes d'Exploitation des Ressources Utiles du Bâtiment Bioclimatique dans son Ilot - `http://anr-merubbi.fr/` [French].

Python homepage - `https://www.python.org/`.

Raillon, Loïc and Christian Ghiaus (2017). "Study of Error Propagation in the Transformations of Dynamic Thermal Models of Buildings". In: *Journal of Control Science and Engineering* 2017, pp. 1–15.

Remmen, Peter et al. (2018). "TEASER: an open tool for urban energy modelling of building stocks". In: *Journal of Building Performance Simulation* 11(1), pp. 84–98.

Reynaud, Quentin et al. (2017). "Using Time Use Surveys in Multi Agent based Simulations of Human Activity". In: *Proceedings of the 9th International Conference on Agents and Artificial Intelligence*. Vol. 1, pp. 67–77.

Ribault, Clément et al. (2017). "Assessing tools relevance for energy simulation at the urban scale: towards decision-support tools for urban design and densification". In: *Energy Procedia* 122, pp. 871–876.

Riederer, Peter et al. (2015). "Development of A simulation Platform For The Evaluation Of District Energy System Performance". In: *14th International Conference of IBPSA*. Hyderabad, India, pp. 2499–2506.

Robinson, D and A Stone (2005). "A simplified radiosity algorithm for general urban radiation exchange". In: *Building Services Engineering Research and Technology* 26(4), pp. 271–284.

Robinson, Darren, Urs Wilke, and Frédéric Haldi (2011). "Multi agent simulation of occupants' presence and behaviour". In: *Proceedings of building simulation*, pp. 2110–2117.

Robinson, Darren et al. (2009). "CitySim: Comprehensive micro-simulation of resource flows for sustainable urban planning". In: *Eleventh International IBPSA Conference*, pp. 1083–1090.

Rochard, Ulrich et al. (2015). *Bâtiments résidentiels - Typologie du parc existant et solutions exemplaires pour la rénovation énergétique en France [French]*. Tech. rep. POUGET consultants.

Roux, Jean-Jacques (1984). "Proposition de modèles simplifiés pour l'étude du comportement thermique des bâtiments [French]". PhD thesis. INSA de Lyon.

Cette thèse est accessible à l'adresse : http://theses.insa-lyon.fr/publication/2018LYSEI071/these.pdf
© [L. Frayssinet], [2018], INSA Lyon, tous droits réservés

Roy, Bernard (1985). *Méthodologie multicritère d'aide à la décision [French]*. Economica.
Saltelli, Andrea et al. (2008). *Global Sensitivity Analysis: The Primer*. John Wiley & Sons.
Schumann, Mathieu et al. (2016). "BuildSysPro : une bibliothèque Modelica open-source pour l'énergétique des bâtiments et des quartiers [French]". In: *Conférence IBPSA France*. Marne-la-Vallée.
SketchUp homepage - https://www.sketchup.com/.
Strzalka, Aneta et al. (2011). "3D City modeling for urban scale heating energy demand forcasting". In: *HVAC&R Research* 17:4, pp. 526–539.
Swan, Lukas G. and V. Ismet Ugursal (2009). "Modeling of end-use energy consumption in the residential sector: A review of modeling techniques". In: *Renewable and Sustainable Energy Reviews* 13(8), pp. 1819–1835.
Talebi, Behrang, Fariborz Haghighat, and Parham A. Mirzaei (2017). "Simplified model to predict the thermal demand profile of districts". In: *Energy and Buildings* 145, pp. 213 –225.
Talebi, Behrang et al. (2016). "A Review of District Heating Systems: Modeling and Optimization". In: *Frontiers in Built Environment* 2, p. 22.
Thebault, Simon (2017). "Contribution a l'évaluation in situ des performances d isolation thermique de l'enveloppe des batiments [French]". PhD thesis.
Tian, Wei (2013). "A review of sensitivity analysis methods in building energy analysis". In: *Renewable and Sustainable Energy Reviews* 20, pp. 411–419.
Tittelein, Pierre et al. (2016). "Comparaison des bibliothèques libres de Modelica pour la simulation thermique dynamique du bâtiment [French]". In: *Conférence IBPSA France*. Marne-la-Vallée.
UN (2014). *Department of Population; Division Economic and Social Affairs. World urbanization prospects: the 2014 revision*.
UN (2015). *Paris Agreement*.
Vorger, Eric (2014). "Etude de l'influence du comportement des occupants sur la performance énergétique des bâtiments [French]". PhD thesis. Mines ParisTech.
Vorger, Eric, Patrick Schalbart, and Bruno Peuportier (2014). "Integration of a comprehensive stochastic model of occupancy in building simulation to study how inhabitants influence energy performance". In: *Proceedings PLEA 2014*, pp. 16–18.
Wetter, Michael and Christoph van Treeck (2017). *New Generation Computational Tools for Building & Community Energy Systems*. Tech. rep. Annex 60 Fnial Report. International Energy Agency.
Yan, Da et al. (2015). "Occupant behavior modeling for building performance simulation: Current state and future challenges". In: *Energy and Buildings* 107, pp. 264–278.

Cette thèse est accessible à l'adresse : http://theses.insa-lyon.fr/publication/2018LYSEI071/these.pdf
© [L. Frayssinet], [2018], INSA Lyon, tous droits réservés

Cette thèse est accessible à l'adresse : http://theses.insa-lyon.fr/publication/2018LYSEI071/these.pdf
© [L. Frayssinet], [2018], INSA Lyon, tous droits réservés

Appendix A

Calculation details

A.1 Reflected part of incoming solar flux

Let consider a wall ($wall$) surrounded by a ground (gnd) and the sky vault (sky) enclosing the 2D scene (Fig. A.1). In addition to the solar flow coming from the sky and the sun (respectively diffuse and direct part of the solar flow, Eq. 2.24), the wall received flow from the ground due to reflections ($\Phi_{gnd\rightarrow wall}$). A part of the ground incident solar flow coming from the sky ($\Phi_{sky\rightarrow gnd}$) is diffusely reflected ($\times\varrho_{sol.gnd}$), and only a part $F_{gnd,wall}$ reach the wall:

$$\Phi_{gnd\rightarrow wall} = \varrho_{sol.gnd} \cdot F_{gnd,wall} \cdot \Phi_{sky\rightarrow gnd} \tag{A.1}$$

According to the reciprocity relationship between view factor:

$$\frac{\Phi_{gnd\rightarrow wall}}{S_{wall}} = \phi_{gnd\rightarrow wall} = \varrho_{sol.gnd} \cdot F_{wall,gnd} \cdot \frac{\Phi_{s\rightarrow gnd}}{S_{gnd}} = \varrho_{sol.gnd} \cdot F_{w,gnd} \cdot \phi_{sky\rightarrow gnd} \tag{A.2}$$

Similarly to Eq. 2.24, assuming a ground sky view factor nearly equal to 1 (semi-infinite ground):

$$\phi_{sky\rightarrow gnd} = \phi_{drn.Sol} \cdot \langle \vec{n}_{gnd}, \vec{\gamma} \rangle_+ + \phi_{dfh.Sol} \tag{A.3}$$

Last, because of the complementarity relationship:

$$F_{wall,gnd} + F_{wall,sky} = F_{wall,gnd} + svf = 1 \Rightarrow F_{wall,gnd} = 1 - svf \tag{A.4}$$

Hence we get Eq. 2.24.

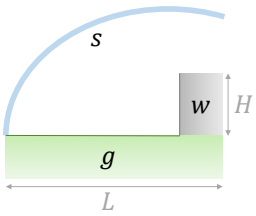

FIGURE A.1: Elements considered

In case of vertical wall of H m high, and a horizontal ground L m long and assuming an infinite longitudinal dimension, the view factor is equal to:

$$F_{wall,gnd} = \frac{1}{2} \cdot \left(1 + \frac{L}{H} - \sqrt{1 + \frac{L^2}{H^2}}\right) \tag{A.5}$$

Cette thèse est accessible à l'adresse : http://theses.insa-lyon.fr/publication/2018LYSEI071/these.pdf
© [L. Frayssinet], [2018], INSA Lyon, tous droits réservés

In case of semi-infinite ground we get $\frac{L}{H} \gg 1$, hence, at the second order:

$$F_{wall,gnd} \simeq \frac{1}{2} \cdot \left(1 + \frac{L}{H} - \sqrt{\frac{L^2}{H^2}}\right) = \frac{1}{2} \tag{A.6}$$

A.2 Equivalent LW parameters

The total net external radiative flow is, according to Eq. 2.23 in its non-linearised form:

$$\begin{aligned} \sum_i^N \Phi_{rad.ext}^{(i)} = & \sum_i^N S^{(i)} \cdot \varepsilon_{ext}^{(i)} \cdot \sigma \cdot svf^{(i)} \cdot (T_{sky}^4 - T_{S.ext}^{(i)4}) \\ & + \sum_i^N S^{(i)} \cdot \varepsilon_{ext}^{(i)} \cdot \sigma \cdot (1 - svf^{(i)}) \cdot (T_{air}^4 - T_{S.ext}^{(i)4}) \end{aligned} \tag{A.7}$$

Similarly, the flow for the equivalent wall is:

$$\begin{aligned} \Phi_{rad.ext.eq} = & S_{eq} \cdot \varepsilon_{ext.eq} \cdot \sigma \cdot svf_{eq} \cdot (T_{sky}^4 - T_{S.ext.eq}^4) \\ & + S_{eq} \cdot \varepsilon_{ext.eq} \cdot \sigma \cdot (1 - svf_{eq}) \cdot (T_{air}^4 - T_{S.ext.eq}^4) \end{aligned} \tag{A.8}$$

The objective is to define $\varepsilon_{ext.eq}$ and svf_{eq} so that $\sum_i^N \Phi_{rad.ext}^{(i)} = \Phi_{rad.ext.eq}$, and even more the two terms identified in the previous equations (sky and ground parts). We assumed that for all i, $T_{S.ext}^{(i)} \approx T_{S.ext.eq}$. Hence:

$$S_{eq} \cdot \varepsilon_{ext.eq} \cdot svf_{eq} = \sum_i^N S^{(i)} \cdot \varepsilon_{ext}^{(i)} \cdot \cdot svf^{(i)} \tag{A.9}$$

We defined:

$$\varepsilon_{ext.eq} = \sum_i^N \frac{S^{(i)} \cdot \varepsilon_{ext}^{(i)}}{S_{eq}} \tag{A.10}$$

and consequently:

$$svf_{eq} = \sum_i^N \frac{S^{(i)} \cdot \varepsilon_{ext}^{(i)} \cdot svf^{(i)}}{S_{eq} \cdot \varepsilon_{ext.eq}} \tag{A.11}$$

A.3 Long and short modes

The d-th equation of Eq. 2.31 is:

$$\dot{x_d}(t) = -\frac{x_d(t)}{\tau_d} + \sum_k B''_{d,k} \cdot U_k(t) \tag{A.12}$$

The solution of this equation is:

$$x_d(t) = e^{-\frac{t-t_0}{\tau_d}} \cdot x_d(t_0) + \int_{t_0}^{t} e^{-\frac{t-\xi}{\tau_d}} \cdot \sum_k B''_{d,k} \cdot U_k(\xi) d\xi \tag{A.13}$$

If using time discretisation with a time step δt

$$x_d(t_n + \delta t) = e^{-\frac{\delta t}{\tau_d}} \cdot x_d(t_n) + \int_{t_n}^{t_n+\delta t} e^{-\frac{t_n+\delta t-\xi}{\tau_d}} \cdot \sum_k B''_{d,k} \cdot U_k(\xi) d\xi \tag{A.14}$$

Cette thèse est accessible à l'adresse : http://theses.insa-lyon.fr/publication/2018LYSEI071/these.pdf
© [L. Frayssinet], [2018], INSA Lyon, tous droits réservés

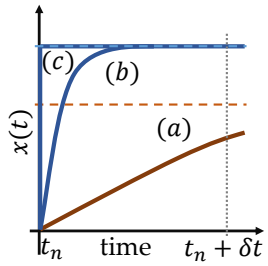

FIGURE A.2: Illustration of the mode reduction
(Adapted from (Marshall, 1966))

Therefore, if the mode is short ($\delta t \gg \tau_d$) then $e^{-\frac{\delta t}{\tau_d}} \cdot x_d(t_n) \longrightarrow 0$, and consequently the state of the mode at a time step $t_n + \delta t$ does not depend on the state at the previous step t_n, but only on the solicitation. Hence, short modes reach their stationary state between time steps ((b) in Fig.A.2) and the dynamic behaviour can be neglected ((c) in Fig.A.2), by contrast with long modes ((a) in Fig.A.2).

A.4 Dynamic Time Wrapping and adaptations

The Dynamic Time Wrapping method were developed to resolve the main drawback of the Euclidian one-to-one comparison of 2 time-series. Indeed, time-shift between the time series may cause high Euclidian one-to-one deviations whereas they are just time-shifted (Fig. A.3a). The DTW method aims to 're-synchronise' the time-series before comparing them.

Let $A = \{a_i, i \in [1, N]\}$ and $B = \{b_i, i \in [1, N]\}$ the 2 times series to compare. The $\mathbf{W}$ matrix is computed so that $\mathbf{W}_{j,k} = |b_j - a_k|$ (bottom of Fig. A.3b, dark indicates null values while white maximal ones). Thanks to the specific algorithm of the method, the time-series were re-synchronise for the comparison thanks to a definition of a path in $\mathbf{W}$ that minimizes the global deviation (with some specific constraints). This path is made of the index of the one-to-one compared time-series element: $\Pi = \{\pi_i = (\pi_i^{(b)}, \pi_i^{(a)}), i \in [1, N_\Pi]\}$.

The original method only computes the mean error when following this path, but term-to-term comparison is wanted in our work for the analysis of short time-step effects. Therefore, we defined $D_{DTW} = \{|b_{\pi_i^{(b)}} - a_{\pi_i^{(a)}}|, i \in [1, N_\Pi]\}$. However, this time-series contains more elements than the times-series to compare (N_Π vs. N, because of the path 'tortuosity' the a_m element may be compared to b_j and b_k for example) whereas we need to define one deviation per time-step. To 'regularize' that we synchronise all deviations with the reference (assumed to be A) so that $d_{DTW,i} = |b_{\pi_i^{(b)}} - a_{\pi_i^{(a)}}|$ is synchronous with the index $\pi_i^{(a)}$ (Fig. A.3c). Furthermore, when numerous deviations are associated to the same index, only the minimal one is kept (doted line in Fig. A.3c).

Moreover, this method does not penalise temporal deviation, whereas they may be detrimental when modelling power demand. To prevent this drawback, a 2D distance may be defined but imply to define equivalence between time and power deviation, which depends on the simulation objective.

Last, it is important to note that this method is originally developed for sound recognition, where the same sound may be produced more or less fast but having the same signification. Nonetheless, definitively, this method is not suitable in our case, excepted if using the adaptations introduced.

Cette thèse est accessible à l'adresse : http://theses.insa-lyon.fr/publication/2018LYSEI071/these.pdf
© [L. Frayssinet], [2018], INSA Lyon, tous droits réservés

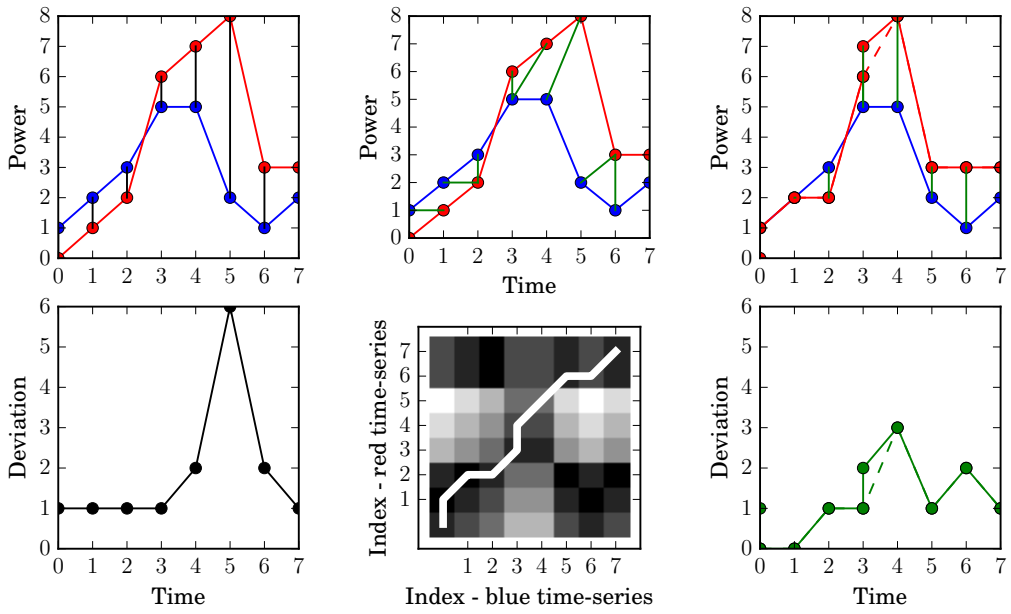

(A) Euclidian comparison (B) DTW method (C) DTW regularisation

FIGURE A.3: DTW method and adaptations

A.5 Haar Wavelet decomposition

Let $A = \{a_i, i \in [1, N]\}$ a time-series. Its Haar wavelet decomposition relies on successive decomposition. The first decomposition of A is:

$$A^{[1]} = \left\{ a_i^{[1]} = \frac{a_{2\cdot i-1} + a_{2\cdot i}}{2}, i \in \left[1, \frac{N}{2}\right] \right\} \tag{A.15}$$

Generally, the h-th decomposition of A is:

$$A^{[h]} = \left\{ a_i^{[h]} = \frac{a_{2\cdot i-1}^{[h-1]} + a_{2\cdot i}^{[h-1]}}{2}, i \in \left[1, \frac{N}{2^h}\right] \right\} \tag{A.16}$$

Hence, the decomposition divide at each step the number of element per 2 by averaging the consecutive values two-to-two (Fig. A.4). The advantage of this method to reduce the time scale, on contrary to interpolation for example, is that the compressed time-series aggregately contains the informations of the original one and that can be reconstituted if computing:

$$R^{[h]} = \left\{ r_i^{[h]} = \frac{r_{2\cdot i-1}^{[h-1]} - r_{2\cdot i}^{[h-1]}}{2}, i \in \left[1, \frac{N}{2^h}\right] \right\} \tag{A.17}$$

Indeed:

$$a_{2\cdot i-1}^{[h-1]} = a_i^{[h]} + r_i^{[h]} \tag{A.18}$$

$$a_{2\cdot i}^{[h-1]} = a_i^{[h]} - r_i^{[h]} \tag{A.19}$$

The original time-series was establish with a time-step of 45 minutes (obtained by

Cette thèse est accessible à l'adresse : http://theses.insa-lyon.fr/publication/2018LYSEI071/these.pdf
© [L. Frayssinet], [2018], INSA Lyon, tous droits réservés

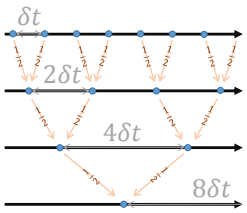

FIGURE A.4: Haar time-series decomposition

interpolation of the 1 hour time-step time-series), so that the time-steps of the decomposition are coherent with usual temporal marker, i.e. 1.5 hours, 3 hours, 6 hours, 12 hours, 1 day, 2 days, 4 days, 8 days ($\approx$ 1 week), 16 days, 32 days ($\approx$ 1 month), 64 days, 128 days and 256 days ($\approx$ a third of a year).

Cette thèse est accessible à l'adresse : http://theses.insa-lyon.fr/publication/2018LYSEI071/these.pdf
© [L. Frayssinet], [2018], INSA Lyon, tous droits réservés

Cette thèse est accessible à l'adresse : http://theses.insa-lyon.fr/publication/2018LYSEI071/these.pdf
© [L. Frayssinet], [2018], INSA Lyon, tous droits réservés

Appendix B

Studied modelling variants

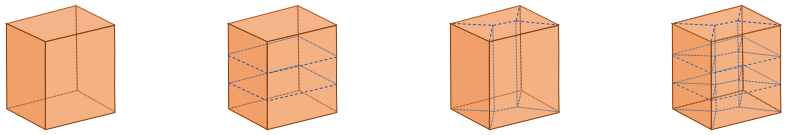

(A) Zoning-0 (B) Zoning-lvl (C) Zoning-ori (D) Zoning-cmb

FIGURE B.1: Zoning variants

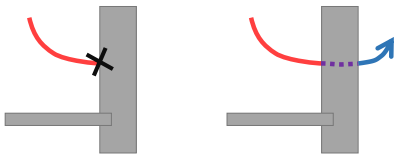

(A) Infil-0 (B) Infil-1

FIGURE B.2: Infiltration model variants

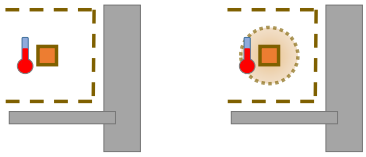

(A) Control-0 (B) Control-1

FIGURE B.3: Controlled temperature variants

Cette thèse est accessible à l'adresse : http://theses.insa-lyon.fr/publication/2018LYSEI071/these.pdf
© [L. Frayssinet], [2018], INSA Lyon, tous droits réservés

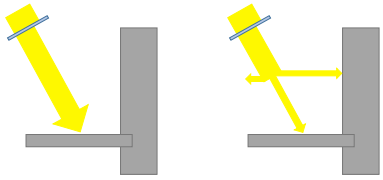

(A) trSol-0 (B) trSol-1

FIGURE B.4: Transmitted solar flux allocation variants

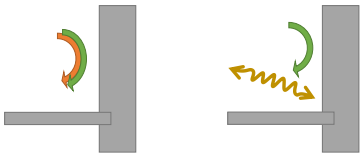

(A) intLW-0 (B) intLW-1

FIGURE B.5: Internal LW radiation modelling variants

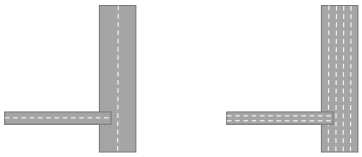

(A) Cond-τ_1 (B) Cond-$\tau_2 > \tau_1$

FIGURE B.6: Conduction discretisation variants

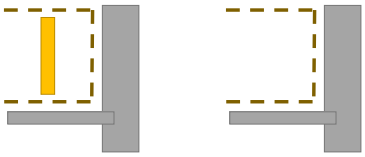

(A) Inertia-0 (B) Inertia-1

FIGURE B.7: Internal inertia modelling variants

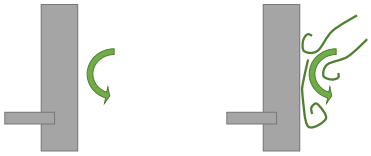

(A) extConv-0 (B) extConv-1

FIGURE B.8: External CHTC modelling variants

Cette thèse est accessible à l'adresse : http://theses.insa-lyon.fr/publication/2018LYSEI071/these.pdf
© [L. Frayssinet], [2018], INSA Lyon, tous droits réservés

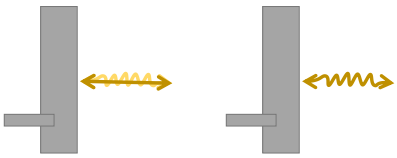

(A) extLW-0 (B) extLW-1

FIGURE B.9: External LW radiative heat transfer coefficient modelling variants

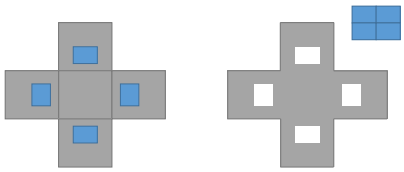

(A) EqEnv-0 (B) EqEnv-1

FIGURE B.10: Equivalent envelope modelling

$$\dot{X} = \begin{pmatrix} \begin{matrix} 0 \\ \vdots \\ 0 \end{matrix} \\ \dot{X}_{\pi+1} \\ \vdots \\ \dot{X}_{\nu} \end{pmatrix}$$

(A) Red-π

FIGURE B.11: Envelope reduction

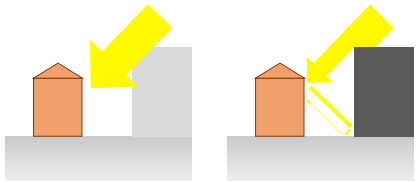

(A) Solar-0 (B) Solar-1

FIGURE B.12: Shadings and reflections modelling variants

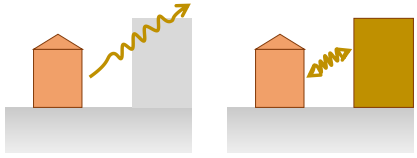

(A) LWRad-0 (B) LWRad-1

FIGURE B.13: Inter-buildings LW radiative exchanges modelling variants

Cette thèse est accessible à l'adresse : http://theses.insa-lyon.fr/publication/2018LYSEI071/these.pdf
© [L. Frayssinet], [2018], INSA Lyon, tous droits réservés

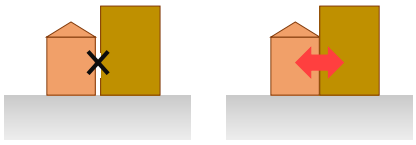

(A) Adjoin-0 (B) Adjoin-1

FIGURE B.14: Adjoining wall modelling variants

Cette thèse est accessible à l'adresse : http://theses.insa-lyon.fr/publication/2018LYSEI071/these.pdf
© [L. Frayssinet], [2018], INSA Lyon, tous droits réservés

Cette thèse est accessible à l'adresse : http://theses.insa-lyon.fr/publication/2018LYSEI071/these.pdf
© [L. Frayssinet], [2018], INSA Lyon, tous droits réservés

Appendix C

Complementary analysis representation

C.1 Boxplot of the time-series differences

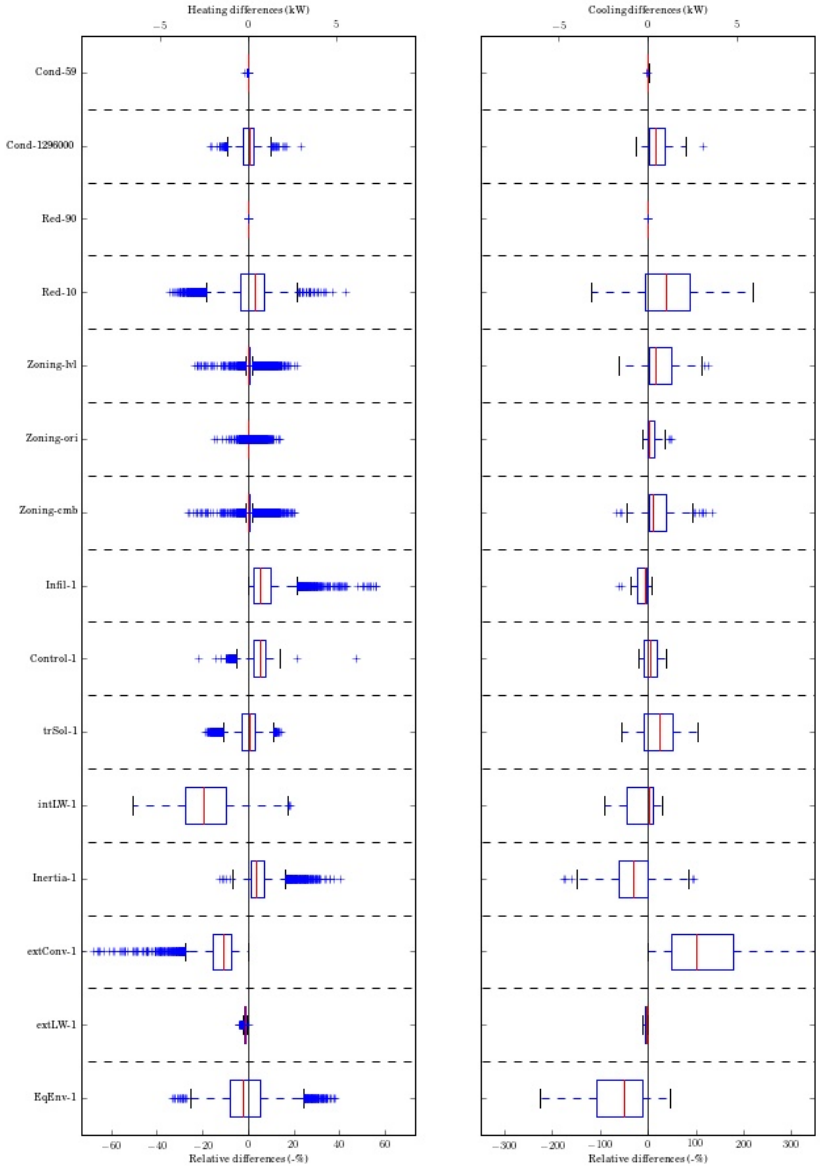

Cette thèse est accessible à l'adresse : http://theses.insa-lyon.fr/publication/2018LYSEI071/these.pdf
© [L. Frayssinet], [2018], INSA Lyon, tous droits réservés

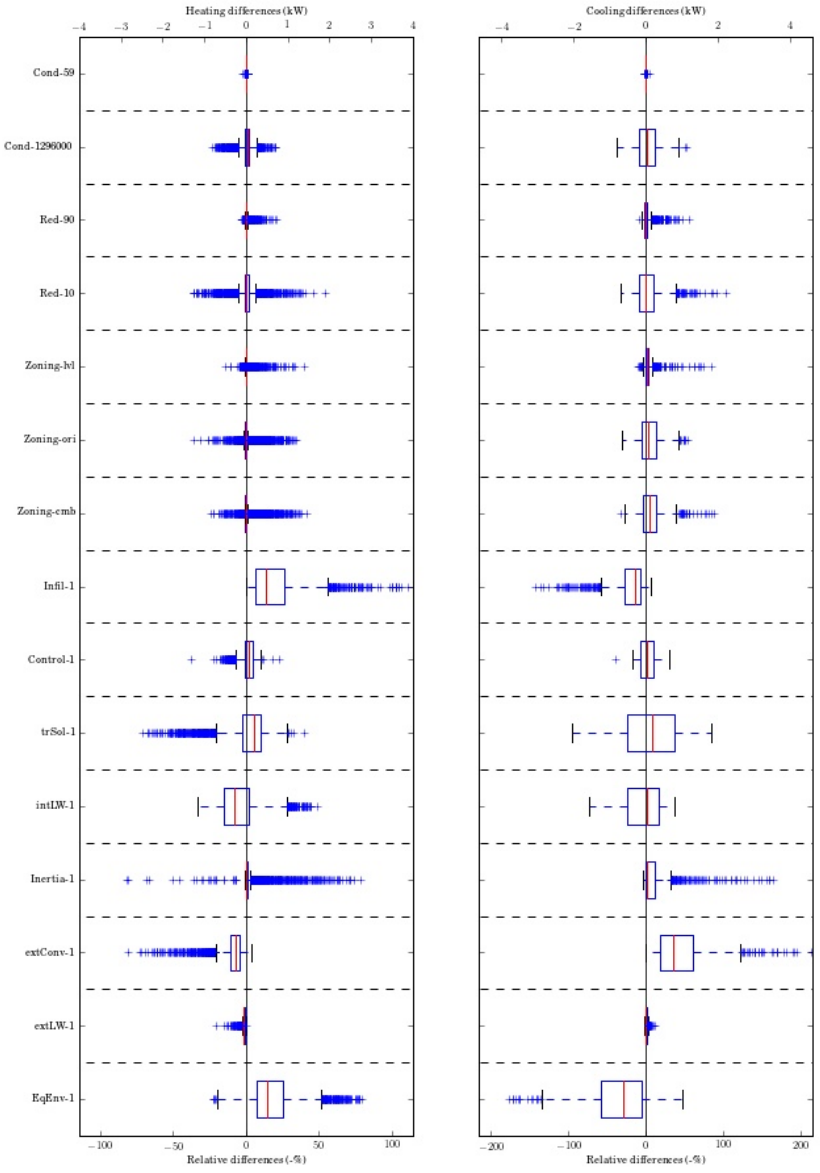

(A) *Perf*

Cette thèse est accessible à l'adresse : http://theses.insa-lyon.fr/publication/2018LYSEI071/these.pdf
© [L. Frayssinet], [2018], INSA Lyon, tous droits réservés

C.2 Correlations

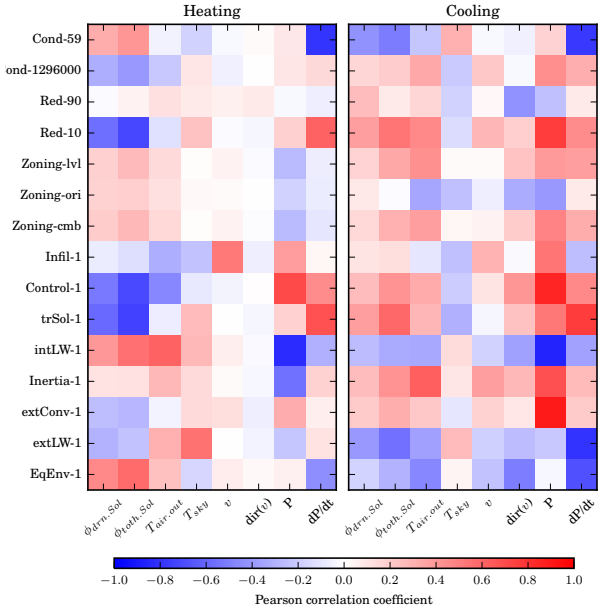

FIGURE C.3: Init

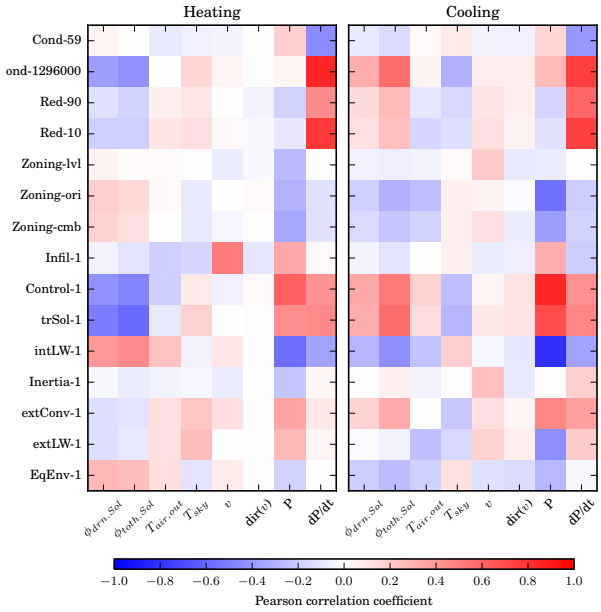

FIGURE C.4: Perf

Cette thèse est accessible à l'adresse : http://theses.insa-lyon.fr/publication/2018LYSEI071/these.pdf
© [L. Frayssinet], [2018], INSA Lyon, tous droits réservés

C.3 Other complementary representations

Cond-59

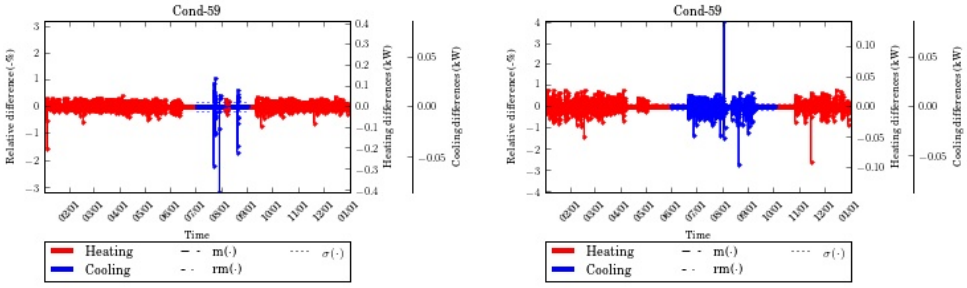

(A) *Init* (B) *Perf*

FIGURE C.5: Relative differences temporal evolution

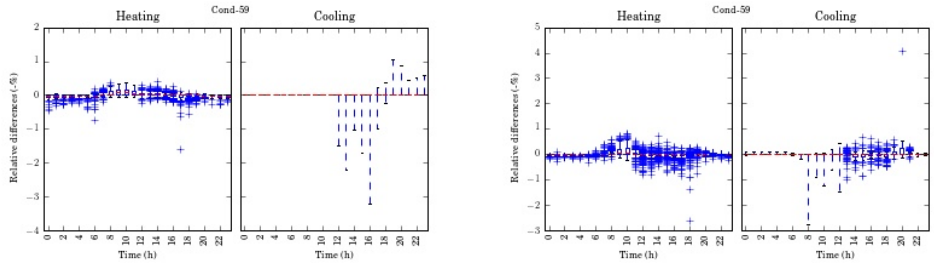

(A) *Init* (B) *Perf*

FIGURE C.6: Daily boxplot representation of the differences

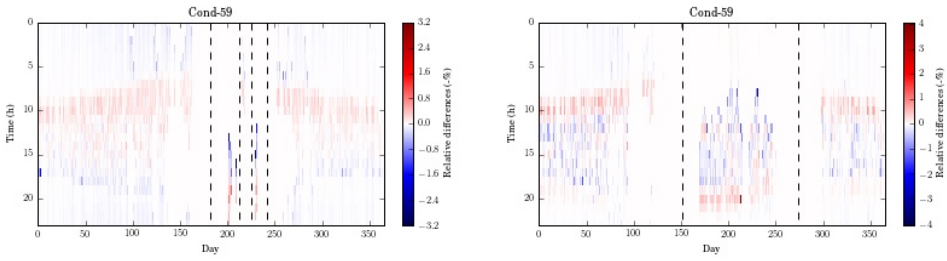

(A) *Init* (B) *Perf*

FIGURE C.7: Heatmap representation of the relative differences

Cette thèse est accessible à l'adresse : http://theses.insa-lyon.fr/publication/2018LYSEI071/these.pdf
© [L. Frayssinet], [2018], INSA Lyon, tous droits réservés

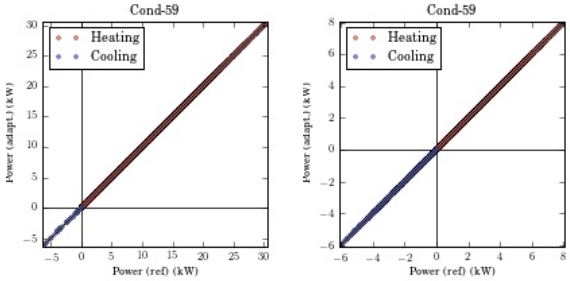

(A) *Init* (B) *Perf*

FIGURE C.8: Adapted model results versus reference results

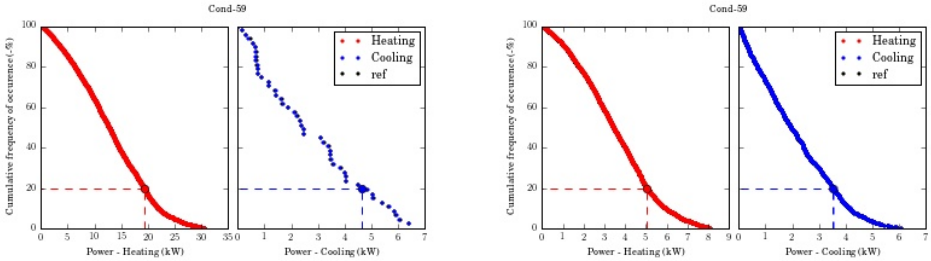

(A) *Init* (B) *Perf*

FIGURE C.9: Cumulative frequency of higher occurences curves curves

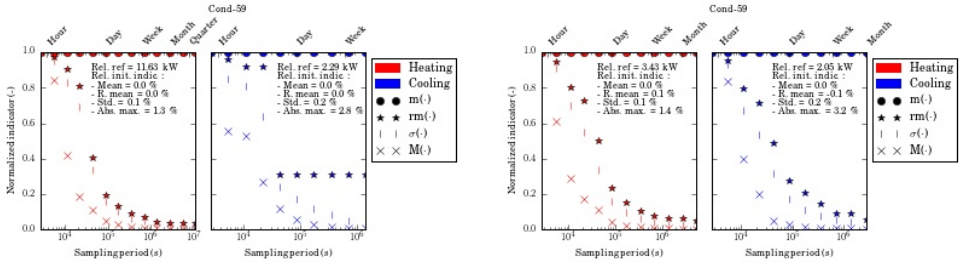

(A) *Init* (B) *Perf*

FIGURE C.10: Sampling influence on the indicators

Cond-1296000

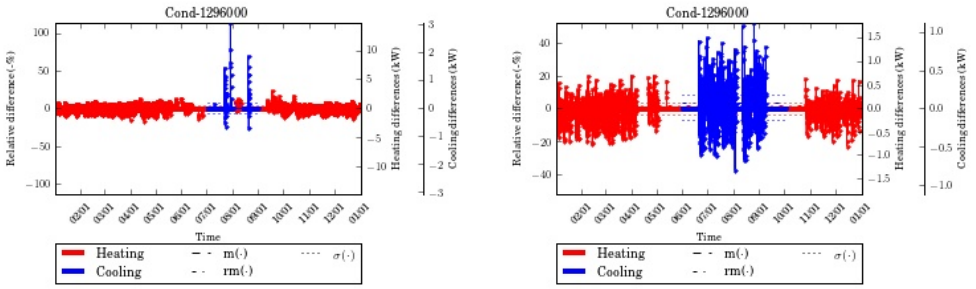

(A) *Init* (B) *Perf*

FIGURE C.11: Relative differences temporal evolution

Cette thèse est accessible à l'adresse : http://theses.insa-lyon.fr/publication/2018LYSEI071/these.pdf
© [L. Frayssinet], [2018], INSA Lyon, tous droits réservés

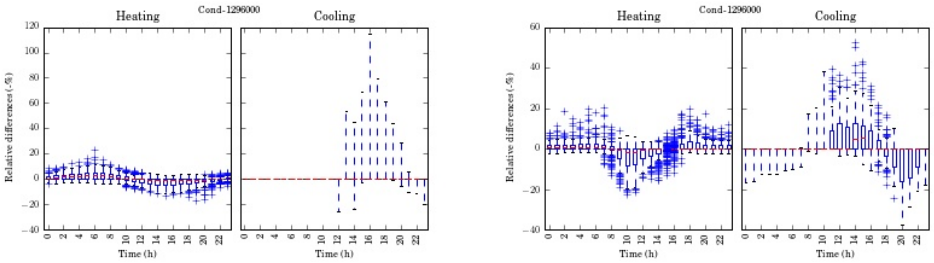

(A) *Init* (B) *Perf*

FIGURE C.12: Daily boxplot representation of the differences

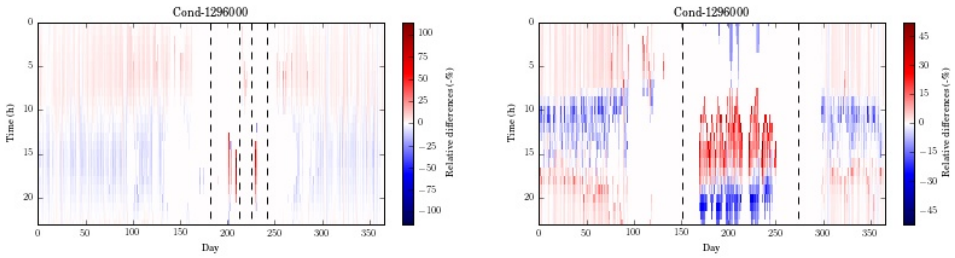

(A) *Init* (B) *Perf*

FIGURE C.13: Heatmap representation of the relative differences

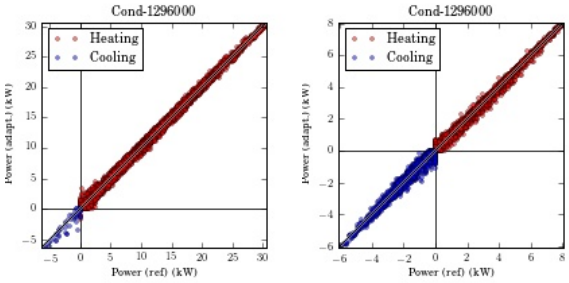

(A) *Init* (B) *Perf*

FIGURE C.14: Adapted model results versus reference results

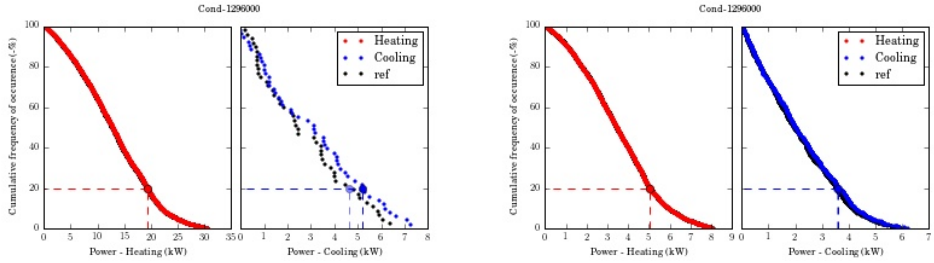

(A) *Init* (B) *Perf*

FIGURE C.15: Cumulative frequency of higher occurences curves

Cette thèse est accessible à l'adresse : http://theses.insa-lyon.fr/publication/2018LYSEI071/these.pdf
© [L. Frayssinet], [2018], INSA Lyon, tous droits réservés

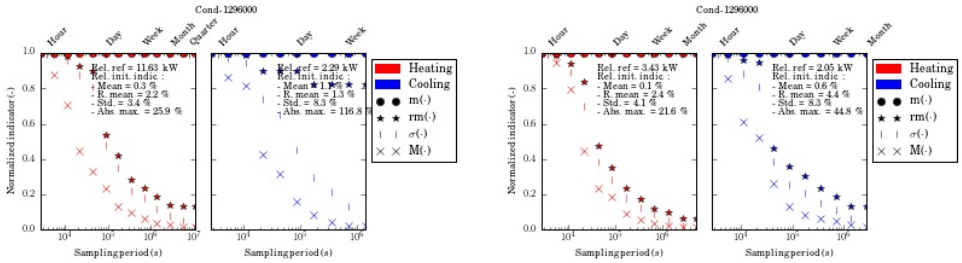

(A) *Init* (B) *Perf*

FIGURE C.16: Sampling influence on the indicators

Red-90

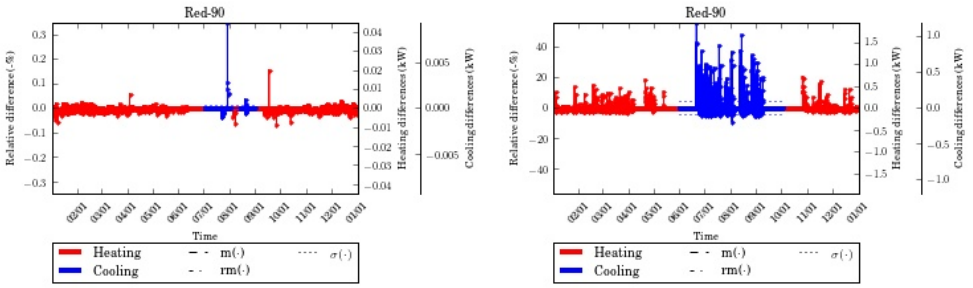

(A) *Init* (B) *Perf*

FIGURE C.17: Relative differences temporal evolution

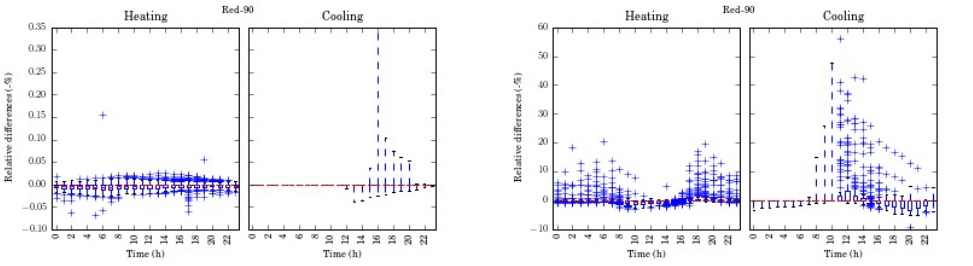

(A) *Init* (B) *Perf*

FIGURE C.18: Daily boxplot representation of the differences

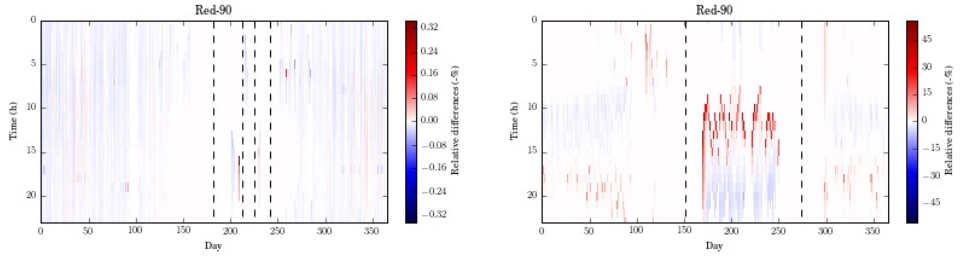

(A) *Init* (B) *Perf*

FIGURE C.19: Heatmap representation of the relative differences

Cette thèse est accessible à l'adresse : http://theses.insa-lyon.fr/publication/2018LYSEI071/these.pdf
© [L. Frayssinet], [2018], INSA Lyon, tous droits réservés

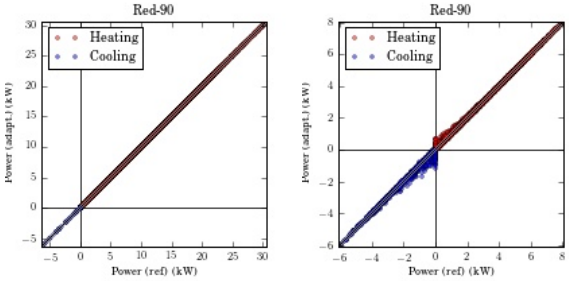

(A) *Init* (B) *Perf*

FIGURE C.20: Adapted model results versus reference results

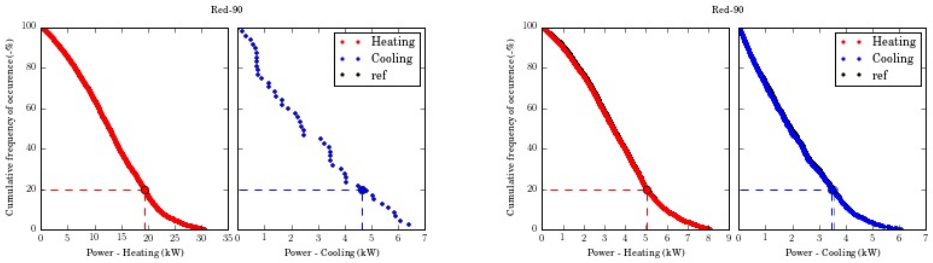

(A) *Init* (B) *Perf*

FIGURE C.21: Cumulative frequency of higher occurences curves

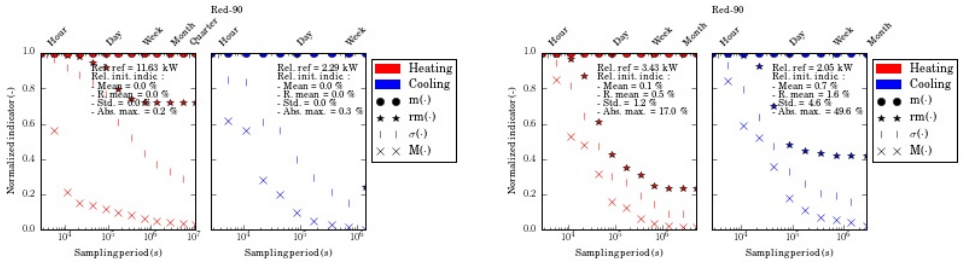

(A) *Init* (B) *Perf*

FIGURE C.22: Sampling influence on the indicators

Red-10

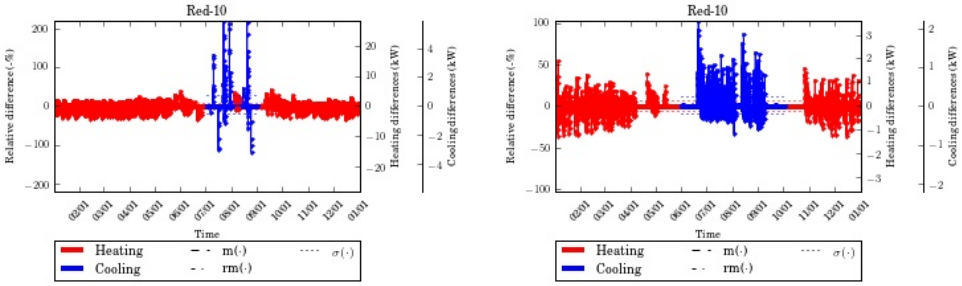

(A) *Init* (B) *Perf*

FIGURE C.23: Relative differences temporal evolution

Cette thèse est accessible à l'adresse : http://theses.insa-lyon.fr/publication/2018LYSEI071/these.pdf
© [L. Frayssinet], [2018], INSA Lyon, tous droits réservés

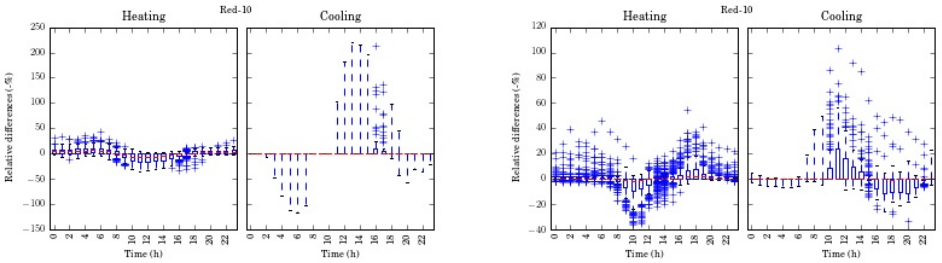

(A) *Init* (B) *Perf*

FIGURE C.24: Daily boxplot representation of the differences

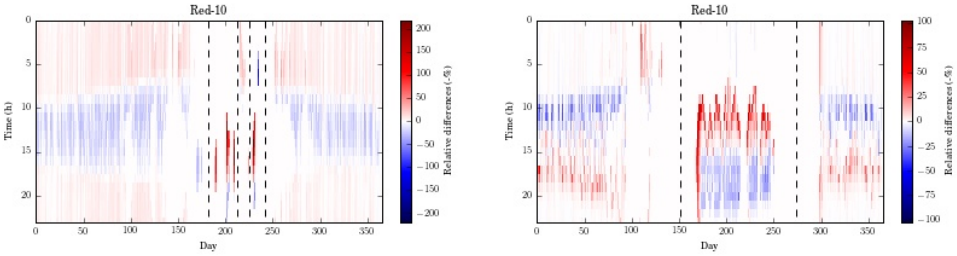

(A) *Init* (B) *Perf*

FIGURE C.25: Heatmap representation of the relative differences

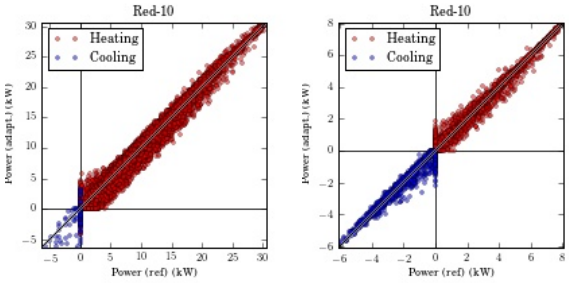

(A) *Init* (B) *Perf*

FIGURE C.26: Adapted model results versus reference results

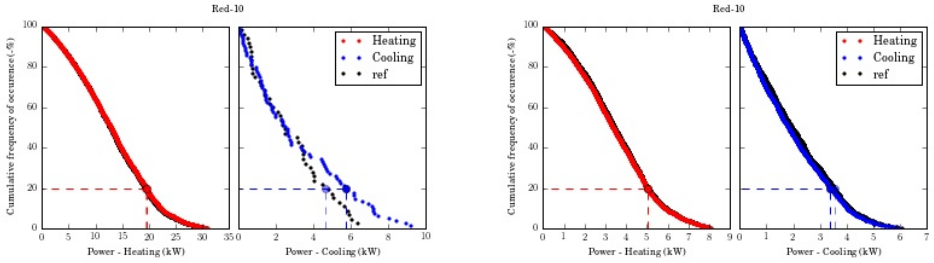

(A) *Init* (B) *Perf*

FIGURE C.27: Cumulative frequency of higher occurences curves

Cette thèse est accessible à l'adresse : http://theses.insa-lyon.fr/publication/2018LYSEI071/these.pdf
© [L. Frayssinet], [2018], INSA Lyon, tous droits réservés

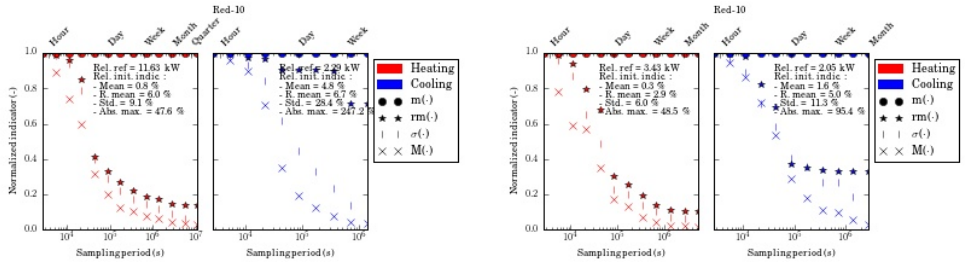

(A) *Init* (B) *Perf*

FIGURE C.28: Sampling influence on the indicators

Infil

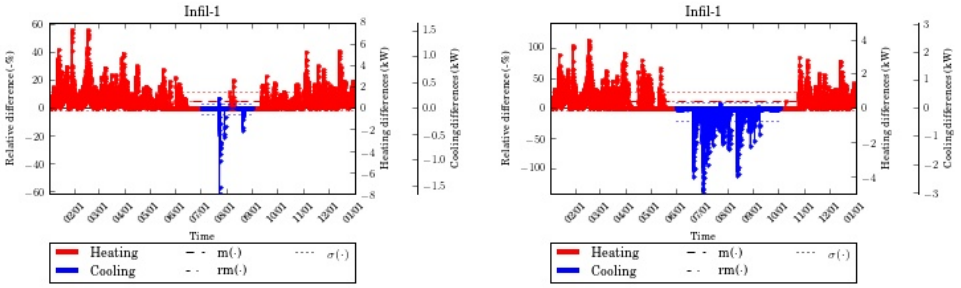

(A) *Init* (B) *Perf*

FIGURE C.29: Relative differences temporal evolution

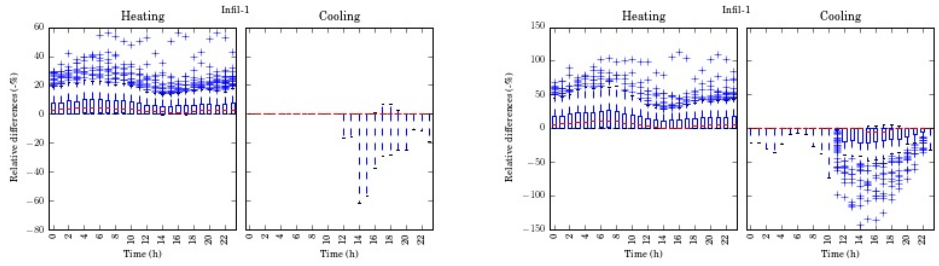

(A) *Init* (B) *Perf*

FIGURE C.30: Daily boxplot representation of the differences

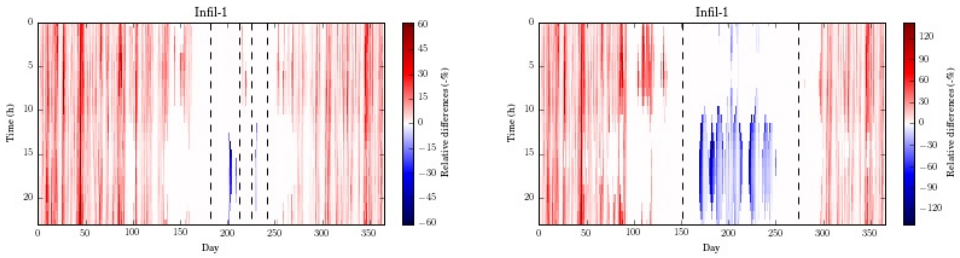

(A) *Init* (B) *Perf*

FIGURE C.31: Heatmap representation of the relative differences

Cette thèse est accessible à l'adresse : http://theses.insa-lyon.fr/publication/2018LYSEI071/these.pdf
© [L. Frayssinet], [2018], INSA Lyon, tous droits réservés

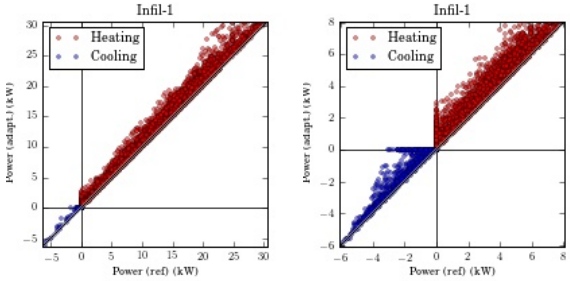

(A) *Init* (B) *Perf*

FIGURE C.32: Adapted model results versus reference results

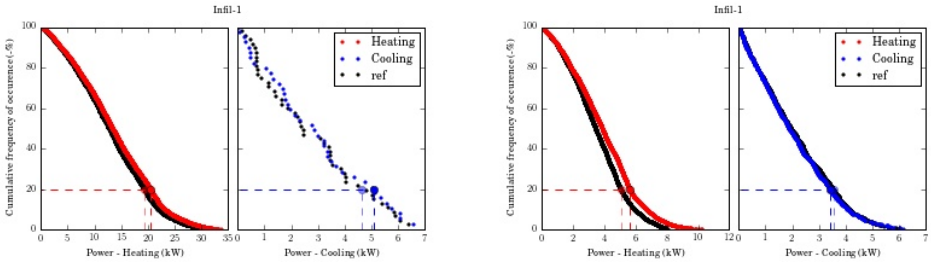

(A) *Init* (B) *Perf*

FIGURE C.33: Cumulative frequency of higher occurences curves

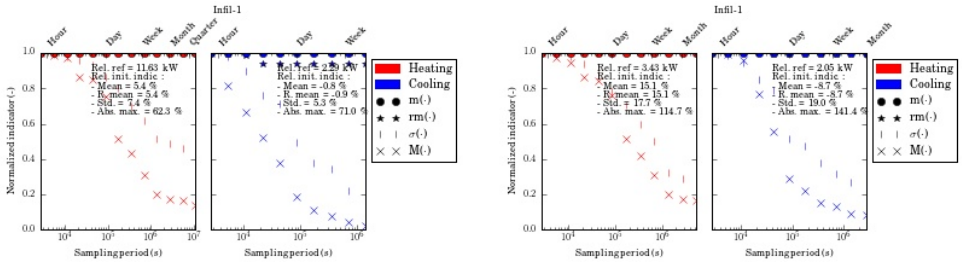

(A) *Init* (B) *Perf*

FIGURE C.34: Sampling influence on the indicators

Control

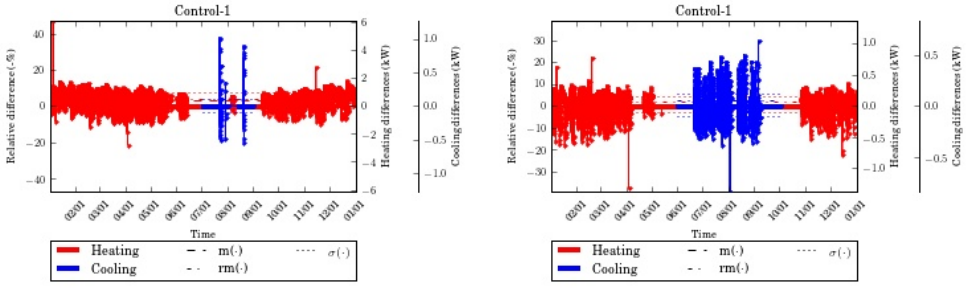

(A) *Init* (B) *Perf*

FIGURE C.35: Relative differences temporal evolution

Cette thèse est accessible à l'adresse : http://theses.insa-lyon.fr/publication/2018LYSEI071/these.pdf
© [L. Frayssinet], [2018], INSA Lyon, tous droits réservés

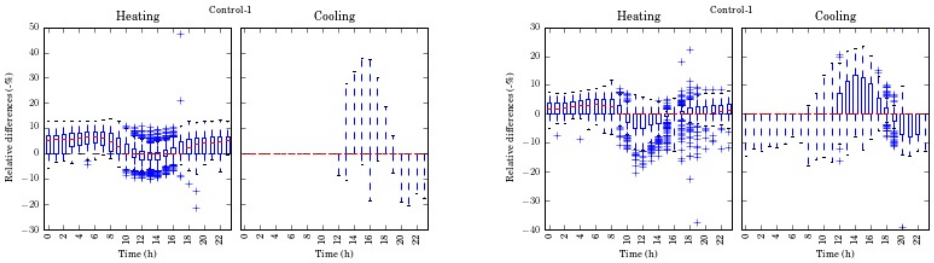

(A) *Init* (B) *Perf*

FIGURE C.36: Daily boxplot representation of the differences

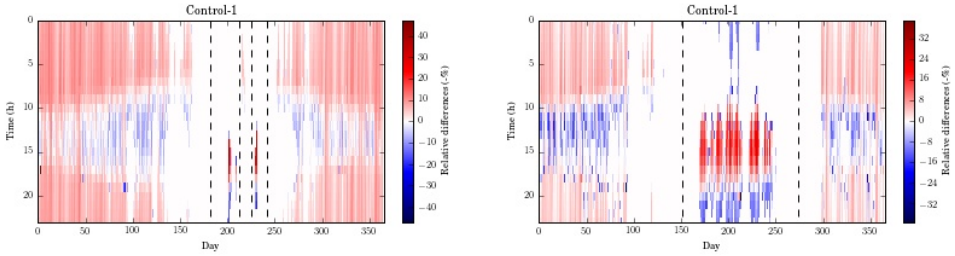

(A) *Init* (B) *Perf*

FIGURE C.37: Heatmap representation of the relative differences

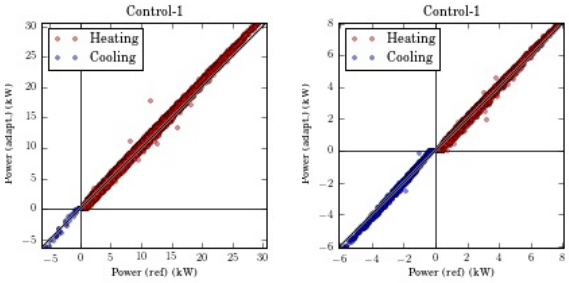

(A) *Init* (B) *Perf*

FIGURE C.38: Adapted model results versus reference results

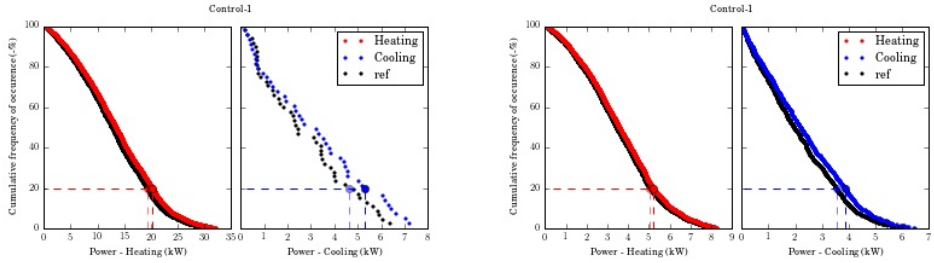

(A) *Init* (B) *Perf*

FIGURE C.39: Cumulative frequency of higher occurences curves

Cette thèse est accessible à l'adresse : http://theses.insa-lyon.fr/publication/2018LYSEI071/these.pdf
© [L. Frayssinet], [2018], INSA Lyon, tous droits réservés

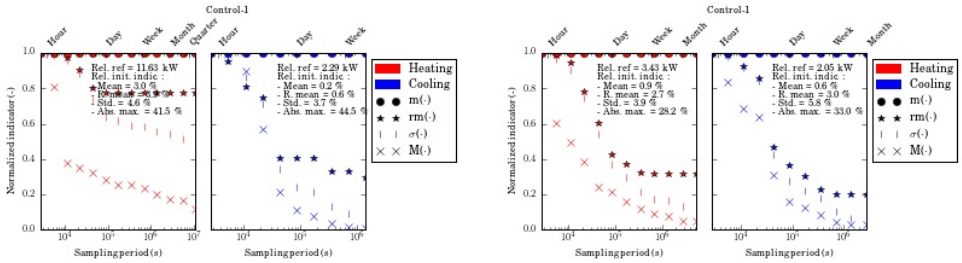

(A) *Init* (B) *Perf*

FIGURE C.40: Sampling influence on the indicators

trSol

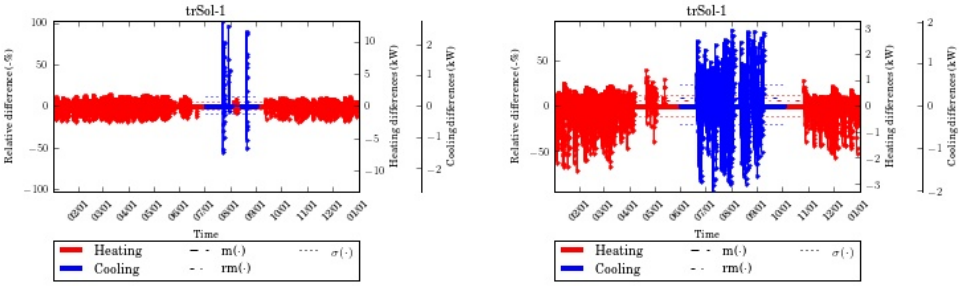

(A) *Init* (B) *Perf*

FIGURE C.41: Relative differences temporal evolution

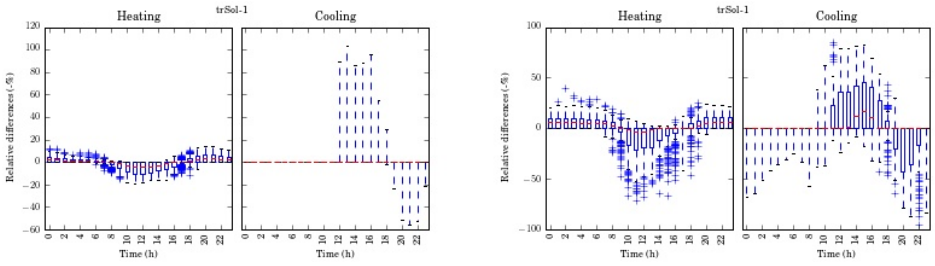

(A) *Init* (B) *Perf*

FIGURE C.42: Daily boxplot representation of the differences

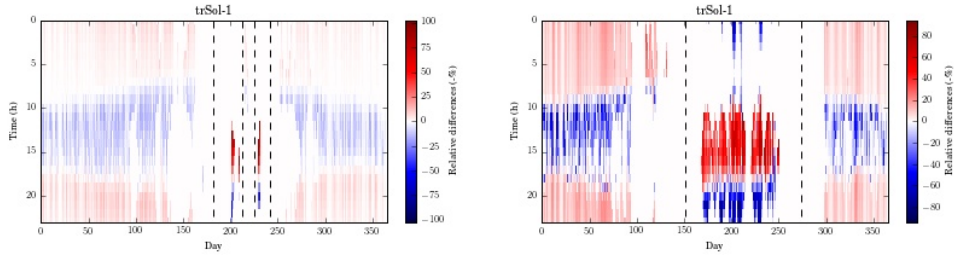

(A) *Init* (B) *Perf*

FIGURE C.43: Heatmap representation of the relative differences

Cette thèse est accessible à l'adresse : http://theses.insa-lyon.fr/publication/2018LYSEI071/these.pdf
© [L. Frayssinet], [2018], INSA Lyon, tous droits réservés

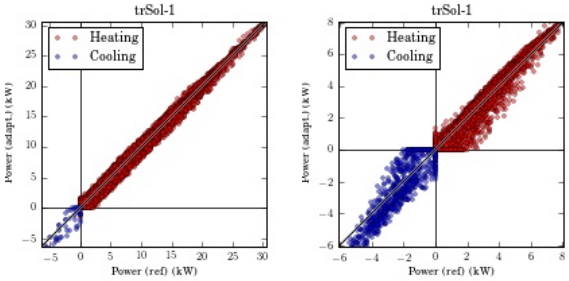

(A) *Init* (B) *Perf*

FIGURE C.44: Adapted model results versus reference results

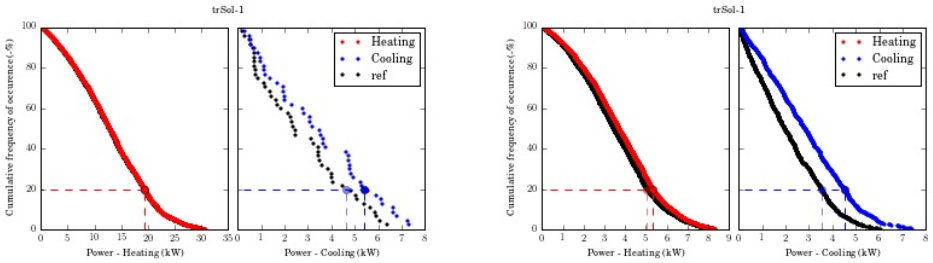

(A) *Init* (B) *Perf*

FIGURE C.45: Cumulative frequency of higher occurences curves

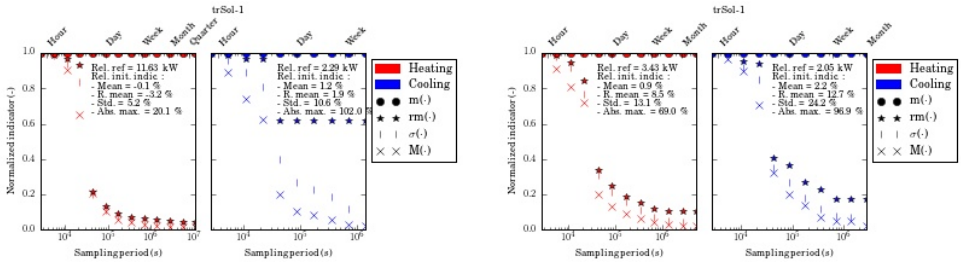

(A) *Init* (B) *Perf*

FIGURE C.46: Sampling influence on the indicators

intLW

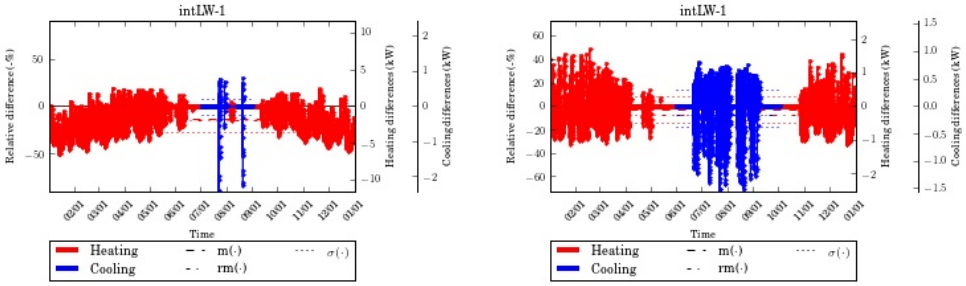

(A) *Init* (B) *Perf*

FIGURE C.47: Relative differences temporal evolution

Cette thèse est accessible à l'adresse : http://theses.insa-lyon.fr/publication/2018LYSEI071/these.pdf
© [L. Frayssinet], [2018], INSA Lyon, tous droits réservés

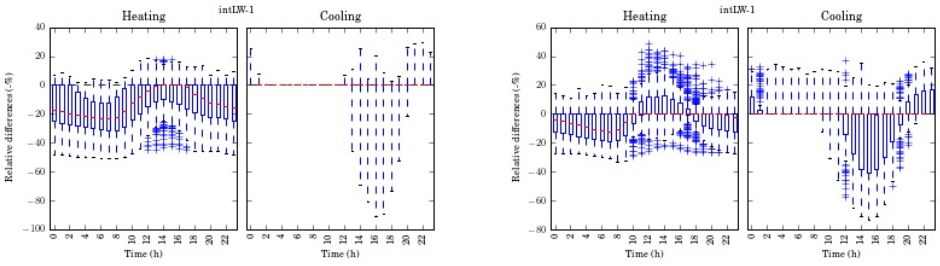

(A) *Init* (B) *Perf*

FIGURE C.48: Daily boxplot representation of the differences

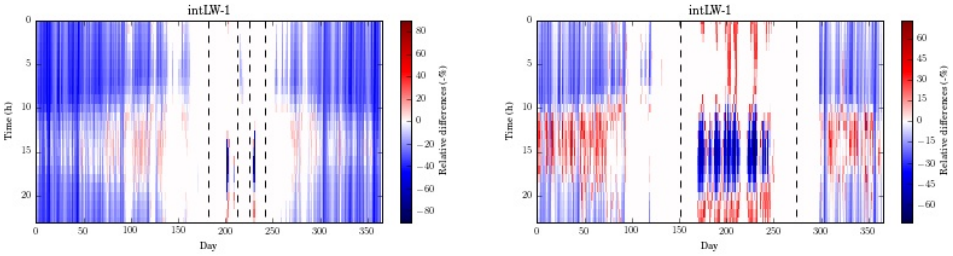

(A) *Init* (B) *Perf*

FIGURE C.49: Heatmap representation of the relative differences

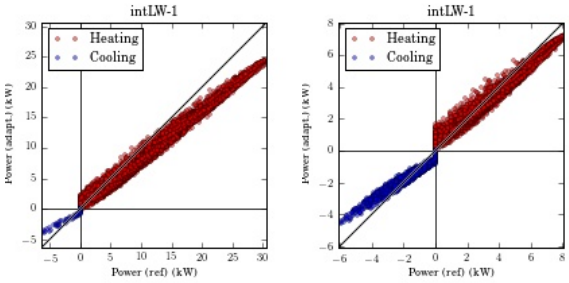

(A) *Init* (B) *Perf*

FIGURE C.50: Adapted model results versus reference results

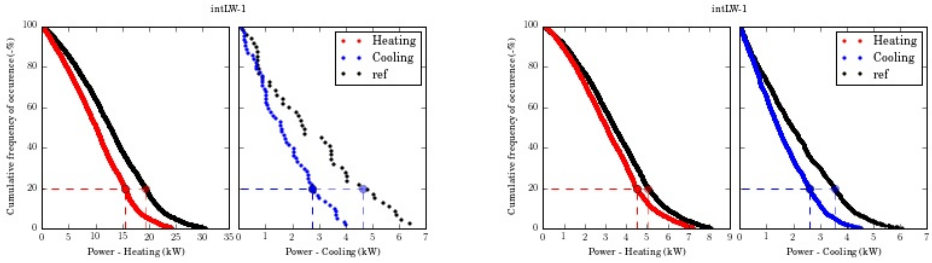

(A) *Init* (B) *Perf*

FIGURE C.51: Cumulative frequency of higher occurences curves

Cette thèse est accessible à l'adresse : http://theses.insa-lyon.fr/publication/2018LYSEI071/these.pdf
© [L. Frayssinet], [2018], INSA Lyon, tous droits réservés

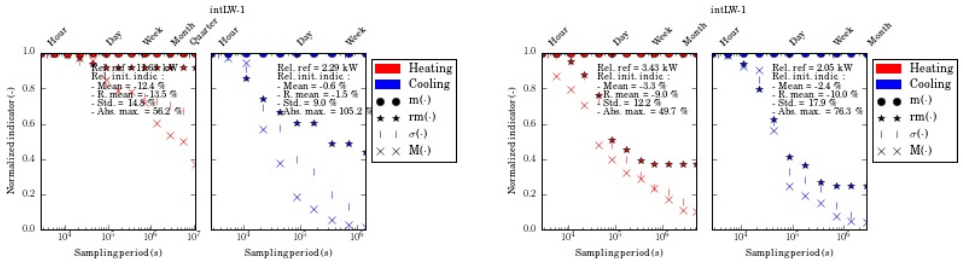

(A) *Init* (B) *Perf*

FIGURE C.52: Sampling influence on the indicators

Inertia

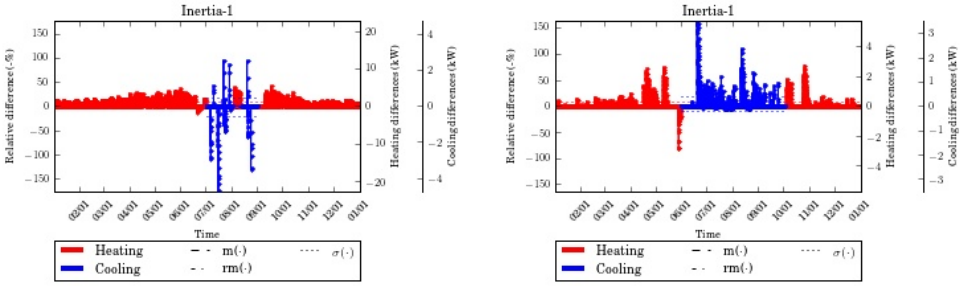

(A) *Init* (B) *Perf*

FIGURE C.53: Relative differences temporal evolution

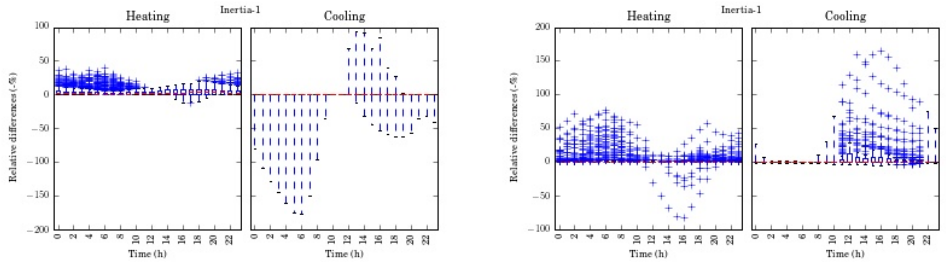

(A) *Init* (B) *Perf*

FIGURE C.54: Daily boxplot representation of the differences

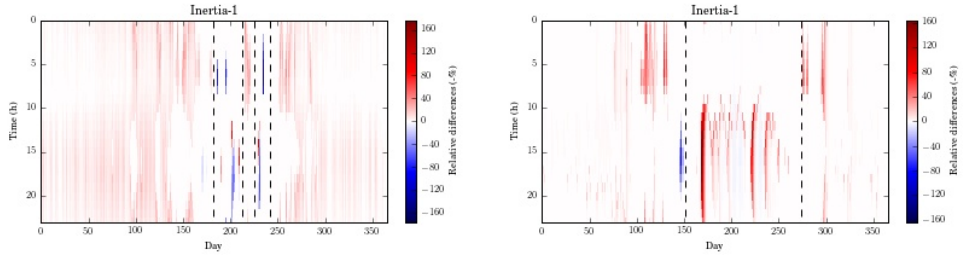

(A) *Init* (B) *Perf*

FIGURE C.55: Heatmap representation of the relative differences

Cette thèse est accessible à l'adresse : http://theses.insa-lyon.fr/publication/2018LYSEI071/these.pdf
© [L. Frayssinet], [2018], INSA Lyon, tous droits réservés

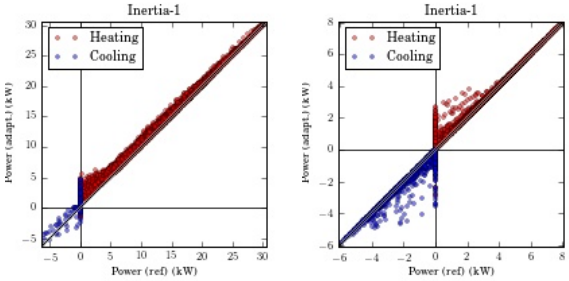

(A) *Init* (B) *Perf*

FIGURE C.56: Adapted model results versus reference results

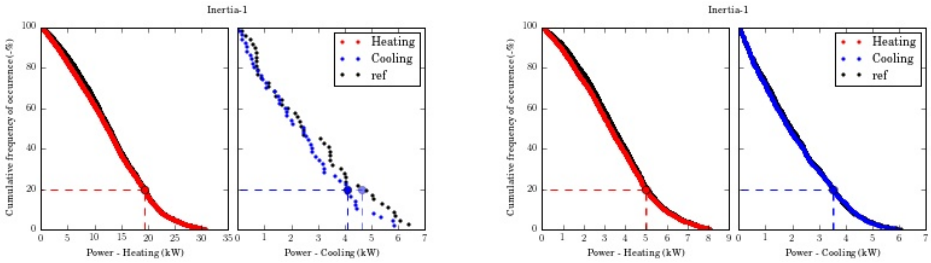

(A) *Init* (B) *Perf*

FIGURE C.57: Cumulative frequency of higher occurences curves

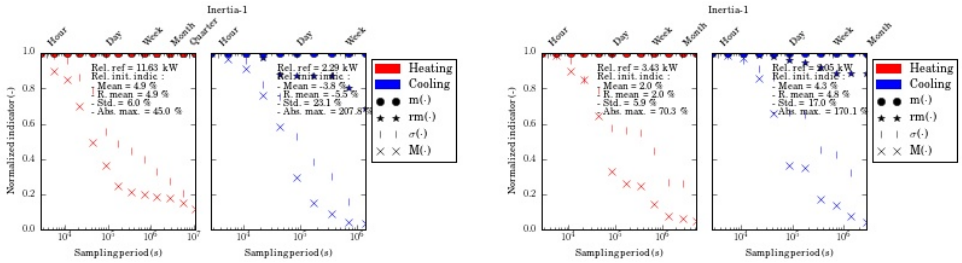

(A) *Init* (B) *Perf*

FIGURE C.58: Cumulative frequency of higher occurences curves

extConv

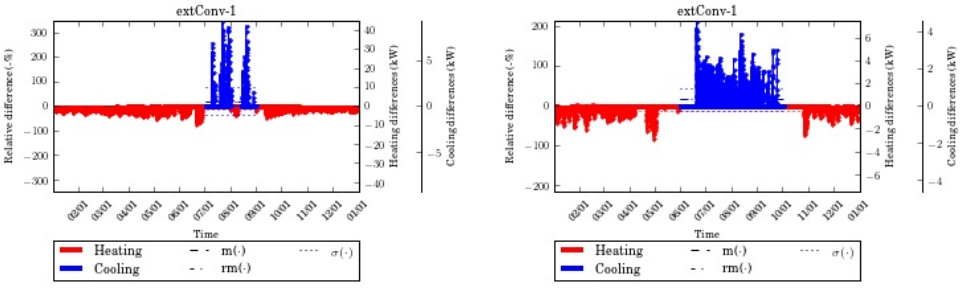

(A) *Init* (B) *Perf*

FIGURE C.59: Relative differences temporal evolution

Cette thèse est accessible à l'adresse : http://theses.insa-lyon.fr/publication/2018LYSEI071/these.pdf
© [L. Frayssinet], [2018], INSA Lyon, tous droits réservés

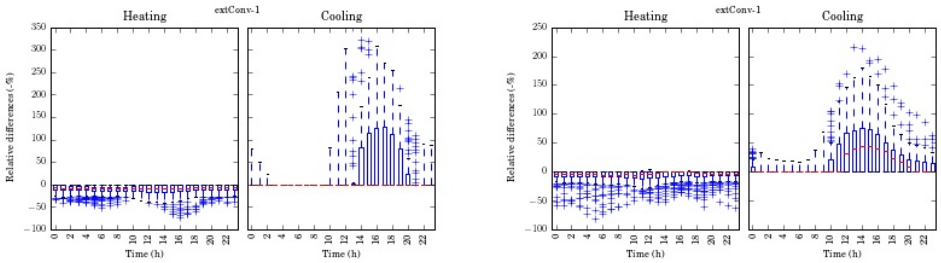

(A) *Init* (B) *Perf*

FIGURE C.60: Daily boxplot representation of the differences

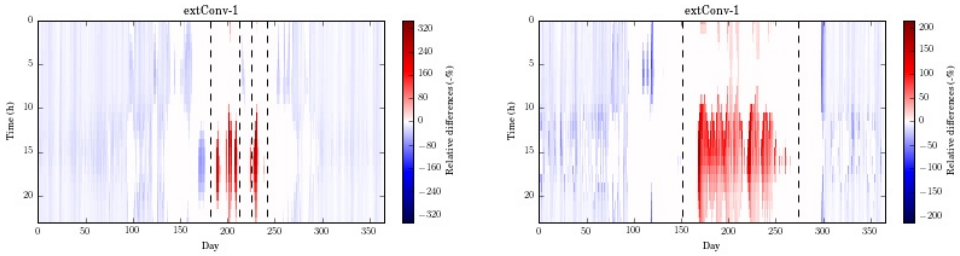

(A) *Init* (B) *Perf*

FIGURE C.61: Heatmap representation of the relative differences

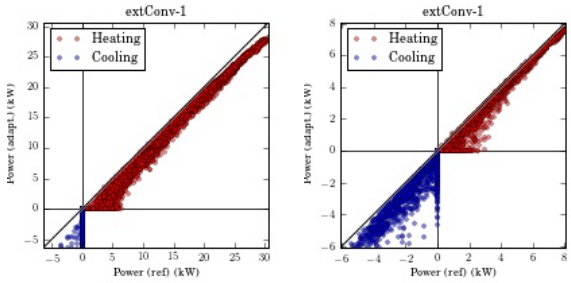

(A) *Init* (B) *Perf*

FIGURE C.62: Adapted model results versus reference results

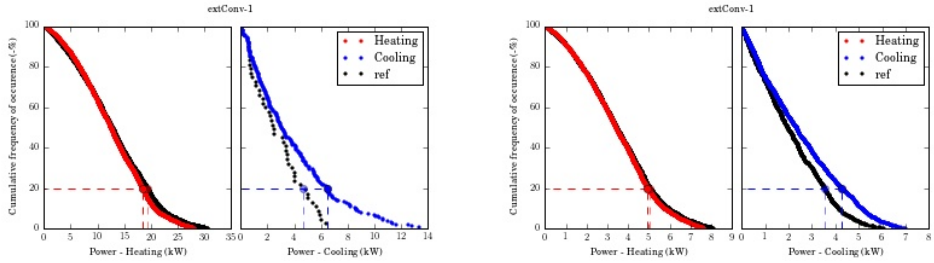

(A) *Init* (B) *Perf*

FIGURE C.63: Cumulative frequency of higher occurences curves

Cette thèse est accessible à l'adresse : http://theses.insa-lyon.fr/publication/2018LYSEI071/these.pdf
© [L. Frayssinet], [2018], INSA Lyon, tous droits réservés

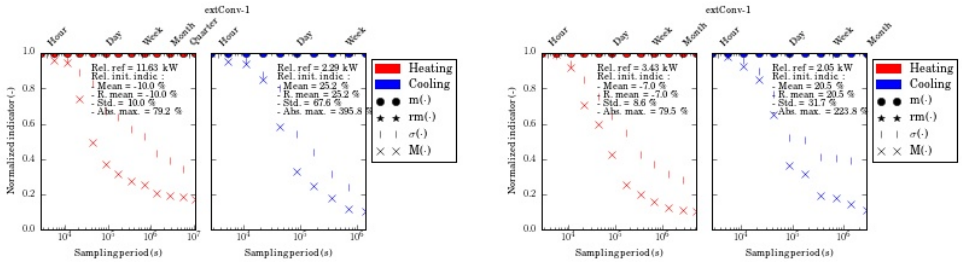

(A) *Init* (B) *Perf*

FIGURE C.64: Sampling influence on the indicators

extLW

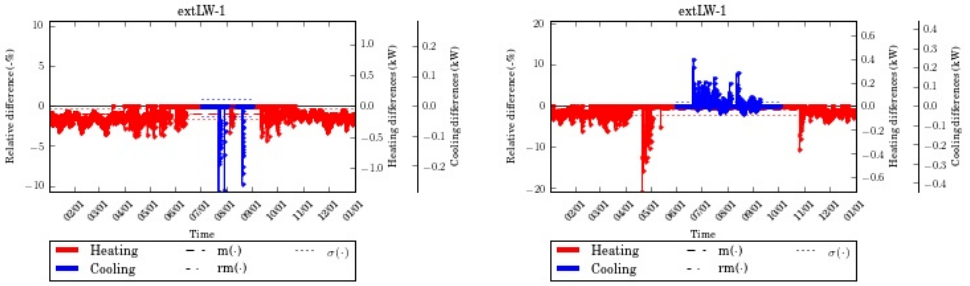

(A) *Init* (B) *Perf*

FIGURE C.65: Relative differences temporal evolution

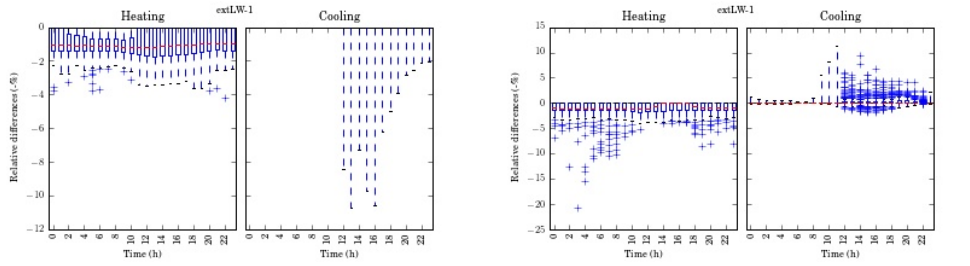

(A) *Init* (B) *Perf*

FIGURE C.66: Daily boxplot representation of the differences

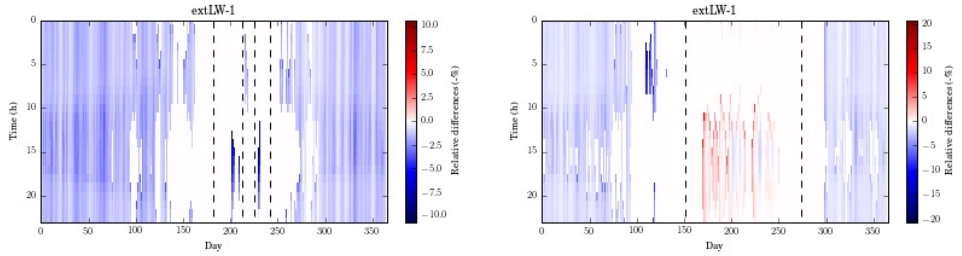

(A) *Init* (B) *Perf*

FIGURE C.67: Heatmap representation of the relative differences

Cette thèse est accessible à l'adresse : http://theses.insa-lyon.fr/publication/2018LYSEI071/these.pdf
© [L. Frayssinet], [2018], INSA Lyon, tous droits réservés

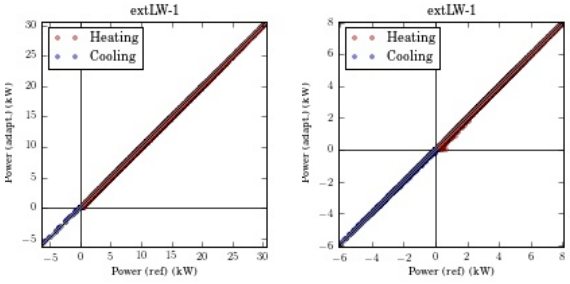

(A) *Init* (B) *Perf*

FIGURE C.68: Adapted model results versus reference results

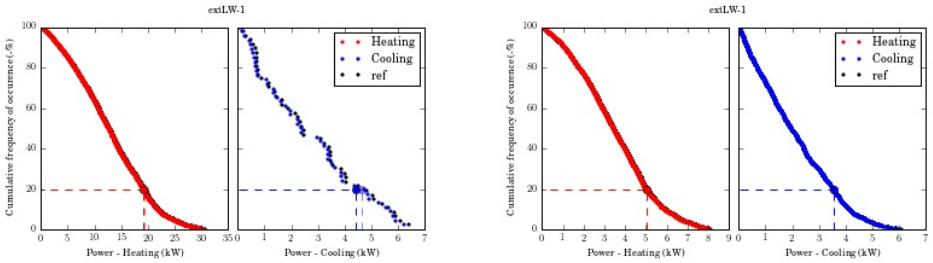

(A) *Init* (B) *Perf*

FIGURE C.69: Cumulative frequency of higher occurences curves

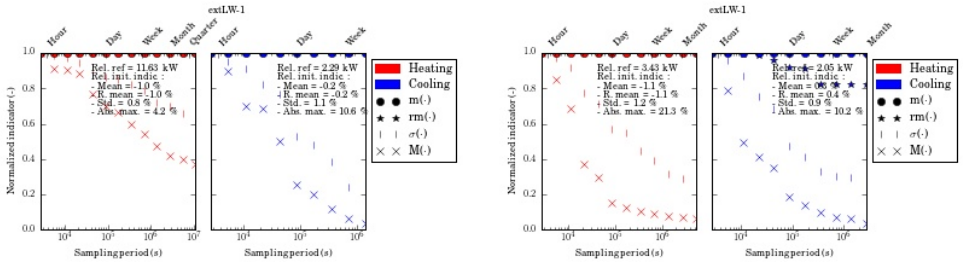

(A) *Init* (B) *Perf*

FIGURE C.70: Sampling influence on the indicators

EqEnv

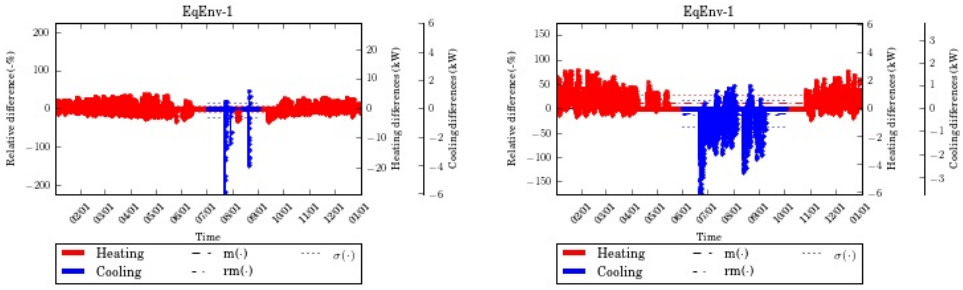

(A) *Init* (B) *Perf*

FIGURE C.71: Relative differences temporal evolution

Cette thèse est accessible à l'adresse : http://theses.insa-lyon.fr/publication/2018LYSEI071/these.pdf
© [L. Frayssinet], [2018], INSA Lyon, tous droits réservés

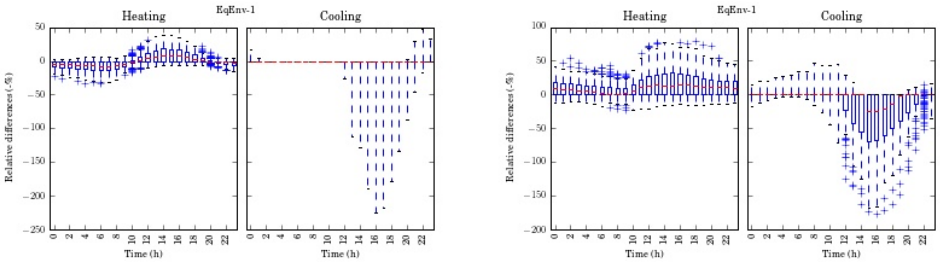

(A) *Init* (B) *Perf*

FIGURE C.72: Daily boxplot representation of the differences

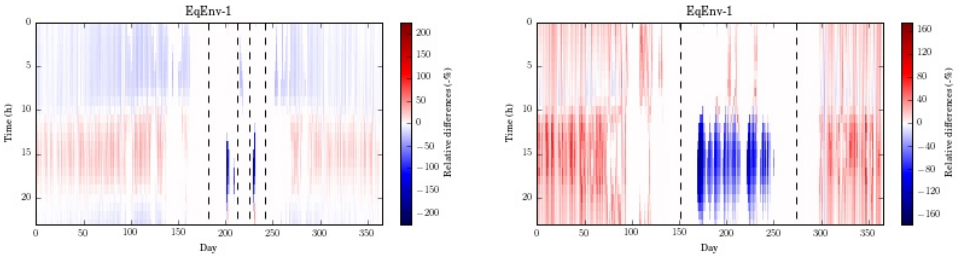

(A) *Init* (B) *Perf*

FIGURE C.73: Heatmap representation of the relative differences

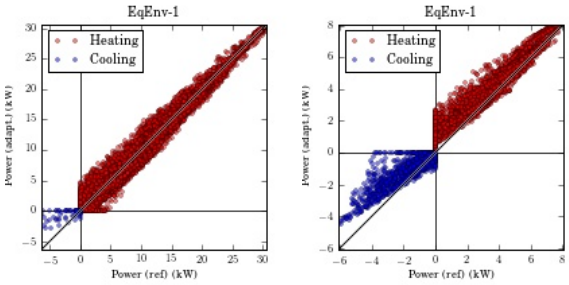

(A) *Init* (B) *Perf*

FIGURE C.74: Adapted model results versus reference results

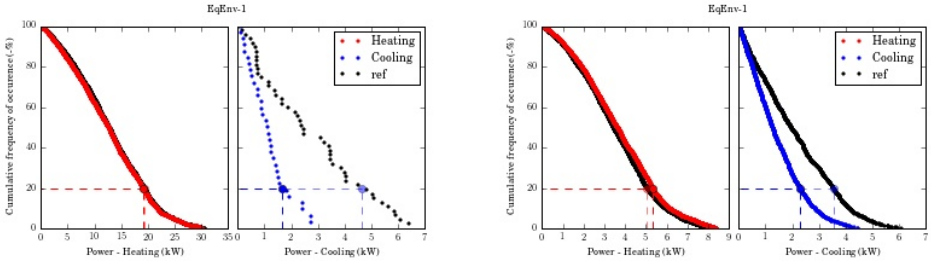

(A) *Init* (B) *Perf*

FIGURE C.75: Cumulative frequency of higher occurences curves

Cette thèse est accessible à l'adresse : http://theses.insa-lyon.fr/publication/2018LYSEI071/these.pdf
© [L. Frayssinet], [2018], INSA Lyon, tous droits réservés

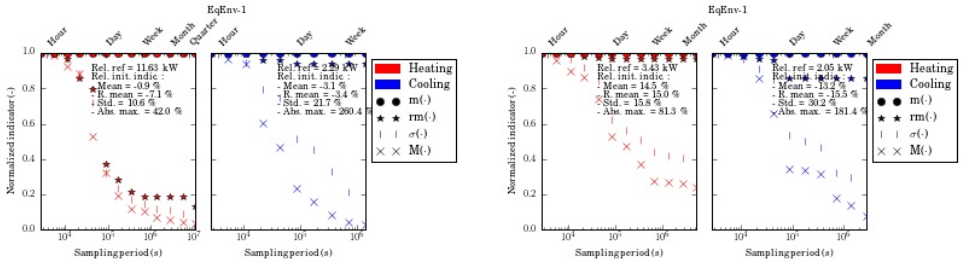

(A) *Init* (B) *Perf*

FIGURE C.76: Sampling influence on the indicators

Zoning-lvl

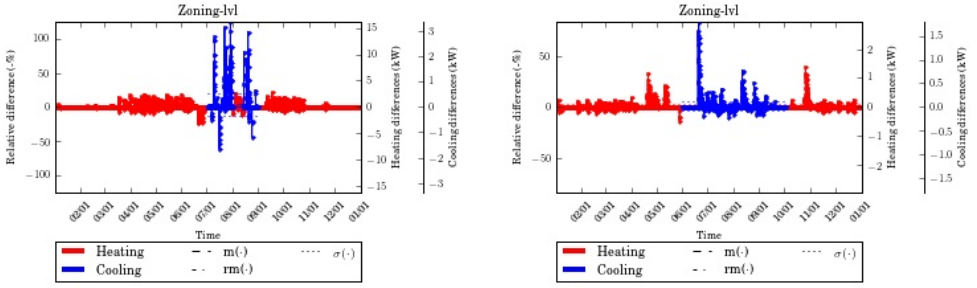

(A) *Init* (B) *Perf*

FIGURE C.77: Relative differences temporal evolution

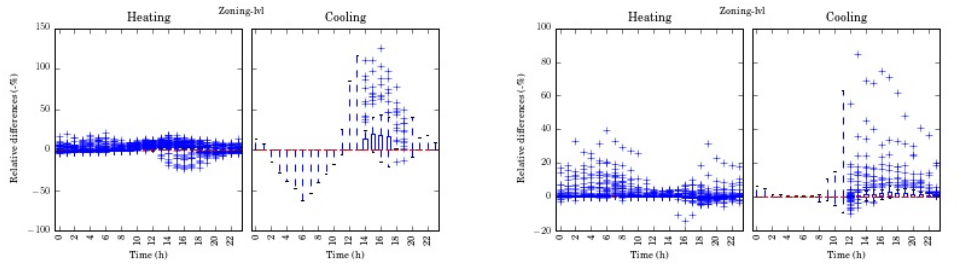

(A) *Init* (B) *Perf*

FIGURE C.78: Daily boxplot representation of the differences

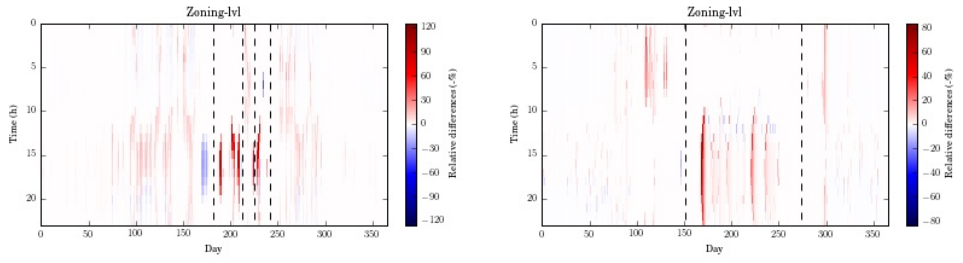

(A) *Init* (B) *Perf*

FIGURE C.79: Heatmap representation of the relative differences

Cette thèse est accessible à l'adresse : http://theses.insa-lyon.fr/publication/2018LYSEI071/these.pdf
© [L. Frayssinet], [2018], INSA Lyon, tous droits réservés

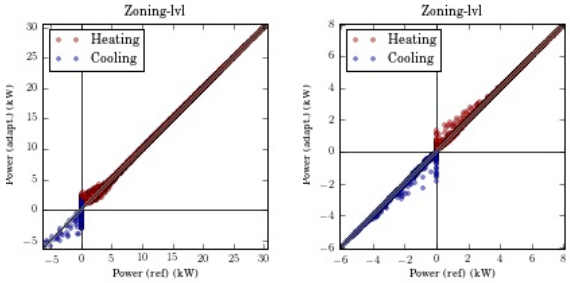

(A) *Init* (B) *Perf*

FIGURE C.80: Adapted model results versus reference results

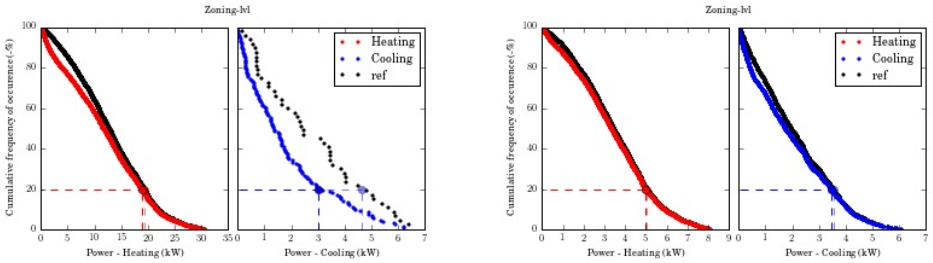

(A) *Init* (B) *Perf*

FIGURE C.81: Cumulative frequency of higher occurences curves

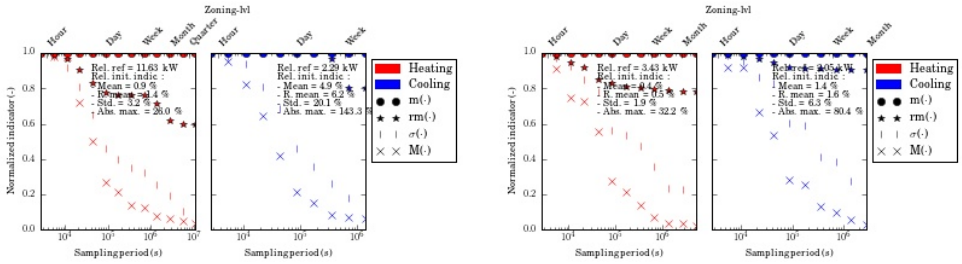

(A) *Init* (B) *Perf*

FIGURE C.82: Sampling influence on the indicators

Zoning-ori

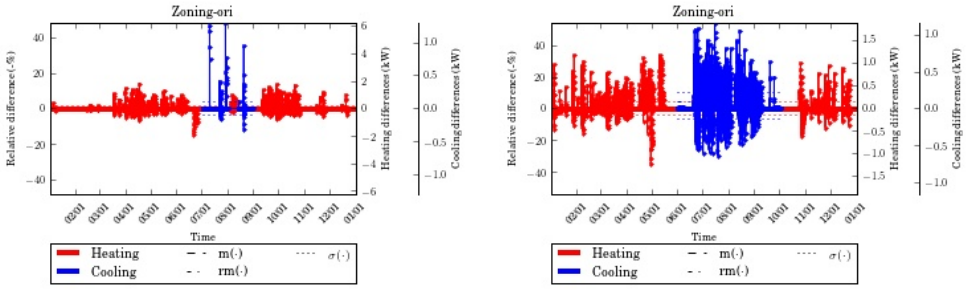

(A) *Init* (B) *Perf*

FIGURE C.83: Relative differences temporal evolution

Cette thèse est accessible à l'adresse : http://theses.insa-lyon.fr/publication/2018LYSEI071/these.pdf
© [L. Frayssinet], [2018], INSA Lyon, tous droits réservés

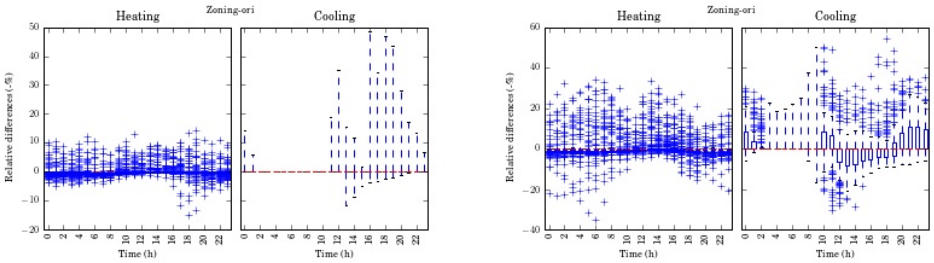

(A) *Init* (B) *Perf*

FIGURE C.84: Daily boxplot representation of the differences

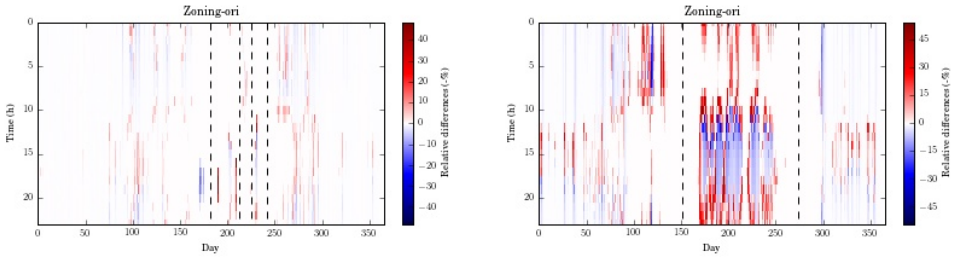

(A) *Init* (B) *Perf*

FIGURE C.85: Heatmap representation of the relative differences

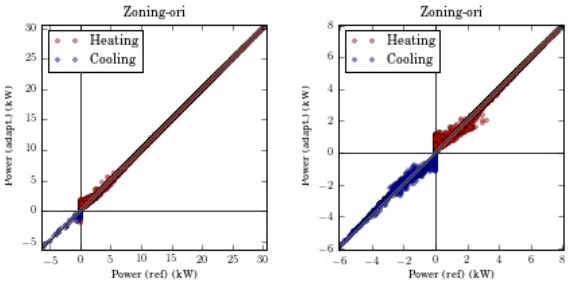

(A) *Init* (B) *Perf*

FIGURE C.86: Adapted model results versus reference results

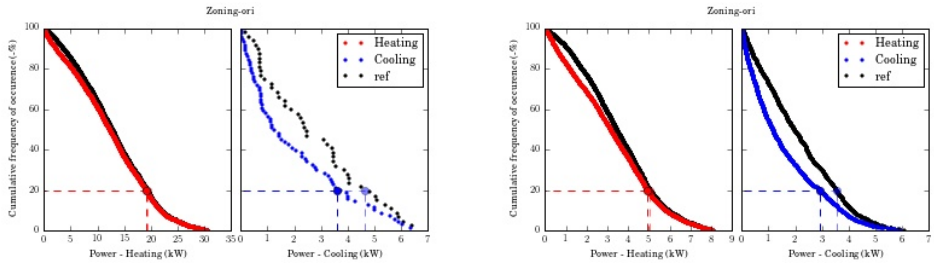

(A) *Init* (B) *Perf*

FIGURE C.87: Cumulative frequency of higher occurences curves

Cette thèse est accessible à l'adresse : http://theses.insa-lyon.fr/publication/2018LYSEI071/these.pdf
© [L. Frayssinet], [2018], INSA Lyon, tous droits réservés

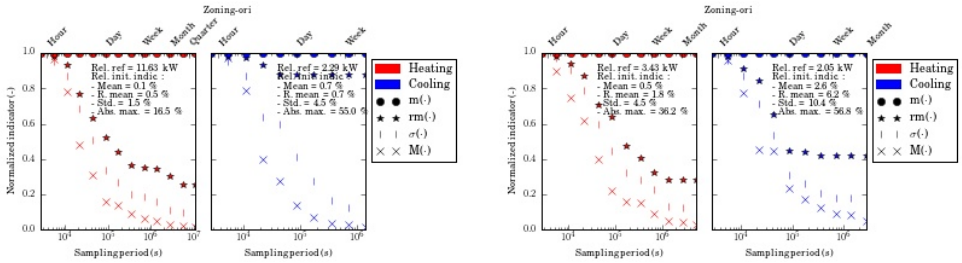

(A) *Init* (B) *Perf*

FIGURE C.88: Sampling influence on the indicators

Zoning-cmb

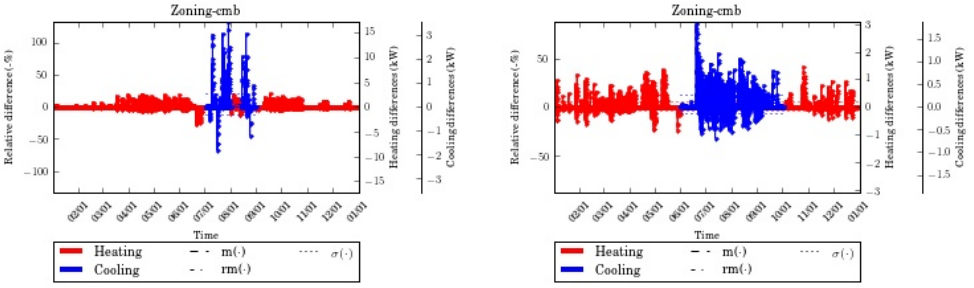

(A) *Init* (B) *Perf*

FIGURE C.89: Relative differences temporal evolution

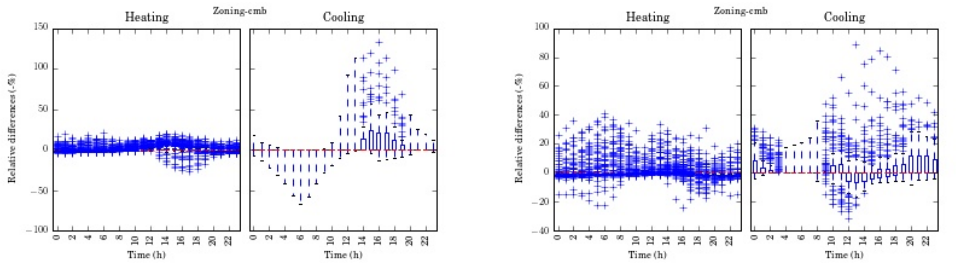

(A) *Init* (B) *Perf*

FIGURE C.90: Daily boxplot representation of the differences

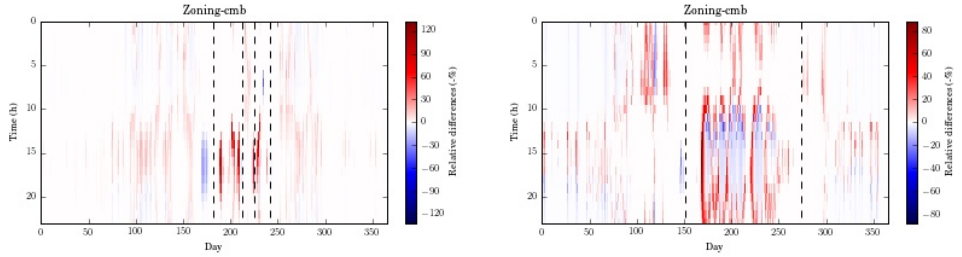

(A) *Init* (B) *Perf*

FIGURE C.91: Heatmap representation of the relative differences

Cette thèse est accessible à l'adresse : http://theses.insa-lyon.fr/publication/2018LYSEI071/these.pdf
© [L. Frayssinet], [2018], INSA Lyon, tous droits réservés

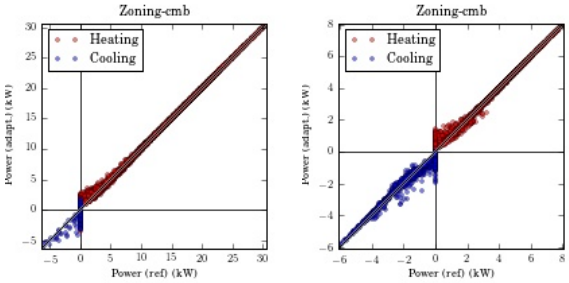

(A) *Init* (B) *Perf*

FIGURE C.92: Adapted model results versus reference results

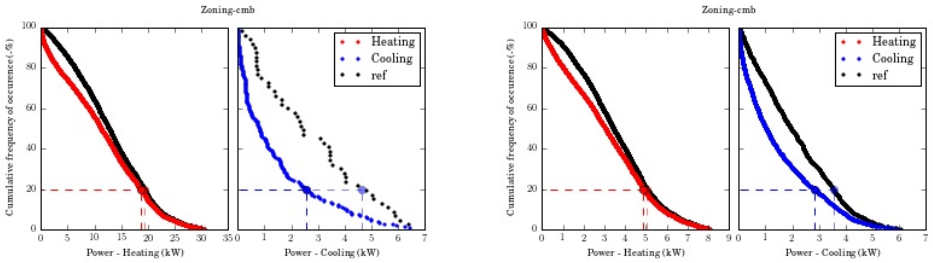

(A) *Init* (B) *Perf*

FIGURE C.93: Cumulative frequency of higher occurences curves

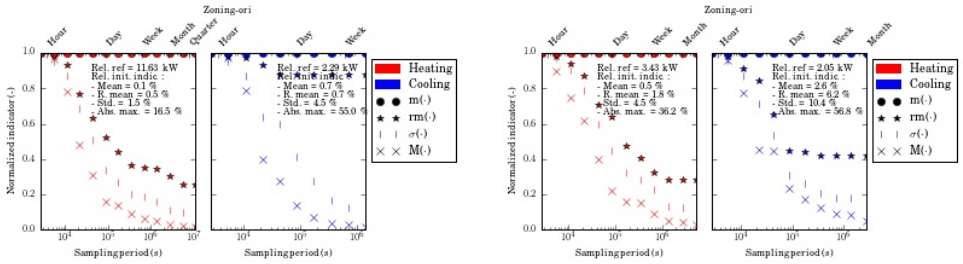

(A) *Init* (B) *Perf*

FIGURE C.94: Sampling influence on the indicators

Cette thèse est accessible à l'adresse : http://theses.insa-lyon.fr/publication/2018LYSEI071/these.pdf
© [L. Frayssinet], [2018], INSA Lyon, tous droits réservés

Solar-0

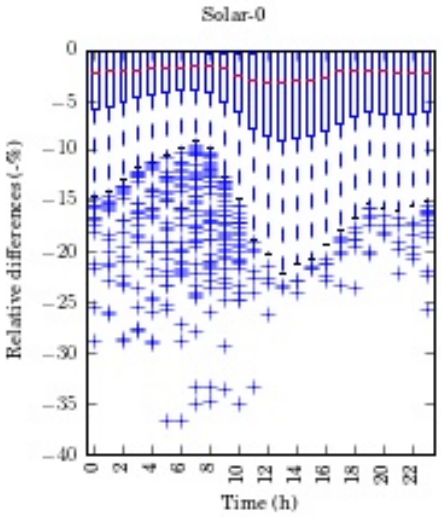

FIGURE C.95: Daily boxplot representation of the differences

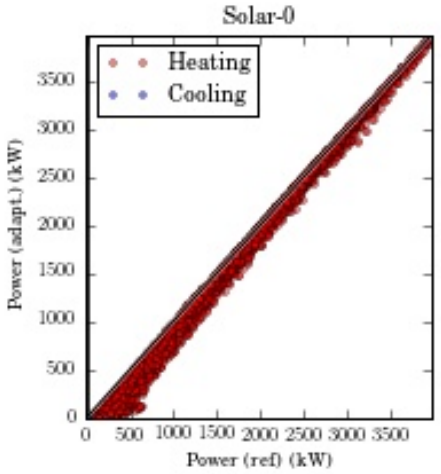

FIGURE C.96: Adapted model results versus reference results

Cette thèse est accessible à l'adresse : http://theses.insa-lyon.fr/publication/2018LYSEI071/these.pdf
© [L. Frayssinet], [2018], INSA Lyon, tous droits réservés

LWRad-0

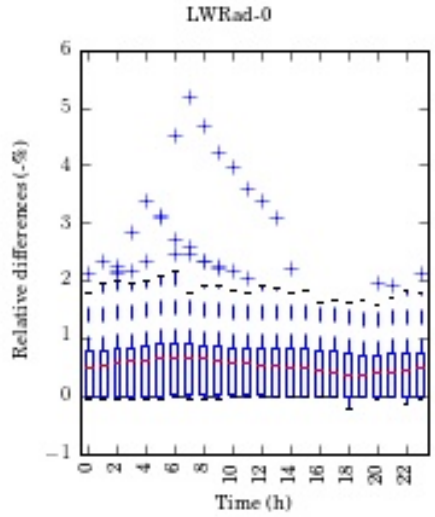

FIGURE C.97: Daily boxplot representation of the differences

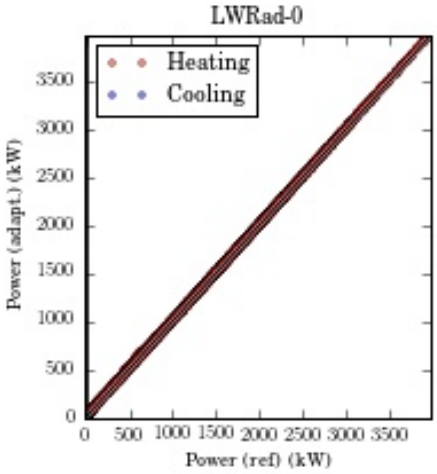

FIGURE C.98: Adapted model results versus reference results

Cette thèse est accessible à l'adresse : http://theses.insa-lyon.fr/publication/2018LYSEI071/these.pdf
© [L. Frayssinet], [2018], INSA Lyon, tous droits réservés

Adjoin-0

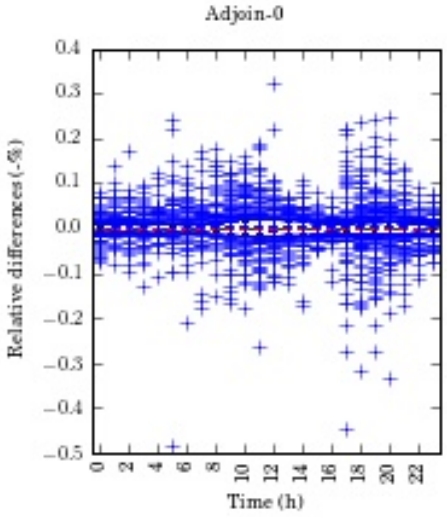

FIGURE C.99: Daily boxplot representation of the differences

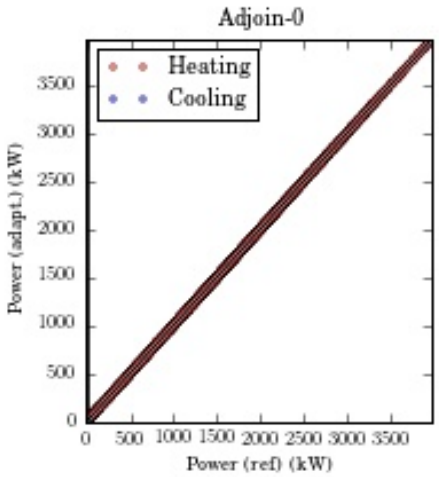

FIGURE C.100: Adapted model results versus reference results

Cette thèse est accessible à l'adresse : http://theses.insa-lyon.fr/publication/2018LYSEI071/these.pdf
© [L. Frayssinet], [2018], INSA Lyon, tous droits réservés

C.4 Effects for the buildings of the district

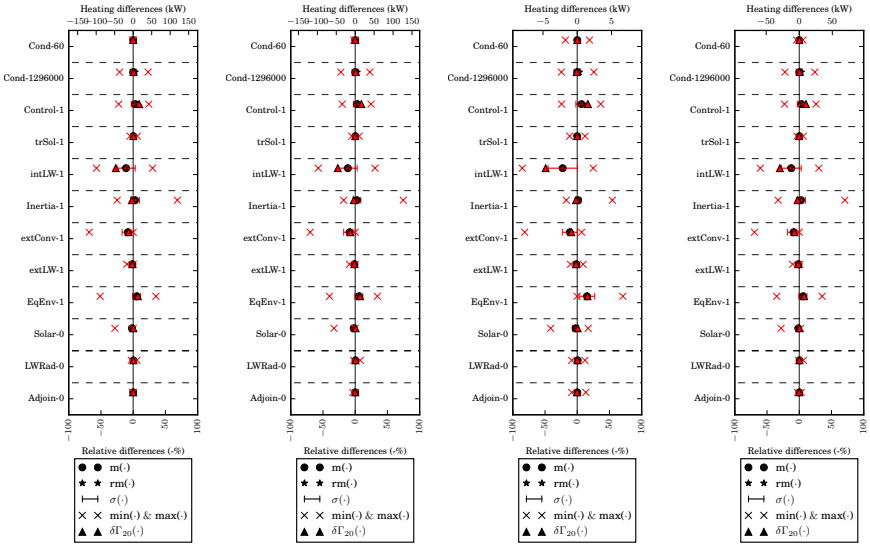

(A) *Building 1* (B) *Building 2* (C) *Building 3* (D) *Building 4*

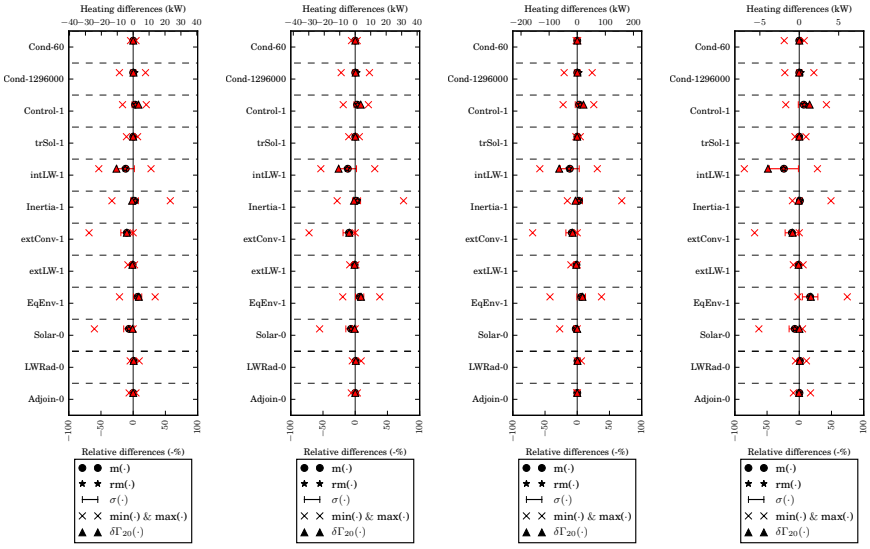

(A) *Building 5* (B) *Building 6* (C) *Building 7* (D) *Building 8*

Cette thèse est accessible à l'adresse : http://theses.insa-lyon.fr/publication/2018LYSEI071/these.pdf
© [L. Frayssinet], [2018], INSA Lyon, tous droits réservés

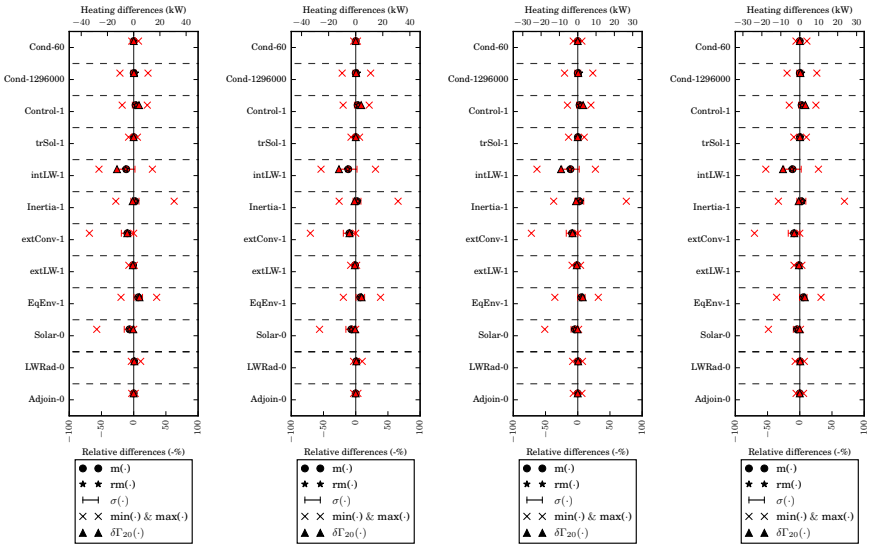

(A) *Building 9* (B) *Building 10* (C) *Building 11* (D) *Building 12*

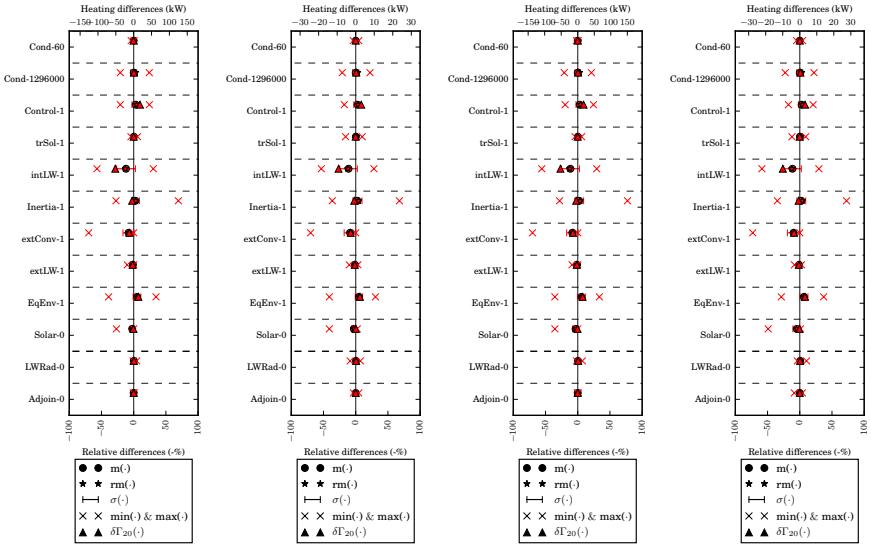

(A) *Building 13* (B) *Building 14* (C) *Building 15* (D) *Building 16*

Cette thèse est accessible à l'adresse : http://theses.insa-lyon.fr/publication/2018LYSEI071/these.pdf
© [L. Frayssinet], [2018], INSA Lyon, tous droits réservés

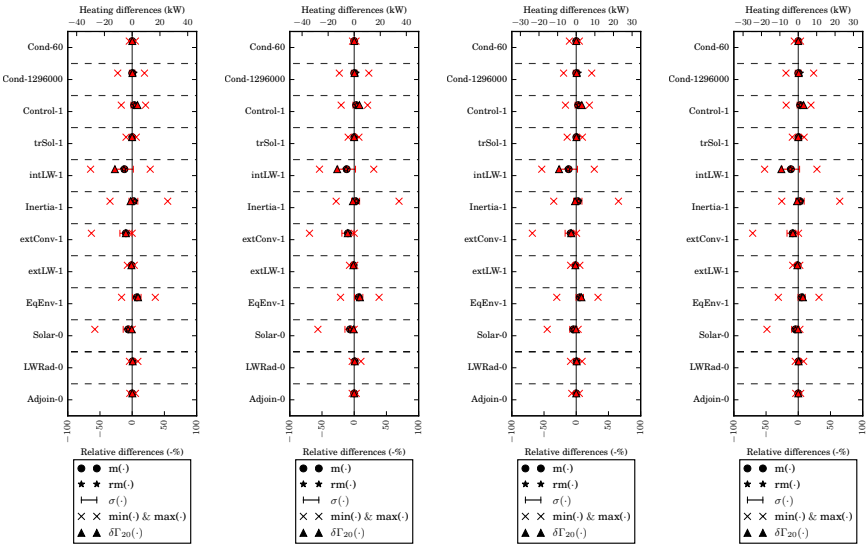

(A) *Building 17* (B) *Building 18* (C) *Building 19* (D) *Building 20*

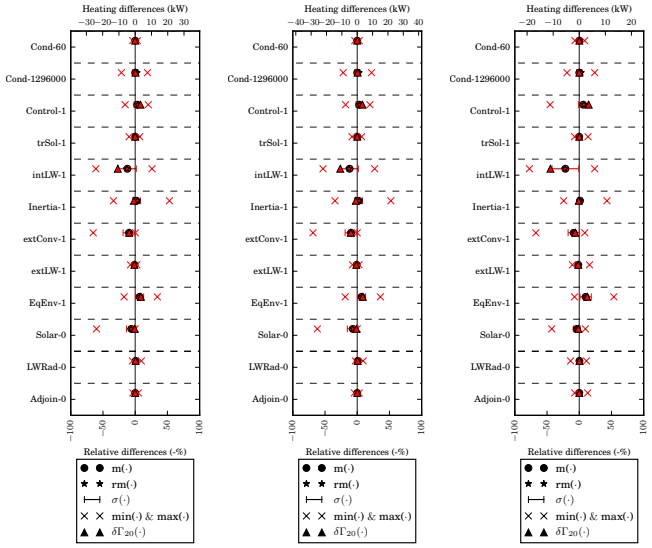

(A) *Building 21* (B) *Building 22* (C) *Building 23*

Cette thèse est accessible à l'adresse : http://theses.insa-lyon.fr/publication/2018LYSEI071/these.pdf
© [L. Frayssinet], [2018], INSA Lyon, tous droits réservés

Cette thèse est accessible à l'adresse : http://theses.insa-lyon.fr/publication/2018LYSEI071/these.pdf
© [L. Frayssinet], [2018], INSA Lyon, tous droits réservés

Appendix D

Author related articles

Cette thèse est accessible à l'adresse : http://theses.insa-lyon.fr/publication/2018LYSEI071/these.pdf
© [L. Frayssinet], [2018], INSA Lyon, tous droits réservés

Renewable and Sustainable Energy Reviews 81 (2018) 2318–2327

Contents lists available at ScienceDirect

Renewable and Sustainable Energy Reviews

journal homepage: www.elsevier.com/locate/rser

Modeling the heating and cooling energy demand of urban buildings at city scale

Loïc Frayssinet[a,b,*], Lucie Merlier[a,b], Frédéric Kuznik[a,b], Jean-Luc Hubert[a,c], Maya Milliez[a,c], Jean-Jacques Roux[a,b]

[a] BHEE, CETHIL-EDF Joint Laboratory, France
[b] Univ Lyon, CNRS, INSA-Lyon, Université Claude Bernard Lyon 1, CETHIL, UMR5008, F-69621 Villeurbanne, France
[c] EdF R & D - Enerbat Department Avenue des Renardières – Ecuelles, F-77818 Moret sur Loing, France

ARTICLE INFO

Keywords:
Heating and cooling in buildings
Power demand prediction
District
City

ABSTRACT

Many computational approaches exist to estimate heating and cooling energy demand of buildings at city scale, but few existing models can explicitly consider every buildings of an urban area, and even less can address hourly -or less- energy demand. However, both aspects are critical for urban energy supply designers. Therefore, this paper gives an overview of city energy simulation models from the point of view of short energy dynamics, and reviews the related modeling techniques, which generally involve detailed approaches. Analysis highlights computational costs of such simulations as key issue to overcome towards reliable microsimulation of the power demand of urban areas. Relevant physical and mathematical simplifications as well as efficient numerical and computational techniques based on uncertainties analysis and error quantification should thus be implemented.

* Corresponding author at: Univ Lyon, CNRS, INSA-Lyon, Université Claude Bernard Lyon 1, CETHIL, UMR5008, F-69621 Villeurbanne, France.
E-mail address: loic.frayssinet@insa-lyon.fr (L. Frayssinet).

http://dx.doi.org/10.1016/j.rser.2017.06.040
Received 18 March 2016; Received in revised form 20 March 2017; Accepted 16 June 2017
Available online 23 June 2017
1364-0321/ © 2017 Elsevier Ltd. All rights reserved.

Cette thèse est accessible à l'adresse : http://theses.insa-lyon.fr/publication/2018LYSEI071/these.pdf
© [L. Frayssinet], [2018], INSA Lyon, tous droits réservés

On the impact of local microclimate on building performance simulation. Part I: Prediction of building external conditions.

Lucie Merlier[a,1,*], Loïc Frayssinet[a,1], Kévyn Johannes[a,1], Frédéric Kuznik[a,1]

[a] *Univ Lyon, CNRS, INSA-Lyon, Université Claude Bernard Lyon 1, CETHIL UMR5008, F-69621, Villeurbanne, France*
[b] *BHEE: High Energy Efficiency Buildings, joint laboratory CETHIL / EDF, France*

Abstract

Towards a better prediction of the effective energy performance of buildings in cities, this study addresses the modeling of local external radiative, thermal and aeraulic conditions. After reviewing existing modeling approaches suitable to estimate building boundary conditions for energy simulation, this paper analyses external conditions derived from a building energy model (BuildSysPro) or a microclimatic model (SOLENE microclimat). Comparison is made for the different faces of a generic building standing alone or located in a urban environment, and having a thermally efficient envelope, or not. Results highlight significant deviations on estimated radiative temperatures as well as on wind-based quantities around the isolated building when adjusting the modeling approach. When accounting for surrounding buildings, results show a substantial reduction of shortwave radiative fluxes explained by an imbalance between solar masks and multireflexions, as well

*Corresponding author. Tel.: +33-472-437-483; Fax: +33-472-438-522
Email address: lucie.merlier@insa-lyon.fr (Lucie Merlier)

Cette thèse est accessible à l'adresse : http://theses.insa-lyon.fr/publication/2018LYSEI071/these.pdf
© [L. Frayssinet], [2018], INSA Lyon, tous droits réservés

as of the wind driven ventilation potential.

Keywords: Urban micro-climate, Building external conditions, Microclimatic simulation, Building energy simulation.

Highlights

1. Building external conditions derived from a building energy model and a microclimatic model are compared
2. Differences induced by the modeling approach and built configuration are evaluated
3. Both thermo-radiative and aeraulic environmental variables are addressed
4. Two built configurations / envelope performances / seasons are studied
5. Results can be further applied to the uncertainty quantification of meteorological inputs for building energy simulations

Cette thèse est accessible à l'adresse : http://theses.insa-lyon.fr/publication/2018LYSEI071/these.pdf
© [L. Frayssinet], [2018], INSA Lyon, tous droits réservés

Nomenclature

λ	Thermal conductivity [$\mathrm{W\,m^{-1}\,K^{-1}}$]
ϕ	Short-wave solar radiation flux [$\mathrm{W\,m^{-2}}$]
ρ	Density [$\mathrm{kg\,m^{-3}}$]
θ	Wind incidence angle [rad]
c_p	Specific thermal capacity [$\mathrm{J\,kg^{-1}\,K^{-1}}$]
Cp	Pressure coefficient [Pa]
K_v	Obstruction factor [$-$]
N	Power law exponent [$-$]
e	Layer thickness [m]
H	Building height [m]
h	Convective heat transfer coefficient [$\mathrm{W\,m^{-2}\,K^{-1}}$]
S	Aspect ratio [-]
T	Temperature [K or °C]
U	Wind velocity [$\mathrm{m\,s^{-1}}$]

Cette thèse est accessible à l'adresse : http://theses.insa-lyon.fr/publication/2018LYSEI071/these.pdf
© [L. Frayssinet], [2018], INSA Lyon, tous droits réservés

Introduction

Urban areas change properties of the atmospheric boundary layer both thermally and dynamically on different scales, and thus ambient conditions around buildings. From the smallest to the largest urban atmospheric scales (about 10 cm, less than one minute time scale, to 10 km and one day), urban areas having an effect on turbulence, building wakes, thermals, convection, urban heat island as well as deep convection (Schlünzen et al., 2011; Blocken, 2015). Such effects arise from the particular structure and energy balance of cities: the 3D geometry, thermo-physical properties of urban materials and surfaces as well as anthropogenic heat and pollution releases influence physical exchanges developing in cities, including short and long wave radiation, thermal storage, evaporation as well as turbulent sensible and latent heat transfers (Oke, 2002).

[Figure 1 about here.]

Resulting urban micro-climatic conditions are often characterized by higher temperatures and reduced mean wind velocities than in the surrounding rural area. These conditions can substantially alter the energy needs of urban buildings compared to rural buildings (Santamouris, 2014; Santamouris et al., 2015) by modifying heat and mass transfers through its envelope. In particular, as shown in Fig. 1 (Santamouris et al., 2001; Malys et al., 2015):

- solar exposure / masks and multi-reflections influence solar heating,
- reduced sky view factor and surrounding warmed-up surface temperatures alter potential radiative cooling,

Cette thèse est accessible à l'adresse : http://theses.insa-lyon.fr/publication/2018LYSEI071/these.pdf
© [L. Frayssinet], [2018], INSA Lyon, tous droits réservés

- wind / pressure fields and air temperature affect convective heat exchanges at building outer walls as well as thermal effects of ventilation and infiltration.

Nonetheless, despite a growing awareness about the specificities of urban areas (Nunez and Oke, 1977; Oke, 1982; Santamouris et al., 2001; de la Flor and Domìnguez, 2004), building energy simulations commonly use on typical weather files as meteorological inputs. These weather data are usually derived from airport measurements and may be coarsely modified to account for some urban effects (Sun et al., 2011, 2014; Goffart, 2016; Roux and Kuznik, 2016). Building energy models also commonly consider general values, secondary sources, empirical correlations or simplified approaches to estimate heat and mass transfers at building outer walls, e.g. through convective or pressure coefficients (Còstola et al., 2009; Mirsadeghi et al., 2013; Penicaud, 2016). Such assumptions can lead to substantial errors, especially when aiming to understand properly the energy behavior of a building in its actual built environment (Còstola et al., 2009; Mirsadeghi et al., 2013). Such inaccuracies incite using of appropriate boundary conditions for urban buildings. However, account for relevant radiative, thermal and aeraulic external conditions for building energy simulation is challenging because of the complexity of the physical processes developing in cities and buildings. This is even more true when addressing current problems of peak power loads, renewable energy intermittency and thermal comfort in highly energy efficient buildings that involve passive cooling strategies. Because of their different dynamics and physical couplings, these problems are more complex to study than the annual energy consumption of standard buildings, for which building energy

Cette thèse est accessible à l'adresse : http://theses.insa-lyon.fr/publication/2018LYSEI071/these.pdf
© [L. Frayssinet], [2018], INSA Lyon, tous droits réservés

simulation tools were primarily developed (Clarke, 2007)

Towards more integrated building energy simulations, external conditions could be evaluated based on on-site measurements, reduced scale models or numerical simulations (Moonen et al., 2012). Each of these techniques has advantages and drawbacks, but computational approaches appear particularly suited to generally study building external conditions. Indeed, although such an approach necessarily involves some physical, mathematical and numerical assumptions, this technique is free from similarity constraints, allows boundary condition to be controlled, whole flow field data to be estimated, and parametric studies to be performed on virtual configurations. Hence, computational approaches are valuable to evaluate specific external radiative, thermal and aeraulic conditions and, further, their effects on the dynamic energy behavior of buildings. Taking advantage of this technique, microclimatic numerical studies generally identify urban effects on short and long wave radiation fluxes as well as convective heat transfers as influential on the energy behavior of urban buildings (Bouyer et al., 2011; Yang et al., 2012; Allegrini et al., 2012; Malys et al., 2015). Increased air temperatures are also shown influential on the energy behavior of urban buildings through natural ventilation / infiltration (Allegrini et al., 2013; Yang et al., 2012), especially during summer. However, to the best knowledge of the authors, almost only dedicated studies addressed consequences of local wind features on building energy needs due to aeraulic transfers (Ghiaus et al., 2006; Jokisalo et al., 2009; Ramponi et al., 2014). When addressing this aspect, such studies generally highlight a substantial decrease of the building ventilation potential due to the surrounding built structures. Therefore, consequences of local

Cette thèse est accessible à l'adresse : http://theses.insa-lyon.fr/publication/2018LYSEI071/these.pdf
© [L. Frayssinet], [2018], INSA Lyon, tous droits réservés

wind alteration by surrounding constructions on the aeraulic-induced thermal loads should be considered along with the other radiative an thermal contributions.

Hence, towards the uncertainty quantification of meteorological inputs and radiative, thermal and aeraulic boundary conditions for building energy simulation as initiated in Sun et al. (2011), the objective of the present study is twofold. First, it aims to discuss limitation of usual building energy models to integrate accurately external conditions in energy simulation. For this purpose, external conditions around a building standing alone obtained using two modeling approaches are compared. The first set of external conditions is based on possible inputs of a building energy model, and the second set of external conditions is derived from an explicit microclimatic simulation of the building environment. Second, it aims at quantifying the modification of building external conditions induced by an urban environment. For this purpose, a third set of external conditions is derived from an explicit microclimatic simulation of a generic neighborhood around the building of interest. Given current challenges linked with building refurbishment in most of European countries, an old and a recent buildings are considered.

Five parts compose the present paper. First, Sec. 1 gives an overview of existing urban climate modeling approaches usable for building energy studies. On this basis, Sec. 2 and 3 present the test cases as well as the developed modeling approaches. Then, Sec. 4 compares the different building external conditions derived from the different modeling approaches and built configurations. Finally, Sec. 5 discuss the main results of the study and open perspectives. A second part of this article further addresses the influence of

Cette thèse est accessible à l'adresse : http://theses.insa-lyon.fr/publication/2018LYSEI071/these.pdf
© [L. Frayssinet], [2018], INSA Lyon, tous droits réservés

building boundary conditions on its energy behavior (Merlier et al., 2018b).

1. Overview of climatic modelings used to upgrade energy simulations of urban buildings

Given current sustainable urban development issues, different physically-based computational models were developed during the last decade to characterize urban microclimates and their effects on the energy behavior of buildings. From the largest to the smallest scales, they are urban canopy models, city energy models, zonal models, microclimatic models and extended building energy models. These different approaches were basically developed following different objectives such as estimating the energy balance of urban areas for mesoscale meteorological models or providing detailed boundary conditions for a specific urban building (Musy et al., 2012; Bozonnet et al., 2015; Musy and Bozonnet, 2016). Therefore, these approaches involve different spatial resolutions and modeling assumptions.

Urban canopy models are relatively large scale models, in which the urban geometry is generally not explicitly modeled. Representative values of morphometric properties as well as other urban features are used to evaluate the energy balance of an urban area. Models such as Town Energy Balance (Masson, 2000; Lemonsu et al., 2004) often rely on the equivalent street canyon assumption. They differentiate roofs, walls and roads to compute different thermal exchanges, and derive inner canopy wind profiles from correlations. Coupled with a mesoscale model or forced with measurements data or usual weather files, urban canopy models may provide typical local heat island effect and long wave radiative exchanges between urban surfaces. Results can

Cette thèse est accessible à l'adresse : http://theses.insa-lyon.fr/publication/2018LYSEI071/these.pdf
© [L. Frayssinet], [2018], INSA Lyon, tous droits réservés

be further used to assess their typical influence on the energy behavior of urban buildings (Sun and Augenbroe, 2014; Pigeon et al., 2014). Using such an approach together with a simplified boundary layer model, (spatialized) urban weather generators (Bueno et al., 2013; Le Bras and Masson, 2015) are also able to provide inner canopy temperatures, which may be used as boundary conditions for building energy simulations (Masson et al., 2014).

City energy models such as CitySim (Robinson et al., 2009) enable urban built structures to be explicitly represented. They are not primarily devoted to the study of urban microclimates. They often model urban microclimatic effects only considering radiative exchanges to adapt building conditions for energy simulation (Allegrini et al., 2015; Frayssinet et al., 2017).

On smaller scales, zonal approaches mainly apply for air flows on the street canyon scale and can involve different levels of complexity in the thermo-radiative modeling (de la Flor and Domìnguez, 2004; Bozonnet, 2006). Their spatial resolution and physical bases enable local microclimatic conditions, including some wind-related effects, to be modeled without requiring high computational costs. Integrated boundary conditions can thus be rather rapidly estimated for the energy simulation of urban buildings. Furthermore, although such models initially addressed typical street canyon configurations, the recently developed model EnviBatE (Gros et al., 2016) can handle realistic urban configurations and can estimate yearly energy consumption of urban buildings.

Even more detailed, microclimatic models such as SOLENE microclimat (Musy et al., 2015), ENVImet (Bruse, 2004) or Coupled_Simulation (Chen et al., 2004) enable the geometry of a neighborhood to be explicitly repre-

Cette thèse est accessible à l'adresse : http://theses.insa-lyon.fr/publication/2018LYSEI071/these.pdf
© [L. Frayssinet], [2018], INSA Lyon, tous droits réservés

sented and properties of each elementary surface to be differentiated. Such models rely on a coupling between a thermo-radiative and computational fluid dynamics (CFD, generally with a Reynolds Averaged Navier–Stokes (RANS) turbulence closure) codes. They can compute surface and air temperatures as well as air flows theoretically down to a meter characteristic length scale or less. Therefore, using an internal or external coupling with a detailed building energy model, it is possible to analyze effects of very local urban conditions, including short and long wave radiations, convective heat transfers and air temperatures, on the energy behavior of specific buildings (Bouyer et al., 2011; Malys et al., 2015; Yang et al., 2012; Chen et al., 2004).

Finally, typical meteorological inputs and boundary conditions of usual building energy models may also be adjusted using preliminary CFD studies and adapted modeling (Allegrini et al., 2013; Yi and Feng, 2013). It is also possible to use or implement specific sub-models in the general building energy model to perform more integrated energy simulations of urban buildings (as in BuildSysPro (2018) and EnergyPlus (2018) for instance).

Hence, the different modeling approaches reviewed above may provide more or less specific external conditions to be used in the energy modeling of a given building. Being the most specific and detailed, the last two cited approaches are the most suited to further assess and understand the effective dynamic behavior of an urban building in its actual environment. Therefore, this study discusses the ability of a currently available building energy and microclimatic tools, namely BuildSysPro and SOLENE-microclimat, to provide appropriate external radiative, thermal and aeraulic conditions for the energy simulation of urban buildings.

Cette thèse est accessible à l'adresse : http://theses.insa-lyon.fr/publication/2018LYSEI071/these.pdf
© [L. Frayssinet], [2018], INSA Lyon, tous droits réservés

2. Case study

2.1. Test cases

As a basic study, this work deals with generic, yet representative, built configurations (Toparlar et al., 2017; Merlier et al., 2018c). More specifically, this study focuses on an isolated H = 10 m high cubic located on a mineral $100 \times 100\,m^2$ area and oriented according to the four cardinal directions in order to facilitate a face by face analysis of external conditions. To represent an isolated or an urban configuration, the building is assumed standing alone or located in a 4×4 regular array of similar buildings (Fig. 2).

[Figure 2 about here.]

Although the array-type urban pattern does not correspond to usual building arrangements found for multi-family houses built before 1915 in France, this building typology is the most represented type of the collective residential building in France (Rochard et al., 2015). Therefore, basic thermal properties of this building typology were chosen to specify the envelope properties of the modeled buildings. As shown on Tab. 1, corresponding constructions were initially massive, made of stone or brick and did not benefit of thermal insulation nor exterior cladding -*Initial* state. These buildings could have been renovated, thus substantially increasing their thermal performance -*Renovated* state. According to Rochard et al. (2015), the improvement of insulation, air tightness and ventilation system efficiency induced a typical decrease of heating needs of 61 %. Their facade glazing ratio equals 23 %.

Cette thèse est accessible à l'adresse : http://theses.insa-lyon.fr/publication/2018LYSEI071/these.pdf
© [L. Frayssinet], [2018], INSA Lyon, tous droits réservés

2.2. Geographical and meteorological context

This study focuses on the climate of Lyon, France (latitude: 45.75° North, longitude: 4.75° East). It is temperate, but semi-continental, i.e. characterized with relatively hot summer days and cold winter days. Two specific days are more particularly considered to address both seasons: the 09 July and the 06 November.[1]

[Figure 3 about here.]

Based on the Meteonorm weather files for Lyon Satolas, the mean temperatures of the selected days are 23.5 °C and 4.4 °C (Fig. 3). With respect to the mean monthly air temperature, the mean temperatures of the selected days are close to the lowest maximal normal summer air temperature and highest minimal normal winter air temperature recorded over the 1981-2010 period for this location (Météo France, 2017). Representative heating and cooling needs can thus be analyzed. The slight exceeding of these reference temperatures,by 0.8 and 0.6 °C respectively in summer and winter, might be further conceived as resulting from an urban heat island effect. Nonetheless, the temperature distribution over the day should be analyzed for this interpretation to be effectively founded. With an averaged wind velocity of about $4\,\mathrm{m\,s^{-1}}$, the selected days are also relatively windy days, so that maximum convective effect and wind driven ventilation potential could be further analyzed.

[1] Although this winter day is not really a representative winter day, it is selected because of its particular air temperature and wind speed conditions, while being relatively close to the winter solstice, thus showing low sun height and short day length.

Cette thèse est accessible à l'adresse : http://theses.insa-lyon.fr/publication/2018LYSEI071/these.pdf
© [L. Frayssinet], [2018], INSA Lyon, tous droits réservés

3. Modeling approach

To study the ability of currently available tools to model building external conditions and the effect of urban environments on them, this study develops two modeling approaches:

- estimating building external conditions using possibilities of a building energy model built using BuildSysPro - *Default* approach;
- deriving building external conditions from a microclimatic simulation performed using SOLENE-microclimat - *Microclimatic* approach - for an isolated building located on a mineral ground - *Isolated* configuration - or a building located in a theoretical urban environment - *Array* configuration.

3.1. Default approach

BuildSysPro is a 0D / 1D building energy Modelica library developed by EDF R&D (Plessis et al., 2014; Schumann et al., 2016). This library is suited to study the energy behavior of French buildings using modular and detailed dynamic models. The performance of BuildSysPro was verified by different validation studies (Bontemps et al., 2013, 2016), especially regarding thermally efficient buildings.

In the present study, the 10 m high cubic building was modeled isolated as guidelines to adjust building external conditions to model an urban building are generally lacking. This means that no solar mask was modeled and the meteorological wind speed was processed as follows:

$$U_H = K_v \times U_{meteo,z=10m} \times \left(\frac{H}{10}\right)^N \quad (1)$$

Cette thèse est accessible à l'adresse : http://theses.insa-lyon.fr/publication/2018LYSEI071/these.pdf
© [L. Frayssinet], [2018], INSA Lyon, tous droits réservés

with $K_v = 0.68$ the obstruction factor, $N = 0.17$ the power law exponent, U_H the wind speed at building height H, and $U_{meteo,z=10m}$ the meteorological wind speed, assumed measured at 10 m high.

As shown on Fig. 5, he direct and atmospheric diffuse short wave radiation fluxes which were taken from SOLENE-microclimat simulations (see Sec. 3.2) for sake of comparability. Other meteorological quantities were taken from the weather file. On this basis, a relatively detailed approach given usual abilities of building energy models was implemented in BuildSysPro to assess building external conditions at the different building outer walls. In the following the subscript '$face$' refers to this differentiation.

More specifically, the different inputs were processed using sub-models to estimate the (i) short wave radiation fluxes reflected by the environment, (ii) environmental radiant temperature, (iii) convective heat transfers coefficient (CHTC) as well as (iv) pressure coefficient (Cp), as follows:

- (i) The part of the short wave radiation flux received by the ground ($\phi_{\rightarrow ground}$, Eq. 2) that is reflected towards vertical surfaces ($\phi_{refl.ground \rightarrow face}$) was estimated following Eq. 3 thanks to the view factor reciprocal relation (Eq. 3):

$$\phi_{\rightarrow ground} = \phi_{SW,dir,horiz.} + \phi_{SW,diff.atm.,horiz.} \tag{2}$$

$$\phi_{refl.ground \rightarrow face} = \rho_{ground} \times F_{ground,face} \times \phi_{\rightarrow ground} \tag{3}$$

  with $\phi_{SW,dir,horiz.}$ and $\phi_{SW,diff.atm.,horiz.}$ the direct and diffuse short-wave solar fluxes received by a horizontal plane, $\rho_{ground} = 0.15$ the ground albedo and $F_{ground,face}$ the view factor of the ground from the

Cette thèse est accessible à l'adresse : http://theses.insa-lyon.fr/publication/2018LYSEI071/these.pdf
© [L. Frayssinet], [2018], INSA Lyon, tous droits réservés

wall approximated by 0.5 for vertical walls[2] and 0 for the roof.

- (ii) An environmental radiant temperature ($T_{rad,env}$) was estimated based on the Stefan-Boltzmann's law (Eq. 4):

$$T_{rad,env} = \sqrt[4]{F_{sky,face} \times T_{sky}^4 + (1 - F_{sky,face}) \times T_{air}^4} \quad (4)$$

with T_{sky} the sky temperature, available in the weather file, and $F_{sky,face}$ the sky view factor, assumed equal to 0.5 and 1 respectively for the vertical walls and roof.

- (iii) The correlation function of the local wind speed suggested in the French thermal regulation (CSTB, 2012) was used to estimate CHTC (Eq. 5):

$$CHTC_{face} = 4 + 4 \times U_{H,face} \quad (5)$$

with $U_{H,face}$ the local wind speed projected according to the faces orientation. Note that as an azimuth should be specified for the building roof, which is actually horizontal, an East orientation was set.

- (iv) Finally, Cp at building outer walls were estimated using the Swami and Chandra formula (BuildSysPro, 2018) as follows:

$$\begin{aligned} Cp_{face} = \Bigg[C_0 \times \ln \Bigg(& 1.248 - 0.703 \times \sin(\frac{\theta}{2}) \\ & -1.175 \times \sin^2(\theta) + 0.131 \times \sin^3(2 \times \theta \cdot S) + 0.769 \times (\frac{\theta}{2}) \\ & +0.07 \times S^2 \times \sin^2(\frac{\theta}{2}) + 0.717 \times \cos^2(\frac{\theta}{2}) \Bigg) \Bigg] \end{aligned} \quad (6)$$

[2]View factor of an infinite horizontal ground view from a vertical surface infinitely wide.

Cette thèse est accessible à l'adresse : http://theses.insa-lyon.fr/publication/2018LYSEI071/these.pdf
© [L. Frayssinet], [2018], INSA Lyon, tous droits réservés

with θ the face orientation in relation to the prevailing wind incidence, S the face aspect ratio, C_0 the averaged pressure coefficient for wind orthogonal to the surface, assumed equal to 0.6, and $S = 1$ in case of a cubic buildings.

Simulations were run using the Dymola environment for the 6th November and the 9 July in order to record the related external conditions.

3.2. Microclimatic approach

SOLENE-microclimat is a software suite developed by the CRENAU, Nantes, France (Musy et al., 2015; Morille et al., 2015; Malys et al., 2015). This tool relies on an external coupling between the improved thermo-radiative code SOLENE and the CFD code Code_Saturne as shown in the upper part of Fig. 4. More precisely, SOLENE relies on the radiosity algorithm and an iterative process is embedded to compute surface temperatures. An iterative process also underlies the coupled steady state RANS $k-\varepsilon$ CFD simulations.

In this study, extending best practice guidelines (Franke, 2006; Tominaga et al., 2008) to account for different wind orientations, computational domains were enlarged by 15 H in the four cardinal directions and 5 H in height, leading to $310 \times 310 \times 60\,\mathrm{m}^3$ and $370 \times 370 \times 60\,\mathrm{m}^3$ large computational domains respectively for the isolated and array configurations. With a mesh dimensioning of 1 m on the building edges and 3 m on the edges of the mineral surface as well as a global mesh size factor of 0.2, the total number of 3D cells reaches 95×10^3 and that of facets reaches 6×10^3 for the isolated configuration. With the same settings but the dimensioning of the mineral surface edges set to 1.5 m because of its proximity to buildings, the total

Cette thèse est accessible à l'adresse : http://theses.insa-lyon.fr/publication/2018LYSEI071/these.pdf
© [L. Frayssinet], [2018], INSA Lyon, tous droits réservés

number of 3D cells reaches 289×10^3 and facets reaches 637×10^3 for the array configuration.

With the exception of short wave direct and diffuse atmospheric fluxes, which are computed by SOLENE, input meteorological conditions were based on the Meteonorm weather file of Lyon. By default in the general model, the sky is assumed clear, the inlet wind profile follows a 0.3 power law, and no buoyancy nor roughness effect is accounted for. All buildings were similarly modeled using a simple global exchange coefficient for the envelope and an indoor temperature equal to 26 °C in summer and 18 °C in winter. As no windows were differentiated from walls, the global exchange coefficient was estimated based on equivalent wall properties resulting from an averaging of opaque and glazed surfaces. Tab. 1 synthesizes the equivalent envelope and mineral surface properties set in the model. Note that as no transmittance value could be relevantly assigned to walls and albedos were fixed depending on surfaces properties, absorbed heat by building surfaces may be overestimated.

[Table 1 about here.]

[Figure 4 about here.]

Eight simulations were run considering the two seasons, building states and built configurations. Simulations were run for two days in summer and in winter, because of the involved computational cost,[3]. The first days served as numerical initialization of the model.

[3]At each hourly time step, 2000 iterations of Code_Saturne were run for convergence,

Cette thèse est accessible à l'adresse : http://theses.insa-lyon.fr/publication/2018LYSEI071/these.pdf
© [L. Frayssinet], [2018], INSA Lyon, tous droits réservés

To compose the set of building external conditions, direct, atmospheric and reflected diffuse short wave radiative fluxes, local air and environmental radiant temperatures, CHTC and relative pressure next to building faces were recorded at each time step. Surface or first cell quantities were then averaged by face. Radiative quantities were also interpolated in time to match BuildSysPro time steps (bottom part of Fig. 4). As such, similar types of building external conditions were derived from the default and microclimatic approaches (Fig. 5).

[Figure 5 about here.]

4. Results analysis

To highlight the differences of external conditions induced by the modeling approaches and built environments, Fig. 6 and 7 compare face by face the (a, b, c) received direct, diffuse and reflected short wave radiative fluxes, (d, e, g, h) environmental radiant and air temperatures, as well as (f) CHTC and (i) pressure values derived from the different simulations. Tab. 2 indicates the corresponding spatially (over the different faces) and temporally (over the day) averaged values. Note that only the estimated air and radiant temperatures are differentiated depending on the state of the building envelope as other variables are independent from it. Tab. 2 also precises the normal-

which was checked based on the normalized residuals. Considering simulation initialization, more than 96×10^3 iterations were thus run for each simulation. A 40 cores computer with 62 GB of RAM was used.

Cette thèse est accessible à l'adresse : http://theses.insa-lyon.fr/publication/2018LYSEI071/these.pdf
© [L. Frayssinet], [2018], INSA Lyon, tous droits réservés

ized ventilation potential resulting from the mass balance of the building due to pressure differences.

[Figure 6 about here.]

[Figure 7 about here.]

[Table 2 about here.]

4.1. Effects of the modeling approach - stand alone building

Short-wave radiation fluxes. Deviations due to the modeling approach are only observed for the reflected fluxes received on vertical walls as other solar fluxes are directly derived from the SOLENE-microclimat simulations in both approaches. Both in summer and winter, the reflected flux on the different building faces is about two times lower according to the microclimatic approach than according to the default approach. This can be explained by the limited extent of the mineral ground assumed in the microclimatic model. Furthermore, as the building is not centered on the ground in the microclimatic approach, the reflected flux slightly differs depending on wall orientation.

On average, the microclimatic approach induces a reduction of the total received solar flux by 4 % and 6 % respectively in winter and summer compared to the flux estimated by the default approach. This small difference is explained by the fact that the reflected part represents less than 10 % of the total received short wave radiative energy.

Cette thèse est accessible à l'adresse : http://theses.insa-lyon.fr/publication/2018LYSEI071/these.pdf
© [L. Frayssinet], [2018], INSA Lyon, tous droits réservés

Temperatures. Being based on the meteorological air (and sky) temperature, temperatures are similar for the different faces of the building in the default approach. The radiant temperature around the roof differs from the others because of its sky view factor. Conversely, local temperatures predicted by the microclimatic approach differ depending on faces. They appear directly correlated with solar loads, which overheats building surfaces following a characteristic temporal pattern. In summer, air temperatures next to the East and North faces increases first, temperature increases then next to the roof and West faces. Conversely, in winter, air temperature almost only increases next to the South face. Because of the link between solar loads and local air temperatures in the microclimatic approach, the deviation between the microclimatic and the default air temperatures is maximum around midday. Maximum face averaged deviations reach 1.7 °C and 2.8 °C, respectively in winter and in summer, which is 4 up to 6 times higher than the day averaged deviation.

Being directly determined using very different assumptions, estimations of radiant temperature substantially differ depending on the modeling approach. This is especially the case on vertical surfaces as the roof only faces the sky, and on the North face as it faces shaded areas. On average in summer, radiant temperature differences are of 7.3 °C, with a maximum of 17.5 °C. This difference is one order of magnitude higher that for the the averaged air temperature. On average in winter, the mean and maximal deviations respectively are 3.3 °C and 8.9 °C. These differences are again explained by solar loads, which overheat sunlit surfaces, potentially leading to very high ground surface temperatures in the microclimatic approach. As

Cette thèse est accessible à l'adresse : http://theses.insa-lyon.fr/publication/2018LYSEI071/these.pdf
© [L. Frayssinet], [2018], INSA Lyon, tous droits réservés

the external surface temperatures are linked to solar radiation, the peak of the radiant temperature estimated with the microclimatic approach occurs also around midday. Being linked with the air temperature, it occurs later in the default approach. As a result, this difference induces a 3 h time shift between the estimated peaks in summer.

Moreover, it could be noticed that, according to the building model embedded in SOLENE-microclimat, the sensitivity of local air and radiant temperatures to the building envelope state is rather negligible.

Wind-based quantities. CHTC and relative pressures estimated by both approaches are consistent as airflow is assumed not influenced by thermal effects in the present study. Windward faces show higher CHTC and positive pressure values, while CHTC are low and pressure negative in recirculation regions according to both the default and the microclimatic approaches.

Nonetheless, CHTC and relative pressure values locally deviate. In particular, regarding intensities, results show that the obstruction factor used to scale the wind profile in the default approach induces lower CHTC and absolute pressure values than in the microclimatic approach. Moreover, based on the default approach, CHTC values often equal $4\,\mathrm{W\,m^{-2}\,K^{-1}}$ for leeward faces, which corresponds to a zero wind speed according to Eq. 5. This value is not reached in the microclimatic approach, which indicates that a residual wind velocity always exists next to leeward faces. As a result, on average, CHTC values predicted by the microclimatic approach exceed those of the default approach by 41 % and 64 %, respectively for the winter and summer day.

Relative pressure also deviate between the default and the microclimatic

Cette thèse est accessible à l'adresse : http://theses.insa-lyon.fr/publication/2018LYSEI071/these.pdf
© [L. Frayssinet], [2018], INSA Lyon, tous droits réservés

approaches. Deviation even reaches 100 %. On average, the higher pressure differences derived from the microclimatic approach induce a 41 % and 60 % higher ventilation potential respectively in winter and summer than according to the default approach. These deviations exceed the reduction of the meteorological mean wind intensity induced by Kv, highlighting differences in Cp distributions.

4.2. Effects of the built configuration - Microclimatic approach

Short-wave radiation fluxes. Solar radiative fluxes are logically reduced in the array configuration due to solar masks compared to the isolated configuration. On average, reduction is of 11 % for the direct and 4 % for the diffuse part in summer. Corresponding reduction is of 27 % and 10 % in winter. The subsequent reduction of the total received short wave radiation energy is of 9 % in summer and 23 % in summer. Oppositely, reflection is almost doubled in the array compared to the isolated configuration. This increase of short wave radiation flux is especially observed in winter on the North face around midday as this face is directly opposite the sunlit face. Nonetheless, similarly to Sec. 4.1, the contribution of the reflected flux to the total short wave radiative flux is small. As a result, the general effect of the urban environment on solar loads is a reduction of total short wave radiative energy by 8 % in summer and 22 % in winter. Relative and absolute urban environment effects on solar fluxes are more important in winter than in summer due to the low solar inclination, which induces more shadings.

Temperatures. Local air temperatures are increased in the array compared to the isolated configuration because of radiation trapping, larger built sur-

Cette thèse est accessible à l'adresse : http://theses.insa-lyon.fr/publication/2018LYSEI071/these.pdf
© [L. Frayssinet], [2018], INSA Lyon, tous droits réservés

faces and reduced ventilation potential. Maximum averaged air temperature differences reaches 2.7 °C in summer, which can substantially alter summer comfort. Nonetheless, on average, air temperature differences appear limited as the mean increase is of 0.5 °C in summer and less than 0.1 °C in winter.

The increase of radiant temperatures in the array compared to the isolated configuration is much higher than that of air temperature. On average, deviation is about 1 °C in winter and 1.5 °C in summer. The maximum averaged difference reaches 3.0 °C in summer. This deviation is mainly explained by the fact that a large part of the radiant temperature is due to the surface temperatures of surrounding building walls, which are higher than the sky temperature. Consequently, the influence of the envelope performance on the radiant temperature is more noticeable than in Sec. 4.1 although this difference remains small: less than 0.4 °C.

Although the temporal variations of temperatures are consistent in the isolated and array configurations, the differences between different faces is less important in the array than in the isolated configuration. This can be explained by the presence of warmed-up vertical surfaces that compensate shaded areas, especially with respect to the North face. In addition, it can be noticed that radiant temperatures remain higher during nighttime. This can be explained by the increase of thermal mass as well as the alteration of the radiative and convective cooling potential of the urban areas because caused by surrounding buildings.

Wind-based quantities. Temporal variations of CHTC are consistent in the isolated and array configurations in both seasons. However, distributions of the relative pressure substantially differ as recirculation flows develop all

Cette thèse est accessible à l'adresse : http://theses.insa-lyon.fr/publication/2018LYSEI071/these.pdf
© [L. Frayssinet], [2018], INSA Lyon, tous droits réservés

around the building. The general wind sheltering effect of the urban environment leads thus to lower CHTC than in the isolated configuration as well as negative relative pressures in the array. On average, the CHTC is reduced by 18% in summer and 4% in winter. The ventilation potential is also reduced by 70 % in summer - which is very prejudicial for the natural ventilation cooling potential - and by 56 % in winter.

5. Conclusion

In order to better understand and predict the energy behavior of urban buildings, this paper compared comprehensive sets of external radiative, thermal and aeraulic conditions. These different conditions were estimated using two modeling approaches, i.e. possibilities of a building and a microclimatic simulation tools. Two built configurations were assessed: a building standing alone or located in a theoretical urban environment. Buildings were specified with low or high thermal performance envelopes and typical sunny and windy days of cold and hot seasons were considered. Thus, the maximum impact of the modeling approach and urban environment on the estimated external conditions could be analyzed depending on the performance of the building stock. On this basis, the individual or combined effects of the different external conditions on the averaged or dynamic energy behavior of buildings could be quantified to address energy needs, power loads or thermal comfort issues.

The comparison of the different modeling approaches for the building standing alone suggests that the contribution of reflection to the total received short wave radiation flux is rather negligible. Therefore, as long as

Cette thèse est accessible à l'adresse : http://theses.insa-lyon.fr/publication/2018LYSEI071/these.pdf
© [L. Frayssinet], [2018], INSA Lyon, tous droits réservés

the albedo remains small, an accurate modeling of this contribution appears not mandatory. On the contrary, an accurate knowledge of the mean wind profile is highlighted important to estimate appropriately relative pressures and CTHC at building outer walls. An appropriate estimation of the environmental radiant temperature, and thus of surrounding surface temperatures even if it is only a ground, appears also critical as the temperature of sunlit surfaces could be substantially higher than air temperatures.

The comparison of external conditions simulated around an isolated or an urban building showed that solar masks substantially reduce short wave radiative fluxes, especially in winter. Multi reflections do not balance this effect, but can locally substantially affect surface loads. Wind masks also significantly alter aeraulic and convective conditions, leading to an important reduction of the natural ventilation potential of buildings. In addition, the presence of surrounding buildings alter the distribution of the different external conditions over the different faces of buildings. This effect tends to homogenize conditions around buildings compared to an isolated configuration. This is especially the case for wind-based quantities, as well as, to a lesser extent, environmental radiant temperature.

Although the microclimatic simulation of the built environment can still be improved to provide more accurate external conditions, especially regarding the resolution of conductive and convective heat transfers as well as heat storage, present results show that such an approach can provide crucial information for building energy modeling. Indeed, although relatively simple models for building walls (global coefficient), solid/air interface (correlation) as well as CFD approach (steady RANS $k-\varepsilon$ without buoyancy effects) were

Cette thèse est accessible à l'adresse : http://theses.insa-lyon.fr/publication/2018LYSEI071/these.pdf
© [L. Frayssinet], [2018], INSA Lyon, tous droits réservés

used, potentially leading to quite high surface temperatures in recirculation regions, the provided information can contribute to better understand the energy behavior of urban buildings. They can also be used to improve building energy engineering practices by taking more accurate boundary conditions or quantified uncertainties of inputs into account in models. Hence, towards a global sensitivity analysis of the energy behavior of urban buildings to their external radiative, thermal and aeraulic conditions, subsequent extension of this study evaluate the impact of these different set of boundary conditions on the dynamic thermal behavior of buildings (Merlier et al., 2018a).

Acknowledgments

Authors warmly thank Jean-Luc Hubert and Maya Milliez from EDF R&D and the BHEE for their support during this work, as well as the CRENAU laboratory for providing SOLENE microclimat.

References

Allegrini, J., Dorer, V., Carmeliet, J., 2012. Influence of the urban microclimate in street canyons on the energy demand for space cooling and heating of buildings. Energy and Buildings 55, 823–832.

Allegrini, J., Kämpf, J. H., Dorer, V., Carmeliet, J., 2013. Modelling the urban microclimate and its influence on building energy demands of an urban neighbourhood. In: Proceedings of CISBAT 2013 Cleantech for Smart Cities and Buildings. Vol. 2. EPFL Solar Energy and Building Physics Laboratory (LESO-PB), pp. 867–872.

Cette thèse est accessible à l'adresse : http://theses.insa-lyon.fr/publication/2018LYSEI071/these.pdf
© [L. Frayssinet], [2018], INSA Lyon, tous droits réservés

Allegrini, J., Orehounig, K., Mavromatidis, G., Ruesch, F., Dorer, V., Evins, R., Dec. 2015. A review of modelling approaches and tools for the simulation of district-scale energy systems. Renewable and Sustainable Energy Reviews 52, 1391–1404.

Blocken, B., Sep. 2015. Computational Fluid Dynamics for urban physics: Importance, scales, possibilities, limitations and ten tips and tricks towards accurate and reliable simulations. Building and Environment 91, 219–245.

Bontemps, S., Kaemmerlen, A., Blatman, G., Mora, L., 2013. Reliability of dynamic simulation models for building energy in the context of low-energy buildings.

Bontemps, S., Mora, L., Schumann, M., 2016. Validation exprimentale applique la modlisation dune cellule test de type basse consommation. In: Confrence IBPSA France. Marne-la-Valle.

Bouyer, J., Inard, C., Musy, M., Jul. 2011. Microclimatic coupling as a solution to improve building energy simulation in an urban context. Energy and Buildings 43 (7), 1549–1559.

Bozonnet, E., 2006. Les micro climats urbains et la demande énergétique du bâti.

Bozonnet, E., Musy, M., Calmet, I., Rodriguez, F., Mar. 2015. Modeling methods to assess urban fluxes and heat island mitigation measures from street to city scale. International Journal of Low-Carbon Technologies 10 (1), 62–77.

Cette thèse est accessible à l'adresse : http://theses.insa-lyon.fr/publication/2018LYSEI071/these.pdf
© [L. Frayssinet], [2018], INSA Lyon, tous droits réservés

552 Bruse, M., 2004. Envi-met 3.0: Updated model overview.

553 Bueno, B., Norford, L., Hidalgo, J., Pigeon, G., Jul. 2013. The urban weather
554 generator. Journal of Building Performance Simulation 6 (4), 269–281.

555 BuildSysPro, 2018. Documentation, EDF R & D.

556 Chen, H., Ooka, R., Harayama, K., Kato, S., Li, X., Dec. 2004. Study on
557 outdoor thermal environment of apartment block in Shenzhen, China with
558 coupled simulation of convection, radiation and conduction. Energy and
559 Buildings 36 (12), 1247–1258.

560 Clarke, J., 2007. Energy simulation in building design. Routledge.

561 Còstola, D., Blocken, B., Hensen, J., Oct. 2009. Overview of pressure coef-
562 ficient data in building energy simulation and airflow network programs.
563 Building and Environment 44 (10), 2027–2036.

564 CSTB, 2012. RT2012: Règles Th-U, fascicule 4 : parois opaques.

565 de la Flor, F. S., Domìnguez, S. A., May 2004. Modelling microclimate in
566 urban environments and assessing its influence on the performance of sur-
567 rounding buildings. Energy and Buildings 36 (5), 403–413.

568 EnergyPlus, 2018. Documentation, U.S. Department of Energy.

569 Franke, J., 2006. Recommendations of the COST action C14 on the use of
570 CFD in predicting pedestrian wind environment. In: The fourth interna-
571 tional symposium on computational wind engineering, Yokohama, Japan.
572 pp. 529–532.

Cette thèse est accessible à l'adresse : http://theses.insa-lyon.fr/publication/2018LYSEI071/these.pdf
© [L. Frayssinet], [2018], INSA Lyon, tous droits réservés

573 Frayssinet, L., Merlier, L., Kuznik, F., Hubert, J.-L., Milliez, M., Roux, J.-J.,
574 2017. Modeling the heating and cooling energy demand of urban buildings
575 at city scale. Renewable and Sustainable Energy Reviews.

576 Ghiaus, C., Allard, F., Santamouris, M., Georgakis, C., Nicol, F., Apr. 2006.
577 Urban environment influence on natural ventilation potential. Building and
578 Environment 41 (4), 395–406.

579 Goffart, J., 2016. Données d'entrée: climat. In: Energétique des bâtiments
580 et simulation thermique. Blanche BTP. Eyrolles, pp. 231–240.

581 Gros, A., Bozonnet, E., Inard, C., Musy, M., Feb. 2016. Simulation tools to
582 assess microclimate and building energy A case study on the design of a
583 new district. Energy and Buildings 114, 112–122.

584 Jokisalo, J., Kurnitski, J., Korpi, M., Kalamees, T., Vinha, J., Feb. 2009.
585 Building leakage, infiltration, and energy performance analyses for Finnish
586 detached houses. Building and Environment 44 (2), 377–387.

587 Le Bras, J., Masson, V., Jun. 2015. A fast and spatialized urban weather
588 generator for long-term urban studies at the city-scale. Frontiers in Earth
589 Science 3.

590 Lemonsu, A., Grimmond, C. S. B., Masson, V., 2004. Modeling the surface
591 energy balance of the core of an old mediterranean city: Marseille. Journal
592 of Applied Meteorology 43 (2), 312–327.

593 Malys, L., Musy, M., Inard, C., Jul. 2015. Microclimate and building energy
594 consumption: study of different coupling methods. Advances in Building
595 Energy Research 9 (2), 151–174.

Cette thèse est accessible à l'adresse : http://theses.insa-lyon.fr/publication/2018LYSEI071/these.pdf
© [L. Frayssinet], [2018], INSA Lyon, tous droits réservés

596 Masson, V., 2000. A physically based scheme for the urban energy budget in
597 atmospheric models. Boundary layer meteorology 94, 357–397.

598 Masson, V., Marchadier, C., Adolphe, L., Aguejdad, R., Avner, P., Bon-
599 homme, M., Bretagne, G., Briottet, X., Bueno, B., de Munck, C., Doukari,
600 O., Hallegatte, S., Hidalgo, J., Houet, T., Le Bras, J., Lemonsu, A., Long,
601 N., Moine, M.-P., Morel, T., Nolorgues, L., Pigeon, G., Salagnac, J.-L.,
602 Viguié, V., Zibouche, K., Dec. 2014. Adapting cities to climate change: A
603 systemic modelling approach. Urban Climate 10, 407–429.

604 Merlier, L., Frayssinet, L., Johannes, K., Kuznik, F., 2018a. On the impact
605 of local microclimate on building performance simulation. part i: Predic-
606 tion of building external conditions. submitted to Building Performance
607 Simulation.

608 Merlier, L., Frayssinet, L., Johannes, K., Kuznik, F., 2018b. On the impact
609 of local microclimate on building performance simulation. part ii: Effect
610 of external conditions on the dynamic thermal behavior of buildings. sub-
611 mitted to Building Performance Simulation.

612 Merlier, L., Kuznik, F., Rusaoun, G., Salat, S., 2018c. Derivation of generic
613 typologies for microscale urban airflow studies. Sustainable Cities and So-
614 ciety 36, 71 – 80.

615 Météo France, 2017. Météo et climat : données climatiques de la station de
616 lyon.

617 Mirsadeghi, M., Còstola, D., Blocken, B., Hensen, J., Jul. 2013. Review
618 of external convective heat transfer coefficient models in building energy

Cette thèse est accessible à l'adresse : http://theses.insa-lyon.fr/publication/2018LYSEI071/these.pdf
© [L. Frayssinet], [2018], INSA Lyon, tous droits réservés

simulation programs: Implementation and uncertainty. Applied Thermal Engineering 56 (1-2), 134–151.

Moonen, P., Defraeye, T., Dorer, V., Blocken, B., Carmeliet, J., Sep. 2012. Urban Physics: Effect of the micro-climate on comfort, health and energy demand. Frontiers of Architectural Research 1 (3), 197–228.

Morille, B., Lauzet, N., Musy, M., Nov. 2015. SOLENE-microclimate: A Tool to Evaluate Envelopes Efficiency on Energy Consumption at District Scale. Energy Procedia 78, 1165–1170.

Musy, M., Bozonnet, E., 2016. Données d'entrée: Microclimat et environnement proche. In: Energétique des bâtiments et simulation thermique. Blanche BTP. Eyrolles, pp. 240–256.

Musy, M., Calmet, I., Bozonnet, E., Rodriguez, F., 2012. Modélisation des interactions ville climat energie. Références Modélisation urbaine: de la représentation au projet, 16–33.

Musy, M., Malys, L., Morille, B., Inard, C., Dec. 2015. The use of SOLENE-microclimat model to assess adaptation strategies at the district scale. Urban Climate 14, 213–223.

Nunez, M., Oke, T., 1977. The Energy Balance of an Urban Canyon. J. Appl. Meteor. 16, 11–19.

Oke, T., 2002. Boundary layer climates, 2nd Edition. Routlege.

Oke, T. R., 1982. The energetic basis of the urban heat island. Quarterly Journal of the Royal Meteorological Society 108 (455), 1–24.

Cette thèse est accessible à l'adresse : http://theses.insa-lyon.fr/publication/2018LYSEI071/these.pdf
© [L. Frayssinet], [2018], INSA Lyon, tous droits réservés

641 Penicaud, H., 2016. Introduction. In: Energétique des bâtiments et simula-
642 tion thermique. Blanche BTP. Eyrolles, pp. 17–21.

643 Pigeon, G., Zibouche, K., Bueno, B., Le Bras, J., Masson, V., Jun. 2014.
644 Improving the capabilities of the Town Energy Balance model with up-
645 to-date building energy simulation algorithms: an application to a set of
646 representative buildings in Paris. Energy and Buildings 76, 1–14.

647 Plessis, G., Kaemmerlen, A., Lindsay, A., Mar. 2014. BuildSysPro: a Model-
648 ica library for modelling buildings and energy systems. Lund, Sweden, pp.
649 1161–1169.

650 Ramponi, R., Gaetani, I., Angelotti, A., Aug. 2014. Influence of the urban
651 environment on the effectiveness of natural night-ventilation of an office
652 building. Energy and Buildings 78, 25–34.

653 Robinson, D., Haldi, F., Kämpf, J., Leroux, P., Perez, D., Rasheed, A.,
654 Wilke, U., 2009. CitySim: Comprehensive micro-simulation of resource
655 flows for sustainable urban planning. In: Eleventh International IBPSA
656 Conference. pp. 1083–1090.

657 Rochard, U., Shanthirablan, S., Brejon, C., Chateau le Bras, M., 2015.
658 Bâtiments résidentiels: Typologie du parc existant et solutions exemplaires
659 pour la rénovation énergétique en France. Tech. rep.

660 Roux, J., Kuznik, F., 2016. Modélisation thermique du bâtiment. In: En-
661 ergétique des bâtiments et simulation thermique. Blanche BTP. Eyrolles,
662 pp. 26–43.

Cette thèse est accessible à l'adresse : http://theses.insa-lyon.fr/publication/2018LYSEI071/these.pdf
© [L. Frayssinet], [2018], INSA Lyon, tous droits réservés

663 Santamouris, M., Oct. 2014. On the energy impact of urban heat island and
664 global warming on buildings. Energy and Buildings 82, 100–113.

665 Santamouris, M., Cartalis, C., Synnefa, A., Kolokotsa, D., Jul. 2015. On the
666 impact of urban heat island and global warming on the power demand
667 and electricity consumption of buildingsA review. Energy and Buildings
668 98, 119–124.

669 Santamouris, M., Papanikolaou, N., Livada, I., Koronakis, I., Georgakis, C.,
670 Argiriou, A., Assimakopoulos, D. N., 2001. On the impact of urban climate
671 on the energy consumption of buildings. Solar energy 70 (3), 201–216.

672 Schlünzen, K. H., Grawe, D., Bohnenstengel, S. I., Schlüter, I., Koppmann,
673 R., Apr. 2011. Joint modelling of obstacle induced and mesoscale changes-
674 Current limits and challenges. Journal of Wind Engineering and Industrial
675 Aerodynamics 99 (4), 217–225.

676 Schumann, M., Charrier, B., Plessis, G., Wall-Ribot, B., 2016. BuildSysPro
677 un bibliothèque Modelica open source pour l'énergétique des bâtiments et
678 des quartiers. In: Conférence IBPSA France. Marne la Vallée, France.

679 Sun, Y., Augenbroe, G., Jul. 2014. Urban heat island effect on energy appli-
680 cation studies of office buildings. Energy and Buildings 77, 171–179.

681 Sun, Y., Heo, Y., Tan, M., Xie, H., Jeff Wu, C., Augenbroe, G., Jan. 2014.
682 Uncertainty quantification of microclimate variables in building energy
683 models. Journal of Building Performance Simulation 7 (1), 17–32.

684 Sun, Y., Heo, Y., Xie, H., Tan, M., Wu, J., Augenbroe, G., 2011. Uncertain-
685 ity quantification of microclimate variables in building energy simulation.

Cette thèse est accessible à l'adresse : http://theses.insa-lyon.fr/publication/2018LYSEI071/these.pdf
© [L. Frayssinet], [2018], INSA Lyon, tous droits réservés

In: Proceedings of Building Simulation 2011: 12th Conference of International Building Performance Simulation Association. Sydney, Australia, pp. 2423–2430.

Tominaga, Y., Mochida, A., Yoshie, R., Kataoka, H., Nozu, T., Yoshikawa, M., Shirasawa, T., 2008. AIJ guidelines for practical applications of CFD to pedestrian wind environment around buildings. Journal of Wind Engineering and Industrial Aerodynamics 96, 1749–1761.

Toparlar, Y., Blocken, B., Maiheu, B., van Heijst, G., 2017. A review on the cfd analysis of urban microclimate. Renewable and Sustainable Energy Reviews 80, 1613 – 1640.

Yang, X., Zhao, L., Bruse, M., Meng, Q., Nov. 2012. An integrated simulation method for building energy performance assessment in urban environments. Energy and Buildings 54, 243–251.

Yi, Y. K., Feng, N., Sep. 2013. Dynamic integration between building energy simulation (BES) and computational fluid dynamics (CFD) simulation for building exterior surface. Building Simulation 6 (3), 297–308.

Cette thèse est accessible à l'adresse : http://theses.insa-lyon.fr/publication/2018LYSEI071/these.pdf
© [L. Frayssinet], [2018], INSA Lyon, tous droits réservés

List of Figures

Cette thèse est accessible à l'adresse : http://theses.insa-lyon.fr/publication/2018LYSEI071/these.pdf
© [L. Frayssinet], [2018], INSA Lyon, tous droits réservés

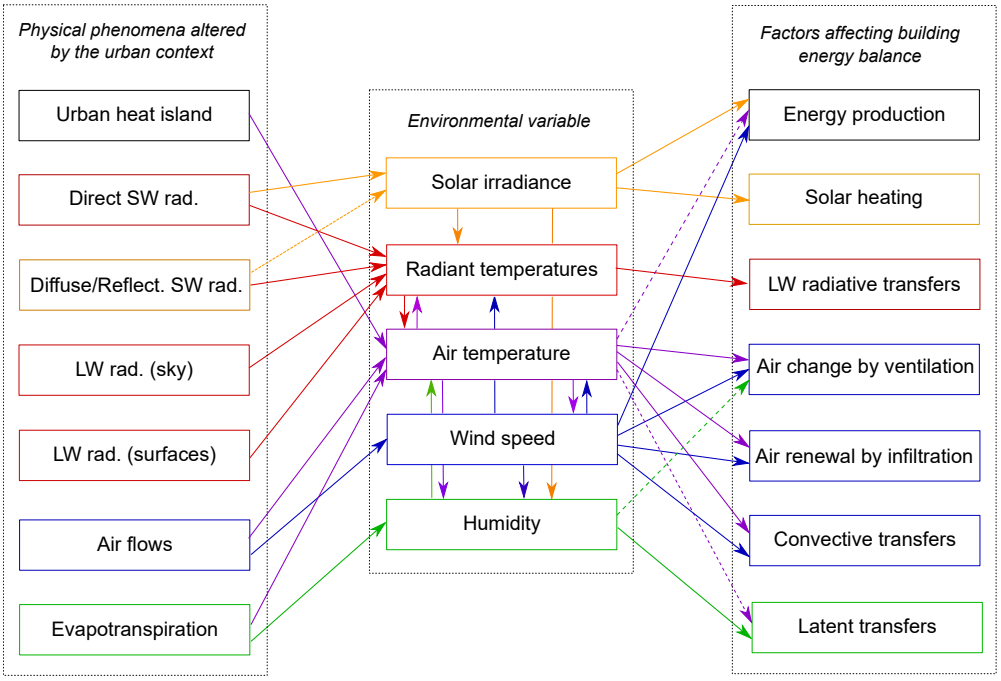

Figure 1: Urban environmental effects on building energy behavior

Cette thèse est accessible à l'adresse : http://theses.insa-lyon.fr/publication/2018LYSEI071/these.pdf
© [L. Frayssinet], [2018], INSA Lyon, tous droits réservés

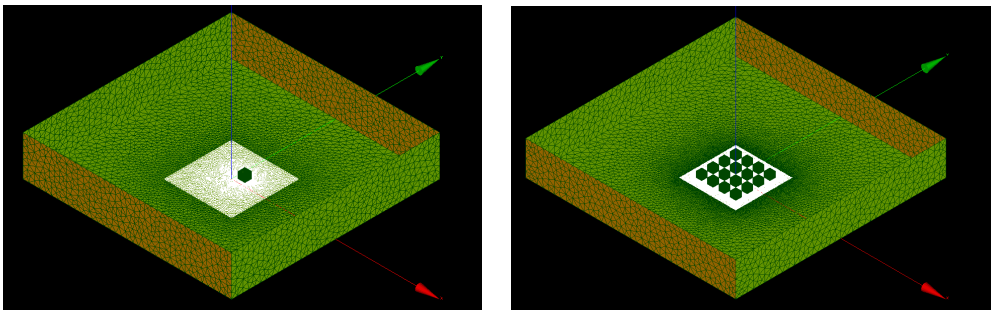

(a) Isolated (b) Array

Figure 2: Studied generic configurations: geometry and mesh.

Cette thèse est accessible à l'adresse : http://theses.insa-lyon.fr/publication/2018LYSEI071/these.pdf
© [L. Frayssinet], [2018], INSA Lyon, tous droits réservés

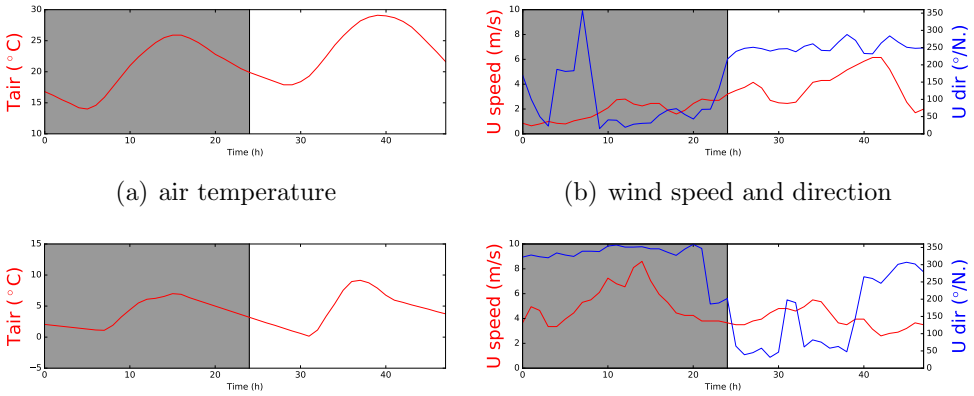

(a) air temperature (b) wind speed and direction

(c) air temperature (d) wind speed and direction

Figure 3: Weather data for the studied summer (a,b) and winter days (c,d).

Cette thèse est accessible à l'adresse : http://theses.insa-lyon.fr/publication/2018LYSEI071/these.pdf
© [L. Frayssinet], [2018], INSA Lyon, tous droits réservés

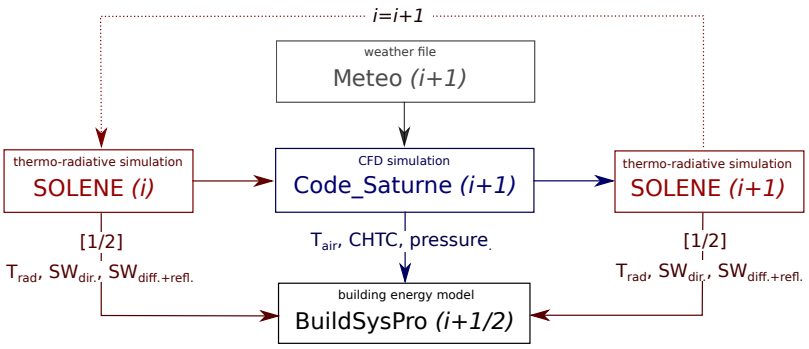

Figure 4: Principle of the coupling between SOLENE and Code_Saturne as well as between SOLENE-microclimat and BuildSysPro

Cette thèse est accessible à l'adresse : http://theses.insa-lyon.fr/publication/2018LYSEI071/these.pdf
© [L. Frayssinet], [2018], INSA Lyon, tous droits réservés

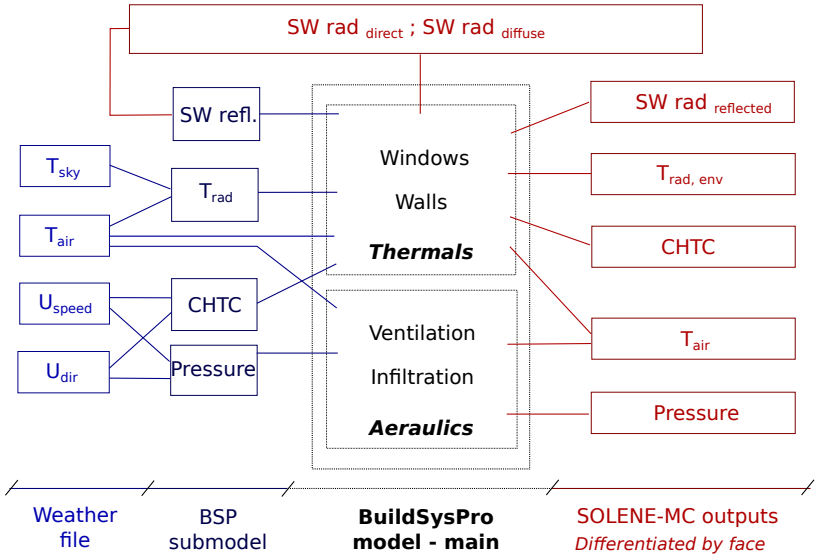

Figure 5: Setting of the different exeternal conditions in the BuildSysPro model

Cette thèse est accessible à l'adresse : http://theses.insa-lyon.fr/publication/2018LYSEI071/these.pdf
© [L. Frayssinet], [2018], INSA Lyon, tous droits réservés

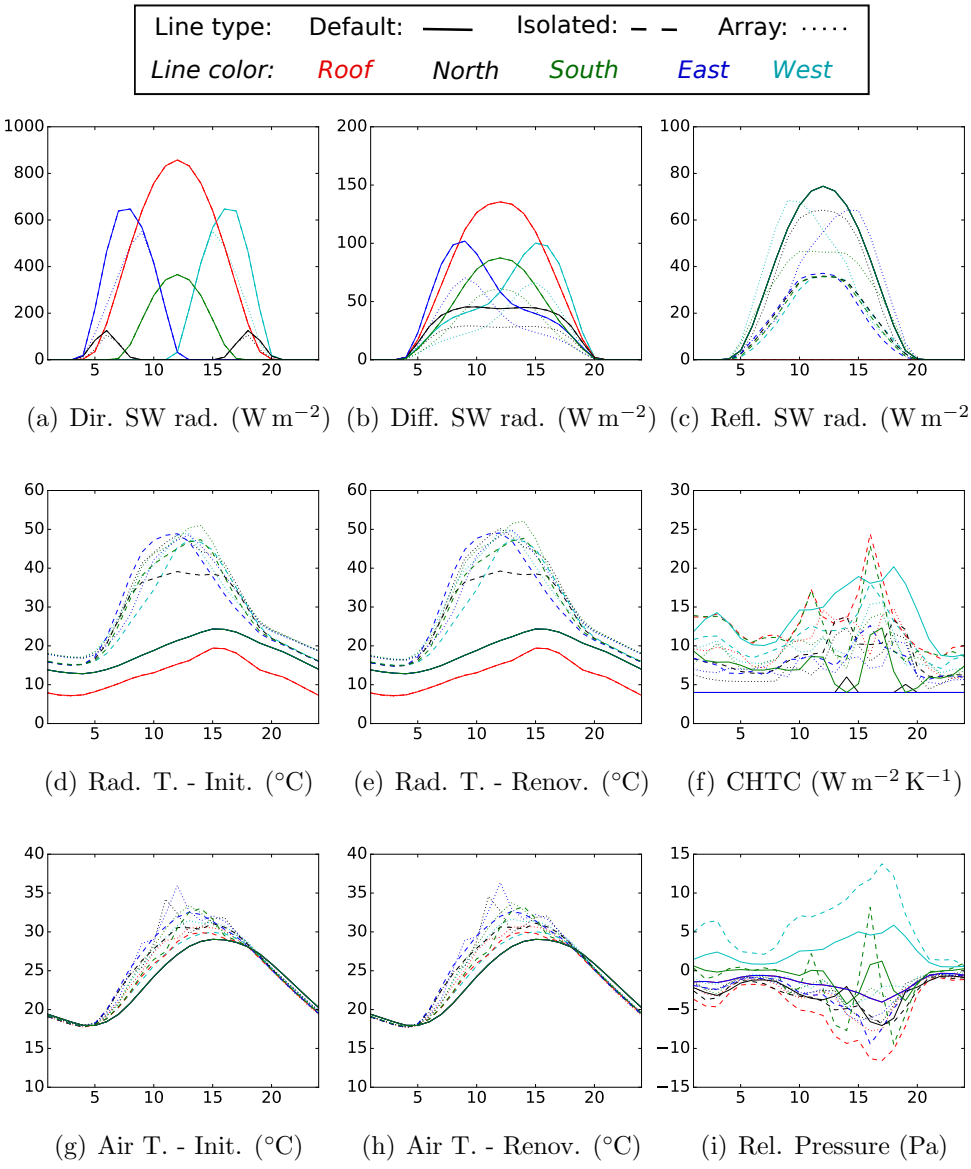

(a) Dir. SW rad. ($\mathrm{W\,m^{-2}}$) (b) Diff. SW rad. ($\mathrm{W\,m^{-2}}$) (c) Refl. SW rad. ($\mathrm{W\,m^{-2}}$)

(d) Rad. T. - Init. (°C) (e) Rad. T. - Renov. (°C) (f) CHTC ($\mathrm{W\,m^{-2}\,K^{-1}}$)

(g) Air T. - Init. (°C) (h) Air T. - Renov. (°C) (i) Rel. Pressure (Pa)

Figure 6: Comparison of the different building external conditions in summer (09 July).

Cette thèse est accessible à l'adresse : http://theses.insa-lyon.fr/publication/2018LYSEI071/these.pdf
© [L. Frayssinet], [2018], INSA Lyon, tous droits réservés

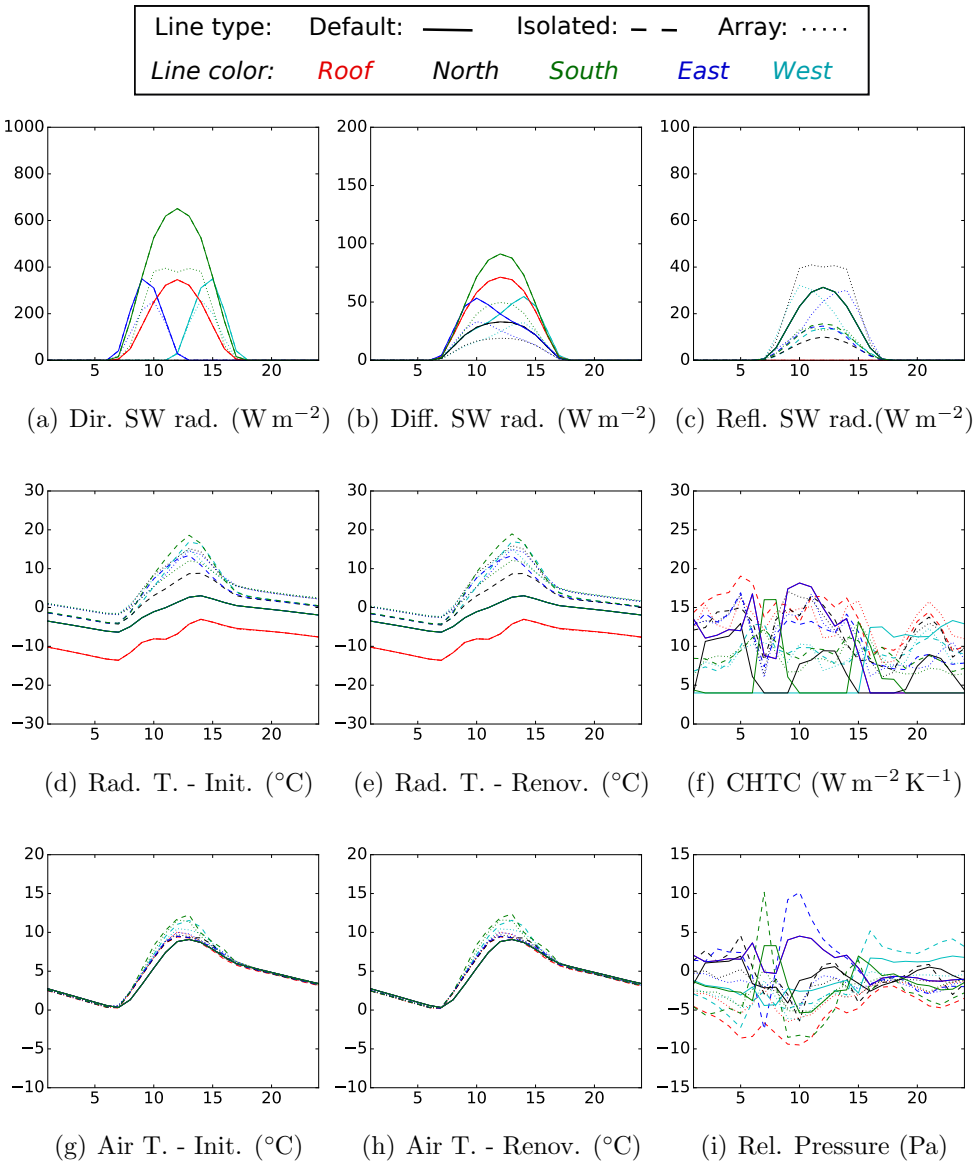

(a) Dir. SW rad. ($\mathrm{W\,m^{-2}}$) (b) Diff. SW rad. ($\mathrm{W\,m^{-2}}$) (c) Refl. SW rad.($\mathrm{W\,m^{-2}}$)

(d) Rad. T. - Init. (°C) (e) Rad. T. - Renov. (°C) (f) CHTC ($\mathrm{W\,m^{-2}\,K^{-1}}$)

(g) Air T. - Init. (°C) (h) Air T. - Renov. (°C) (i) Rel. Pressure (Pa)

Figure 7: Comparison of the different building external conditions in winter (11 November).

Cette thèse est accessible à l'adresse : http://theses.insa-lyon.fr/publication/2018LYSEI071/these.pdf
© [L. Frayssinet], [2018], INSA Lyon, tous droits réservés

List of Tables

Cette thèse est accessible à l'adresse : http://theses.insa-lyon.fr/publication/2018LYSEI071/these.pdf
© [L. Frayssinet], [2018], INSA Lyon, tous droits réservés

	Facade	Roof		Ground	
	Eq. layer	Structure	Insul.	Superficial	Core
albedo [-]	0.33	0.4	-	0.15	-
emissivity [-]	0.9	0.9	-	0.9	-
Initial state					
e [m]	0.31	0.07	-	0.1	1.9
λ [$\mathrm{W\,m^{-1}\,K^{-1}}$]	0.91	0.12	-	0.75	1.75
ρ [$\mathrm{kg\,m^{-3}}$]	1682	1150	-	2100	2300
c_p [$\mathrm{J\,kg^{-1}\,K^{-1}}$]	992	1050	-	950	1000
Renovated					
e [m]	0.54	0.073	0.3	0.1	1.9
λ [$\mathrm{W\,m^{-1}\,K^{-1}}$]	0.26	0.13	0.07	0.75	1.75
ρ [$\mathrm{kg\,m^{-3}}$]	1037	1150	102	2100	2300
c_p [$\mathrm{J\,kg^{-1}\,K^{-1}}$]	996	1050	1672	950	1000

Table 1: Equivalent building / surface properties used in the microclimatic model. With e the layer thickness, λ the thermal conductivity, ρ the density, c_p the specific thermal capacity

Cette thèse est accessible à l'adresse : http://theses.insa-lyon.fr/publication/2018LYSEI071/these.pdf
© [L. Frayssinet], [2018], INSA Lyon, tous droits réservés

Approach	Default	Microclimatic	
		Isolated Configuration	Array Configuration
Summer			
Dir. SW rad. [$W\,m^{-2}$]	137.2	137.2	122.4
Tot. diff. SW rad. [$W\,m^{-1}$]	57.1	45.7	44.1
Air T. [°C]	23.6	24.3 / 24.4	24.8 / 24.9
Rad. T. [°C]	16.9	24.7 / 24.7	26.3 / 26.5
CHTC [$W\,m^{-2}\,K^{-1}$]	6.6	10.5	8.6
Normalized infiltration flow[4]	0.27	0.43	0.13
Winter			
Dir. SW rad. [$W\,m^{-2}$]	67.9	67.9	49.6
Tot. diff. SW rad. [$W\,m^{-2}$]	21.4	18.1	16.2
Air T. [°C]	4.4	4.7 / 4.7	4.8 / 4.7
Rad. T. [°C]	-2.9	0.6 / 0.5	1.8 / 1.4
CHTC [$W\,m^{-2}\,K^{-1}$]	7.9	11.0	10.6
Normalized infiltration flow	0.32	0.45	0.20

Table 2: Averaged values of exetrnal conditions. When two values are given, the left value corresponds to the initial state, and the right value corresponds to the renovated state

Cette thèse est accessible à l'adresse : http://theses.insa-lyon.fr/publication/2018LYSEI071/these.pdf
© [L. Frayssinet], [2018], INSA Lyon, tous droits réservés

On the impact of local microclimate on building performance simulation. Part II: Effect of external conditions on the dynamic thermal behavior of buildings

Lucie Merlier[a,1,*], Loïc Frayssinet[a,1], Kévyn Johannes[a,1], Frédéric Kuznik[a,1]

[a] *Univ Lyon, CNRS, INSA-Lyon, Université Claude Bernard Lyon 1, CETHIL UMR5008, F-69621, Villeurbanne, France*
[b] *BHEE: High Energy Efficiency Buildings, joint laboratory CETHIL / EDF, France*

Abstract

Most of building energy models being not suited to integrate properly local urban ambient conditions, this study initiate a sensitivity analysis of the heating and cooling needs and operative temperature of buildings to local radiative, thermal and aeraulic external conditions. These conditions were estimated using possibilities of a building energy model (based on the BuildSysPro Modelica library) or derived from microclimatic simulations (SOLENE microclimat) for a generic isolated or urban building. The thermal behaviors of both an energy inefficient and efficient buildings in summer and winter are examined. Results show major effects of short and long wave radiative heat transfers as well as aeraulics. According to present results, and given current urban growth and climate change challenges as well as the development of energy conservative buildings, this last point may become particularly critical in the future.

*Corresponding author. Tel.: +33-472-437-483; Fax: +33-472-438-522
Email address: lucie.merlier@insa-lyon.fr (Lucie Merlier)

Cette thèse est accessible à l'adresse : http://theses.insa-lyon.fr/publication/2018LYSEI071/these.pdf
© [L. Frayssinet], [2018], INSA Lyon, tous droits réservés

Keywords: Building energy simulation, Environmental variables, Power needs, Thermal comfort, Heating and cooling, Ventilation.

Highlights

1. Effects of building external radiative, thermal and aeraulic conditions on building energy behavior are analyzed
2. Cooling and heating power loads as well as summer comfort are addressed
3. Modeling assumptions for the boundary conditions of an isolated building are discussed
4. Effects of an urban environment is examined

Cette thèse est accessible à l'adresse : http://theses.insa-lyon.fr/publication/2018LYSEI071/these.pdf
© [L. Frayssinet], [2018], INSA Lyon, tous droits réservés

Nomenclature

ϕ_{conv}	Convective heat flux [$\mathrm{W\,m^{-2}}$]
ϕ_{LW}	Long-wave radiation flux [$\mathrm{W\,m^{-2}}$]
σ	Stefan–Boltzmann constant [$\approx 5.67 \cdot 10^{-8}$ $\mathrm{Wm^{-2}K^{-4}}$]
h	Convective heat transfer coefficient [$\mathrm{W\,m^{-2}\,K^{-1}}$]
K	Air permeability [$\mathrm{m^3h^{-1}Pa^{-2/3}}$]
P	Pressure [Pa]
Q	Air flow rate [$\mathrm{m^3\,h^{-1}}$]
T	Temperature [K]

Cette thèse est accessible à l'adresse : http://theses.insa-lyon.fr/publication/2018LYSEI071/these.pdf
© [L. Frayssinet], [2018], INSA Lyon, tous droits réservés

Introduction

Because of their basic scope of application –modeling heat transfers *in* a building– common building energy simulation tools are generally not suited to integrate accurately building external conditions. This is even more true when considering urban buildings as simulations generally use typical weather files to specify external boundary conditions. As they characterize open terrains, weather data do not correspond to urban conditions. Indeed, in cities, the urban structure substantially affects building external conditions in terms of short wave radiation fluxes, air and radiant temperatures and wind related fluxes (Sun et al., 2011; Sun and Augenbroe, 2014; Merlier et al., 2018a). In addition, empirical correlations or generic surface averaged quantities are generally used to specify building boundary conditions, which leads to additional accuracy and errors in the modeling (Còstola et al., 2010; Mirsadeghi et al., 2013). Therefore, substantial physical uncertainties underlay usual energy simulations of urban buildings

As these biases become critical given the current urban growth and the development of energy conservative buildings in the context of climate change, several studies were developed during the last decade, to evaluate urban effects on building energy behavior at different scales. When based on measurements of external conditions around urban buildings, studies generally highlighted a decrease of heating needs and an increase of cooling needs compared to rural conditions, especially in hot regions (Zinzi et al., 2018; Salvati et al., 2017). As computational studies allow the computational domain to be controlled and parametric studies to be performed although necessarily involving some physical, mathematical and numerical assumptions, it

Cette thèse est accessible à l'adresse : http://theses.insa-lyon.fr/publication/2018LYSEI071/these.pdf
© [L. Frayssinet], [2018], INSA Lyon, tous droits réservés

is possible to further analyze these trends beyond measurement campaign limitations. Different approaches could be used for this purpose. In particular, Pigeon et al. (2014) used an urban canopy model (TEB (CNRM, 2015; Masson, 2000)) to estimate the building external conditions of typical old detached houses and evaluated their effects on building energy loads using the embedded building energy model. Results showed that long wave radiative heat exchanges between urban surfaces may increase cooling loads by 18 % and decrease heating load by 6 % in dense urban area compared to an open environment. Using more detailed approaches to model urban environments but on smaller scales, i.e. using microclimatic models such as SOLENE-microclimat or ENVImet, internally or externally coupled with a dynamic building energy model, Bouyer et al. (2011); Yang et al. (2012); Malys et al. (2015) evaluated the impact of adjusted external conditions due to the presence of a specific urban environment on building energy needs. Solar loads, infrared exchanges and convective heat transfers were more particularly analyzed. Results highlighted the substantial influence of the urban radiative environment on building energy needs. Solar masks were shown to reduce cooling loads and increase heating loads respectively by 18.8 % and 0.8 % in Yang et al. (2012), and long wave radiative heat exchanges generally constituted heat gains for buildings. More particularly, the urban thermo radiative environments were shown to increase the cooling needs of a newly built highly glazed office building by about 20 % (Bouyer et al., 2011) and to decrease the heating needs of a usual slab by about 7 % (Malys et al., 2015). Alteration of convective heat exchanges by surrounding buildings were shown less influential and even negligible for well insulated buildings. Effects

Cette thèse est accessible à l'adresse : http://theses.insa-lyon.fr/publication/2018LYSEI071/these.pdf
© [L. Frayssinet], [2018], INSA Lyon, tous droits réservés

of aeraulics are less studied, Yang et al. (2012) showed that an increase of outdoor air temperature by about 1 °C on average during daytime may impact on buildings cooling needs through air renewal by around 10 %. However, to accurately estimate aeraulic induced thermal loads, pressure contribution should be considered along, as it determines the wind driven infiltration and natural ventilation potential of buildings. Indeed, dedicated studies show that the natural ventilation potential of buildings strongly decreases with urban density, potentially up to 50 % (Ramponi et al., 2014), which strongly limits natural free cooling.

Hence, urban environments significantly influence the energy behavior of urban buildings by modifying external conditions and thus radiative, thermal and aeraulic exchanges between the building and its built environment compared to a rural configuration. But studies rarely consider simultaneously aeraulic, radiative and thermal conditions. In consequence, this research aims at providing a deeper knowledge on the influence of boundary conditions on the thermal behavior of buildings. It notably considers dynamic influences, and highlights coupled effects. For this purpose, different sets of building external conditions were derived from state-of-the-art approaches for the cold and hot seasons. These conditions were more particularly assessed using (see Part I (Merlier et al., 2018a)).

- (1) possibilities of a building energy model, namely BuildSysPro (Plessis et al., 2014; Schumann et al., 2016), for a building standing alone given the lack of general guidelines relative to the modeling of urban conditions - *Default* approach;
- (2) a microclimatic simulation – *microclimatic* approach – performed

Cette thèse est accessible à l'adresse : http://theses.insa-lyon.fr/publication/2018LYSEI071/these.pdf
© [L. Frayssinet], [2018], INSA Lyon, tous droits réservés

using SOLENE-microclimat (Morille et al., 2015; Musy et al., 2015) for the same isolated building, but assumed located on a mineral ground - *Isolated* configuration

- (3) and the same microclimatic approach, but considering the building located in a theoretical urban environment composed of a regular array of 4×4 similar buildings - *Array* configuration.

Corresponding local external conditions were used to set boundary conditions to a detailed building energy model (Sec. 1) in order to compare winter and summer energy needs and summer comfort (Sec. 2). On this basis, the influence of adjusting the different external conditions due to changes of modeling approach (1-2) and urban environment (2-3) on the dynamic behavior of the modeled building is discussed (Sec. 3).

1. Building model

1.1. General settings

A monozone 10 m high cubic building model was built using BuildSysPro, a Modelica library focusing on French building stock developed by EDF R&D (Plessis et al., 2014; Schumann et al., 2016) (for more details, see Part I Merlier et al. (2018a)).

To relevantly integrate the contribution of the different boundary conditions, the building model includes two sub-models (Fig. 1). First, the aeraulic sub-model models infiltration and ventilation flow rates and the related heat transfers to the air node. Second, the thermal sub-model models the convective, radiative and conductive heat transfers through opaque walls and

Cette thèse est accessible à l'adresse : http://theses.insa-lyon.fr/publication/2018LYSEI071/these.pdf
© [L. Frayssinet], [2018], INSA Lyon, tous droits réservés

windows and in the indoor volume. The resolution of convective heat transfers being based on a finite volume approach, each wall layer was discretized with more than 10 nodes per meter, depending on the thermal diffusivity of materials to relevantly study building dynamics (Frayssinet et al., 2017a). The lower the diffusivity, the finer the discretization.

The thermal properties of the building envelope were set to match TABULA indications (Rochard et al., 2015) for the most represented multifamily houses in France. This typology of buildings corresponds to uninsulated buildings built before 1915 – *Initial* building. These buildings could be renovated – *Renovated* building –, thus substantially improving their thermal performance (see Tab. 2). The glazed ratio of these buildings equals 23 %. In the model, glazed surfaces were assumed equally distributed over the four vertical faces.

[Figure 1 about here.]

For simulation, either a heating set point equal to 19 °C and a cooling set point equal to 28 °C, or a floating temperature evolution in summer was specified. A ventilation air flow rate of 1 ACH was assumed along with a wall permeability under a pressure difference of 4 Pa (reference infiltrated air flow rate per meter square of envelope Q_{4Pa}) equal to $Q_{4Pa} = 2\,\mathrm{m^3\,h^{-1}\,m^{-2}}$ for the initial building or ten times less for renovated building. Neither model for humidity was considered as air moisture impact is assumed small in temperate climates; nor energy system, internal gains, free cooling nor shading are neither considered in order to evaluate the intrinsic response of the building to its external conditions.

Cette thèse est accessible à l'adresse : http://theses.insa-lyon.fr/publication/2018LYSEI071/these.pdf
© [L. Frayssinet], [2018], INSA Lyon, tous droits réservés

[Table 1 about here.]

1.2. Boundary conditions

Based on the three sets of data detailed in the introduction, building external conditions were assigned by face in the building model. These conditions are the direct and diffuse short wave radiative fluxes, radiant and air temperatures, convective heat transfer coefficient ($CHTC$) and relative pressure.

The developed methodology enables the different sets of conditions to be mixed in order to highlight specific contributions of one or several external conditions on simulation outputs. Note that, although being actually similar, air temperature for the thermal or the aeraulic sub-models were differentiated to characterize separately the respective contribution of each type of transfer. In the following, T_{vent} stands for the temperature used as input to the aeraulic sub-model and T_{air} stands for the input used by the thermal sub-model.

In addition, to integrate and further evaluate the respective contributions of each external condition, different sub-models were set or implemented in the building energy model to specify boundary conditions. Especially, considering a wall i in the aeraulic model, infiltration air flow rates ($Q_{face,i}$) were estimated thanks to the mass balance of the indoor air volume assuming a uniform permeability (K_i) for the roof and walls and a power low function (Eq. 1):

$$Q_{face,i} = \pm K_i \times |P_{ext,i} - P_{int}|^{2/3} \quad \text{and} \quad \sum_i Q_{face,i} = 0 \tag{1}$$

with $P_{ext,i} - P_{int}$ the outdoors / indoors face pressure difference. Inlet T_{vent} used for ventilation was assumed equal to the average of T_{vent} estimated next

Cette thèse est accessible à l'adresse : http://theses.insa-lyon.fr/publication/2018LYSEI071/these.pdf
© [L. Frayssinet], [2018], INSA Lyon, tous droits réservés

to the four vertical faces of the building, while $T_{vent,i}$ used for infiltration are differentiated for each face and used accordingly.

Regarding the thermal model, long wave radiative heat transfers at building outer surfaces (ϕ_{LW}) were evaluated based on the Stefan-Boltzmann law (Eq. 2):

$$\phi_{LW,i} = \sigma \times (T^4_{rad,env,i} - T^4_{surf,i}) \tag{2}$$

with σ the Stefan–Boltzmann constant.

Convective heat transfers ($\phi_{conv,i}$) were estimated using local CHTC and air temperature, following Eq. 3:

$$\phi_{conv,i} = CHTC \times (T_{air,i} - T_{surf,i}) \tag{3}$$

with $T_{surf,i}$, the surface temperature estimated using the surface balance considering the conductive, convective and radiative contributions.

Short wave radiation fluxes transmitted by windows were distributed over the floor.

Based on these different settings, simulations were run using the Dymola simulation environment, looping 10 times on the same day, i.e. the 06 November for winter and the 09 July for summer.[1] Results of the simulated tenth day were kept for analysis, the nine first loops being used for the model initialization.

[1]Individual annual simulation lasting between 1 and 2 minutes on a 2.5 GHz processor and 8 GB of RAM computer

Cette thèse est accessible à l'adresse : http://theses.insa-lyon.fr/publication/2018LYSEI071/these.pdf
© [L. Frayssinet], [2018], INSA Lyon, tous droits réservés

2. Result Analysis

Considering the three sets of external conditions used to specify boundary conditions to the building energy model, i.e. the default and microclimatic approaches and isolated and array configurations, the following analyses results regarding:

- The temporal evolution of the global energy needs and operative temperature (Figures 2, 3 and 4). These results highlight differences induced by the different modeling approaches and configurations, i.e. considering one or another set of boundary conditions.

- The dynamic contribution of each external condition on heating and cooling needs as well as operative temperature (Figures 5, 6 and 7). These results highlight the impact of each distinct external sollicitation on the building thermal behavior.

Tab. 3 and 1 complete Fig. 2–7 by precising the mean and maximum differences of heating and cooling needs as well as operative temperature, induced by the different types of heat transfers, i.e. short wave and long wave radiative, convective as well as aeraulic-induced heat transfers.

2.1. Impact of the modeling approach

[Figure 2 about here.]

[Figure 3 about here.]

[Table 2 about here.]

Cette thèse est accessible à l'adresse : http://theses.insa-lyon.fr/publication/2018LYSEI071/these.pdf
© [L. Frayssinet], [2018], INSA Lyon, tous droits réservés

2.1.1. Heating needs

Considering a building standing alone, Fig.2 shows that renovation induces an averaged reduction of heating needs by a factor of four thanks to the improved thermal insulation and air tightness. As a consequence, renovation also tends to reduce the influence of the modeling approach on it. More precisely, using the boundary conditions derived from the microclimatic approach induces lower heating needs than estimated based on the default approach: the averaged difference equals 6 % and 3 % respectively for the initial and renovated buildings. The difference is mostly due to the contribution of the environmental radiant temperature, which is higher in the microclimatic approach, especially during daytime. This higher temperature decreases heating needs by 9 % and 3 % respectively for the initial and renovated buildings.

With respect to other boundary conditions, the sensitivity of the renovated building to the modification of wind-induced heat transfers is rather negligible. These effects are more substantial in the initial building, for which modifying the aeraulic fluxes increases the daily heating needs by 3 % because of higher infiltrated air flow rate, which are not compensated by the slight increase of air temperature. Conversely, convective heat losses are reduced by 2 % when based on the microclimatic rather than the default approach, probably due to higher air temperature. Taking the smaller short-wave solar reflections derived from the microclimatic approach into account instead of the default flux, slightly increases the heating needs by 1 % and 2 % respectively for the initial and renovated buildings.

Cette thèse est accessible à l'adresse : http://theses.insa-lyon.fr/publication/2018LYSEI071/these.pdf
© [L. Frayssinet], [2018], INSA Lyon, tous droits réservés

2.1.2. Cooling needs

Contrary to heating needs, renovation does not substantially reduced cooling needs. Indeed, cooling needs are about six times smaller than heating needs for initial building whereas they are comparable for the renovated building. Considering the default set of boundary conditions, renovation even tends to substantially increase the cooling period, which leads to an increase of energy needs by 60 %. The cooling period is also increased in the renovated building when considering boundary conditions derived from the microclimatic approach, but to a lesser extent. As the corresponding maximal power loads are decreased by 30 %, estimates of energy needs are similar for both the initial and renovated buildings according to the microclimatic approach.

Regarding the contribution of the different boundary conditions, and similarly to Sec. 2.1.1, the contribution of long wave radiative heat transfers mostly explains the differences of cooling needs observed when considering boundary conditions derived form the microclimatic instead of the default approach. This contribution explains both the earlier need of cooling and the increased power needs. As a result, modifying the environmental radiant temperature increases cooling needs by 33 % and 9 % respectively for the initial and renovated buildings respectively. Simultaneously modifying all boundary conditions increases cooling needs by 25 % and 10 % still for the initial and renovated buildings respectively.

Modifying other external conditions and associated heat transfers induces deviations of the same order of magnitude for both building states. The second most important change in cooling needs is induced by the modification

Cette thèse est accessible à l'adresse : http://theses.insa-lyon.fr/publication/2018LYSEI071/these.pdf
© [L. Frayssinet], [2018], INSA Lyon, tous droits réservés

of short wave radiation fluxes. As the received reflected fluxes are lower in the microclimatic than in the default approach, corresponding cooling needs are reduced by 6 % for both building states. Conversely, as the microclimatic approach estimates higher infiltrated air flow rates and local air temperatures, the aeraulic-induced heat transfers increase cooling needs by 4 % when based on corresponding data. Regarding convective heat transfers, considering the increased CHTC and local air temperature derived from the microclimatic approach induces a decrease of cooling needs by 6 % and 8 % respectively in the initial and renovated buildings. This counter-intuitive contribution can be explained by a higher solar heat removal at building outer surfaces, which limits overheating.

2.1.3. Summer comfort

Indoor operative temperatures are generally higher than the outdoor air temperature and show much smaller variation. Because of inertia, the operative temperature range in both the initial and the renovated buildings is of 3 °C, which is four times smaller than the range of meteorological air temperature. In addition, because of the improved thermal insulation and air tightness of the renovated building, the mean operative temperature is more than 4.5 °C higher than in the initial building. Indoor operative temperature even reaches 35 °C during the afternoon in this configuration, which substantially exceeds summer comfort requirements.

With respect to the respective influence of boundary conditions, observed trends are comparable to Sec. 2.1.2 as external conditions and building properties are similar. Nonetheless, because of the buffer effect of thermal inertia, effects are almost constant over the simulated period. The contribution

Cette thèse est accessible à l'adresse : http://theses.insa-lyon.fr/publication/2018LYSEI071/these.pdf
© [L. Frayssinet], [2018], INSA Lyon, tous droits réservés

of long wave radiation is the most important factor affecting the operative temperature. The higher environmental radiant temperature induces an increase of the indoor operative temperature of 2.2 °C and 1.3 °C respectively for the initial and renovated buildings. As a result, taking all the boundary conditions derived from the microclimatic approach into account instead of conditions derived from the default approach tends to increase operative temperature by 1.6 °C and 1.3 °C respectively for the initial and renovated buildings.

2.2. Impact of the urban environment

[Figure 4 about here.]

[Figure 5 about here.]

Regarding the effects of adjusting the other types of heat transfers on the floating operative temperature, it can be noticed that the aeraulic contribution is equivalent to, and even more important than, the contribution of long wave radiation for the initial and renovated buildings. The aeraulic contribution is opposite but comparable to that of short wave radiation in the initial building. It represents the half of it in the renovated building. Hence, to address free cooling issues, Fig. 8 further analyzes the free cooling potential of buildings using natural ventilation, especially regarding the renovated building, which shows hot indoor temperatures. Results highlight that, if decreasing by a factor 10 the air tightness of the renovated building to simulate a volunteer over-ventilation, the operative temperature decreases on average by 1.3 °C in the isolated configuration. Such an effect is more important than the effect of solar masks in the array configuration. The decrease

Cette thèse est accessible à l'adresse : http://theses.insa-lyon.fr/publication/2018LYSEI071/these.pdf
© [L. Frayssinet], [2018], INSA Lyon, tous droits réservés

of operative temperature by volunteer over-ventilation is reduced down to less than 0.4 °C when considering an urban configuration. Indeed, because of wind masks, ventilation air flows are reduced by a factor of three in this configuration, which points out the prejudicial lack of cooling potential in urban environment.

3. Conclusion

Recent applications of building energy simulation, such as the design of passive strategies, integration of renewables, network management or performance guarantee require the use of appropriate boundary conditions. This requirement becomes critical in urban and building physics because of global warming and urban growth issues. However, building energy models were basically not designed to address such problems. Thus, towards more accurate and integrated energy simulation of urban buildings, the present study discussed the dependence of simulation results, and more largely of building energy performance, to adaptive boundary conditions. The objective was to highlight the influence of the modeling approach and of the urban environment on the dynamic thermal behavior of typical urban buildings. For this purpose, radiative, thermal and aeraulic conditions were derived from two state-of-the-art modeling approaches for two built configurations, and used as input for a detailed building energy simulation. On this basis, typical time integrated as well as dynamic behaviors of an old or thermally renovated building for typical sunny and windy summer and winter days under temperate climatic conditions were discussed.

Comparing results obtained for a stand alone building but considering

Cette thèse est accessible à l'adresse : http://theses.insa-lyon.fr/publication/2018LYSEI071/these.pdf
© [L. Frayssinet], [2018], INSA Lyon, tous droits réservés

boundary conditions derived from a building energy or a microclimatic model, results indicated that accounting for the surface temperatures of surrounding surfaces is crucial. Adjusting the environmental radiant temperature was found to be the most influential modification of external conditions on power needs and operative temperature. This major effect has nonetheless to be related to the substantial difference estimated between the air and environmental radiant temperatures highlighted in Merlier et al. (2018a).

Comparing results obtained for an isolated or a urban building, results pointed out the major effect of solar masks on power needs and operative temperature, as they decrease heat gains. This effect was generally found balanced by the modification of other boundary conditions. In particular, effects of aeraulics were shown substantial, especially with respect to the summer comfort in urban environments. Indeed, in this configuration, the absolute influence of wind sheltering was found comparable to that of solar masks and the small urban natural ventilation potential was shown particularly prejudicial for free cooling.

The different above-mentioned effects were shown dependent on the thermal performance of building envelopes. Because of its insulation and air tightness, the renovated building appeared mostly impacted on by the modification of solar fluxes, as well as, to a lesser extent by the environmental radiant temperature and aeraulics. On the contrary, most of the different boundary conditions significantly altered the thermal behavior of the initial building.

Hence, the implemented methodology demonstrated the need of accounting for comprehensive sets of appropriate boundary conditions to address

Cette thèse est accessible à l'adresse : http://theses.insa-lyon.fr/publication/2018LYSEI071/these.pdf
© [L. Frayssinet], [2018], INSA Lyon, tous droits réservés

current building energy issues. Indeed, not only radiative conditions were shown dependent on the general modeling strategy developed and influential on the dynamic thermal behavior of urban buildings. Wind related heat transfers, which also influence long wave radiative exchanges, were also shown dependent on the general modeling strategy and influential on the dynamic thermal behavior of urban buildings. To address these contributions, CFD appears very promising. Indeed, although computational time and turbulence modeling challenges still generally prevent its use for most of building energy problems, recent developments such as lattice Boltzmann large eddy simulations (Obrecht et al., 2015; Merlier et al., 2018b) are likely able to improve the consideration of aeraulic effects in building energy studies. However, in order to extend the present methodology to a whole year, ongoing work focuses on model adaptations to relevantly, but cost effectively, integrate external condition to building models, particularly with respect to short dynamics energy applications (see Frayssinet et al. (2017b)). Indeed, particular rapid physical processes such as transfers linked with aeraulics or solar loads transmitted by windows, which are not smoothed by conduction and inertia, are critical for power loads and thermal comfort analysis.

Acknowledgments

Authors sincerely thank Jean-Luc Hubert and Maya Milliez from the EDF R&D and BHEE for their support when preparing this work.

Cette thèse est accessible à l'adresse : http://theses.insa-lyon.fr/publication/2018LYSEI071/these.pdf
© [L. Frayssinet], [2018], INSA Lyon, tous droits réservés

References

Bouyer, J., Inard, C., Musy, M., Jul. 2011. Microclimatic coupling as a solution to improve building energy simulation in an urban context. Energy and Buildings 43 (7), 1549–1559.

CNRM, M. F., 2015. Town energy balance.
URL `http://http://www.umr-cnrm.fr/spip.php?article199/`

Còstola, D., Blocken, B., Ohba, M., Hensen, J., Jun. 2010. Uncertainty in airflow rate calculations due to the use of surface-averaged pressure coefficients. Energy and Buildings 42 (6), 881–888.

Frayssinet, L., Kuznik, F., Hubert, J.-L., Milliez, M., Roux, J.-J., 2017a. Adaptation of building envelope models for energy simulation at district scale. Energy Procedia 122, 307–312.

Frayssinet, L., Merlier, L., Kuznik, F., Hubert, J.-L., Milliez, M., Roux, J.-J., 2017b. Modeling the heating and cooling energy demand of urban buildings at city scale. submitted to Renewable and Sustainable Energy Reviews.

Malys, L., Musy, M., Inard, C., Jul. 2015. Microclimate and building energy consumption: study of different coupling methods. Advances in Building Energy Research 9 (2), 151–174.

Masson, V., 2000. A physically based scheme for the urban energy budget in atmospheric models. Boundary layer meteorology 94, 357–397.

Cette thèse est accessible à l'adresse : http://theses.insa-lyon.fr/publication/2018LYSEI071/these.pdf
© [L. Frayssinet], [2018], INSA Lyon, tous droits réservés

Merlier, L., Frayssinet, L., Johannes, K., Kuznik, F., 2018a. On the impact of local microclimate on building performance simulation. part i: Prediction of building external conditions. submitted to Building Simulation.

Merlier, L., Jacob, J., Sagaut, P., 2018b. Lattice-Boltzmann Large-Eddy Simulation of pollutant dispersion in street canyons including tree planting effects. submitted.

Mirsadeghi, M., Còstola, D., Blocken, B., Hensen, J., Jul. 2013. Review of external convective heat transfer coefficient models in building energy simulation programs: Implementation and uncertainty. Applied Thermal Engineering 56 (1-2), 134–151.

Morille, B., Lauzet, N., Musy, M., Nov. 2015. SOLENE-microclimate: A Tool to Evaluate Envelopes Efficiency on Energy Consumption at District Scale. Energy Procedia 78, 1165–1170.

Musy, M., Malys, L., Morille, B., Inard, C., Dec. 2015. The use of SOLENE-microclimat model to assess adaptation strategies at the district scale. Urban Climate 14, 213–223.

Obrecht, C., Kuznik, F., Merlier, L., Roux, J.-J., Tourancheau, B., Aug. 2015. Towards aeraulic simulations at urban scale using the lattice Boltzmann method. Environmental Fluid Mechanics 15 (4), 753–770.

Pigeon, G., Zibouche, K., Bueno, B., Le Bras, J., Masson, V., Jun. 2014. Improving the capabilities of the Town Energy Balance model with up-to-date building energy simulation algorithms: an application to a set of representative buildings in Paris. Energy and Buildings 76, 1–14.

Cette thèse est accessible à l'adresse : http://theses.insa-lyon.fr/publication/2018LYSEI071/these.pdf
© [L. Frayssinet], [2018], INSA Lyon, tous droits réservés

Plessis, G., Kaemmerlen, A., Lindsay, A., Mar. 2014. BuildSysPro: a Modelica library for modelling buildings and energy systems. Lund, Sweden, pp. 1161–1169.

Ramponi, R., Gaetani, I., Angelotti, A., Aug. 2014. Influence of the urban environment on the effectiveness of natural night-ventilation of an office building. Energy and Buildings 78, 25–34.

Rochard, U., Shanthirablan, S., Brejon, C., Chateau le Bras, M., 2015. Bâtiments résidentiels: Typologie du parc existant et solutions exemplaires pour la rénovation énergétique en France. Tech. rep.

Salvati, A., Coch Roura, H., Cecere, C., Jul. 2017. Assessing the urban heat island and its energy impact on residential buildings in Mediterranean climate: Barcelona case study. Energy and Buildings 146, 38–54.

Schumann, M., Charrier, B., Plessis, G., Wall-Ribot, B., 2016. BuildSysPro un bibliothèque Modelica open source pour l'énergétique des bâtiments et des quartiers. In: Conférence IBPSA France. Marne la Vallée, France.

Sun, Y., Augenbroe, G., Jul. 2014. Urban heat island effect on energy application studies of office buildings. Energy and Buildings 77, 171–179.

Sun, Y., Heo, Y., Xie, H., Tan, M., Wu, J., Augenbroe, G., 2011. Uncertainity quantification of microclimate variables in building energy simulation. In: Proceedings of Building Simulation 2011: 12th Conference of International Building Performance Simulation Association. Sydney, Australia, pp. 2423–2430.

Cette thèse est accessible à l'adresse : http://theses.insa-lyon.fr/publication/2018LYSEI071/these.pdf
© [L. Frayssinet], [2018], INSA Lyon, tous droits réservés

418 Yang, X., Zhao, L., Bruse, M., Meng, Q., Nov. 2012. An integrated simu-
419 lation method for building energy performance assessment in urban envi-
420 ronments. Energy and Buildings 54, 243–251.

421 Zinzi, M., Carnielo, E., Mattoni, B., Jul. 2018. On the relation between urban
422 climate and energy performance of buildings. A three-years experience in
423 Rome, Italy. Applied Energy 221, 148–160.

Cette thèse est accessible à l'adresse : http://theses.insa-lyon.fr/publication/2018LYSEI071/these.pdf
© [L. Frayssinet], [2018], INSA Lyon, tous droits réservés

List of Figures

Cette thèse est accessible à l'adresse : http://theses.insa-lyon.fr/publication/2018LYSEI071/these.pdf
© [L. Frayssinet], [2018], INSA Lyon, tous droits réservés

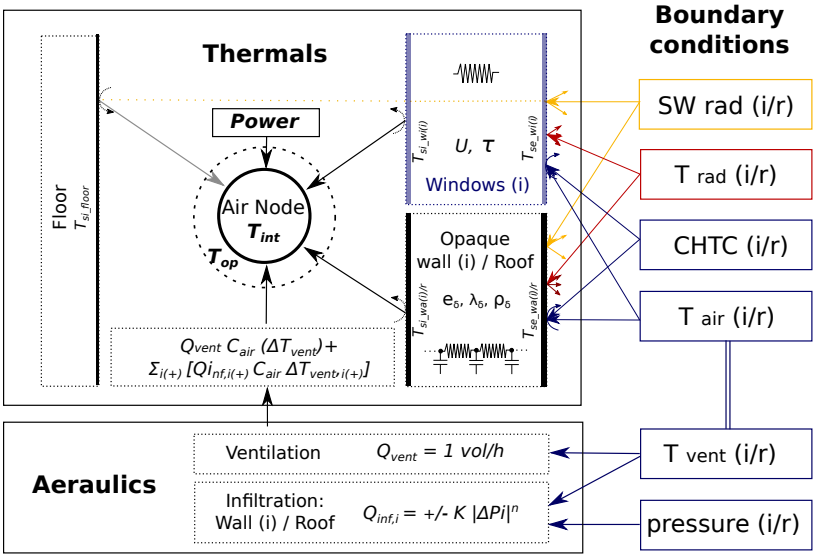

Figure 1: BuildSysPro model

Cette thèse est accessible à l'adresse : http://theses.insa-lyon.fr/publication/2018LYSEI071/these.pdf
© [L. Frayssinet], [2018], INSA Lyon, tous droits réservés

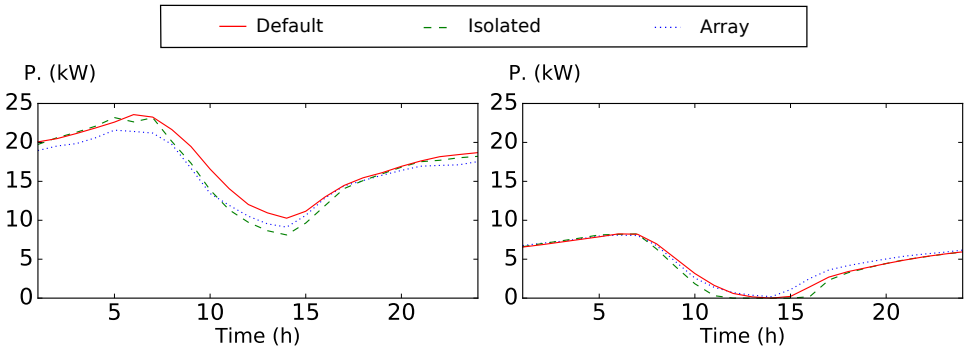

(a) Initial building
Mean power needs: Default = 17.4 kW, Isolated = 16.5 kW, Array = 16.2 kW

(b) Renovated building
Mean power needs: Default = 4.7 kW, Isolated = 4.2 kW, Array = 4.5 kW

Figure 2: Influence of the modeling approach: modification of the heating needs induced by the adjustment of external conditions.

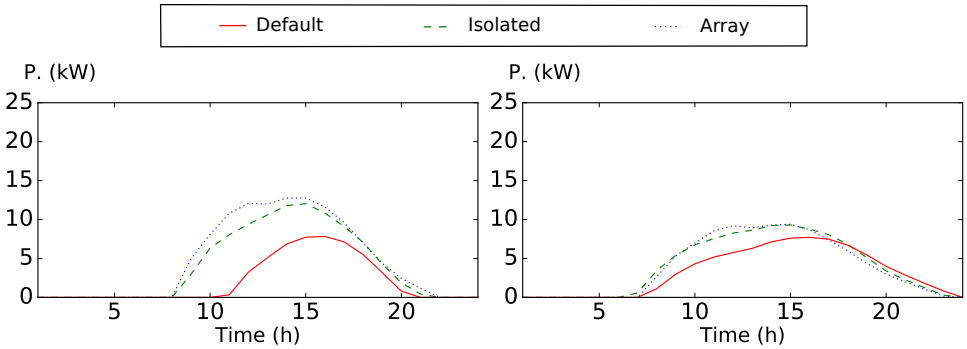

(a) Initial building
Mean power needs: Default = 2.0 kW, Isolated = 3.9 kW, Array = 4.6 kW

(b) Renovated building
Mean power needs: Default = 3.2 kW, Isolated = 4.0 kW, Array = 3.9 kW

Figure 3: Influence of the modeling approach: modification of the cooling needs induced by the adjustment of external conditions.

Cette thèse est accessible à l'adresse : http://theses.insa-lyon.fr/publication/2018LYSEI071/these.pdf
© [L. Frayssinet], [2018], INSA Lyon, tous droits réservés

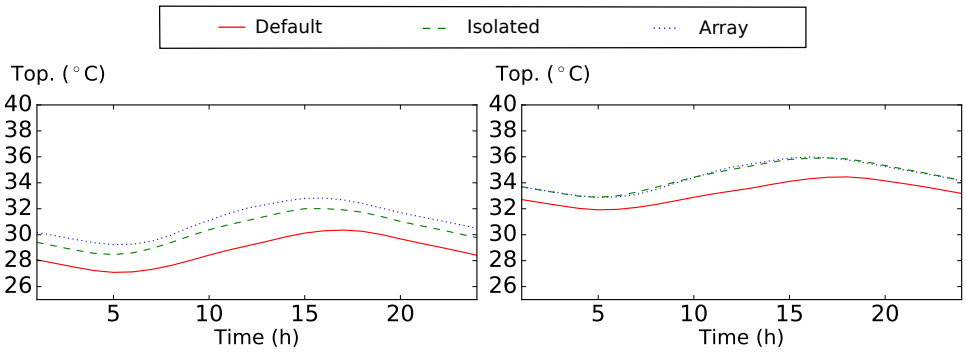

(a) Initial building
Mean operative temp.: Default = 28.7 °C, Isolated = 30.3 °C, Array = 31.1 °C

(b) Renovated building
Mean operative temp.: Default = 33.2 °C, Isolated = 34.5 °C, Array = 34.5 °C

Figure 4: Influence of the modeling approach: modification of the indoor operative temperature induced by the adjustment of external conditions.

Cette thèse est accessible à l'adresse : http://theses.insa-lyon.fr/publication/2018LYSEI071/these.pdf
© [L. Frayssinet], [2018], INSA Lyon, tous droits réservés

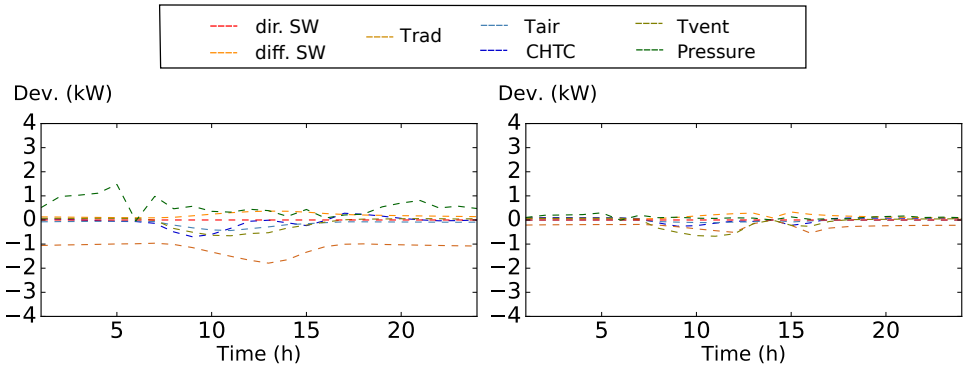

(a) Initial: Isolated−Default

(b) Renovated: Isolated−Default

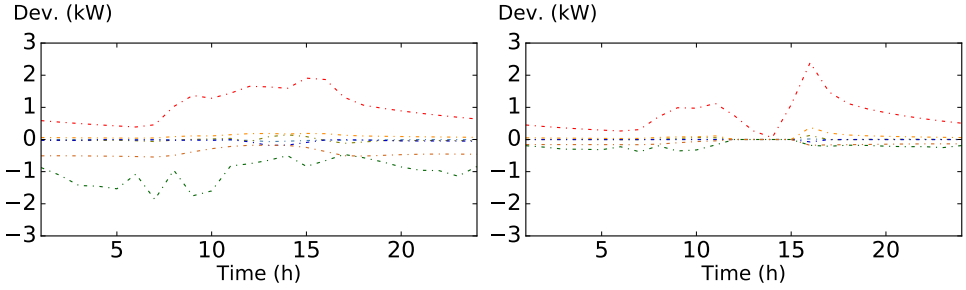

(c) Initial: Array−Isolated

(d) Renovated: Array−Isolated

Figure 5: Influence of the built configuration: modification of the heating needs induced by the adjustment of external conditions.

Cette thèse est accessible à l'adresse : http://theses.insa-lyon.fr/publication/2018LYSEI071/these.pdf
© [L. Frayssinet], [2018], INSA Lyon, tous droits réservés

Mean (and Max.) urban effects (Array - Isolated) [kW]				
Building state	Phenom.	Heating [kW]	Cooling [kW]	Summer comfort [°C]
Initial	SW rad.	1.1 (2.1)	-0.7 (-3.0)	-0.6 (-0.7)
	LW rad.	-0.4 (-0.5)	0.5 (1.4)	0.5 (0.5)
	Aero.	-1.0 (-1.9)	0.3 (1.6)	0.5 (0.6)
	Conv.	-0.1 (-0.2)	0.4 (1.3)	0.4 (0.5)
	Combined	-0.4 (-2.0)	0.6 (2.7)	0.7 (1.0)
Renovated	SW rad.	0.8 (2.5)	-0.6 (-1.9)	-1.1 (-1.2)
	LW rad.	-0.1 (-0.2)	0.2 (0.5)	0.4 (0.5)
	Aero.	-0.2 (-0.4)	0.2 (1.2)	0.6 (0.7)
	Conv.	0.0 (0.0)	0.1 (0.2)	0.1 (0.1)
	Combined	0.5 (2.3)	-0.1 (1.0)	-0.0 (0.2)

Table 1: Influence of the built configuration: effect of boundary conditions
- SW rad.: Short wave rad. ($dir.\ SW+diff.\ SW$), - LW rad.: Long wave rad. (T_{rad}),
- Aero.: Infiltration+ventilation ($Pressure+T_{vent}$), - Conv.: Convection ($CHTC+T_{air}$),
- Combined: Combined effects (all environmental variables)

3.0.1. Heating needs

The general effect of surrounding buildings on heating needs is inverse for the initial and the renovated buildings. In the initial building, the urban environment increases heating needs by 2 % during the day and decreases them by 5 % during the night. As a result, surrounding buildings decrease heating needs by 2 % on average. Regarding the renovated building, the general effect of the urban environment appears negligible during the night but its effect during daytime leads to an average increase of heating needs by 6 %.

This effect of surrounding buildings on heating needs is mainly explained by the sun shading induced by surrounding buildings, which is the most influential modification of external conditions affecting heating loads. This effect is major during daytime as the East and West and mainly the South faces are masked. Reduced short wave fluxes increase heating needs of the initial building by 7 %. The increase is of 10 % for the renovated building, which evidences its higher sensibility to solar flux. Heating is even needed around midday in this configuration, which is not the case for the isolated

Cette thèse est accessible à l'adresse : http://theses.insa-lyon.fr/publication/2018LYSEI071/these.pdf
© [L. Frayssinet], [2018], INSA Lyon, tous droits réservés

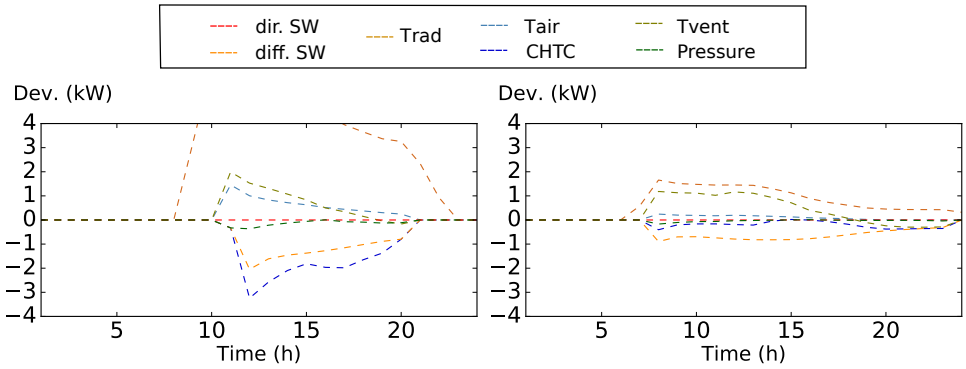

(a) Initial: Isolated−Default

(b) Renovated: Isolated−Default

(c) Initial: Array−Isolated

(d) Renovated: Array−Isolated

Figure 6: Influence of the built configuration: modification of the cooling needs induced by the adjustment of external conditions.

Cette thèse est accessible à l'adresse : http://theses.insa-lyon.fr/publication/2018LYSEI071/these.pdf
© [L. Frayssinet], [2018], INSA Lyon, tous droits réservés

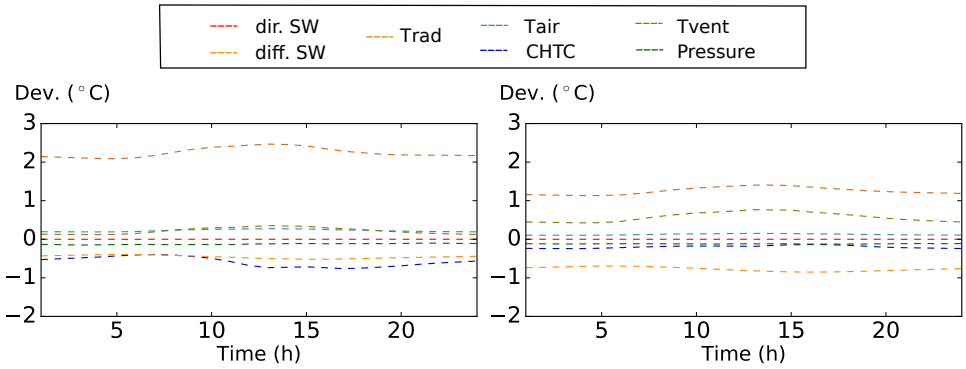

(a) Initial: Isolated−Default

(b) Renovated: Isolated−Default

(c) Initial: Array−Isolated

(d) Renovated: Array−Isolated

Figure 7: Influence of the built configuration: modification of the indoor operative temperature induced by the adjustment of external conditions.

Cette thèse est accessible à l'adresse : http://theses.insa-lyon.fr/publication/2018LYSEI071/these.pdf
© [L. Frayssinet], [2018], INSA Lyon, tous droits réservés

building.

The influence of surrounding buildings on other external conditions counterbalance the effect of solar masks. In particular, aeraulic effects nearly compensate the effect of the reduced short wave radiative flux for the initial building, which support a higher sensitivity of the this building to other boundary conditions than the renovated building. The alteration of aeraulic induced heat transfers, as well as of long wave radiative heat transfer, by surrounding buildings is three times less influential in the renovated than in the initial building (-2 % and -1 % versus -7 %and -3 % respectively), and the contribution of convective heat transfers is negligible for both building states.

3.0.2. Cooling needs

On average, the general effect of surrounding buildings is an increase of cooling needs by 5 % for the initial building. The effect of the urban environment is especially visible during the morning. On the contrary, the presence of surrounding buildings tends to slightly decrease the cooling needs by 1 % for the renovated building.

As for heating, the modification of short wave radiative fluxes due to surrounding buildings is the most influential contribution affecting cooling needs for both building states. Although being slightly modulated by increased reflexion, solar masks reduce cooling needs by 6 and 7 % for the initial and renovated buildings respectively. This decrease of cooling needs is particularly due to two main gaps occurring in the morning and afternoon, which respectively correspond to the shading of the East and West faces.

The modification of the other boundary conditions, i.e. the increase of environmental radiant temperature, the decrease of ventilation potential and of convective heat transfers are opposite to the effects of the reduced solar loads. For the initial building, their combined effect is even higher than the effect of solar masks. This is also the case for the renovated building, but only during midday. Indeed, in this configuration, solar effects remains dominant during the early morning and the evening.

3.0.3. Summer comfort

Results analysis highlights comparable trends for the operative temperature as for cooling needs. On average, the urban environment increases the operative temperature of the initial building by 0.7 °C while the operative temperature of the renovated building remains similar in the array and

Cette thèse est accessible à l'adresse : http://theses.insa-lyon.fr/publication/2018LYSEI071/these.pdf
© [L. Frayssinet], [2018], INSA Lyon, tous droits réservés

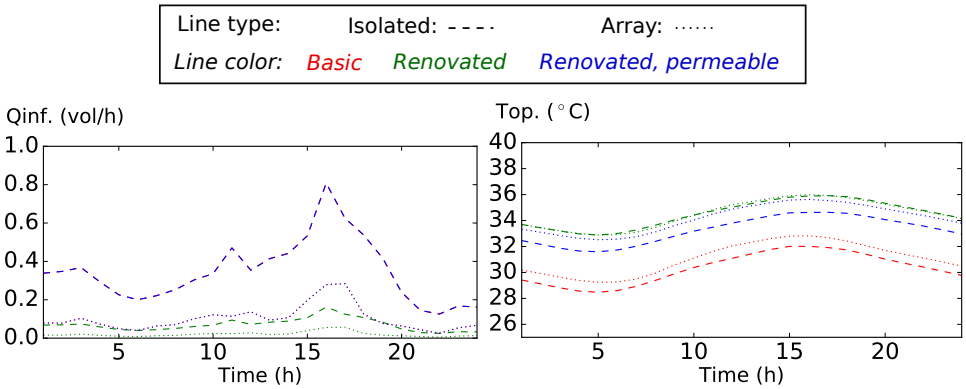

(a) Infiltrated air flow rates (b) Operative temperature

Figure 8: Effect of pressure on free cooling potential.

494 in the isolated configuration because of compensations. The modification
495 of short wave radiation induced by surrounding buildings is the most influ-
496 ential effect on the building thermal behavior. It decreases the operative
497 temperature by 0.6 °C and 1.1 °C respectively for the initial and renovated
498 buildings.

Cette thèse est accessible à l'adresse : http://theses.insa-lyon.fr/publication/2018LYSEI071/these.pdf
© [L. Frayssinet], [2018], INSA Lyon, tous droits réservés

List of Tables

Cette thèse est accessible à l'adresse : http://theses.insa-lyon.fr/publication/2018LYSEI071/these.pdf
© [L. Frayssinet], [2018], INSA Lyon, tous droits réservés

	Wall	Window	Roof
Initial state			
Surface [m^2]	250	77	140
Materials	40 cm stone	double glazing	13 cm plaster + 2 cm insul. + tile
U [$W\,m^{-2}\,K^{-1}$]	1.7	2.6	1.35
Renovated			
Materials	12 cm insulation	triple glazing	12 cm insul. + 18 cm wood fiber
U [$W\,m^{-2}\,K^{-1}$]	0.24	1	0.2

Table 2: Thermal properties of the generic test cases.

Cette thèse est accessible à l'adresse : http://theses.insa-lyon.fr/publication/2018LYSEI071/these.pdf
© [L. Frayssinet], [2018], INSA Lyon, tous droits réservés

Mean (and Max.) modeling effects (Isolated - Default)				
Building state	Phenom.	Heating [kW]	Cooling [kW]	Summer comfort [°C]
Initial	SW rad.	0.2 (0.4)	-0.5 (-2.0)	-0.5 (0.5)
	LW rad.	-1.2 (-1.8)	2.6 (8.1)	2.2 (2.5)
	Aero.	0.4 (1.6)	0.3 (1.7)	0.1 (0.3)
	Conv.	-0.3 (-0.9)	-0.5 (-1.8)	-0.3 (-0.5)
	Combined	-0.9 (-2.7)	2.0 (7.7)	1.6 (2.0)
Renovated	SW rad.	0.1 (0.3)	-0.4 (-0.9)	-0.8 (-0.9)
	LW rad.	-0.3 (-0.5)	0.7 (1.7)	1.3 (1.4)
	Aero.	0.0 (-0.7)	0.3 (1.2)	0.5 (0.7)
	Conv.	-0.0 (-0.3)	-0.1 (-0.3)	-0.1 (-0.2)
	Combined	-0.3 (-1.3)	0.7 (2.5)	1.3 (1.7)

Table 3: Influence of the modeling approach: effect of boundary conditions
- SW rad.: Short wave rad. ($dir.\ SW+diff.\ SW$), - LW rad.: Long wave rad. (T_{rad}),
- Aero.: Infiltration+ventilation ($Pressure+T_{vent}$), - Conv.: Convection ($CHTC+T_{air}$),
- Combined: Combined effects (all environmental variables)

Cette thèse est accessible à l'adresse : http://theses.insa-lyon.fr/publication/2018LYSEI071/these.pdf
© [L. Frayssinet], [2018], INSA Lyon, tous droits réservés

FOLIO ADMINISTRATIF

THESE DE L'UNIVERSITE DE LYON OPEREE AU SEIN DE L'INSA LYON

NOM : Frayssinet DATE de SOUTENANCE : 26/10/2018

Prénoms : Loïc

TITRE : Adapter les modèles de chauffage et climatisation des bâtiments en puissance à l'échelle du quartier

NATURE : Doctorat Numéro d'ordre : 2018LYSEI071

Ecole doctorale : Mécanique, Energétique, Génie Civil, Acoustique

Spécialité : Thermique Energétique

RESUME :
Les modèles énergétiques des bâtiments à l'échelle du quartier sont généralement simplifiés pour faire face au manque de données et pour réduire le coût de calcul. Cependant, l'impact de ces simplifications sur la validité des modèles n'est pas systématiquement analysée, en particulier lorsqu'on s'intéresse à la courbe de charge.
Pour combler ce manque, une méthodologie permettant de quantifier la validité des simplifications, notamment vis-à-vis de la courbe de charge, est proposée. Cette méthodologie est appliquée aux simplifications couramment utilisée pour les modèles thermiques d'enveloppe de bâtiments grâce à une plateforme numérique développée dans le cadre de cette thèse. Cette plateforme permet de générer et simuler automatiquement des modèles énergétiques de bâtiments, avec différents niveaux de détails, à partir de données issues de systèmes d'information géographique. La parallélisation des simulations énergétiques des bâtiments est utilisée à l'échelle du quartier, afin de tirer avantage de la structure du modèle global et de réduire les temps de calculs.
La définition d'indicateurs spécifiques selon l'objectif de simulation apparait clairement comme l'étape essentielle lorsque l'on s'intéresse à la courbe de charge. Les résultats indiquent que la puissance est plus sensible aux simplifications que la consommation annuelle d'énergie. Les différents effets induits sont quantifiés et analysés physiquement. La capacité de l'échelle du quartier à atténuer les impacts des simplifications et d'intégrer les données statistiques est démontrée. La quantification des impacts des simplifications permet de guider l'adaptation des modèles vis-à-vis des objectifs de simulation et vis-à-vis des contraintes techniques. Cette contribution a pour objectif d'améliorer la performance des simulations énergétiques à l'échelle de la ville, et de favoriser leur développement, afin de répondre aux enjeux futurs.

MOTS-CLÉS : Energétique des bâtiments, échelle quartier

Laboratoire (s) de recherche : CETHIL

Directeur de thèse: Kuznik, Frédéric
Co-directeur de thèse: Roux, Jean-Jacques

Président de jury :

Composition du jury : Duplessis, Bruno ; Fraisse Gilles ; Inard, Christian ; Kuznik, Frédéric ; Musy Marjorie ; Roux, Jean-Jacques.

Cette thèse est accessible à l'adresse : http://theses.insa-lyon.fr/publication/2018LYSEI071/these.pdf
© [L. Frayssinet], [2018], INSA Lyon, tous droits réservés

Cette thèse est accessible à l'adresse : http://theses.insa-lyon.fr/publication/2018LYSEI071/these.pdf
© [L. Frayssinet], [2018], INSA Lyon, tous droits réservés